



ՀԱՅԱՍՏԱՆԻ ՔԻՄԻԱԿԱՆ ՀԱՆԴԵՍ

ХИМИЧЕСКИЙ ЖУРНАЛ АРМЕНИИ

CHEMICAL JOURNAL OF ARMENIA

Издается с 1947 г.
Выходит 4 раза в год на русском, армянском и английском языках

ՄԱՆԹԱՇՅԱՆ Ա.Հ. – գլխավոր խմբագիր
ԻՆՃԻԿՅԱՆ Մ.Հ. – գլխավոր խմբագրի տեղակալ
ՍԱՀԱԿՅԱՆ Ս.Ս. – պատասխանատու քարտուղար

ԽՐԱԳՐԱԿԱՆ ԿՈԼԵԳԻԱ

ՀԱՅՐԱՊԵՏՅԱՆ Ս.Ս., ՎԱՐԴԱՆՅԱՆ Ի.Ա. (պատասխանատու խմբագիր), ԶԱՎԱԴՅԱՆ Վ.Գ., ԿՈՍՏԱՆՅԱՆ Կ.Ա. (պատասխանատու խմբագիր), ԿՈՒՐՏԻԿՅԱՆ Տ.Ս., ՄԱՐԳԱՐՅԱՆ Է.Ա., ՄԱՏՆԻՇՅԱՆ Հ.Ա. (պատասխանատու խմբագիր), ՄԻՐԶՈՅԱՆ Ֆ.Վ., ՆԵՐՍԻՍՅԱՆ Ս.Ա., ՀՈՎԱԿԻՄՅԱՆ Մ.Ժ. (պատասխանատու խմբագիր), ՓԱՆՈՍՅԱՆ Գ.Ա., ՍԱՀՅԱՆ Ա.Ս., ԽԱՉԱՏՐՅԱՆ Հ.Գ. (պատասխանատու խմբագիր)

ԽՐԱԳՐԱԿԱՆ ԽՈՐՀՈՒՐԴ

ԱՎԵՏԻՍՅԱՆ Ա.Ա., ԲԱԲԱՅԱՆ Հ.Գ., ԲԱԲԱՅԱՆ Ս.Գ., ԲԵԼԵՏԿԱՅԱ Ի.Պ. (Ռուսաստան), ԲԵՐԼԻՆ Ա.Ա. (Ռուսաստան), ԲՈՐԻՍՈՎ Ա.Ա. (Ռուսաստան), ԳԵՎՈՐԿՅԱՆ Ա.Հ., ԳՐԻԳՈՐՅԱՆ Ս.Կ., ԳՅՈՒՆԱԶԱՐՅԱՆ Ա.Խ., ԴԱՎԹՅԱՆ Ս.Պ., ՀԱՍՐԱԹՅԱՆ Գ.Վ., ՆՈՐԱՎՅԱՆ Ա.Ս., ՍԱՐԿԻՍՈՎ Օ.Մ. (Ռուսաստան), ԹԱՎԱԴՅԱՆ Լ.Ա.

МАНТАШЯН А.А. – главный редактор
ИНДЖИКЯН М.Г. – заместитель главного редактора
СААКЯН С.С. – ответственный секретарь

РЕДАКЦИОННАЯ КОЛЛЕГИЯ

АЙРАПЕТЯН С.М., ВАРДАНЯН И.А. (ответств. редактор), ДЖАБАДЯН В.Г., КОСТАНИЯН К.А. (ответств. редактор), КУРТИКЯН Т.С., МАРКАРЯН Э.А., МАТНИШЯН А.А. (ответств. редактор), МИРЗОЯН Ф.В., НЕРСЕСЯН С.А., ОВАКИМЯН М.Ж. (ответств. редактор), ПАНОСЯН Г.А., САГИЯН А.С., ХАЧАТРИАН А.Г. (ответств. редактор)

РЕДАКЦИОННЫЙ СОВЕТ

АВETИСЯН А.А., АСПРЯН Г.В., БАБАЯН Г.Г., БАБАЯН С.Г., БЕЛЕЦКАЯ И.П. (Россия), БЕРЛИН А.А. (Россия), БОРИСОВ А.А. (Россия), ГЕВОРКЯН А.А., ГРИГОРЯН С.К., ГЮЛЬНАЗАРЯН А.Х., ДАВТЯН С.П., НОРАВЯН А.С., САРКИСОВ О.М. (Россия), ТАВАДЯН Л.А.

MANTASHYAN A.A. – Editor-in-chief
INJIKYAN M.H. – Deputy Editor
SAHAKYAN S.S. – Technical Editor

EDITORIAL BOARD

HAYRAPETYAN S.M., VARDANYAN I.A. (executive editor), JAVADYAN V.G., KOSTANYAN K.A. (executive editor), KURTIKYAN T.S., MARGARYAN E.A., MATNISHYAN H.A. (executive editor), MIRZOYAN F.V., NERSISYAN S.A., HOVAKIMYAN M.Zh. (executive editor), PANOSYAN H.A., SAGYAN A.S., KHACHATRYAN H.G. (executive editor)

EDITORIAL COUNCIL

AVETISSYAN A.A., BABAYAN H.G., BABAYAN S.G., BELETSKAYA I.P. (Russia), BERLIN A.A. (Russia), BORISOV A.A. (Russia), GEVORKYAN A.A., GRIGORYAN S.K., GYULNAZARYAN A.Kh., DAVTYAN S.P., HASRATYAN G.V., NORAVYAN A.S., SARKISOV O.M. (Russia), TAVADYAN L.A.

*“Химический журнал Армении” реферируется
в “Chemical Abstracts” (США) и РЖХим (Россия).*

<http://chemjournal.sci.am>

☐ Издательство “Гитутюн” НАН Республики Армения
Химический журнал Армении, 2007

В настоящем номере публикуются материалы докладов международной конференции “Неизотермические явления и процессы”, которая проходила с 27 ноября по 1 декабря 2006 г. в Ереване.

Статьи публикуются в авторском варианте без дополнительного редактирования.

This issue contains the contributions presented at the International Conference “Nonisothermal Phenomena and Processes” held 27 November – 01 December 2006 in Yerevan.

Articles are published from author's copy without additional editing.

Все расходы по выпуску данного номера журнала предоставлены Фондом “Технологическое горение и материаловедение” (www.chph.sci.am/csms_fund.htm)

Publication expenses of this issue of the Journal were fully supported by the “Combustion synthesis and Materials science” Fund (www.chph.sci.am/csms_fund.htm)

Ответственный за номер *Харатян С.Л.*

Responsible for the issue *Kharatyan S.L.*

Международная конференция «Неизотермические явления и процессы»

27 ноября - 1 декабря 2006 г., Ереван, Армения

С 27-го ноября по 1-ое декабря в Ереване проводилась Международная конференция «Неизотермические явления и процессы», приуроченная к 75-летию академика РАН и иностранного члена НАН Республики Армения Александра Григорьевича Мержанова. Организаторы конференции: Институт химической физики Национальной Академии Наук Армении, Академия Наук Российской Федерации, Министерство Образования и Науки Армении, Мировая Академия Керамики.

На конференции рассматривались неизотермические явления и процессы, протекающие преимущественно в химически реагирующих средах под влиянием внутренних источников тепла и/или под воздействием внешних тепловых полей.

Обсуждались следующие проблемы:

- неизотермическая кинетика;
- самораспространяющийся высокотемпературный синтез;
- неизотермические явления и процессы в физике и механике;
- тепловой взрыв, зажигание и распространение пламени в газифицирующихся средах;
- саморазогрев, самовозгорание и сгорание горючих веществ в окислительной среде.

На конференции присутствовали и выступили с устными или стендовыми докладами около 120 ученых, сотрудники известных в мире научных центров и университетов из России (40 участников), Армении (50 участников), США (6 участников), Великобритании (5 участников), Испании (4 участника), Грузии (4 участника), Китая (2 участника), Италии (2 участника), Израиля (2 участника), Франции (1 участник), Польши (1 участник), Казахстана (1 участник). Церемонии открытия и закрытия Конференции проходили в здании Президиума НАН Армении, а основные заседания – в двух залах гостиницы Ани Плаза. На церемонии открытия с приветственными речами выступили президент НАН Армении Р. М. Мартиросян, зам.министра образования и науки А. С. Аветисян и другие. Кроме поздравлений и теплых слов в адрес юбиляра, оценки его большого вклада в науку России и мира, отмечались также его большие заслуги в деле развития науки, образования и промышленности Армении. Президент НАН Армении Р. М. Мартиросян в торжественных условиях вручил А. Г. Мержанову диплом иностранного члена Академии Наук Армении, а зам.министра А. С. Аветисян – золотую медаль министерства образования и науки Армении. Зачитывались также поздравительные телеграммы, поступившие от президента России В.В. Путина, Президиума АН РФ и многих известных ученых из различных научных центров

РФ. Вечером 27-го ноября был организован торжественный ужин, где А. Г. Мержанова поздравляли и вручали подарки и поздравительные адреса представители многих научных центров из разных стран. Особое праздничное настроение на вечере поддерживалось фольклорным ансамблем «Акунк» Государственного радио Армении, с высоким мастерством исполнившим армянские национальные песни и танцы.

На рабочих заседаниях конференции по приглашению Оргкомитета с пленарными докладами выступили известные ученые: Дж.К. Джонс (Великобритания), Д. Шехтман (Израиль), Ю. Д. Третьяков (Россия), Н. Тадани (США), А. С. Штейнберг (США), Р. Пампук (Польша), Т. Ивлева (Россия), А. А. Мантасян (Армения), С. П. Давтян (Армения).

Были представлены также 45 устных и 35 стендовых докладов. Среди докладчиков было много молодых специалистов. Особый интерес вызвали и активно обсуждались доклады академика АН РФ Ю.Д.Третьякова, профессоров Д. Шехтмана, Н. Тадани, А. Хейхерста, О. Одавары, Т. П. Ивлевой, А. Е. Сычева и др., в которых обсуждались новейшие научные достижения в соответствующей области.

В результате заинтересованных обсуждений выдвигались предложения о новых возможностях сотрудничества между различными научными центрами.

Для гостей конференции, помимо научной, была организована также содержательная культурная программа. В частности, были организованы экскурсии в хранилище древних рукописей Матенадаран, Кафедральный собор св. Эчмиадзина, Ереванский коньячный завод, языческий храм Гарни, монастырь Гегард, Государственный Академический театр им. А. Спендиаряна (опера «Ануш») и т.д.

Конференция, несомненно, благоприятствовала установлению новых связей между научными центрами стран-участниц и развитию международного научного сотрудничества.

Успешному проведению конференции во многом способствовала финансовая поддержка министерства образования и науки Армении, фонда «Технологическое горение и материаловедение» и Национального фонда науки и передовых технологий (NFSAT).

**ՀԱՅԱՍՏԱՆԻ ՀԱՆՐԱՊԵՏՈՒԹՅԱՆ ԳԻՏՈՒԹՅՈՒՆՆԵՐԻ
ԱԶԳԱՅԻՆ ԱԿԱԴԵՄԻԱ
НАЦИОНАЛЬНАЯ АКАДЕМИЯ НАУК РЕСПУБЛИКИ
АРМЕНИЯ**

Հայաստանի քիմիական հանդես **60, №2, 2007** Химический журнал Армении

**REFLECTIONS ON COMBUSTION PRINCIPLES AS THEY RELATE
TO A MISCELLANY OF PRACTICAL FUELS**

J.C. JONES

University of Aberdeen, Scotland

1. Introduction.

I recently visited one of the island communities to the north of Scotland in order to give advice on a project whereby waste cardboard is made into fuel briquettes. I thought it preferable if at all possible to conduct a combustion test on the briquettes during the few days that I was there. We therefore borrowed a pair of thermocouples and a multimeter from the local power station. We took those and four of the cardboard briquettes to the home of one of the local participants in the project, where we placed the four briquettes in a domestic stove and ignited them. We placed one thermocouple in the assembly of briquettes and the other in ice contained in a beaker such as one might serve tea or coffee in. We wrote down the e.m.f. displayed at the multimeter, at first every 30 seconds and later less frequently.

Experimental work does not come any cruder than that, yet we were able to glean a considerable amount of semi-quantitative information from the results, sufficient to answer relevant questions on the part of a potential purchaser of the briquettes. These results will be discussed later in the paper. We also consider the following and examine them according to combustion principles including the now very important one of possible carbon neutrality.

Solid biomass fuels

Tyre-derived fuels

Fuels for SI engines other than gasoline

Fuels for CI engines other than diesel

Also:

Liquid explosives, in relation to the recent terrorist threat at Heathrow Airport.

2. Solid biomass fuels.

2.1. Preamble.

Wood has of course also found fuel use for a very long time: it was not until the 1890s that coal usage exceeded wood usage in the USA. In this paper however we consider wood and other cellulosic fuels in the modern sense, as 'biofuels', 'renewables' and 'carbon neutral' fuels. The last of these terms will be explained in full as it is the 'selling point' of biomass fuels in the modern world.

2.2. Carbon neutrality.

A fuel is said to be carbon neutral if its combustion makes no net contribution to the carbon dioxide content of the atmosphere. The ultimate in carbon neutrality is of course hydrogen fuel: the fuel itself contains no carbon and so obviously cannot produce carbon dioxide. That is why at some scenes of natural gas production, including the Miller Field in the North Sea, natural gas is reformed to hydrogen for subsequent use in power generation. When biomass fuels are considered the term carbon neutrality has to be thought about more carefully. A related calculation follows.

Suppose it is required to produce heat at 10 MW. How much carbon dioxide per hour will this produce:

(a) If the fuel is bituminous coal of carbon content 85% and calorific value 30 MJ kg^{-1} ?

(b) If the fuel is wood waste of carbon content 55% and calorific value 17 MJ kg^{-1} ?

Solution:

(a) Rate of requirement of fuel = $(10^7 \text{ J s}^{-1} / 30 \times 10^6 \text{ J kg}^{-1}) \times 3600 \text{ s hour}^{-1}$
= $1200 \text{ kg hour}^{-1} \Rightarrow 1020 \text{ kg hour}^{-1}$ of carbon burnt $\Rightarrow 3740 \text{ kg CO}_2$

(b) Rate of requirement of fuel = $(10^7 \text{ J s}^{-1} / 17 \times 10^6 \text{ J kg}^{-1}) \times 3600 \text{ s hour}^{-1}$
= $2117 \text{ kg hour}^{-1} \Rightarrow 1164 \text{ kg hour}^{-1}$ of carbon burnt $\Rightarrow 4270 \text{ kg CO}_2$

It is clear then that the carbon neutral fuel produces significantly more carbon dioxide than the conventional fuel per unit heat produced. The above calculation uses arbitrary though typical values for the quantities involved, and that wood fuel produces more carbon dioxide than the coal other things being equal is in fact a general result. Why then is the wood fuel to be preferred on carbon dioxide emission terms? Simply that unlike the carbon in coal the carbon in wood fuel was in the recent past carbon dioxide in the atmosphere, so when the wood is burnt it is simply being put back where it came from. To burn coal (or a petroleum based fuel) is to introduce carbon dioxide into the atmosphere. To burn wood is to put carbon dioxide back into the atmosphere after its

uptake by the wood in growth. A fully grown tree absorbs about 25 kg per year from the atmosphere which is returned there when the dead wood is burnt.

In order that non-renewables obligations are met, biomass and coal might be co-fired. Imagine that in our above example where the total heat release rate is 10 MW that the coal-derived CO₂ has to be reduced by 5% to comply with local non-renewables requirements. The calculation is in the box below.

Coal-derived CO₂ to be reduced from 3740 kg per hour to 3553 kg per hour.

Carbon burnt to be reduced from 1020 to 969 kg per hour.

Coal burnt reduced from 1200 to 1140 kg per hour.

Heat to be provided by the biomass per hour = $60 \times 30 \text{ MJ} = 1800 \text{ MJ}$ requiring $1800/17 = 106 \text{ kg biomass}$ releasing $(106 \times 0.55 \times 44/12) \text{ kg CO}_2 = 214 \text{ kg CO}_2$.

Total CO₂ release per hour = $(3553 + 214) \text{ kg} = 3766 \text{ kg}$

There is therefore a slight increase (0.7 of 1%) of total CO₂ due to partial substitution of the biomass for coal but a reduction as required of 5% of the CO₂ from coal which of course is not carbon neutral.

In relation to the above calculation we should remember that the wood will contain a significant amount of oxygen in its organic structure, and the coal will contain some, perhaps 2-3% for the coal in the example. The carbon dioxide produced will therefore not arise solely from combustion: part of it will be from devolatilisation and in such carbon dioxide the oxygen atoms come not from the air oxidant but from the oxygen content of the fuel. The most helpful way to view this is that the fuel is already, before combustion, partly oxidised. This makes no difference to the calculation of carbon dioxide emissions: it does make a difference when the air requirement to burn a fuel is being calculated and the oxygen content of the fuel must be deducted from the oxygen theoretically required to oxidise the carbon content and the hydrogen content of the fuel. This is standard practice in fuel technology, e.g., in boiler operation. Devolatilisation products of solid fuels include methane and other light hydrocarbons, CO, tars and oils which are of course flammable. In a biomass fuel the combustible devolatilisation products, a.k.a. 'volatiles', will account for well over half of the heat value. That not accounted for by the volatiles is of course in the residual char. This is considered more fully in the next section.

2.3. Devolatilisation.

As stated in the previous paragraph, flammable volatiles are tars/oils, light hydrocarbons such as methane, ethylene and ethane, and carbon monoxide. Non-flammable volatiles,

much less abundantly yielded than the flammable ones, are carbon dioxide and water. When a high-volatile fuel is burnt devolatilisation occurs concurrently with combustion; heat from the burning of the flammable volatiles feeds back to the remaining solid to promote further devolatilisation. The extent of devolatilisation as a function of temperature can be represented by suitable Arrhenius parameters. Devolatilisation involves many reactions within the solid fuel structure including methyl group removal, decarboxylation and cleavage of parts of the organic structure. The overall heat effect is the resultant of the individual heat effects of all such reactions occurring and might be net positive (endothermic) or net negative (exothermic). It will however, regardless of its sign in the thermodynamic sense, be small in comparison with the heat of subsequent *combustion* of volatiles so released. Whether carbon is burnt as a volatile, e.g., a tar fragment, or as part of the residual solid is of course irrelevant to the matter of carbon neutrality. Biomass is always higher than coals in volatile matter; even so, low-rank coals such as the brown coals of the Latrobe Valley in Australia and the similar ones in the deposit which straddles North Dakota USA and Saskatchewan Canada lose 50% or more of their weight by devolatilisation at temperatures in the neighbourhood of 1000°C. The extent of devolatilisation has a moderate dependence on the heating rate as has the distribution of products, e.g., of oxygen in the fuel between CO and CO₂ in the volatiles.

2.4. Control of burning of a high-volatile fuel by ventilation.

We return here to the highly primitive test on the combustion of cardboard briquettes referred to in the introduction. These were burnt in a domestic stove where ideally one would require slow, flameless burning. Flameless burning normally occurs only with fuels already denuded of volatiles such as coke and charcoal. In our tests however the cardboard briquettes did burn flamelessly and the four briquettes, each weighing about 180g, were still burning when temperature measurement ceased after an hour. The reason clearly was under-ventilation resulting in escape of the volatiles with the smoke instead of their combustion in the gas phase. This happened by chance in our test but indicates that a high-volatile fuel which with full ventilation would burn with a vigorous flame can be made to burn like charcoal if ventilation is controlled. Of course, escape of flammable volatiles represents wastage of energy and an enterprise using such fuel on a large scale, e.g., for steam raising (as is proposed for the cardboard fuel which was being examined) would need to avoid this. It is however doubtful whether such ‘uneconomic’ burning would matter on the scale of a domestic fire, although one might want to consider the release of unburnt hydrocarbons into the atmosphere which such burning would result in.

There were considerable temperature variations in the burning assembly of briquettes. About half way through the test the measuring thermocouple was reading just over 500°C and was moved to a part of the fuel bed glowing red whereupon the reading rose to 800°C. Further deliberations on this point form Appendix 1 of the paper.

2.5. Some examples of biomass fuels.

Examples of these are given briefly below with at least one country of usage in brackets in each case. Biomass fuels include: sugar cane residue (a.k.a. bagasse, Australia and Fiji); citrus peel (Florida USA); coconut waste (The Philippines); coffee waste (El Salvador); waste from maize, rice and mustard collectively called crop waste (India); forest thinnings, obtained from removal of wood from trees to reduce the fire susceptibility of the forest of which they are a part (Colorado USA); Mangrove, a tropical shrub (Malaysia and other far East countries); straw (Ely, UK and also Croatia) and Teak waste (Thailand). The points made above about solid biomass fuels generally, including the very important one of carbon neutrality, apply to all of these.

3. Tyre-derived fuel (TDF).

3.1. Preamble.

There are huge amounts of used tyres requiring disposal at any one time. As a rule of thumb in ‘developed’ countries the number of new tyres sold each year is roughly equal to the population, and of course one new tyre bought means one old tyre needing disposal. Fuel use of tyres is fairly widely practised and has been the subject of a recent critique which will be discussed below. The calorific value of the rubber component of tyres is much higher than that of biomass, up to about 40 MJ kg^{-1} . This is higher than the calorific values of even higher rank, low-ash coals which very seldom if ever exceed 35 MJ kg^{-1} .

3.2. Summary of a recent critique of fuel use of waste tyres [2].

The salient points are as follows.

- (a) Tyre waste fuel can reasonably be viewed as carbon neutral in that rubber is a vegetable material.
- (b) The alternative to fuel uses of tyre waste are two: simple incineration and landfill. In the former case there is carbon dioxide release without any return on the heat. In the second decomposition over time will lead to the release of methane, which is a much more powerful greenhouse gas than carbon dioxide. (Each of these points also applies to biomass fuels such as wood which were considered in the previous part of the paper.)
- (c) Tyres tend to burn smokily and the combustion therefore needs to be over-ventilated to minimise smoke. This reduces the combustion temperature.

3.3. Selected scenes of significant usage of tyre waste as fuel.

These include two US electricity utilities: Bay Front, Wisconsin and Marmora NJ. Currently the only plant in Europe which uses waste tyres as a fuel for the generation of electricity is Elm Energy and Recycling in the UK. It has the capacity to burn 100000 tonne of tyres per year and significant power for sale to the grid is possible. A ‘back-of-an-envelope’ calculation of the performance of this facility forms Appendix 2.

4. Fuels for SI engines other than gasoline.

4.1. Introduction.

'Gasoline' can mean mineral gasoline, obtained by refining crude oil or previously retorted shale oil, or manufactured gasoline obtained from coal or other feedstock via synthesis gas or by hydrogenation. The benchmark hydrocarbon against which gasolines are compared in performance terms is of course iso-octane, C_8H_{18} . Natural gas, predominantly methane, is widely used in one of two forms, to be more fully described below, in engines which would otherwise have used gasoline, as is the oxygenated compound methanol.

4.2. Carburetion in SI engines and engine knock.

The working substance in such an engine is of course air, and carburetion takes place in order to provide chemical heat release at the stage in the cycle where it is needed. In a SI engine, ignition is required at a precise stage: ignition ahead of that causes knock, and fuels for SI engines are assessed on the basis of resistance to knock expressed as the octane number. Fuels for SI engines need to be quality controlled at the refining stage for octane rating. Gasoline is the first liquid to come over in refining. If too wide a cut in temperature terms is taken so that the distillate also takes in some of the higher boiling fraction called naphtha it will have too low an octane rating, that is, too low a resistance to knock. This is entirely consistent with the principle that longer hydrocarbon chain lengths signify higher reactivity. Of course, there is no precise upper limit on the fractionation temperature range required to obtain a gasoline of good octane rating or threshold temperature marking the cessation of gasoline production and the commencement of naphtha production. Such matters depend on the composition of the crude oil undergoing distillation, and with some crudes a gasoline fraction obtained even across quite a narrow cut will need to be blended with additives, notably aromatics and branched-chain alkanes, to bring the octane number to the required value.

4.3. Methane as a motor fuel.

Currently unleaded gasoline of research octane number (RON) 95 is widely sold on the forecourts of the world, and one pays extra for gasoline of RON 98. Methane has a RON of 120, significantly better than even the more expensive gasoline. The high resistance to knock of methane is due to its low reactivity; being C_1 it is the least reactive alkane and it is this property which makes it suitable for use in vehicles with SI engines. Spark ignition engines which run on methane are well established, there being many makes and models of car designed to run on compressed natural gas. This of course is simply methane gas a long way above its critical temperature stored under pressure in the vehicle for supply to the engine. As an alternative, the gas can be carried as liquefied natural gas (LNG) and evaporated on its way to the engine. The fuel tank in such a vehicle comprises two membranes with an evacuated space between them.

Whenever a new fuel for motor transport is introduced the confidence not only of the consumer but also of the forecourt operators, whose collective influence is considerable,

has to be won. The author's view is that both LPG and methanol as fuels for vehicles were at least initially adversely affected by lack of such confidence. Consequently much R&D went into making refuelling facilities for vehicles powered by LNG not only user-friendly but familiar so that 'filling with LNG' is, to the motorist, no different from 'filling with petrol'.

4.4. Methanol as a motor fuel.

It very often happens that when an oxygenated hydrocarbon is formed from a simple hydrocarbon the former is more reactive than the latter. Accordingly, methanol is more reactive than methane and in engine use has a lower octane rating than methane. The RON of methanol is actually about 108, better than that of regular gasolines. Of course, methanol and gasoline can be blended to give a target octane number.

Natural gas is not of course carbon neutral, any more than petrol from crude oil or from shale is. Whether methanol is carbon neutral depends upon its origin. If it is made from coal or natural gas via synthesis gas it is not carbon neutral. However methanol (one synonym for which is 'wood alcohol') made from the decomposition of wood is carbon neutral if subsequently used as a fuel. Perhaps more importantly, it is also carbon neutral if it is made from synthesis gas produced from biomass (any of the examples given in Section 2.5, and there are many more!) instead of from coal or natural gas. The carbon neutrality of methanol is therefore ambiguous, having a dependence on the method of manufacture.

4.5. Ethanol as motor fuel.

We fasten on just one example: E85, a blend of ethanol (85%) and gasoline (15%). It is routinely available in certain US states including Illinois and has a research octane number of 105. Table 1 below summarises what has been said about fuels for SI engines in terms of octane number and makes some additional comments.

Table 1. Octane ratings of fuels for SI engines.

Fuel	RON	Comments
Gasoline as sold at most retail outlets.	95 or 98, the latter more expensive.	Adjustment of the octane rating by control of the temperature range of the 'cut' and by inclusion of octane enhancers. Gasoline is obtainable from shale and tar sands as well as from crude oil.

. . . cont.

Natural gas.	120	Higher octane number by reason of lower intrinsic reactivity and therefore lower propensity to knock. Sold in compressed form and (at the present time less widely) in liquefied form.
Methanol.	108	Ambiguous in carbon neutrality terms.
E85.	105	A Flexible-fuel vehicle (FFV) can run on any blend of fuel in the composition range from pure gasoline to E85. Most of the manufacturers which supply cars to the US make FFV versions of at least some of their models available.

5. Fuels for compression ignition (CI) engines other than diesel.

5.1. Introduction.

A fuel for use in such an engine has to be capable of ignition without a spark, the very event which must be avoided in SI engines. The merit of a particular fuel for a CI engine is assessed by its resistance to ignition delay, and the benchmark hydrocarbon is n-cetane $C_{16}H_{34}$ which by definition has a cetane number of 100. In contrast to octane numbers for commercial gasolines, which are close to 100, cetane numbers for routinely available diesel fuels will be in the neighbourhood of 50. Whereas low reactivity favours a good octane rating high reactivity favours a good cetane rating. This point will be enlarged upon when biodiesels are discussed below.

5.2 Biodiesel fuels.

These are plant oils used as substitutes for diesel in compression-ignition engines and obtained from the crushing of seeds. Initial development in this topic was in India in the 1980s where 'Honne oil' was investigated as a diesel substitute with promising results. Currently, widely used plant oils for fuel purposes include Soybean oil and Rapeseed. Being obtained directly from plants, biodiesels are of course carbon neutral.

Equivalence in reactivity terms of biodiesel and mineral diesel requires that the oxygenated organics in the biodiesel, in particular the esters, have a combustion reactivity comparable to that of unsubstituted hydrocarbons up to about the C_{22} in the mineral diesel. The plant oil without any form of processing is sometimes suitable for use as a biodiesel otherwise its properties, not only the chemical reactivity but also certain physical properties including viscosity, can be modified by esterification of the carboxylic acids present in the oil with methanol. The extent of esterification can be matched to a desired cetane number. Alternatively, the plant oils can simply be blended with esters such as methyl oleate, methyl stearate and methyl palmitate (the methyl esters of three of the acids likely to be present, for example, in Soybean oil) to adjust the cetane number whereupon a correlation as simple as:

$$\text{cetane number} = (\text{cetane number of the unprocessed fuel}) + Z \times (\% \text{ esters})$$

where Z is a constant, applies.

Table 2 below identifies some sources of biodiesel and gives brief descriptions of them. It is important to realise that plant oils are not ‘fine chemicals’ of precise composition and that even oils from the same plant vary in properties. Just as when a distillate in the diesel boiling range is obtained its cetane number might have to be adjusted by incorporation of a cetane enhancer such as isopropyl nitrate, so when a plant-derived oil is obtained its cetane number might have to be adjusted by raising its ester content as previously described. Such processing will also affect the viscosity. Viscosity alone can be adjusted by incorporation of small amounts of animal fat (tallow).

Table 2. Sources of biodiesel.

Source.	Description.
Hemp.	Oil from hemp a possible biodiesel. Because of possible misuse of hemp to make a narcotic drug its cultivation requires a licence in many parts of the world including the EU and the US.
Jatropha tree.	‘Beans’ from the Jatropha tree, which occurs in a number of African countries, produce oil at 40% yield which can be made into biodiesel. The Jatropha tree can grow under quite poor conditions of irrigation and nutriment supply.
Oil palm.	Palm oil currently being widely produced internationally as a component of biodiesel. The world’s major producer at present is Malaysia where ≈ 9 million tonne of the material are being produced each year. Fluctuations in the demand for palm oil are due largely to the competition from soybean oil.
Rapeseed.	A major source of biodiesel, 10 million tonnes grown annually in the EU.
Soybean.	Soybean oil is currently the most expensive of the liquids used as a basis for biodiesel but has some advantages over its competitors one being that Soybean-derived biodiesel is particularly suitable for use in colder regions.
Straight vegetable oil (SVO).	Vegetable oil sold for culinary purposes requiring no stringent viscosity specification. Vehicles can be adapted to run on this sort of oil in unused or in waste form, though in the latter case filtration is necessary. The adaptations to make a diesel vehicle run reliably on SVO are fairly major. Vehicular use of SVO purchased for kitchen use is illegal in many countries including the UK.

5.3. Simple alcohols in CI engines.

The cetane numbers of pure methanol and ethanol are about 3 and 8 respectively and this clearly precludes their use in CI engines. There are however blends of diesel and alcohol which can be used. C₁ and C₂ compounds even when oxygenated would be expected to be less reactive than the C₁₆₊ ingredients of diesel and therefore to blend a diesel with methanol or ethanol is to lower its cetane number. However, to use ethanol as a blendstock is to make the fuel 'greener' as that component of it, unlike the diesel to which it is added, is carbon neutral. Experience in a number of countries is that ethanol at up to 15% by weight blended with mineral diesel will not cause the cetane number to move outside the range of values suitable for diesel cars and commercials and it will, as noted, have greenhouse benefits.

6. Liquid explosives with special reference to the terrorist scare in August 2006.

6.1. Introduction.

In August 2006 a plot to blow up an airliner in flight by means of a liquid explosive was foiled. In the days that followed there was much media discussion of 'liquid explosives' to which the writer of this article contributed. He also wrote for one of the professional periodicals the following piece [3]:

The author responded to many media enquiries concerning the 'liquid bomb' threat at Heathrow in August 2006 and broadcast on the topic on UK and Australian radio. He has had some feedback from someone professionally involved in explosives and would like to put his responses to that in the public domain by means of this note. Some commercial explosives are of course liquids, probably the best known being nitroglycerine a.k.a. 'blasting oil'. However, the term liquid explosive can be extended to a pair of liquids which:

- (a) will react together exothermically, and*
- (b) in so doing will create an overpressure.*

Clearly in such a two-component explosive one liquid will be the fuel and one the oxidiser. The former might for example be mineral turpentine, the latter peroxide or bleach. Development work would establish what size and shape of vessel containing the mixed liquids would lead to an explosion with overpressure.

It is also relevant to note that detonation is not essential for there to be an overpressure.

In detonation, of course, speeds are supersonic. However, a deflagration, in which speeds are sub-sonic, can have sufficient overpressure to cause death or injury to persons as well as damage to structures (e.g., an aeroplane fuselage). Hydrocarbon accidents in the refining and processing industries in fact lead to deflagration, not to detonation.

6.2. The inevitability of explosion under adiabatic or close-to-adiabatic conditions.

We should note in addition to what is in italics above that any exothermic reaction has the potential to ignite: it is certain to ignite if it takes place under adiabatic conditions.

This brings us to the distinction between ‘explosion’ and ‘ignition’, if indeed there be a non-arbitrary distinction between them. For the purposes of this debate we can equate the two, as any ignition of interest will involve gas release with pressure effects. The only ignition known to the author which does not involve product gases is that of certain pyrotechnics, which are said to be ‘gasless’, and these are such an obscure example that maybe the exception proves the rule!

7. Concluding remarks.

The author is now at a stage where, to coin a euphemism, he seems to be older than the majority of his colleagues. He has had tens of years of teaching, research, writing and consultancy in fuels and combustion and has found that the fundamental principles of thermal sciences have become not less but more helpful and appealing to him. When confronted with a new problem he invokes such principles with more confidence than he might have done at a much earlier career stage, often mentally by-passing more advanced approaches which he has encountered. This paper in a sense invokes a ‘return to simplicity’ in the approach to particular issues in fuels and combustion including those discussed in the text.

8. References.

- [1] Holman J.P. ‘Heat Transfer’ McGraw-Hill, NY, any available edition.
- [2] Jones J.C. Fuel Processing Technology 87 753 (2006).
- [3] Jones J.C. ‘On the use of the term “liquid explosive”’ International Fire Fighter, expected to appear in the November 2006 issue.

9. Appendices.

Appendix 1.

Semi-quantitative calculations apropos of the red glow observed in the combustion test.

Using Wien’s displacement law [1]:

$$(\lambda T)_{\max} = 2897.8 \mu\text{m K}$$

$(\lambda T)_{\max}$ being the product of the wavelength and temperature corresponding to the maximum emissive power. Now for combustion at 800°C (1073 K) the calculated wavelength is 2.7 μm which is outside the visible range and at the low wavelength end of the infra-red range. Red light, at the high wavelength end of the visible range, has a wavelength of 0.75 μm . Light of this sort of wavelength is emitted only at a rate of the order of 10 W: this can be reliably inferred from the very dim illumination of the stove interior caused by the glow, less than that which a domestic light bulb of say 40 W would have provided. The glow would have been a very small proportion of the total radiation from the fuel bed, most of which was at wavelengths higher than those of the visible range. Where the bed was at 500°C (773 K) the value of λ from Wien’s displacement law is 3.7 μm , also in the infra-red range.

Appendix 2.

Electrical power from the combustion of tyre waste at the Elm Energy and Recycling plant.

100000 tonne = 10^8 kg

Taking the calorific value to be about 35 MJ kg^{-1}

Heat released in a year = $3.5 \times 10^{15} \text{ J}$

$\times 10^8 \text{ W}$ of heat

Taking the generation using a Rankine cycle to be about 30% efficient, electricity is produced at 33 MW

ՀԱՅԱՍՏԱՆԻ ՀԱՆՐԱՊԵՏՈՒԹՅԱՆ ԳԻՏՈՒԹՅՈՒՆՆԵՐԻ
ԱԶԳԱՅԻՆ ԱԿԱԴԵՄԻԱ
НАЦИОНАЛЬНАЯ АКАДЕМИЯ НАУК РЕСПУБЛИКИ
АРМЕНИЯ

Հայաստանի քիմիական հանդես 60, №2, 2007 Химический журнал Армении

INTRINSIC STRUCTURAL-BALLISTIC INTERACTIONS
IN COMPOSITE ENERGETIC MATERIALS

PART I - EXPERIMENTS

G. SANDRI TUSSIWAND^a, F. MAGGI^b, A. BANDERA^a and L.T. De LUCA^{c*}

^a PhD candidate, SPLab, Politecnico di Milano, 34 via La Masa, 20158 Milan, Italy

^b PhD, SPLab, Politecnico di Milano, 34 via La Masa, 20158 Milan, Italy

^c Professor, SPLab, Politecnico di Milano, 34 via La Masa, 20158 Milan, Italy

* luigi.deluca@tiscali.it

ABSTRACT

Among the various aspects of the deflagration of composite solid rocket propellants, one deserving further attention is the dependence of the propellant regression rate on its mechanical state, properties and applied loads during deflagration. Beside structural-ballistic interaction phenomena occurring on a motor level, i.e. affecting the whole grain or large portions of it, the structural properties of a propellant and the mechanical loads acting during deflagration can significantly alter its combustion behavior on a microscopic scale, leading to what can be considered as an “intrinsic” coupling mechanism. This can affect the performance of a solid rocket motor even without the presence of macroscopic cracks or excessive grain deformation, and has been the subject of several experimental and theoretical investigations performed at the SPLab (Space Propulsion Laboratory) of Politecnico di Milano on AP-HTPB based composite propellant formulations. The same mechanism could also alter the IM properties of an energetic material which has been subjected to mechanical damage and chemical aging.

Nomenclature

a	<i>thermal diffusivity or crack length</i>
a'	<i>rate of crack propagation</i>
E	<i>Stiffness</i>
$E(t)$	<i>relaxation modulus in tension</i>
G	<i>Cross flow in the bore</i>

$g(\epsilon)$	<i>Strain softening function – Swanson & Christensen’s NLVE model</i>
H/C	<i>Hydrocarbon</i>
k	<i>thermal conductivity</i>
LVE	<i>Linear viscoelastic material model</i>
IM	<i>Insensitive Munition (here mainly slow and fast cookoff)</i>
$NLVE$	<i>Non-linear viscoelastic material model</i>
PBX	<i>Plastic bonded explosive</i>
q	<i>thermal energy flux</i>
r_b	<i>burning rate</i>
T	<i>Temperature</i>
t	<i>Time</i>
T_f	<i>Final flame temperature</i>
T_s	<i>surface temperature</i>
T_0	<i>soak temperature</i>
ϵ'	<i>strain rate</i>
ϵ	<i>Strain</i>
λ	<i>Average size of the largest particles in a propellant</i>
ρ	<i>density</i>
σ	<i>Stress</i>

Introduction

Global structural-ballistic interactions on a motor level are those which alter significantly the expected burning behavior of the grain either through excessive deformation of its geometry or through crack propagation in the grain and the associated generation of additional burning surface. They have detrimental effects on the thrust and pressure histories of the complete motor and may cause catastrophic failure of the system.

Another kind of structural-ballistic interactions, which can be denoted as “intrinsic”, are those influencing the speed of deflagration of the propellant itself. Their effect is on a microscopic scale, without any occurrence of structural collapse of the grain by crack generation and propagation or excessive deformation. Their triggering cause is mechanical damage, particularly the presence of porosity, kept open by a tensile stress/strain field and generated by mechanical damage on a microscopic scale, i.e. adhesive fracture between the solid particles and the binder or cohesive fracture in the binder itself. This mechanism, known as dewetting, can increase the apparent burning rate of the material.

Intrinsic structural-ballistic interactions are difficult to investigate on a laboratory scale because of the need to keep burning material samples under a constant mechanical load. The amount of burning rate increase caused by mechanical damage seems to be pressure dependent on a sample level; mechanical damage will therefore alter the apparent ballistic exponent of a propellant on a laboratory scale.

The intrinsic interaction effect inside a motor will generally be different: the presence of damage-induced porosity enhances the feedback of thermal energy in depth into the material not only by conduction, but also by radiation and convection; the influence of the two latter mechanism will be dominant inside a grain but seems difficult to reproduce using small propellant samples. For a motor, even neglecting convection, the mere high radiant energy flux emanating from the bore can produce subsurface ignition of smaller oxidizer particles [1], accelerating bulk deflagration. Finally, the coupling of damage-induced porosity and other burning rate enhancing effects such as erosive burning will also contribute to change things on a motor level.

IM properties of the grain, like its sensitivity to fast and slow cook-off aggressions, might also be altered, changing its overall response to aggressions after cumulative mechanical damage evolved in open porosity.

Activities on the intrinsic interaction effect involved the investigation of the rate of regression of damaged AP-Al-HTPB propellant under mechanical strain and the modeling of the experiments.

So far, the following results have been obtained:

- For materials containing a bonding agent, the regression rate is significantly altered if the applied level of tensile strain exceeds the onset of dewetting between AP particles and the binder. The variation of burning rate is then a “fingerprint” of the state of damage of the material.

- Since the material is not homogeneous, any induced strain field will produce a non homogeneous distribution of damage and load on a microscale. This implies that a bit of material will have a non-homogeneous distribution of burning rate. Experiments on damaged propellant slabs under strain showed indeed an enhanced generation of vorticity on a microscopic level, particularly at spots where the damage distribution was highly inhomogeneous. This means that the “combustion noise” is greatly enhanced in material portions with damage level gradients.

- If the material does not contain an effective bonding agent (e.g. formulations based on nitramines and binder, new formulations for space launchers, PBX, etc.), a progressive increase of the burning rate with the applied strain is to be expected [2]. In this case, the variation of burning rate would be a “fingerprint” of the superposed strain field and will be influenced by the original, specific microscopic structure of the material and by the nature of its constituents.

- The increased mass burning rate is caused by an increased burning surface on a microscopic level. For the samples, debonded AP particles ignite below the “reference” burning surface through conduction in the gas phase between the debonded particles and the binder matrix. This effect would be enhanced and virtually independent on pressure in a motor because of the intense convective and radiant thermal energy exchange.

Part 1 of this work describes the experiments performed on damaged propellants with and without load application. Part 2 [30] describes some simple modeling activities performed to confirm the

physical explanations proposed after observing the experiments and to help understanding the phenomena involved. A correlation between the amount mechanical damage and burning rate augmentation is also suggested.

Literature Survey

Failures caused by global structural-ballistic interactions have been investigated in the past, with much effort occurring in the US after the Titan IV SRMU prequalification test failure on the 1st of April 1991. Material focusing on global collapse caused by excessive deformation and a review of previous work published on the subject in the USA is offered in [3]; a similar, full-scale failure occurred during a Castor II motor firing had been investigated and modeled by Glick, Caveny and Thurman in 1967 [4].

Another valid survey has been published in [5]. Simulations including excessive deformation and the spontaneous initiation and propagation of a crack inside a motor have been recently published by one of the workgroups of the CSAR program at the University of Illinois (e.g., [6]). Previously, a considerable amount of work on failure caused by crack initiation and propagation was carried out by Smirnov and Dimitrienko [7] in the former Soviet Union, and after that in the USA at the Pennsylvania State University by Kumar, Kuo, Lu and others (e.g., [8] and [9]) in the 80s and 90s and by Liu at the Edwards AFB laboratory [10].

Some early material on the intrinsic effect of load and damage on the ballistic properties of a solid propellant was found in [2]. Two of the studies quoted here could not be found, but report intrinsic structural-ballistic interaction as a function of the strain. The authors' comment stresses that the cause of the burning rate acceleration under strain is unclear but suspects dewetting to be the triggering mechanism.

Useful modeling activities or experimental studies are scattered in literature ([5] and [10], for instance), but no dedicated study was found so far.

Material

The composite propellant used in this study belongs to the most employed family used for solid rocket propulsion applications in the western countries. It is a heavily filled elastomer, containing a distribution of rigid AP particles as oxidizer and metal particles as fuel. They make up about 90% of the mass. The binder works as a fuel and is a polyurethane elastomer, using HTPB as base polymer, networked through a polyfunctional isocyanate. Further additives play a fundamental role in determining the mechanical properties of the compound: the plasticizer is an organic oil depositing itself between the binder chain segments, facilitating mutual shearing through weakening of the van-der-Waals bonds existing between different atoms of the chain segments, and the bonding agent is a "hybrid" molecule, containing functional groups capable to react both with the rigid, inorganic AP particles and the binder, thereby establishing strong bonds between the rigid inclusions and the binder itself.

The organic molecules of the binder decompose during combustion and react with the oxidising gases generated by the primary AP flame [11-12], producing a diffusion flame and releasing further thermal energy to sustain stable flame propagation into the solid.

The following formulations were investigated:

- A formulation having a ratio of AP:Aluminum:binder of about 68:18:14, a bimodal AP grain size distribution with peaks at 20 μm and 200 μm and an average Aluminum grain size of 30 μm . Ferric oxide was used as a burning rate modifier. This propellant comes from an industrial batch and the indications are approximate. It contained an effective bonding agent and will be referred to as *formulation 1*.
- A very similar formulation, using a finer AP powder, less Aluminum, a different burning rate modifier and a higher bonding agent and plasticizer content, giving better strain capability, a later onset of dewetting and an excellent toughness. From the point of view of this study it is similar to formulation 1. Both are typical of good quality, industrial grade propellants.
- A self-produced fuel-rich formulation, having a ratio of AP:binder:Aluminum of about 60:20:20, a bimodal AP grain size distribution with peaks at 80 μm and 200 μm , the Aluminum having an average grain size of 70 μm . The saturation degree of the binder was 100%, the propellant contained no bonding agent and less plasticizer than above. As a result, the material was very brittle, exhibiting a very early onset of dewetting, and will be referred to as *formulation 2*.

Experiments

A number of different experiments was designed and carried out to investigate the effect of mechanical damage and load on the burning rate of the energetic material.

Burning rate measurements were performed on undamaged and damaged material, using conventional Crawford samples cut out of dogbone specimens used for uniaxial tensile testing and panels previously loaded under biaxial tensile stress [13]. Obviously, no tensile load was applied to the strand burners during combustion.

Further burning rate measurements were performed with special panel samples loaded in plane stress during burning. The material of these samples belonged to formulation 1 and was cut out of subscale ballistic simulation motors; it was subjected to controlled mechanical damage before the burning rate experiments.

Mechanical characterisation of propellant formulation 1 was performed a priori following the LVE and the Swanson model in order to provide data for the structural analysis of the burning rate specimens and on the onset and amount of microstructural damage in the material.

Irreversible damage in a composite propellant

With damage onset we mean the strain at which truly irreversible damage occurs in the propellant. Other forms of changes in the material's microstructure, like the Mullin's effect, have relevant consequences on its mechanical properties and pose challenges to constitutive modeling [14, 25-28], but do not seem to be completely „irreversible”.

Leaving out the Mullins effect and other long-term mechanisms altering the material, like oxidative cross-linking caused by chemical aging, we just consider fully irreversible damage, i.e. modifications in the propellant caused by mechanically-induced destruction of stronger bonds in the binder or at the particles' interface, such as detachment of bonding agent molecules from the oxidizer particles and/or the binder producing “dewetting” [13 and 29].

The damage patterns observed in the heterogeneous energetic material are related to the size of the oxidizer particles and can be grouped into three types for the purpose of this study:

– **Diffused microcracks/dewetting** (*Fig. 1*), a state of damage where many small fractures occur on a microscopic scale. They are as large as the largest solid particles or particle agglomerates in the propellant, in our case a few hundred microns. Depending on the temperature, the strain rate of the applied load, and the bonding agent effectiveness, the fracture can proceed near the particles [10;15-17] at stress concentration spots, or directly at the particle-binder interface. In the presence of a significant amount of metallic fuel particles one order of magnitude smaller than the larger oxidizer inclusions, we have dewetting of metallic fuel particles from the binder at even lower strains, i.e. a smaller fracture scale of a few tens of microns concentrated at the metal pockets between the larger oxidizer particles [18]. In all cases, the presence of plasticizer means that the particles which lost contact to the binder are, at least initially, partially or completely wetted with a volatile organic liquid.

– **Small Bridged Cracks** (*Fig. 2*). Coalescence and propagation of the above microcracks at favourable spots to form a larger crack of the size of 2-3 large oxidizer particles (e.g. near an agglomerate of small metallic particles, or at a spot with a local enrichment of larger oxidizer particles with surface irregularities). Under load, the crack is still bridged by oriented binder filaments. The crack surface is punctuated by metallic fuel particles, large oxidizer grains and a number of small oxidizer particles, depending on the specific formulation of the propellant; all particles are, at least initially, wetted by plasticizer.

– **Small open Cracks** (*Fig. 3*). Coalescence of the above structures and propagation of the bridged crack patterns described above to form a true crack, which can or cannot be considered to be “microscopic” depending on the scale of observation and on the available diagnostic technique; it might be “microscopic” or undetectable on a motor level if it is smaller than the resolution of an x-ray image, but it will be larger than a few of the bigger oxidizer grain particles. If loaded, the crack is not bridged by binder filaments for a significant portion of its length. Bridging will occur at the crack tips, within a so-called process zone [19].

A characteristic scale to define the damage pattern is the average length of the larger oxidizer particles or the largest agglomerates in the propellant, λ . For the formulations tested in this study, a damage pattern of the first kind has microcracks with $a \leq \lambda$. A damage pattern of the second kind has bridged microcracks with $a \approx 2-3 \lambda$, and a damage pattern of the third kind has $a > 3-4 \lambda$ and

up to 1-2 mm. If no tensile load is applied, the cracks close and a continuity in the material is re-established. Initially disconnected surface bits are held together by weak bonds (van der Waals forces) which collapse as soon as very small tensile loads are applied. The damaged material is not able to transmit the same amount of stress in a region of damage pattern 1 since porosity decreased the bulk stiffness causing softening.

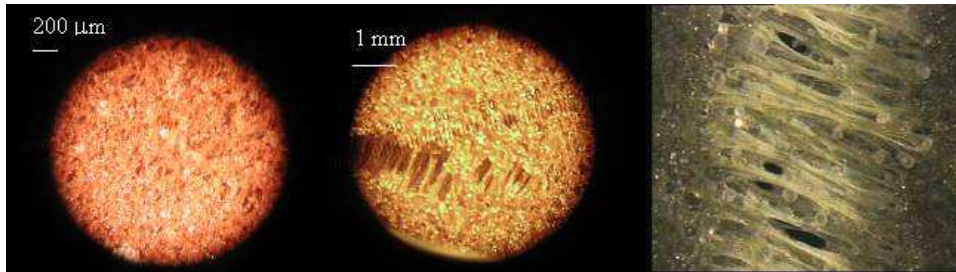


Fig. 1
(left)

Damage pattern 1: diffused oxidizer particle dewetting. Fig. 2 (centre) Damage pattern 2: bridged crack propagated by a few AP particles. The larger particles are embedded in the bulk, so that in the gaps there is effectively a higher local concentration of small particles. Fig. 3 (right) A crack shows all the previously described damage regions: a true crack, ending in a process zone (shown in the picture) beginning with a type 2 region ($\lambda \approx 2-3$ large oxidizer particles) and ending in a type 1 region (dewetting, $\lambda \approx 1$ large oxidizer particle).

In a region like in Fig. 2, the amount of stress transmitted is even more limited, and due to the mere binder filaments bridging the crack surface. In a region of damage pattern 3 (true crack), no stress at all is transmitted except at the tips, in the process zone. The process zone itself has a variable size, depending on temperature and loading rate [19-20]. The initial portion (crack bridged by crazing filaments) is effectively a pattern 2 damage zone, and the final part (microcrack region) is a pattern 1 zone, with dewetting. A fracture in the propellant allows the observation of all three types of damage.

Burning rate measurements on damaged material without load application

To check whether a modification of the burning rate occurred in a damaged material, a preliminary investigation was performed using strand burners belonging to formulations 1 and 2. The strand burners were taken from damaged material samples stretched at 25°C and low strain rate (5 mm/min) to 30% and 5% true strain respectively and kept strained for at least one hour. Both strain levels cause irreversible damage in the material. Formulation 1 material was also loaded using a biaxial plate specimen [13] stretched to 30% true strain in the centre. At centre of the biaxial specimen, an almost equibiaxial state of tension damages the material producing microcracks in the direction of straining and at 90° to it because of incompressibility (the material's contraction is inhibited).

The material strands measured 5x5x30 mm and were tested at atmospheric pressure without load application. Ignition was produced using a hot wire, and the burning rate was measured using

video recordings of the tests through a digital image processing methodology described in [21]. The results obtained were compared to similar measurements performed on undamaged material tested at the same temperature and pressure. Results are summarized in Table 1.

Formulation	State of the material	Loading condition	r_b , mm/s	Max. r_b , mm/s	COV	Remark
2	undamaged	unloaded	1.24	1.27	3.39%	Brittle
2	damaged	unloaded	1.44	1.60	15.8%	strained uniaxially ¹
1	undamaged	unloaded	1.16	1.19	1.82%	Taken from subscale analogs
1	damaged (g = 0.375), 30% true strain	unloaded	1.15	1.19	2.20%	Taken from subscale analogs, strained uniaxially ¹
1	damaged (g = 0.375), 30% true strain	unloaded	1.19	1.26	3.34%	Taken from subscale analogs, strained biaxially ²

Table 1:
burning rates at 1 atm using mechanically damaged samples.

The samples were unloaded during burning.

A significant increase of the burning rate occurs for a damaged brittle formulation without bonding agent even if it is unloaded, in accordance with what is reported in [2].

No effect is recorded using an AP/HTPB formulation with good mechanical properties if the material is damaged through a tensile load producing significant dewetting in the direction of flame propagation (i.e. inducing microcracks parallel to the burning surface) and unloaded during burning, but there seems to be a slight increase in the average burning rate and the measurement dispersion if there is some amount of damage/microcracks produced at 90° to the burning surface, i.e. parallel to the direction of propagation. The increase in burning rate appears more clearly if one focuses on the maximum recorded values. A thorough examination of the test video recordings showed occasional subsurface ignition phenomena (Fig. 4) to be the reason for the average burning rate increase.

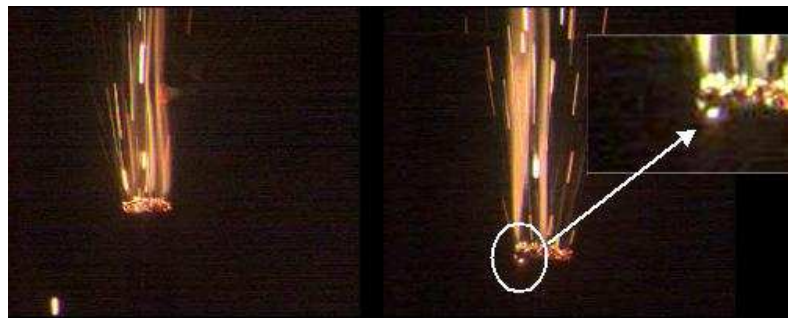


Fig. 4 Left: burning surface of undamaged, formulation 1 samples.

Right: burning surface of samples taken from biaxial tensile specimens, showing accelerated deflagration through ignition below the main surface

¹ Microcracks parallel to the burning surface

² Microcracks parallel and perpendicular to the burning surface

Even if the propellant is unloaded during burning, there seems to be thermal energy exchange below the main burning surface leading to subsurface ignition.

Burning rate measurements on damaged material under load

Propellant samples under load are more representative of the real conditions of the material in the inner part of a motor, at and near the bore surface [13, 22-23]: beside a state of hydrostatic compression generated by the gas pressure in the bore, the part of the grain at the bore is subjected to a tensile load because of the compliance of the case itself, which expands under the internal pressure generated by motor operation. If enhanced flame propagation was occurring through flame spreading into open microcracks, then keeping the material loaded during combustion was supposed to produce some burning rate acceleration effect.

To keep a propellant sample under a reasonably constant average tensile load during combustion, a 2D specimen and a special fixture were designed and manufactured. The sample is a propellant slab of 100x20 mm, 3-4 mm thick. It is held in position and strained using movable clamps with edge screws (see Fig. 5). The movement of the clamps is achieved through a frame made by 4 M3 screws and nuts. The clamps are pushed apart by adjusting the position of the screws and impose a stretching displacement to the propellant sample. Some white spots were drawn on the sample to measure the local tensile displacement under the microscope, and be sure that no slipping occurred at the frame. The average true strain imposed to the material is equal to

$$\epsilon_{xx} = \ln \left(1 + \frac{\Delta W}{W_0} \right) \quad (1)$$

W_0 is the initial width of the sample between the fixture and ΔW is the displacement imposed to the frame. The distribution of strain is shown in the FEA described in the modelling section in part 2. Microcracks develop following the intrinsic heterogeneity of the material and propagate at spots with a higher concentration of large solid particles. When a crack forms, the material nearby is unloaded except at the two tips of the crack. This means that damage will tend to “nucleate” at spots with a higher concentration of larger oxidizer particles and its distribution won't be uniform. Since the specimens had been previously strain cycled beyond the onset of dewetting, the true tensile stress and strain distribution depends on the damage pattern generated during the strain cycling and is not reproducible even if the imposed average strain was the same for all specimens.

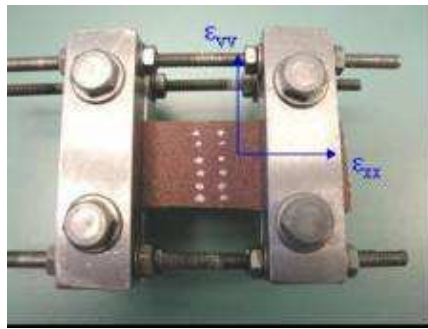


Fig. 5 Fixture and 2D propellant samples to measure the burning rate under load

While loaded, the samples were ignited by a hot wire placed on a stripe of black powder on the upper edge. All samples were burned in nitrogen and were inhibited at the outer surface.

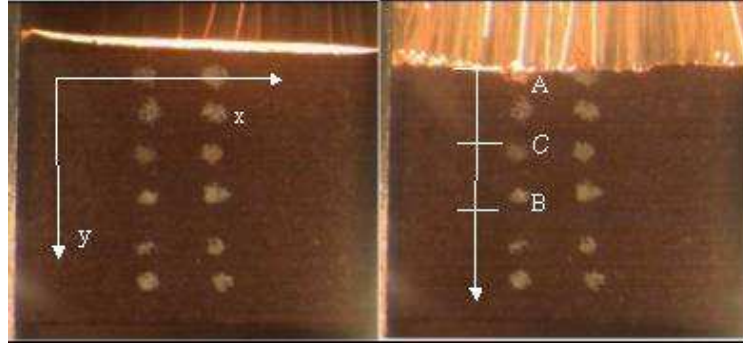


Fig. 6 Ignition of the sample through a hot wire on the top and burning surface advancement from top to bottom during the experiment. The arrow shows the local propagation direction

The burning rate of the material was measured through digital image analysis of the *local* burning front position via the software of the camera used to film the experiments.

A 2D burning rate field was obtained: the position of the local burning surface could be associated at discrete spots on the samples (see A,B, and C in Fig. 6).

$$\bar{r}_{bA-B} = \frac{y_b^B - y_b^A}{t^B - t^A} = \bar{r}_{bC} \quad (2)$$

the average burning rate between spot B and spot A on the sample was obtained with eq. 2, i.e. by dividing the length between the two points by the time needed by the front to reach point B starting from point A. This average burning velocity was then associated to point C, placed at the middle.

The distance between two measurement spots was chosen to minimize the error to about 2.5%.

A whole distribution of burning rates was obtained for the loaded samples. It was found out that the burning rate was the same as with the unloaded strand burners at spots *without* apparent dewetting, and greatly enhanced at zones with uniform dewetting damage. An even higher apparent increase was recorded at spots with damage patterns 2 and 3.

A continuous 2D map of the burning rate was generated by correlating the r_b values obtained at the measurement points. A typical distribution of burning rate can be observed in Fig. 8. The sample from which it was obtained is shown in Fig. 7. The distribution of burning rates is a fingerprint of the damage distribution on the material sample, just like the material stiffness distribution would be. The region of damage pattern 2 (white circle on Fig. 7) is embedded in a region with diffused dewetting. To confirm the results, undamaged 2D specimens were tested under a mechanical load below the threshold of dewetting; the burning rate proved to be the same as the one obtained from

³ see part II of this study



propellant under load.

Table 2
Burning
rates at
1 atm
obtained
using
samples
(10) of
mechanically
damaged

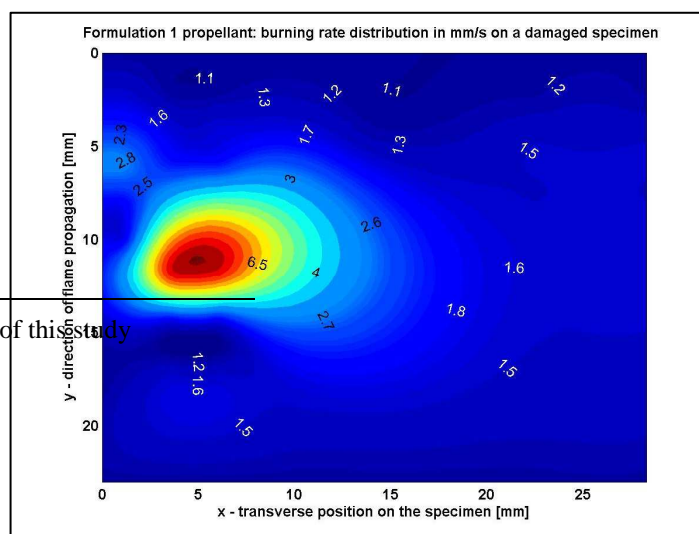


Fig. 8 Typical burning rate distribution for the damaged samples under load. The r_b for the specimen of Fig. 8 was at 55 points. A correlation was performed with Matlab, obtaining a 2D map of the burning rate of the material. The numbers and colors on the contour plot display the local burning rate in mm/s

Final comments

The increase in burning rate for the material zones with a “type 1” damage (diffused particle dewetting) is remarkable and amounts to about **28%** of the burning rate value for the undamaged material. In zones with damage patterns 2 and 3, apparent burning rates of up to 8 times the undamaged values were found. These values are not true burning rates but flame spreading phenomena into small, merely observable cracks. These cracks would be undetected with normal motor diagnostics but their presence might be inferred in future systems with embedded sensors [24 and 25]. Analyzing the videos, a clear distinction can be made between damage pattern 1 material portions and damage pattern 2 and 3 material portions:

- In the first case, only the examination made under the microscope carried out before the test reveals that the material has diffused particle dewetting (Fig.1). During combustion, the flame front proceeds straight and normal, without blurring, and a mere (but remarkable) increase of the rate of propagation of the burning front in the material is recorded.
- In the second case, a small crack is merely observable in the video, and almost as soon as the burning surface reaches the upper crack tip, the flame propagates inside the crack by its entire length. A very high apparent burning rate (4 mm in about 0.5 s) can be associated to this “forward jump” of the burning surface if the length of the crack is divided by the time elapsed from the moment the burning surface reaches the upper crack tip and the bottom of the crack is ignited. It is pointed out that if this time is shorter than the inverse of the frame rate of the camera, this value is not real but a function of the frame rate. Whether the burning rate values associated to propellant with type 2 and type 3 damage patterns can be used as a material property for simulation purposes

using an Eulerian grid fixed on an unflawed grain (regardless of whether bulk mechanical deformation is simulated or not by coupling FEA) depends on the resolution of the grid.

If a single grid cell is larger than the length of a type 2 or type 3 flaw and the material is treated as homogeneous, the burning rate assigned as a material property to the cell should be correspondingly high. If the small crack is detected and the model takes it into account by including a small crack between two neighboring cells, then the neighboring cells should have the same burning rate as undamaged material or a material with a pattern 1 damage assigned as a material property.

Acknowledgement

The help and advise of Prof. Giuseppe Sala, Ms. Rosy Pagano, and Mr. Paolo Bettini (Dept. of Aerospace Engineering, Politecnico di Milano) in conducting mechanical testing is gratefully acknowledged

References

- [1] Cain, J., and Brewster, Q., "Radiative Ignition of Fine Ammonium Perchlorate Composite Propellants" Propellants, Explosives and Pyrotechnics, 31, No.4 278-284, Wiley, 2006.
- [2] Summerfield, M., and Parker, K.H. "Interrelations between combustion phenomena and mechanical properties in solid propellant rocket motors", in "Mechanics and Chemistry of Solid Propellants", Eringen, A.C. editor, 1967.
- [3] Murdock, W. "Flow-Structural Interactions in Solid Rocket Motors", from "Internal Aerodynamics of Solid Rocket Motors", Special Course held at the Von Karman Institute of Fluid Dynamics, 27-31 May 2002.
- [4] Glick, R., Caveny, L., and Thurman, J., "Internal Ballistics of Slotted-Tube, Solid-Propellant Rocket Motors," Journal of Spacecraft, Vol. 4, No. 4, 1967.
- [5] Kuo, K.K., and Kooker, D.E. "Coupling Between Nonsteady Burning and Structural Mechanics of Solid Propellant Grains", in "Nonsteady Burning and Combustion Stability of Solid Propellants" in AIAA Progress in Astronautics and Aeronautics Series, Vol. 143, De Luca, Price, Summerfield editors, 1992.
- [6] Hwang, C., Massa, L., Fiedler, R. and Geubelle, P., "Simulation of convective burning and dynamic fracture in solid propellants", 38th AIAA/ASME/SAE/ASEE JPC Conference and Exhibit, Indianapolis, Indiana. Paper NO. AIAA 2002-4342.
- [7] Smirnov, N.N., and Dimitrienko I.D., „Convective Combustione Regime in a Deformable Solid Fuel with Longitudinal Channels“, Fizika Goreniya i Vzryva, Vol. 22, No.3, pp. -59-67, May-June 1986, Moscow (translation).
- [8] Lu, C., and Kuo, K., "Modelling and numerical simulation of combustion process inside a solid rocket propellant crack", Propellants, Explosives, Pyrotechnics 19, 217-226.

- [9] Lu, Y.C., Kuo, K.K., and Wu, S.R. "Crack Propagation Process in a Burning AP-Based Composite Solid Propellant, AIAA 93-2168, AIAA/SAE/ASME/ASEE 29th Joint Propulsion Conference, 28-30 Jun 1993.
- [10] Liu, C.: 2002, Fracture mechanics and service life prediction research, Technical Report AFRL-PR-ED-AB-2002-208, Edwards AFB CA Propulsion, Directorate West.
- [11] Ramohalli, K.N.R., "Steady State Burning of Composite Propellants under Zero Cross-Flow Situation", in "Fundamentals of Solid Propellant Combustion" AIAA Progress in Astronautics and Aeronautics Series, vol. 90, Kuo and Summerfield eds., 1984.
- [12] Lengellé, G., Duterque, J., and Trubert, J.F. "Combustion of Solid Propellants" from "Internal Aerodynamics of Solid Rocket Motors", Special Course held at the Von Karman Institute of Fluid Dynamics, 27-31 May 2002.
- [13] Agard Advisory Report 350 (AR 350) "Structural Assessment of Solid Propellant Grains", Propulsion and Energetics Panel Working Group 25, North Atlantic Treaty Organization, Dec. 1997.
- [14] Simo, J.C., "On a fully three-dimensional, finite strain viscoelastic damage model: formulation and computational aspects", Computer Methods in Applied Mechanics and Engineering, Vol.60, 1987.
- [15] Shapery, R.A., "A Theory of Mechanical Behavior of Elastic Media with Growing Damage and other Changes in Structure" J.Mech.Phys.Solids, Vol. 38, No.2 pp. 251-253, 1990.
- [16] Shapery, R.A., "Models for Damage Growth and Fracture in Nonlinear Viscoelastic Particulate Composites".
- [17] Schapery, R.A., "A Micromechanical Model for Non-Linear Viscoelastic Behavior of Particle-Reinforced Rubber with Distributed Damage, Eng. Frac. Mech., Vol. 25, Nos 5/6 pp.845-867, 1986.
- [18] Maggi, F., "Heterogeneity Effects on Composite Solid Propellants", PhD. Thesis in Aerospace Engineering, Politecnico di Milano, April 2006.
- [19] Bencher, C., Dauskardt, R. and Ritchie, R.: 1995, "Microstructural damage and fracture processes in a composite solid rocket propellant", Journal of Spacecraft and Rockets 32(2), 328-334.
- [20] Sandri Tussiwand, G., Saouma, V.E., De Luca, L.T., and Terzenbach R., "Fracture Mechanics of a Solid Rocket Motor using an AP-based Composite Propellant" draft paper submitted for publication to the Journal of Propulsion and Power, Sept. 2006
- [21] Maggi F., Bandera A., Petracca A., De Luca L.T. and Annovazzi A. "Grain processing effects on steady burning rate in small-scale test motors", proceedings of the 9-IWCP congress on "Novel energetic materials and applications", 14-18 Sep 2003, Lerici, La Spezia, De Luca, Galfetti e R.A. Pesce-Rodriguez editors.
- [22] NASA SP-8073, "Solid Propellant Grain Structural Integrity Analysis", National Aeronautics and Space Administration, Jun 1973.
- [23] Fitzgerald, J.E., and Hufferd, W.L., "Handbook for the Engineering Structural Analysis of Solid Propellants", CPIA Publ. 214.

- [24] R.R. Little, H. Chelner, and H.J. Buswell, „Development, Testing and Application of Embedded Sensors for Solid Rocket Motor Health Monitoring“ 37th International Annual Conference of ICT, June 2006.
- [25] Sandri Tussiwand, G., Weterings, F.P., Reeling Brouwer, G., and Besser, H.L. ”Application of Embedded Bondline Sensor Technology to a Nozzleless Rocket Motor, 37th International Annual Conference of ICT, June 2006.
- [26] Mullins, L. „Softening of rubber by deformation“, Rubber chemistry and technology, 42, 339-362, 1969.
- [27] Bueche, F. “Network Theories of Reinforcement”, in “Reinforcement of Elastomers”, G. Kraus ed., Wiley, 1965.
- [28] Francis, E.C., and Carlton, C.H., “Some Aspects of Composite Propellant Nonlinear Behavior in Structural Applications”. ICRPG/AIAA 3rd Solid Propulsion Conference, June 1968.
- [29] Farris, R.J., ”The Influence of vacuole formation on the response and failure of highly filled elastomers” Trans.Soc.Rheology 12,315-334, 1968.
- [30] G. Sandri Tussiwand, F. Maggi, A. Bandera, and L.T. De Luca “Intrinsic Structural-Ballistic Interactions in Composite Energetic Materials Part II – Modeling”. International Conference on Non-Isothermal Phenomena and Processes, November, 27 Nov – 01 Dece 06, Yerevan, Armenia.

ՀԱՅԱՍՏԱՆԻ ՀԱՆՐԱՊԵՏՈՒԹՅԱՆ ԳԻՏՈՒԹՅՈՒՆՆԵՐԻ
ԱԶԳԱՅԻՆ ԱԿԱԴԵՄԻԱ
НАЦИОНАЛЬНАЯ АКАДЕМИЯ НАУК РЕСПУБЛИКИ
АРМЕНИЯ

Հայաստանի քիմիական հանդես 60, №2, 2007 Химический журнал Армении

INTRINSIC STRUCTURAL-BALLISTIC INTERACTIONS
IN COMPOSITE ENERGETIC MATERIALS
PART II - MODELING

G. SANDRI TUSSIWAND^a, F. MAGGI^b, A. BANDERA^a and L.T. De LUCA^{c*}

^a PhD candidate, SPLab, Politecnico di Milano, 34 via La Masa, 20158 Milan, Italy

^b PhD, SPLab, Politecnico di Milano, 34 via La Masa, 20158 Milan, Italy

^c Professor, SPLab, Politecnico di Milano, 34 via La Masa, 20158 Milan, Italy

* luigi.deluca@tiscali.it

ABSTRACT

The structural properties of a propellant and the mechanical loads acting on it during deflagration can significantly alter its combustion behavior on a microscopic scale, leading to what can be considered as an “intrinsic” coupling mechanism. This can affect the performance of a solid rocket motor, and has been the subject of a study performed at the SPLab (Space Propulsion Laboratory) of Politecnico di Milano on AP-HTPB based composite propellant formulations. Part II of this study builds up from the results and experiments presented in Part I. Modeling activities were performed to understand and explain the coupling effect observed in the experiments and extrapolate them to motor's conditions. A correlation between the average state of damage of the propellant and the burning rate is suggested.

Nomenclature

a	<i>thermal diffusivity or crack length</i>
a_T	<i>Time-temperature superposition factor</i>
c_p / c_v	<i>Constant pressure/constant volume specific heat</i>
E	<i>Stiffness</i>
$E(t)$	<i>relaxation modulus in tension</i>
G	<i>Cross flow in the bore of a solid rocket motor</i>
g	<i>Strain softening function - Swanson & Christensen's NLVE model</i>
$g(\epsilon)$	<i>Strain softening function – Swanson & Christensen's NLVE model</i>
H/C	<i>Hydrocarbon</i>

k	<i>thermal conductivity</i>
LVE	<i>Linear viscoelastic material model</i>
IM	<i>Insensitive Munition</i>
$NLVE$	<i>Non-linear viscoelastic material model</i>
q	<i>thermal energy flux</i>
r_b	<i>burning rate</i>
S_p	<i>Shapery's damage parameter</i>
T	<i>Temperature</i>
t	<i>Time</i>
T_f	<i>Final flame temperature</i>
T_s	<i>surface temperature</i>
T_0	<i>soak temperature</i>
ϵ'	<i>strain rate</i>
ϵ	<i>Strain</i>
λ	<i>Thermal conductivity</i>
ρ	<i>Density</i>
σ	<i>Stress</i>

Introduction

“Intrinsic” structural-ballistic interactions are those influencing the speed of deflagration of the propellant itself. Their effect is on a microscopic scale, without any occurrence of structural collapse of the grain by crack generation and propagation or excessive deformation. Their triggering cause is mechanical damage: the experiments illustrated in part I showed that the root cause for burning rate augmentation is the presence of porosity, kept open by a tensile stress/strain field and generated by mechanical damage on a microscopic scale, i.e. adhesive fracture between the solid particles and the binder or cohesive fracture in the binder itself. This mechanism, known as dewetting, alters therefore the apparent burning rate of the material, increasing it, as it was suggested by Summerfield and Parker in [1]. Part II of this study describes some simple modelling activities performed to help understanding the physical phenomena involved in burning rate augmentation. A correlation between the amount mechanical damage and burning rate augmentation is also suggested. This information is useful to set a fundamental material property such as the burning rate for damaged portions of the grain within the scope of rocket motor simulations [2].

Preliminary comments on the burning rate experiments

Following results were obtained for damaged material samples of an AP-HTPB based propellant under load [3]:

Focusing on the burning rate measurements of material subjected to dewetting (1.47 mm/s vs. 1.15 mm/s), a few simple calculations give us more insight into the phenomena involved in the combustion of the propellant and explain the large burning rate dispersion measured as well as the maximum recorded values.

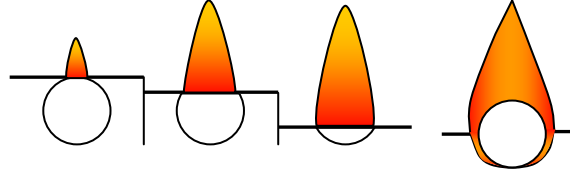
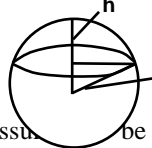


Fig. 1 *Left: Evolution of one of the larger oxidizer particles in an undamaged propellant (Taken from [4]). Right: the evolution of the same particle in a propellant with dewetting.*

Let us consider the evolution of one of the larger oxidizer particles when it is reached by the burning surface in an undamaged portion of propellant (Fig. 1, left). Assuming that the thermal energy feedback from the flame is constant and the rate of AP decomposition (r_b^{AP}) is also constant, then the mass flow generated by the particle is proportional to the instantaneous surface exposed to the flame (the top surface of a truncated sphere) and amounts to:

$$\dot{m} = \rho_{AP} r_b^{AP} A_b(t) = \rho_{AP} r_b^{AP} \pi [r_{AP}^2 - (r_{AP} - h)^2] \quad (1)$$


h is the consumed segment, r_{AP} the particle radius, assume it to be a sphere (see the sketch). The average mass flow generated by the particle until complete consumption is therefore:

$$\bar{\dot{m}} = \frac{2}{3} \rho_{AP} r_b^{AP} \pi r_{AP}^2 \quad (2)$$

Let's now suppose that the particle belongs to a damaged portion of propellant, and is completely detached from the binder (full dewetting: Fig. 1, right). The initial burning surface is equal to the surface of the sphere, and the mass flow amounts to:

$$\dot{m} = \rho_{AP} r_b^{AP} A_b(t) = \rho_{AP} r_b^{AP} 4\pi r_{AP}^2 = \pi D^2 \rho_{AP} r_b^{AP} \quad (3)$$

The average mass flow generated by the dewetted particle until complete consumption is then:

$$\bar{\dot{m}} = \frac{4}{3} \rho_{AP} r_b^{AP} \pi r_{AP}^2 \quad (4)$$

since the size of the two particles is the same, the average burning rate of the material having complete dewetting [3] is predicted to be about twice the rate of the undamaged material.

$$r_{b, \text{ undamaged}} = 1.15 \text{ mm/s}; r_{b, \text{ full dewetting}} = 2.3 \text{ mm/s. (cf. Table 2, third line)} \quad (5)$$

The estimate above would hold for pure AP, but:

– In any propellant formulation, the HTPB-IPDI binder system and the metal fuel are much less than the amount of AP (generally at least 70% in mass), and the fuel sublimation is controlled by the thermal power feedback from the flame.

– The flame itself is controlled by the primary AP flame at low to intermediate pressures [5], and even at higher pressures, and the diffusion flame would be driven by the amount of available oxygen and other oxidising species released by AP decomposition.

As a matter of fact, the predicted value of $r_{b, \text{ full dewetting}} = 2 r_{b, \text{ undamaged}} = 2.3 \text{ mm/s}$ fits rather well with the maximum observed values in propellant stretched to dewetting (2.32 mm/s). Higher burning rates were found only in association with damage pattern 2 and 3 [3], i.e. observable cracks.

The reason why the average burning rate of the damaged material is smaller than twice the rate of the undamaged material (5) might depend on the following:

– An implicit assumption contained in the estimate is that ignition occurs instantaneously around a completely detached particle. Even in propellant portions stretched to severe dewetting, not all particles are completely disconnected from the binder ([3] Fig. 2). Most will be partially bonded to the binder, or wetted by binder and plasticizer residuals. Therefore, not 100% of the AP particle will ignite immediately: latent times for cracking and sublimation of the H/C might be longer than the time needed to normally consume the AP particle [7]

– Another assumption made is that just one particle is detached from the binder. If several successive neighboring particles are detached in depth below the burning surface, then the burning rate increases as: $r_b = k \cdot 2 n_{dw}$ with n_{dw} equal to the number of dewetted particles ignited at the same time as the first one and $k < 1$ a proportionality constant taking into account the actual free, readily ignitable surface with respect to the total surface of the particle.

This two features generate a lot of scatter in the burning rate measurements, and the average burning rate is expected to be between the undamaged value and the one corresponding with full dewetting. In absence of convection, the average burning rate for a 2D sample under load in a layer with dewetting should be inversely proportional to pressure:

$$r_{b, \text{ damaged}} \sim 2(k/p)r_{b, \text{ undamaged}} \quad (6)$$

since the thermal diffusivity is inversely proportional to p : $\alpha \sim 1/p$. This effect would change the overall pressure sensitivity of a propellant tested without convection by accelerating the burning rate at lower pressure. This holds in absence of mechanisms such as those described in [8]. On the other hand, at motor conditions, thermal power transmission will occur through convection and radiation, so that the dewetted particle will ignite rapidly at the free surface at any pressure.

Let's now consider a detached particle near another one which is completely or almost completely bonded to the binder (Fig. 1), as it is the case where a zone with diffused dewetting lays beside another one which is mostly undamaged. Looking at the mass flow generated by such a pair, we observe that the first particle generates a much higher flow (see Fig. 2). This mass flow difference generates vorticity. Vorticity generation produced at a microscopic scale is therefore considerably higher than for an undamaged propellant. In an undamaged propellant [4], the maximum difference

in normalized mass flow generated by two adjacent particles is equal to π ; in a damaged propellant it is 4 times higher. In the case of larger cracks, the production of vorticity is visible in the test video recordings ([3] Fig. 7). Neighboring portions of materials with different damage levels burn at different rates and the burning surface loses planarity. Larger vortices are generated at the surface, with an increase in combustion noise.

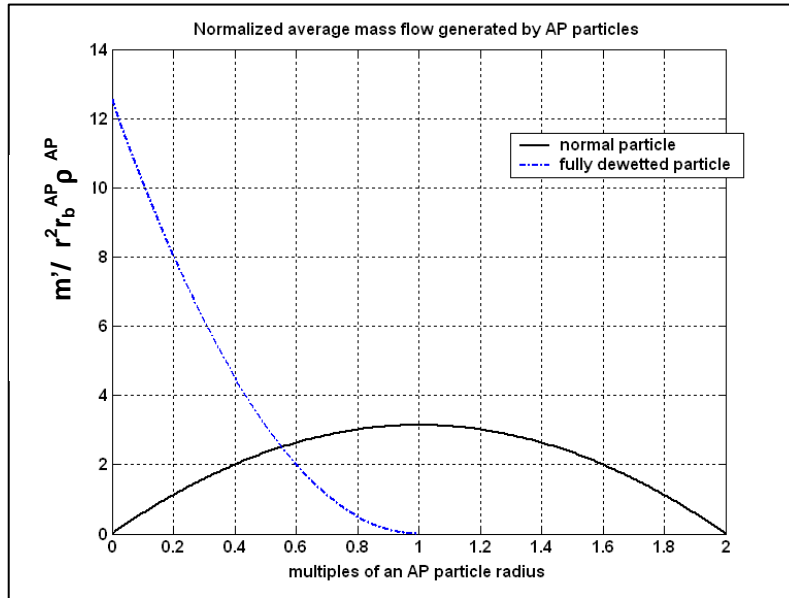


Fig. 2 Normalized mass flow generated by a detached (blue) and an undetached, large AP particle (black). Assuming a constant AP decomposition rate, the abscissa can be expressed in time without changing the shape of the curve: the burning time for an undetached particle is twice the time needed by a completely detached particle.

Modeling

Modeling activities on the 2D burning rate experiments involved structural analysis and transient thermal analysis.

Structural Analysis of unflawed and flawed samples

To investigate the stress, strain and damage distribution for the 2D burning rate samples under load with and without the presence of small cracks, a qualitative structural analysis was performed using Merlin, a FE program developed at the university of Colorado in Boulder for fracture mechanics problems [9].

The sample was modeled using a 2D geometry and plane stress quadratic elements with a Poisson's ratio of 0.495. The propellant was considered to be linearly elastic with a reference modulus chosen following Shapery's principle of correspondence [10,11]:

$$E_R = \frac{1}{\Delta t^*} \int_0^{\Delta t^*} E(t^* - \tau) d\tau \quad (7)$$

with Δt^* the time needed to reach the final strain ϵ_{\max} , applied at constant rate for this particular case; t^* is a reduced time which takes the temperature into account. Results for the unflawed sample show a non-uniform distribution of strain and stress (Fig. 3, left). This generates a non-uniform amount of damage in the material. What happens when dewetting evolves into a small local crack? Results for a model reproducing the 2D sample shown above (Figs. 3-4) indicate that a crack produces a high perturbation of the

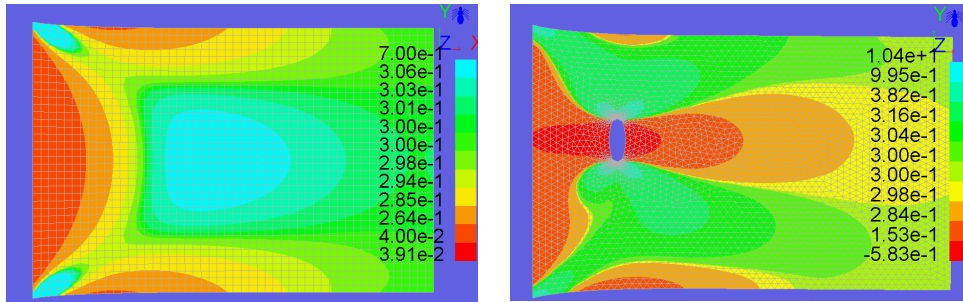


Fig. 3 Left: FEA of the undamaged, loaded sample shown in Fig.7, ref. [3]: strain (ϵ_{xx}) distribution (magnified displacements). **Right:** FEA of the damaged, loaded sample shown in Fig. 7, ref. [3]: strain (ϵ_{xx}) distribution (magnified displacements). Notice the effect of the crack: it takes up the applied displacement and reduces the strain at the corresponding specimen ordinate (red zone), but magnifies the load at the tips (blue, butterfly shape)

strain, stress and displacement field. Locally, much of the stress is not transmitted, but at the stress concentration spots in the process zone region at the tips the material is more loaded than without a crack. Cracks do not necessarily appear at the spots with the highest strain level, but rather where the local load overcomes the local material capability: mixing and casting effects or the very nature of the materials used in a propellant cause concentration gradients of constituents, like a local accumulation of oxidizer or metal fuel particles in the form of agglomerates of complex shapes, or a local enrichment of one phase with respect to the others, such as near the bore or the thermal protection, where the mere presence of a boundary produces an enrichment in terms of binder, fine oxidizer and fine metal fuel particles [22]. This heterogeneity varies from formulation to formulation. It has a different influence when new ingredients, like metal nanopowders, partially replace older constituents, and when particles for which no really effective bonding agent exists are used (like metal fuel, some explosive crystals, etc.). The consequence of this are high failure properties gradients if the scale of observation is small enough.

Mechanical damage

Since mechanical damage and tensile load are both necessary to alter the burning rate, and both are not uniform and not perfectly reproducible, the burning rate on a sample, being the fingerprint of damage and load, will be distributed in different ways on different specimens. This does not fit with the idea of having a function correlating the local load (applied displacement/strain) and damage with the local burning rate, like in [1], where studies are quoted in which it is suggested that for a particular level of applied strain, the burning rate increases by a precise factor.

A practical way to proceed in order to obtain a function correlating burning rate enhancement with mechanical damage for the purpose of ballistic simulations could be calculating a surface average of the burning rate for the damaged sample and assign it to the material layers for which structural analysis predicts a similar average state of damage, i.e. obtain a function of this form:

$$\mathbf{r}_{b, \text{damaged}} = \mathbf{f}(\mathbf{r}_{b, \text{undamaged}}, \text{damage parameter}) \text{ at constant pressure} \quad (8)$$

Tensile load is a pre-requisite for burning rate augmentation effects to occur. Bearing this idea in mind, we considered the non-linear, viscoelastic constitutive model of Swanson and Christensen [12] and chose the scalar strain softening function $\mathbf{g}(\boldsymbol{\epsilon})$ to be a good parameter to express the average state of damage for a continuum element of the material. After this model, the convolution integral of linear viscoelasticity [10,11,13] is corrected as follows for a one-dimensional state of stress:

$$\sigma(t) = g(\epsilon) \int_0^t E_{rel}(t-\tau) \phi(\tau) \frac{\partial \epsilon}{\partial \tau} d\tau \quad (9)$$

or, in general:

$$S'_{ij}(t) = g(\epsilon) \int_0^t 2G_{rel}(t-\tau) \phi(\tau) \frac{\partial E'_{ij}}{\partial \tau} d\tau \quad (10)$$

with $S'_{ij} = S_{ij} - (S_{kk} / 3)I$ the deviatoric part of the Piola-Kirchhoff stress.

ϕ is a function correcting the basic LVE convolution integral for changing temperature-corrected strain rates; $\mathbf{g}(\boldsymbol{\epsilon})$ is in general a function of the strain invariants of the deviatoric part of the Green strain tensor, which is valid for large strains:

$$E'_{ij} = E_{ij} - \left(\frac{E_{kk}}{3} I \right) \text{ and } E_{ij} = 1/2 (F_{ji} F_{ij} - I) \quad (11)$$

For a uniaxial state of stress (like in a uniaxial tensile test at constant strain rate), $\mathbf{g}(\boldsymbol{\epsilon})$ is a scalar function expressing the ratio of the Cauchy stress as measured during the test to the one that would be obtained applying the LVE constitutive model.

$$g(\epsilon, \epsilon' a_T) = \frac{\sigma_{test}(\epsilon, \epsilon' a_T)}{\sigma_{LVE}(\epsilon, \epsilon' a_T)} \quad (12)$$

Therefore, $\mathbf{g}(\boldsymbol{\epsilon})$ takes the softening generated by dewetting into account: $g \leq 1$ for $\epsilon \geq 0$. In a propellant like formulation 1, with an effective bonding agent, g decreases progressively only when the onset of damage is reached (Fig. 4). Otherwise, g decreases progressively as soon as a tensile

load is applied. Ref. [12] does not prescribe any particular form for the function g as long as experimental data is fitted well. In [14] following fit was taken to fit uniaxial stress-strain data for a formulation 1 propellant:

$g = c_1 + c_2x + c_3y + c_4xy + (c_5 + c_6x + c_7y + c_8xy) \arctan(c_9 + c_{10}x + c_{11}y + c_{12}xy + c_{13}x^2 + c_{14}x^2y)$ with x = maximum principal tensile strain, $y = \log_{10}(\dot{\epsilon}/a_T)$ the temperature reduced strain rate. c_i was determined via least-square fitting of uniaxial tensile data. In a thermoviscoelastic material both rate and temperature control the amount of available energy for microcrack generation and propagation. The use of the damage factor g allows a good correlation between uniaxial tensile tests and theory (9) with respect to what is obtained applying the mere LVE model (Fig. 4). For the 2D samples of this study (formulation 1), following average damage factor was computed:

$g(\epsilon) = 0.375$. The stress is therefore 37,5% of what would be generated in the undamaged material without load.

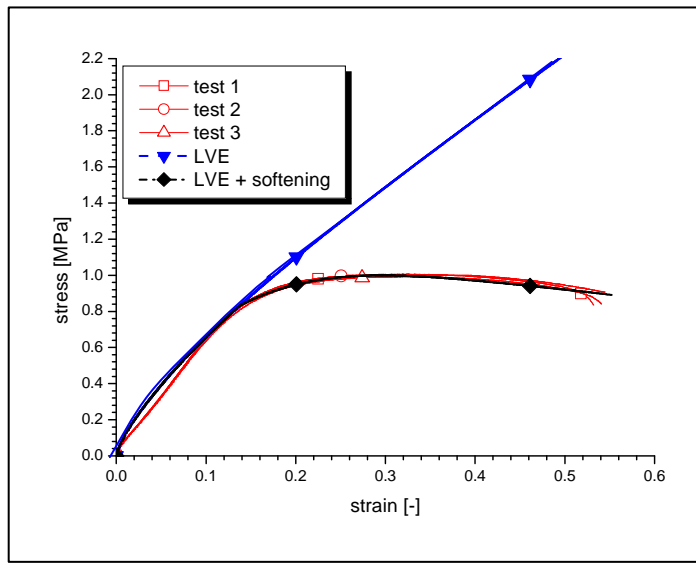


Fig. 4 LVE prediction, Swanson model prediction with a calibrated $g(\epsilon)$ and uniaxial test data, taken from [14]

Thermal simulations

Focusing on (micro)cracks, since the burning rate measurements show faster decomposition rates and subsurface ignition in absence of significant convection, following propagation mechanism for the samples was suggested (Fig. 5) and confirmed by dedicated visualization experiments not reported here:

1. A conduction-induced decomposition of binder and small AP particles producing a high concentration of reactive gases in the crack, followed by:
2. Local ignition near an AP particle producing a jet of gases having $T \approx T_f$. The gas jet impinges the opposite crack surface and ignites it. Finally:
3. Hot reaction gases fill the crack; thermal energy is delivered to the rest of the crack surface and the whole crack ignites.

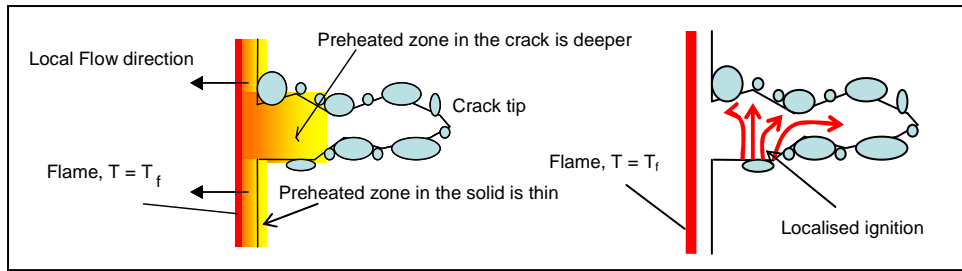


Fig. 5
Sketch
for the
thermal
energy
and
flame
propaga
tion
scenario

into open micro-cracks without convection and radiation

Thermal simulations were performed to check whether this scenario is possible, and in which pressure range it is expected to accelerate the burning rate. If a microcrack is open under the combined action of a previous mechanical damage and tensile load, subsurface ignition is likely to occur in depth if thermal energy can propagate into the crack faster than in the solid phase. Thermal diffusivity, $a = k/\rho c_p$, will therefore play a fundamental role in controlling the energy diffusion through conduction for such a transient diffusion process. Following conditions must be met for the above burning rate augmentation mechanism to hold:

- Thermal energy must propagate faster in the crack than in the solid (the rate of thermal energy propagation in the solid is the burning rate at the pressure and soak temperature under consideration).
- The propagation of thermal energy in the gap is so much faster that the solid heats up to decomposition temperature and ignition occurs in the gas phase before the main burning surface has reached the bottom of the crack.

Considering the thermal diffusivity of the propellant, we have:

$\lambda_{\text{propellant}} = 0.46 \pm 5.6\% \text{ W/mK}$; $a_{\text{propellant}} = 2.7 \cdot 10^{-3} \text{ cm}^2/\text{s}$. (measurement with the hot disk technique on formulation 1).

For the gases in the crack, a depends on pressure (inverse proportionality) through its dependence on ρ [15]. Pressure will therefore play a fundamental role because it decreases the thermal diffusivity of

the gas in the crack and at the same time it increases the burning rate, so that the deflagration wave in the solid moves ahead faster.

For air, the thermal conductivity is one order of magnitude less than for the propellant (λ_{air} at 20°C is about $2.6 \cdot 10^{-2}$ W/mK) but at 1 atm the density is 3 orders of magnitude less, so that a_{air} at 1 atm is about: $a_{\text{air}} = 0.188 \text{ cm}^2/\text{s}$ vs. $a_{\text{propellant}} = 2.7 \cdot 10^{-3} \text{ cm}^2/\text{s}$. At higher pressure, the situation changes, and at about 80 atm the diffusivities match (at a temperature of 20°C).

Considering a moving reference centered on the deflagration wave, we write the energy equation neglecting chemical reactions ahead of the burning surface or in the gas phase of the crack:

$$c_p \rho \frac{\partial T}{\partial t} - \nabla \cdot (\rho u c T - \lambda \nabla T) = 0 \quad (13)$$

Chemical reactions would increase the local temperature, so the estimate is conservative.

An assumption made for the non-stationary simulation was to neglect the fact that the deflagration wave moves forward. This way, we have a fixed frame of reference and can neglect the convective energy term in equation 13, obtaining Fourier's equation. We can partially compensate it through the boundary conditions assuming stationary thermal profiles during the time required to decompose one of the larger AP particles at the sides of the crack. T at $(x, y, t) = (L, \cdot, 0)$ can then be chosen to be the average of the thermal profile in the gas phase, between the surface and L_f . The final flame temperature is calculated at various pressures with Ref. [23] and T_s is taken from [24]. For the formulation investigated we have $T_f = 3050 \text{ K}$ at 1 bar and $T_f = 3500 \text{ K}$ at 60 bar. In our case the boundary condition would be approximately $T = 1990 \text{ K}$ at 1 bar and 2250 K at 60 bar. Following the logic above, we take a characteristic time t_{wave}^* to be the time needed by the deflagration wave to move ahead by the average size of one larger particle: $t_{\text{wave}}^* = D_{\text{AP}} / r_b$ in our case: $t_{\text{wave}}^* = 0.1739 \text{ s}$ at $p = 1 \text{ bar}$ and $t_{\text{wave}}^* = 34 \text{ ms}$ at 60 bar.

Propagation was computed for this time interval for a 2D geometry. At the interface, there is no continuity of physical properties, and the assumption leading to Fourier's equation:

$$\frac{\partial}{\partial x} \left(k \frac{\partial T}{\partial x} \right) \text{ to } k \left(\frac{\partial^2 T}{\partial x^2} \right) \text{ does not hold. The domains were therefore separated into gas phase and}$$

condensed phase, where Fourier's equation holds, and calculations were iterated until the fluxes at the interface matched, i.e. applying following boundary condition:

$$k \nabla T \cdot \hat{n} \Big|_{\text{gas}} = k \nabla T \cdot \hat{n} \Big|_{\text{solid}} \text{ at the interface between gas phase and condensed phase}$$

Results at 1 bar and 60 bar qualitatively confirm the previous estimates (Figs.7-8). At about 60 bar, the temperature at 200-300 μm depth in the crack is just above 620 K, the value at which, according to [16], fast and complete decomposition of AP occurs. Which further reaction will then produce a localized ignition and ignite the rest of the crack walls by impingement/convection depends on pressure. For a premixed flame a temperature of about at least 830 K is necessary (formation of a liquid layer on an AP crystal) [7]: at pressures above 20 bar [6], ammonia and perchloric acid lead to an explosive reaction (the AP premixed monopropellant flame) and localized ignition would occur through this mechanism. At pressures below 20 bar, we know that the AP monopropellant flame generated by HClO_4 and NH_3 does not occur. In this case, HClO_4 would attack the hydrocarbon

molecules coming from some volatilized (and fragmented) binder or plasticizer and produce ignition, i.e. generating the same kind of diffusion flame existing during normal propellant combustion.

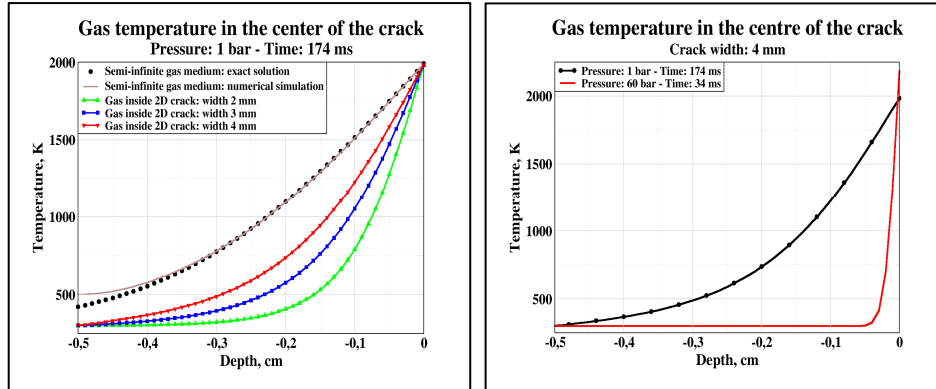


Fig. 7 Left: Temperature profile at the centre of the crack (cracks of different width) at 1 bar after $t=t^*$; Right: Temperature profile at the centre of the crack after $t=t^*$ for a crack of 4 mm width at 1 (dotted line) and 60 bar (continuous)

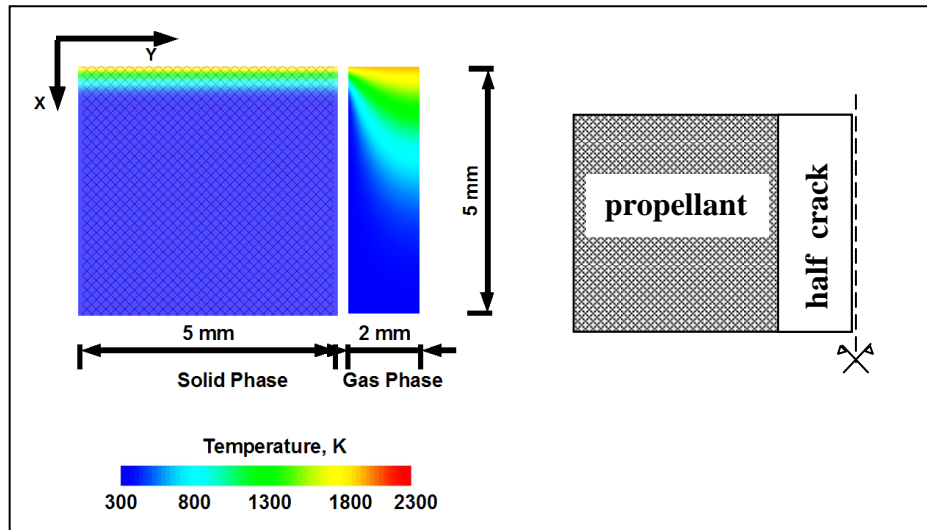


Fig. 8 Contour plot of the temperature distribution inside a crack after $t = t^*$ at 1 bar, showing thermal energy penetration in the crack. Right: 2D field for the simulation

This flame would stabilize the HClO_4 and NH_3 reaction at explosive rates. Notice that according to [16], HClO_4 enhances the volatilization of the binder by fragmenting the molecules at the surface. The source of H/C could be the binder but enough gas could be generated by the plasticizer, which is definitely more prone to evaporation.

At 60 bar, conduction in the gas phase can produce a self-sustained decomposition of AP by a depth equal to the size of a larger AP particle. At most at this pressure, no subsurface ignition in an observable crack will occur. The situation in a motor would be different, because thermal energy exchange by convection of the combustion products in the bore will quickly ignite any small crack.

Correlation of average damage factor and average burning rate

For our samples, we suggest that in the presence of damage caused by dewetting and the action of tensile load, the burning rate is:

$$r_{b,damaged} = \frac{k}{p} \left(\frac{1}{g(\epsilon)} \right) r_{b,undamaged} \quad (14)$$

the average $g(\epsilon)$ was determined to be 0.375. At 1 bar the rate of augmentation was 1.28; k is therefore 0.48. This formula should be validated with more experiments at different damage levels and pressures, since pressure dependence might be more complex. The constants are material-specific would need to be determined by least-square.

In a motor, the thermal energy exchange in microcracks is radically different; convection and hot particles impingement during the ignition transient and normal burning would ignite any microcrack exposed to the burning surface, with significant effects on motor performance [2, 17]. Even radiation alone would produce ignition [18]. An empirical property relationship for damaged material layers for a motor would therefore be:

$$r_{b,damaged} = \left(\frac{k}{g(\epsilon)} \right) r_{b,undamaged} \quad (15)$$

Coupling effects with erosive burning mechanisms are possible: if the propellant zone near the surface of the bore or at other highly stressed areas is damaged and is kept under tension because of the compliance of a lightweight case [10,11,13], enhanced thermal energy transfer induced by a high cross-flow might be affected by the different nature of the propellant surface. Widely used semi-empirical models, like Lenoir and Robillard's, have constants which are fitted to match the pressure traces from development motors [19]; these constants would turn out to be different for a damaged lightweight motor if the surface porosity affects the thermal energy exchange in boundary layer.

Effects on motor level

Applying structural analysis [11, 13] to a flightweight motor we observe that under internal pressure the inner region of the grain at the bore is subjected to tensile strain because of the case compliance. A mechanically aged grain would satisfy the conditions investigated in this study if some microcrack-induced softening occurred before ignition: it would have layers of propellant with microcracks kept open by a tensile load during the first phase of burning. Depending on the motor's geometry and load history a quick estimate indicates that the inner portion of the grain could be affected by dewetting and microcracks if the motor has been subjected to thermal cycling and is

designed to achieve a good performance (high web fraction). Notice that chemical aging affects the same zone of the grain making it more brittle through oxidative cross-linking [20]. An excellent structural simulation of a large motor showing the distribution of porosity in the grain at the bore can be found in reference [21]. An average 1.5-fold increase of the burning rate in the inner 10% of the web would produce a 5 % decrease in the total burning time, with consequences on the overall performance of the system.

Conclusions

The coupled effect of mechanical damage and load using AP:HTPB propellant samples has been modeled, with following results:

For the samples described in Ref. [3], thermal energy propagates quickly into cracks and microcracks at low pressures. Cracks will ignite starting from hot spots. On the other hand, material previously subjected to dewetting but without cracks burns faster (up to twice as fast).

Mechanical damage coupled with a tensile load changes the burning rate: a correlation between the burning rate increase and the average state of damage using the definitions provided by Swanson and Christensen's NLVE material model was obtained.

If a propellant has an optimal degree of saturation of the binder and an effective bonding agent, the onset of mechanical damage is delayed and nothing happens at strain levels below the threshold of damage. This confirms Summerfield's suggestions indicated in ref. [1]. On the other hand, if for some reason the mechanical properties of the material are poor (e.g. if effective bonding agents for new oxidizer crystals do not exist), then augmented burning rate is expected already at very low strains, since microcracks are generated continuously starting from very low strains.

While the thermal energy exchange into micro- or macro-cracks for the samples of this study is driven by conduction, on a system level, thermal energy exchange into a layer of damaged propellant at the bore would be heavily intensified by radiation and convection; a burning rate increase would occur at all pressures, with potential consequences on a system level.

References

- [1] Summerfield, M., and Parker, K.H. "Interrelations between combustion phenomena and mechanical properties in solid propellant rocket motors", da: "Mechanics and Chemistry of Solid Propellants" Eringen, A.C., editor, 1967.
- [2] Hwang, C., Massa, L., Fiedler, R. and Geubelle, P., "Simulation of convective burning and dynamic fracture in solid propellants", 38th AIAA/ASME/SAE/ASEE JPC Conference and Exhibit, Indianapolis, Indiana. Paper No. AIAA 2002-4342.
- [3] Sandri Tussiwand, G., Maggi, F., Bandera, A., and De Luca, L.T. "Intrinsic Structural-Ballistic Interactions in Composite Energetic Materials Part I – Experiments". International Conference on Non-Isothermal Phenomena and Processes, November, 27 Nov – 01 Dec 06, Yerevan, Armenia.

- [4] Glick, R.L., "Comment on Using Heterogeneous Propellant Burning Simulations as Subgrid Components of Rocket Simulations" Technical Comment prepared for submission to the AIAA Journal, private communication.
- [5] Ramohalli, K.N.R., "Steady State Burning of Composite Propellants under Zero Cross-Flow Situation", in "Fundamentals of Solid Propellant Combustion" AIAA Progress in Astronautics and Aeronautics Series, vol. 90, Kuo and Summerfield eds., 1984.
- [6] Boggs, T.L. Deflagration Rate, Surface Structure and Subsurface Profile of Self-Deflagrating Single Crystals of Ammonium Perchlorate. AIAA Journal Vol.8, No.5, May 1970.
- [7] Lengellé, G., Duterque, J., Trubert, J.F. "Combustion of Solid Propellants" from "Internal Aerodynamics of Solid Rocket Motors", Special Course held at the Von Karman Institute of Fluid Dynamics, 27-31 May 2002.
- [8] Krier, H., and Gokhale, S. S., "Modeling of Convective Mode Combustion through Granulated Propellant to Predict Detonation Transition", AIAA Journal, Vol. 16, No.2, Feb 1978, pp. 177-183.
- [9] Saouma, V., "Merlin, a three-dimensional finite element program based on a mixed-iterative solution strategy for problems in elasticity, plasticity, and linear and nonlinear fracture mechanics; user's manual", University of Colorado at Boulder, 06 May 2006. <http://ceae.colorado.edu/~saouma/>.
- [10] Agard Advisory Report 350 (AR 350) "Structural Assessment of Solid Propellant Grains", Propulsion and Energetics Panel Working Group 25, North Atlantic Treaty Organization, Dec 1997.
- [11] NASA SP-8073 "Solid Propellant Grain Structural Integrity Analysis", National Aeronautics and Space Administration, Jun 1973.
- [12] Swanson, S.R., and Christensen, L.W. "A Constitutive Formulation for High-Elongation Propellants", Journal of Spacecraft, Nov - Dec 1983.
- [13] Fitzgerald, J.E., and Hufferd, W.L., "Handbook for the Engineering Structural Analysis of Solid Propellants", CPIA Publ. 214.
- [14] Sandri Tussiwand, G., Weterings, F.P., Reeling Brouwer, G., and Besser, H.L. "Application of Embedded Bondline Sensor Technology to a Nozzleless Rocket Motor, 37th International Annual Conference of ICT, June 2006.
- [15] Borghi, R., and Destriau, M. "Combustion and Flames – Chemical and Physical Principles", Editions Technip, 1998.
- [16] Kishore, K., and Gayathri, V., "Chemistry of Ignition and Combustion of Ammonium Perchlorate-Based Propellants", AIAA Progress in Astronautics and Aeronautics, vol. 90 – Fundamentals of Solid Propellant Combustion, Kuo K.K. and Summerfield M., editors, AIAA 1984.
- [17] Smirnov, N.N., and Dimitrienko, I.D., "Convective Combustion Regime in a Deformable Solid Fuel with Longitudinal Channels", Fizika Goreniya i Vzryva, Vol. 22, No.3, pp. 59-67, May-June 1986, Moscow (translation).
- [18] Cain, J., and Brewster, Q., "Radiative Ignition of Fine Ammonium Perchlorate Composite Propellants" Propellants, Explosives and Pyrotechnics, 31, No.4 278-284, Wiley, 2006.

- [19] Razdan, M.K., and Kuo, K.K. "Erosive burning of Solid Propellants", AIAA Progress in Astronautics and Aeronautics, Vol. 90 – Fundamentals of Solid Propellant Combustion, Kuo K.K. and Summerfield M., editors, AIAA 1984.
- [20] Reeling Brouwer, G., Weterings, F.P., and Keizers, H., "Evaluation of Ageing in Composite Propellant Grains", AIAA 2005-3803, 41st Joint Propulsion Conference, July 2005, AZ.
- [21] Namazifard A., Hjelmstad K., Sofronis P., Nakshatrala K., Tortorelli D., and Fiedler, R. "Simulations of Propellant Slumping in the Titan IV SRMU Using Constitutive Models with Damage Evolution", AIAA-2005-3994, Joint Propulsion Conference & Exhibit, 10-13 Jul 2005.
- [22] Maggi, F., "Heterogeneity Effects on Composite Solid Propellants", PhD. Thesis in Aerospace Engineering, Politecnico di Milano, April 2006.
- [23] Cpropep v 1.0, 2000 by Antoine Lefebvre. Thermodynamic data from B. Mac Bride, NASA Glenn Research Center.
- [24] Zanutti, C., Volpi, A., Bianchessi, M., and De Luca, L.T., "Measuring Thermodynamic Properties of Burning Propellants", in "Nonsteady Burning and Combustion Stability of Solid Propellants" in AIAA Progress in Astronautics and Aeronautics Series, Vol. 143, De Luca, Price, Summerfield editors, 1992.

ՀԱՅԱՍՏԱՆԻ ՀԱՆՐԱՊԵՏՈՒԹՅԱՆ ԳԻՏՈՒԹՅՈՒՆՆԵՐԻ
ԱԶԳԱՅԻՆ ԱԿԱԴԵՄԻԱ
НАЦИОНАЛЬНАЯ АКАДЕМИЯ НАУК РЕСПУБЛИКИ
АРМЕНИЯ

Հայաստանի քիմիական հանդես 60, №2, 2007 Химический журнал Армении

**A SCALING AND NUMERICAL ANALYSIS OF THE EFFECTS OF NATURAL
CONVECTION WHEN SAL'NIKOV'S REACTION: $P \rightarrow A \rightarrow B$ OCCURS,
TOGETHER WITH DIFFUSION AND HEAT TRANSFER IN A SPHERICAL BATCH
REACTOR**

A.N. CAMPBELL, S.S.S. CARDOSO AND A.N. HAYHURST*

Department of Chemical Engineering, University of Cambridge, Pembroke Street,
Cambridge CB2 3RA, England.

*anh1000@hermes.cam.ac.uk

Abstract

Sal'nikov's reaction: $P \rightarrow A \rightarrow B$ involves a precursor, P, in two consecutive, first-order chemical reactions, yielding a final product B *via* an intermediate A. Partly as an academic exercise, but partly because of its relationship with cool flames, the situation is considered where the second step is faster than the first one, which is taken to be thermoneutral without an activation energy. The second step is assumed to have a significant activation energy, although it is exothermic. The reaction proceeds batchwise inside a spherical reactor, whose walls are held at a constant temperature, but do not participate chemically. Natural convection becomes important, once the temperature is high enough for the Rayleigh number (Ra) to reach $\sim 10^3$. The subsequent behaviour of the system depends on the interaction between convection, diffusion of heat and mass, and chemical kinetics. By examining the governing equations, we develop and evaluate scales for the characteristic velocity, the concentration of the intermediate A and the temperature rise during the progress of the reaction, for the two extreme cases when transport is dominated, in turn, by diffusion and then by natural convection. These scales depend on the characteristic timescales for the interacting phenomena of chemical reaction, diffusion and natural convection. Typically, the characteristic velocity in a relatively small reactor of radius 0.27 m is as large as 0.3 m s^{-1} , when the temperature rise is $\approx 100 \text{ K}$ near the centre of the vessel. These theoretical predictions from scaling are verified by full numerical simulations. Oscillations of both the temperature and the concentration of the intermediate, A, can occur and the conditions for their appearance are identified. Any accompanying flow field proves to be toroidal, with the fluid ascending close to the reactor's axis, but descending adjacent to its walls.

In addition, the effects of variables, such as the initial temperature of the batch reactor and its contents, the pressure and also the size of the reactor are all assessed, together with a consideration of what happens when the reaction proceeds in the liquid phase. In this case, because of the different physical properties of a liquid and a gas, natural convection is more intense than in the gas-phase and is quite likely to lead to turbulence and good mixing.

NOMENCLATURE

a	concentration of intermediate A
a'	dimensionless concentration of A, $a' = a / a_0$
a_0	scale for concentration of A
C_P	specific heat at constant pressure
C_V	specific heat at constant volume
D_A	diffusion coefficient of species A
E_i	activation energy of step i of Sal'nikov's reaction (I)
g	acceleration due to gravity
k_i	rate constant of step i of the reaction
$k_{2,0}$	rate constant of step 2 evaluated at $T = T_0$
L	characteristic length of the reactor
Le	Lewis number = κ / D_A
p	concentration of precursor P
p'	dimensionless concentration of P, $p' = p / p_0$
p_0	initial concentration of P
\mathcal{P}	pressure in the reactor
\mathcal{P}'	dimensionless pressure, $\mathcal{P}' = (\mathcal{P} - \mathcal{P}_0) / \rho_0 U^2$
\mathcal{P}_0	initial pressure
Pr	Prandtl Number, $Pr = \nu / \kappa$
q_i	exothermicity of step i of the reaction
R	universal gas constant
Ra	Rayleigh number, $Ra = \beta g \Delta T L^3 / (\kappa \nu)$
t	time
t'	dimensionless time, $t' = U t / L$
T	temperature
T'	dimensionless temperature, $T' = (T - T_0) / \Delta T$
T_0	constant wall temperature
\underline{u}	velocity vector
\underline{u}'	dimensionless velocity vector, $\underline{u}' = \underline{u} / U$
U	scale for velocity
\underline{x}	spatial coordinates
\underline{x}'	dimensionless spatial coordinates, $\underline{x}' = \underline{x} / L$

Z_2	pre-exponential factor in Arrhenius expression for k_2
β	coefficient of thermal expansion, $\beta = 1 / T$
γ	ratio of specific heats $= C_p / C_v$
ΔT	scale for temperature increase
ΔT_{ad}	adiabatic temperature increase, $\Delta T_{ad} = q_2 / C_v$
κ	thermal diffusivity
ν	kinematic viscosity
ρ	density
ρ_0	density at $T = T_0$
$\tau_{convection}$	timescale for convection
$\tau_{diffusion A}$	timescale for diffusion of species A
$\tau_{diffusion H}$	timescale for diffusion of heat
$\tau_{step i}$	timescale for step i of reaction (I)

1. Introduction

During any exothermic reaction in a batch reactor, spatial temperature gradients develop. If these gradients are sufficiently large, natural convection occurs. The intensity of the flow resulting from natural convection is determined by the Rayleigh number, $Ra = \beta g L^3 \Delta T / \kappa \nu$. In general, the overall behaviour of the system will be determined by the interaction of three of its basic properties: chemical reaction, diffusion (of both heat and matter) and natural convection. Several exothermic reactions exhibit oscillations in both the local temperature and concentration of intermediates (Gray & Scott, 1990). One example is a ‘cool flame’, as displayed by a mixture of a paraffin and oxygen, in which the temperature and concentration of an intermediate display sustained oscillations.

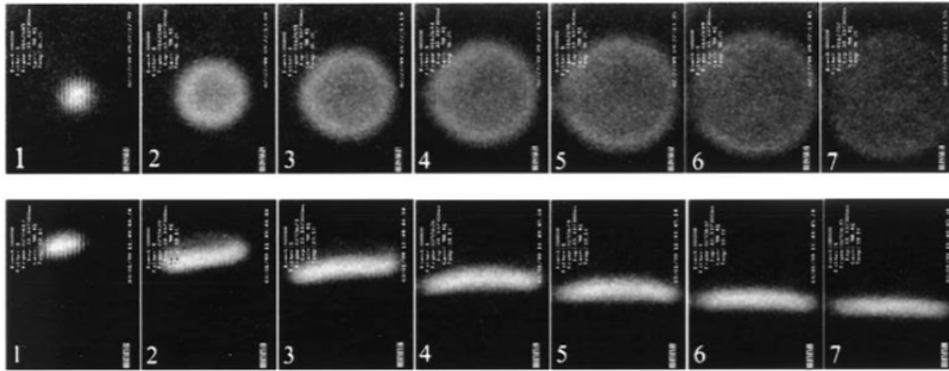


Fig. 1. Cool flame of butane + oxygen in (a) micro- and (b) terrestrial gravity. From <http://www.grc.nasa.gov/WWW/RT1999/6000/6711wu.html>

Figure 1(a) shows the development of a real cool flame in a mixture of butane and oxygen without natural convection, as achieved under microgravity. If this is compared with Fig. 1(b), which shows

the equivalent cool flame under full gravity, we can see that natural convection removes the spherical symmetry. Instead, a horizontal ‘flat’ flame moves vertically downwards through the mixture of reactants. This is seen below to depend on the interaction of chemical kinetics, diffusion of both heat and matter, and also natural convection. These interactions have attracted the attention of Professor Merzhanov (Merzhanov & Shtessel, 1973). This contribution is offered as a tribute to Merzhanov, as well as to celebrate his 75th birthday and wish him “Many Happy Returns”.

2. Sal’nikov’s Reaction

Interestingly, Sal’nikov’s reaction (1949) is probably the simplest way of modelling the chemical reactions in a cool flame (Bardwell & Hinshelwood, 1951). Of course, it fails to describe all the complexities (Griffiths & Barnard, 1995), but it facilitates an exploration of the interaction between chemical reaction, diffusion (of both heat and matter) and natural convection. The reaction consists of two, consecutive first-order steps:



This scheme is the simplest to display thermokinetic oscillations and so is investigated here in some detail. The first step of the reaction is assumed here to be thermoneutral (*i.e.* E_1 and q_1 , the activation energy and exothermicity of the reaction are both zero). Step 2 is exothermic with E_2 and $q_2 > 0$. Oscillations occur due to the nonlinear thermal feedback arising from the Arrhenius temperature dependence of the rate of step 2.

3. Governing Equations

We consider, initially pure, gaseous P undergoing Sal’nikov’s reaction in a closed spherical vessel of radius L , whose wall is held at a constant temperature, T_0 . The equation for a , the concentration of the active intermediate A, is

$$\frac{\partial a}{\partial t} + \underline{u} \cdot \nabla a = D_A \nabla^2 a + k_1 p_0 \exp(-k_1 t) - k_2 a, \quad (1)$$

where p_0 is the initial concentration of P. It is assumed in this equation that the concentration of P in the reactor is initially uniform, and that it remains so, equal to $p_0 \exp(-k_1 t)$, throughout the course of the reaction. This assumption depends on k_1 being independent of temperature (because $E_1 = 0$) and holds only for relatively small increases in temperature. The conservation of energy is:

$$\frac{C_V}{C_P} \frac{\partial T}{\partial t} + \underline{u} \cdot \nabla T = \kappa \nabla^2 T + \frac{q_2 k_2}{\rho_0 C_P} a, \quad (2)$$

where ρ_0 is the density at the initial temperature T_0 . The Navier-Stokes equations describe the conservation of momentum in:

$$\frac{\partial \underline{u}}{\partial t} + \underline{u} \cdot \nabla \underline{u} = -\frac{1}{\rho_0} \nabla (\mathcal{P} - \mathcal{P}_0) + \nu \nabla^2 \underline{u} + \frac{\rho - \rho_0}{\rho_0} \underline{g}, \quad (3)$$

where P_0 is the initial pressure in the reactor. The conventional Boussinesq approximation is adopted, *i.e.* it is assumed that the density only varies in the buoyancy term of the Navier-Stokes equations. In this term the density varies as $\rho = \rho_0[1 - \beta (T - T_0)]$, where β is the coefficient of thermal expansion. The final equation required is the continuity equation. The adoption of the Boussinesq approximation allows the continuity equation to be written in its incompressible form, *i.e.*

$$\nabla \cdot \underline{u} = 0 \quad (4)$$

Initially the gas is pure P at a temperature T_0 , and is motionless. The wall of the reaction vessel is held at T_0 throughout, and the usual no-slip condition applies. There is also assumed to be no flux of any species at the wall, where no heterogeneous reactions occur. However, there is of course heat transfer to the wall.

4. Scaling Analysis

In order to make equations (1) – (4) dimensionless, the following seven dimensionless variables can be defined:

$$a' = \frac{a}{a_0}; p' = \frac{p}{p_0}; T' = \frac{T - T_0}{\Delta T}; u' = \frac{u}{U}; P' = \frac{P - P_0}{\rho_0 U^2}; x' = \frac{x}{L} \text{ and } t' = \frac{Ut}{L}, \quad (5 \text{ a – g})$$

where a_0 is a characteristic value of the concentration of species A, ΔT is the characteristic temperature rise and U is the characteristic velocity. At this stage, these three scales are unknown, whereas p_0 and L (the radius of the reactor) are defined for a given system. It is also useful at this stage to define five characteristic timescales:

$$\tau_{\text{step 1}} = \frac{1}{k_1}; \tau_{\text{step 2}} = \frac{1}{k_{2,0}}; \tau_{\text{diffusion H}} = \frac{L^2}{\kappa}; \tau_{\text{diffusion A}} = \frac{L^2}{D_A} \text{ and } \tau_{\text{convection}} = \frac{L}{U}, \quad (6 \text{ a – e})$$

for the various interacting phenomena in the system, namely the two steps of reaction (I), diffusion of both heat and the intermediate A and finally convection. Here $k_{2,0}$ is k_2 evaluated at the wall's temperature, T_0 . The relative values of these timescales will determine the behaviour of the system. For a gas $\tau_{\text{diffusion A}} = \tau_{\text{diffusion H}}$. This implies that $\kappa = D_A$ or the Lewis number $Le = \kappa / D_A$ is unity.

This leaves four characteristic timescales. In fact, it can be shown (Campbell et al., 2005a,b) that if the initial temperature, T_0 , is fixed, together with the variables: C_p , C_v , D_A , κ , ν , and q_2 , the behaviour of the system is totally defined by the three dimensionless groups:

$$\frac{\tau_{\text{step 2}}}{\tau_{\text{step 1}}} p' = \frac{k_1}{k_{2,0}} \frac{p}{p_0}; \quad \frac{\tau_{\text{step 2}}}{\tau_{\text{diffusion}}} = \frac{\kappa}{k_{2,0} L^2}; \quad \frac{\tau_{\text{step 2}}}{\tau_{\text{convection}}} = \frac{U}{k_{2,0} L} \quad (7)$$

Thus it turns out that in general the behaviour of the system is determined by the position of a point on Fig. 2, the regime diagram. This plots ratios of the above four time constants, as indicated by Eq. (7). On Fig. 2 a straight line is drawn in the vertical plane defined by the axes: $\tau_{\text{step 2}} / \tau_{\text{diffusion}}$ and $\tau_{\text{step 2}} / \tau_{\text{convection}}$. This line passes through the origin of Fig. 2 and can be shown to have a slope of $1/(RaPr)^{1/2}$. The line is accordingly the locus of constant Ra .

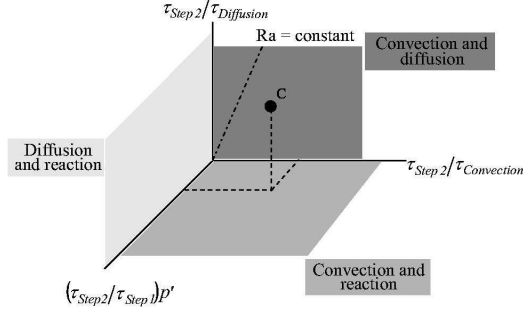


Fig. 2. The general 3-D regime diagram describing the system, when both natural convection and diffusion are important. The axes represent ratios of the characteristic timescales for the two chemical steps, as well as of diffusion and convection. A line of constant Rayleigh number (Ra) is shown.

Figure 3 is a plot derived from Fig. 2 for constant $(\tau_{step\ 2}/\tau_{step\ 1})\ p'$. It shows the available space divided by the lines for $Ra = 10^3$ and 10^6 . Thus for $Ra \ll 10^3$ no natural convection is expected, for $10^3 < Ra < 10^6$ natural convection will be laminar, but will be turbulent for $Ra > 10^6$.

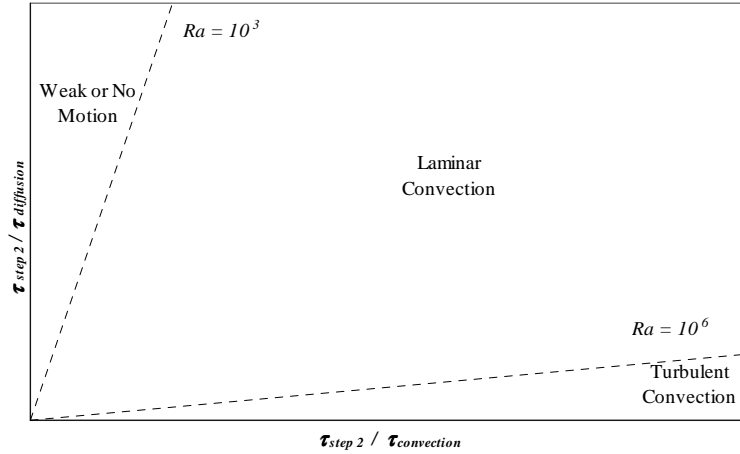


Fig. 3. Simplified 2-D regime diagram, showing (for a fixed $\tau_{step\ 2}/\tau_{step\ 1}\ p'$) two lines of constant Ra , and the nature of the flow in each region.

Of course, transport can be controlled by either diffusion or convection, and the form of the unknown scales (a_0 , ΔT , U) will depend on which mechanism dominates. We examine each case, in turn, in order to determine the most appropriate scales in that case. It is important to note that in Fig. 3, a straight line through the origin has a slope $1/(RaPr)^{1/2}$, with $Pr \sim 1$ for a gas, but $Pr = 6.6$ for liquid water at 22°C.

4.1 Transport Controlled by Diffusion

For Rayleigh numbers less than a threshold value (of $\approx 10^3$) (Tyler, 1966; Turner, 1979), natural convection will be unimportant, so that diffusion will be the dominant mechanism for the transfer of mass. Likewise, heat transfer is by thermal conduction, *i.e.* the diffusion of heat. When diffusion dominates transport, the temperature and concentration fields are approximately spherically symmetric, with the maximum temperature occurring close to the centre of the reactor. In this case, the characteristic velocity, U , is given by D / L , where D is either the thermal or the molecular diffusivity. We firstly assume that Eq. (1) for species A is dominated by the kinetic terms. This yields a scale for the characteristic concentration of species A:

$$a_0 \sim \frac{k_1}{k_{2,0}} p_0 = \frac{\tau_{step\ 2}}{\tau_{step\ 1}} p_0, \quad (8)$$

i.e. the steady state hypothesis. If we similarly assume that the diffusion and generation terms dominate in the dimensionless version of the energy balance (2), we can derive a scale for ΔT as:

$$\Delta T \sim \frac{q_2 k_1 L^2}{C_p \kappa} = \frac{\Delta T_{ad}}{\gamma} \frac{\tau_{diffusion\ H}}{\tau_{step\ 1}}, \quad (9)$$

where ΔT_{ad} is the adiabatic temperature increase ($= q_2 / C_v$) and γ is the ratio of specific heats (C_p / C_v). This scaling assumes that $\tau_{convection} \gg \tau_{diffusion} \gg \tau_{step\ 2}$, *i.e.* the working point in Fig. 3 is to be found in the region of low Ra .

4.2 Transport Controlled by Convection

When the Rayleigh number becomes sufficiently large, natural convection becomes the dominant transport mechanism. Thus for $10^3 < Ra < 10^6$, the convective flow is expected (Turner, 1979) to be laminar. Natural convection distorts the spherical symmetry observed when diffusion dominates transport; it also leads to the formation of a hot zone above the centre of the reactor (Cardoso *et al.*, 2004a, b). If we assume that the convective and buoyancy terms dominate in the Navier-Stokes Eqs. (3), we can define an appropriate scale for the characteristic velocity as

$$U \sim [\beta g L (\Delta T)]^{1/2}. \quad (10)$$

Similarly, if we assume that the chemical kinetic terms dominate Eq. (1) (as in the previous section) and that convection and the generation of heat dominate the thermal balance (2), we can define a scale for ΔT as:

$$\Delta T \sim \left(\frac{q_2}{C_p} \right)^{2/3} \left(\frac{k_1^2 L}{\beta g} \right)^{1/3} = \frac{\Delta T_{ad}}{\gamma} \frac{\tau_{convection}}{\tau_{step\ 1}}. \quad (11)$$

This scaling for ΔT assumes that $\tau_{diffusion} \gg \tau_{convection} \gg \tau_{step\ 2}$. Interestingly, by assuming that convection and the generation of A in step 1 dominate Eq. (1) one obtains:

$$a_0 \sim \frac{k_1 p_0 L}{U} = \frac{\tau_{convection}}{\tau_{step\ 1}} p_0. \quad (12)$$

This is for the working point being located on Fig. 3 in a region of medium Ra . In the next section we compare these scales to the results of a full numerical solution of all the governing equations, for the two separate cases where either diffusion or natural convection is the dominant mode of transport.

5. Numerical Solution

Equations (1) – (4) were solved numerically for a spherical batch reactor with a fixed wall temperature, T_0 , containing initially pure gas P, which then undergoes Sal'nikov's reaction. The equations were solved using *Fastflo* (Fastflo Tutorial Guide, 2000), which is a PDE solver utilising the finite element method. The algorithm used was the same as that outlined by Cardoso *et al.* (2004b).

For the purpose of the numerical simulations, we take physical and chemical data for the thermal decomposition of di-*t*-butyl peroxide in a spherical reactor. This reaction was chosen, because it can be shown to behave like Sal'nikov's reaction under certain conditions (Griffiths *et al.*, 1988; Gray and Griffiths, 1989); thus experimental studies using a semi-batch reactor with the slow admission of reactant mimics the effect of step 1 in Sal'nikov's reaction. Such an arrangement is suitable for investigating Sal'nikov's reaction in the well-mixed limit; however, it is not suitable for cases which are not spatially uniform. Sal'nikov's reaction has been studied numerically by Fairlie and Griffiths (2002) in both the well-mixed and zero-gravity extremes, as well as by Cardoso *et al.* (2004a, b) when natural convection is important. The following constants were chosen to match those used by Cardoso *et al.* (2004a, b). The temperature of the wall of the spherical reactor, T_0 , was held constant at 500 K and the physicochemical properties used were as follows: the initial molar density $\rho_0 = 8.2 \text{ mol m}^{-3}$ (corresponding to a pressure of 0.34 bar at 500 K), the heat capacity at constant volume $C_V = 190 \text{ J mol}^{-1} \text{ K}^{-1}$, and the exothermicity of step 2, $q_2 = 400 \text{ kJ mol}^{-1}$. We define the base case chemistry such that the rate constant $k_1 = 0.025 \text{ s}^{-1}$, corresponding to $\tau_{\text{step } 1} = 40 \text{ s}$, and $k_2 = Z_2 \exp(-E_2 / R T)$ with $Z_2 = 2 \times 10^{15} \text{ s}^{-1}$ and $E_2 / R = 18280 \text{ K}$. These values give $k_{2,0} = 0.265 \text{ s}^{-1}$, and hence $\tau_{\text{step } 2} = 3.77 \text{ s}$, which is thus approximately an order of magnitude faster than step 1. Furthermore, the simplifying assumption that the Lewis and Prandtl numbers are unity was made. Computations were done for reactors of different sizes at several values of Ra , both in the region where diffusion controls transport and when convection dominates. To further verify the scales developed, the kinetic rate constants were also varied. Given that the two scales for ΔT (Eqs. (9) and (11)) depend on k_1 only, a range of values for k_1 was considered. The pre-exponential factor in k_2 was hypothetically halved to confirm that ΔT is indeed independent of k_2 .

6. NUMERICAL RESULTS

6.1 Diffusive Regime

We begin by exploring all the cases when diffusion controls transport by considering in detail the cases $Ra = 0$ and $Ra \sim 600$. This means that as far as Fig. 3 is concerned, we are only considering systems on, or very near, the vertical axis (so $g \sim 0$),

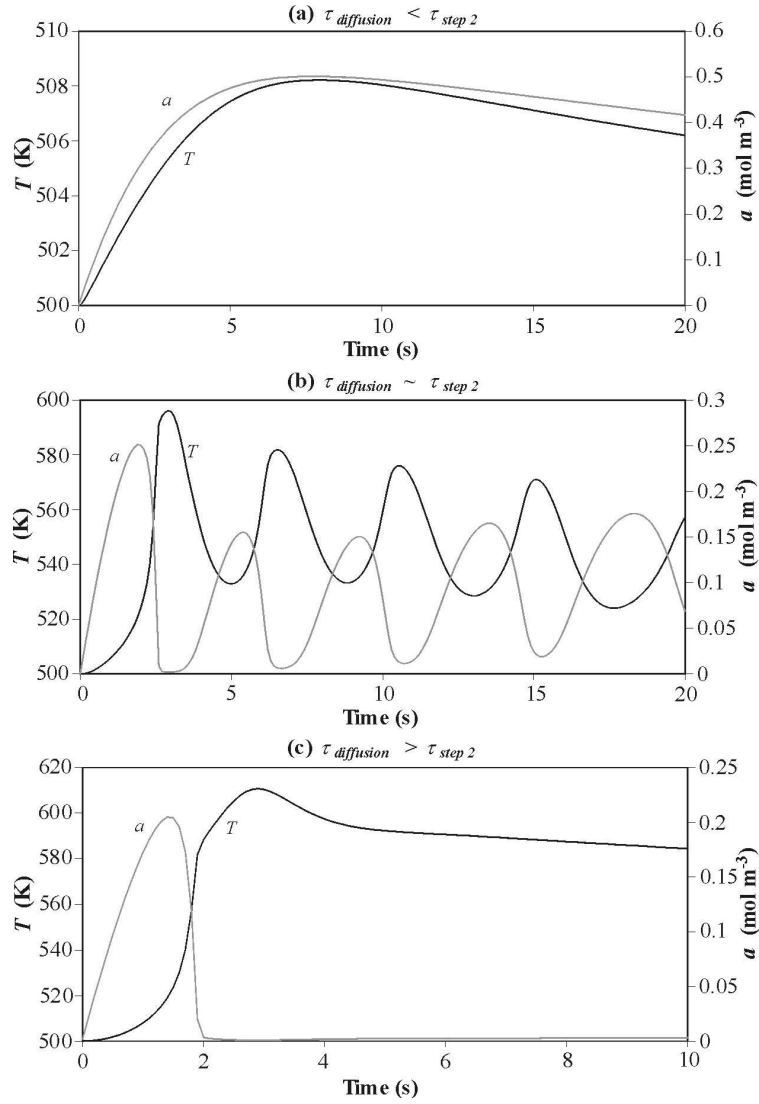


Fig. 4. Plots of the temperature (T) and concentration (a) of the intermediate A at the centre of the reactor against time, when diffusion controls transport for: (a) $\tau_{diffusion} = 1$ s; $L = 10$ mm (b) $\tau_{diffusion} = 4$ s; $L = 20$ mm (c) $\tau_{diffusion} = 9$ s; $L = 30$ mm, all for the base-case chemistry with $g = 0$ m s⁻² and $\kappa = 1 \times 10^{-4}$ m² s⁻¹.

where only diffusion and reaction occur. Another example of Ra being low is a gaseous system at a low pressure; in this context it is noted below that Ra is proportional to the square of the pressure. Nevertheless, it turns out that there are three identifiable regions, where the system behaves differently, as shown more clearly in Fig. 4(a – c). The temporal development of the temperature and the concentration of A at the centre of the reactor for three different values of $\tau_{diffusion}$ are plotted. In the three cases presented, the chemistry is that of the base case, *i.e.* $\tau_{step\ 1} = 40$ s and $\tau_{step\ 2} = 3.77$ s at

500 K, and $\tau_{diffusion}$ has been varied by changing the radius, L , of the reactor (in this case the graphs represent $L = 10, 20$ and 30 mm, respectively). For a small reactor ($L < 0.01$ m), the working point is on the vertical axis of Fig. 3, far away from the origin. For this case, Fig. 4(a) shows slow growths and decays of both the temperature and the concentration of A with time. In addition, there is only a relatively small increase in temperature (of ~ 8 K) to the maximum at the centre of the reactor, so the system behaves almost isothermally. For these cases with a small $\tau_{diffusion}$, we would expect the temperature and concentration fields to be in effect spatially uniform, with the exception of the thermal and concentration boundary layers at the wall. This approximate spatial uniformity decreases the magnitude of the convective and diffusive terms in Eq. (1) relative to that of the reaction terms. Therefore, we expect ΔT to have the form of Eq. (9), *i.e.* there is a dependence on k_1 , but not k_2 . Indeed, the concentration and temperature fields obtained numerically were virtually uniform in these cases. The temperature and concentration only change by $\sim 1\%$, on moving from the wall to the centre of the reactor. This small variation in temperature and concentration leads us to describing the system as approximately spatially uniform. Additionally our numerical results show that the decay in temperature and concentration (as shown by Fig. 4(a)) is proportional to $\exp(-k_1 t)$, thus lending support to the hypothesis that k_1 is the dominant kinetic parameter in this system. In all three cases plotted in Fig. 4(a-c), the fields of temperature and of the concentration of the intermediate A were in fact spherically symmetric.

When we increase the size of the reactor, we move into a region of instability, where the temperature and the concentration of A exhibit temporal oscillations, as shown in Fig. 4(b) for the centre of the reactor. In fact, the concentration of A oscillates in anti-phase with the temperature, as has been shown previously (Cardoso *et al.* 2004a, b). It was found that oscillations only occurred for values of the reactor's radius, L , in a narrow band, whose location depended on the physical and kinetic parameters used. It seems that (see below), when diffusion is the dominant transport mechanism, the range of L , over which oscillatory behaviour is observed, corresponds to the region where the characteristic timescales for diffusion and reaction in step 2 are of similar magnitude, *i.e.* $\tau_{diffusion} \approx \tau_{step\ 2}$.

For $L > 0.03$ m, the working point moves along the vertical axis of Fig. 3 closer to the origin. Now the temporal evolutions of temperature and the concentration of A at the centre of the reactor are shown by Fig. 4(c). Instead of the oscillations, there is now an initial peak in the concentration curve, which then rapidly decays to almost zero. The temperature now rises by ~ 100 K, because of heat removal from a larger vessel being slower. The plot in Fig. 4(c) shows an initially fast rise in temperature and then there is a distinct 'kink' in the curve (at ~ 2 s), when the concentration of the intermediate reaches a steady value, close to zero. The 'kink' in the temperature curve can be explained by examining Eq. (2) for the conservation of energy. When the concentration of A falls rapidly to virtually zero, the heat generation term in Eq. (2) effectively disappears. It is this swift change in the form of the governing equation that causes the observed change in the temporal development of the temperature.

The plot in Fig. 5 checks Eq. (9) by showing the computed values of $\gamma (\Delta T / \Delta T_{ad})$ plotted against $(\tau_{diffusion} / \tau_{step\ 1})$ for when diffusion is the dominant transport mechanism. The temperature rise was

taken to be that at the centre of the reactor, because this is where ΔT is at its maximum value, due to the spherical symmetry. Figure 5 evidently reveals three regimes. There is linearity for high and very low ($\tau_{diffusion} / \tau_{step 1}$); the region between them is where oscillations occur. Equation (9) suggests that there should be a linear plot in Fig. 5. Therefore our scale, Eq. (9), for ΔT is of the correct form. When $\tau_{diffusion} / \tau_{step 1} > 0.1$, Eq. (13) can be modified by adding a constant factor, which can be found from Fig. 5 by the least squares method. Thus the characteristic temperature rise is given by:

$$\gamma \frac{\Delta T}{\Delta T_{ad}} = (0.141 \pm 0.002) \frac{\tau_{diffusion}}{\tau_{step 1}}, \left(\frac{\tau_{diffusion}}{\tau_{step 1}} < 0.04 \right) \quad (13)$$

$$\text{and } \gamma \frac{\Delta T}{\Delta T_{ad}} = (0.100 \pm 0.003) \frac{\tau_{diffusion}}{\tau_{step 1}} + (0.030 \pm 0.002), \left(\frac{\tau_{diffusion}}{\tau_{step 1}} > 0.1 \right). \quad (14)$$

In the narrow region between these two linear regimes, where oscillations occur, the ‘error bars’ in Fig. 5 show the range of the oscillations, measured from the first peak to the first trough. Oscillations were only observed in this narrow band, where $\tau_{diffusion} \sim \tau_{step 2}$, as noted above.

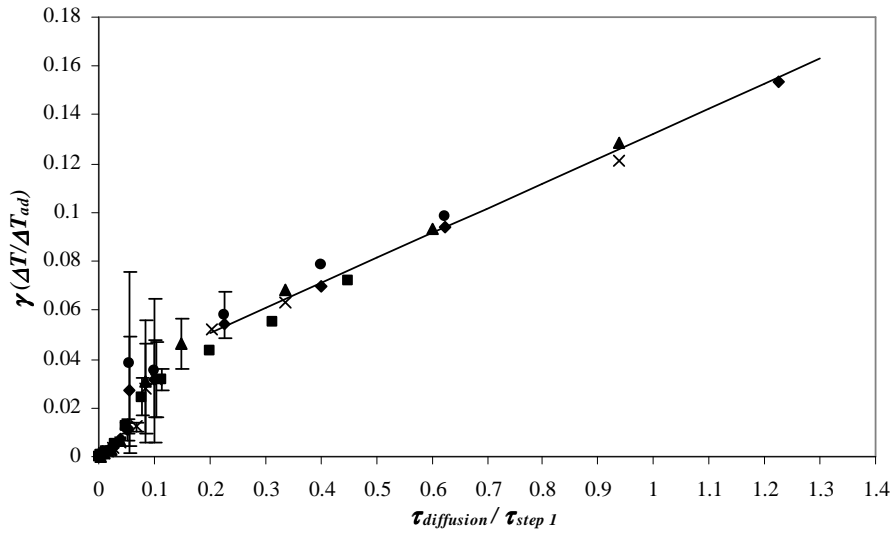


Fig. 5. Plot of $\gamma(\Delta T / \Delta T_{ad})$ against $\tau_{diffusion} / \tau_{step 1}$ in the diffusive regime. The line shown corresponds to Eq. (14). (◆ $k_l = 0.025 \text{ s}^{-1}$, $k_{2,0} = 0.265 \text{ s}^{-1}$, $Ra = 0$; ■ $k_l = 0.0125 \text{ s}^{-1}$, $k_{2,0} = 0.265 \text{ s}^{-1}$, $Ra = 0$; ▲ $k_l = 0.0375 \text{ s}^{-1}$, $k_{2,0} = 0.265 \text{ s}^{-1}$, $Ra = 0$; ● $k_l = 0.025 \text{ s}^{-1}$, $k_{2,0} = 0.132 \text{ s}^{-1}$, $Ra = 0$; × $k_l = 0.025 \text{ s}^{-1}$, $k_{2,0} = 0.265 \text{ s}^{-1}$, $Ra \sim 600$).

6.2 Oscillations in Microgravity

A region of oscillations was identified by performing very many simulations for when diffusion is the only transport mechanism, as in microgravity, but for different $\tau_{step 1} / \tau_{step 2}$. Figure 6 shows the approximate regions defined through simulations for $g = 0$ and different $\tau_{step 1} / \tau_{step 2}$. The axes of the regime diagram in Fig. 6 are the reciprocal of those in Fig. 2. This is to ensure that the region of

oscillations is closed. Also, p' has been omitted from the abscissa, because it is a function of the two quantities being plotted in Fig. 6, when the precursor P is uniformly distributed throughout the reactor. Regions of sustained and damped oscillations were found. These areas in Fig. 6 are an order of magnitude larger than the region of oscillations defined analytically for a pseudo-1-D system by Gray and Scott (1990). An example of a sustained oscillation was seen in Fig. 4(a). Interestingly, these sustained oscillations disappear when $Ra > 10^3$ and the oscillations become noticeably damped. The dotted lines shown in Fig. 6 correspond to areas where the numerical scheme broke down. As an aside, one of our initial assumptions was that $\tau_{step\ 2} < \tau_{step\ 1}$, which partly explains the dotted lines in Fig. 6. The oscillations occur in the region defined approximately by $0.04\ \tau_{step\ 1} < \tau_{diffusion} < 0.2\ \tau_{step\ 1}$, subject to the constraint that $\tau_{diffusion} < 4\ \tau_{step\ 2}$. Before, for $Ra < 10^3$ it was decided that $\tau_{diffusion} \sim \tau_{step\ 2}$ for oscillations to occur. Figure 6 for $Ra = 0$ broadens that criterion by also considering the importance of $\tau_{step\ 2}/\tau_{step\ 1}$. In addition to the region of oscillations, two distinct types of non-oscillatory behaviour are shown in Fig. 6. These correspond to a slow reaction with a low temperature rise, and a rapid reaction with a large temperature rise. This situation is very similar to the conditions for the occurrence of cool flames, which on an ignition diagram are found to lie between those for a rapid thermal explosion and a very slow reaction.

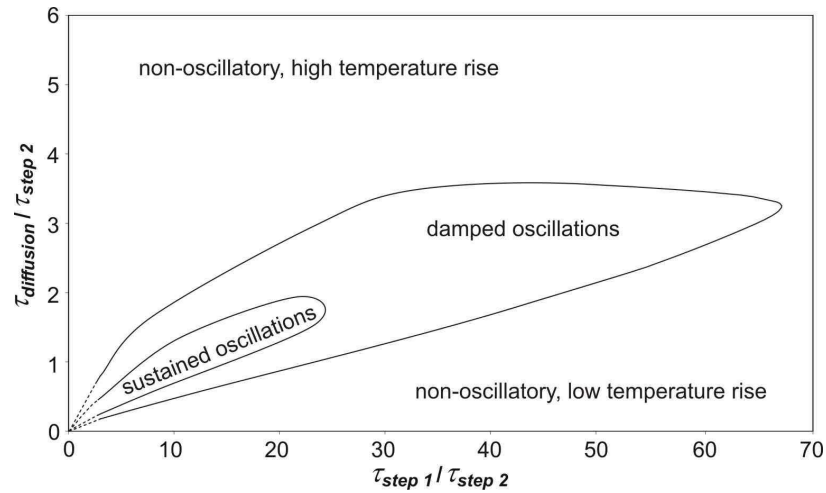


Fig. 6. A 2-D regime diagram showing the approximate region of oscillations for zero-gravity, as identified after many simulations. The dashed lines are extrapolations of the boundaries into regions where the numerical scheme and model broke down.

6.3 Convective Regime

The behaviour of the system when convection is more important than diffusional transport was investigated by again examining full numerical solutions, but for $Ra \sim 5000$ and 21500 . The convective flow in both these cases should be laminar. The flow-field is such that the gas rises vertically along the axis of symmetry and falls downwards close to the cooler walls, thus forming a toroidal vortex. Figure 7(a) plots the streamlines computed for the flow induced by natural convection. In outline, the system behaves as follows. The walls of the reactor are held at a constant

temperature. Whilst reaction proceeds, heat is released and consequently the temperature of the gas rises. Because the gas becomes hotter than the walls, heat is removed from the system at the walls. This coupling of heat generation and loss causes a hot zone to form at the centre of the reactor. This in turn results in a gravitationally unstable density distribution in the top section of the reactor and so leads to the development of the familiar Rayleigh-Bénard convection (Turner, 1979). Figure 7(b) plots the temperature and density along the vertical axis of the reactor. The hot gas near the centre of the reactor rises quickly initially and moves into the hottest part of the reactor (in the top half). However, it slows as it passes through the hot zone, due to the decreased density difference. The hot gas then contacts the relatively cold walls, where it cools and descends relatively rapidly due to the large density differential. In the lower half of the reactor the density distribution is intrinsically stable, with the flow being induced by the descending, cooler gas at the wall. This downward flow of cool gas results in a relatively slow upward flow (around the centreline of the reactor) of gas displaced from the bottom of the reactor. Whilst this gas rises, it heats up and hence accelerates. The situation in Fig. 7 refers not just to Sal'nikov's mechanism, but to any exothermic reaction proceeding in a similar vessel.

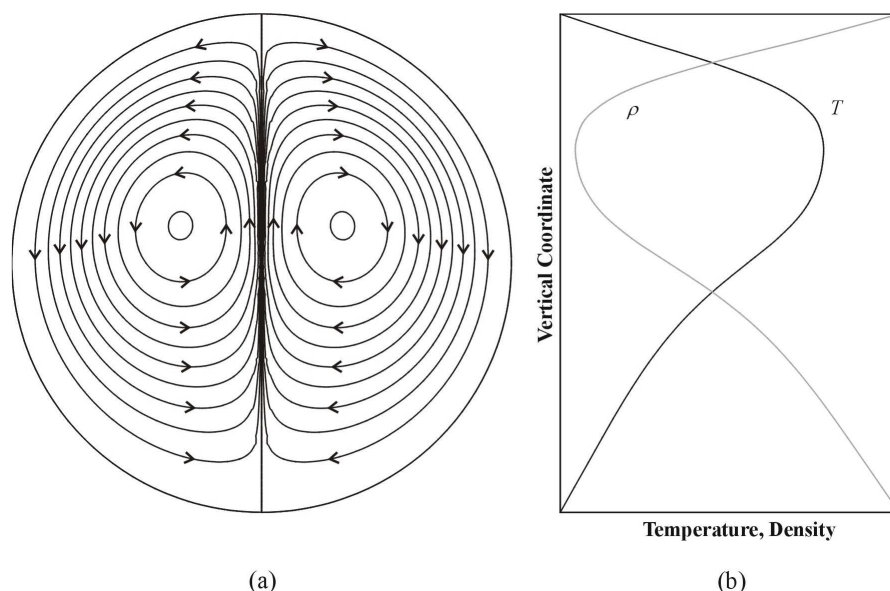


Fig. 7. (a) Streamlines of the flow due to natural convection in a vertical cross section through the axis of the reactor. The toroidal vortex typifying the flow (upwards near the axis, downwards near the wall) is shown. (b) Temperature and density profiles along the vertical axis of the reactor, showing the unstable density distribution in the top half of the reactor, which drives flow, and the stable density distribution in the bottom half of the reactor, where flow is driven by conditions in the boundary layers.

As mentioned previously, the spherical symmetry of the temperature and concentration fields seen in the diffusive regime is disrupted by the convective flow. Because of the 'hot zone' above the

centre of the reactor (Cardoso *et al.*, 2004a, b), we examine below, the temperature rise, ΔT , at a point $L/2$ above the centre of the reactor (*i.e.* a point three quarters of the way up the vertical axis), instead of at the centre, to give a better indication of the maximum value of ΔT within the reactor. Oscillations were observed over a much wider range of values than in the diffusive regime, and in fact, virtually every case studied when convection was significant exhibited oscillations.

Figure 8 shows a plot of the computed maximum vertical velocity at the centre of the reactor against $(gL^2)^{1/3}$, which arises from substituting Eq. (11) into (10). The ‘error bars’ show the range of the observed oscillations in the velocity. The linear form of this plot indicates that our scale, Eq. (10), is of the correct form. It is interesting to note that for a 10 cm diameter vessel undergoing a reaction in terrestrial conditions (*i.e.* $g = 9.81 \text{ m s}^{-2}$), velocities of $\sim 10 \text{ cm s}^{-1}$ were observed. Velocities of up to 30 cm s^{-1} were computed for similarly sized vessels for larger values of g ($= 30 \text{ m s}^{-2}$). The characteristic velocity, U , can therefore be expressed as:

$$U = (0.31 \pm 0.02) [\beta g L (\Delta T)]^{1/2}. \quad (15)$$

This equation contains ΔT . To check its magnitude, Fig. 9 shows $\gamma (\Delta T / \Delta T_{ad})$ plotted against $\tau_{convection} / \tau_{step 1}$; as predicted by Eq. (11), there is a clear linear relationship. In fact, the characteristic temperature rise when convection dominates transport can be expressed as:

$$\gamma \frac{\Delta T}{\Delta T_{ad}} = (4.00 \pm 0.08) \frac{\tau_{convection}}{\tau_{step 1}}. \quad (16)$$

Thus our numerical simulations have confirmed the form of the scales developed above, when diffusion and convection are, respectively, the dominant transport mechanism. These scales allow the general behaviour of any given system to be predicted. It should be noted, however, that these scales were developed for a system where $\tau_{step 1}$ is the dominant kinetic timescale. Thus, the behaviour may well change if $\tau_{step 1}$ and $\tau_{step 2}$ are of similar magnitude.

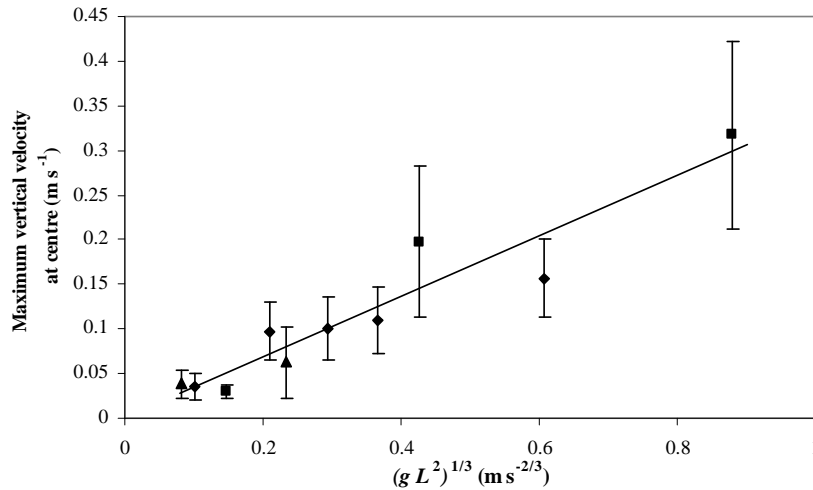


Fig. 8. Plot of the maximum vertical velocity of the gas at the centre of the reactor, versus $(gL^2)^{1/3}$. The line shown corresponds to Eq (15), $Ra \sim 21500$. (◆ $g = 9.81 \text{ m s}^{-2}$, $k_I = 0.025 \text{ s}^{-1}$, $k_{2,0} = 0.265 \text{ s}^{-1}$; ▲ $g = 4.9 \text{ m s}^{-2}$, $k_I = 0.025 \text{ s}^{-1}$, $k_{2,0} = 0.265 \text{ s}^{-1}$; ■ $g = 30 \text{ m s}^{-2}$, $k_I = 0.025 \text{ s}^{-1}$, $k_{2,0} = 0.265 \text{ s}^{-1}$).

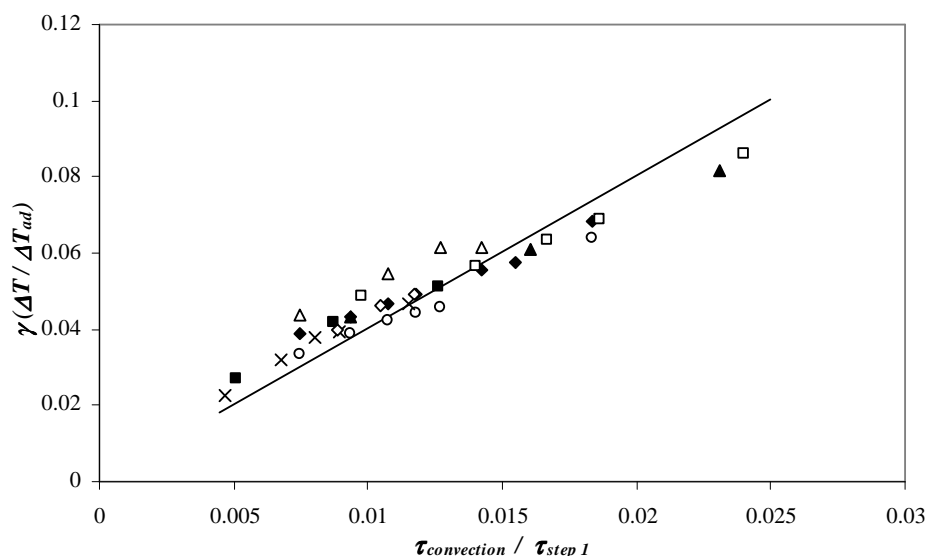


Fig. 9. Plot of $\gamma(\Delta T / \Delta T_{ad})$ versus $\tau_{convection} / \tau_{step 1}$ in the laminar convection regime. The line shown corresponds to Eq. (16). ‘Error bars’ showing the range of oscillations have been suppressed for clarity. (\blacklozenge $g = 9.81 \text{ m s}^{-2}$, $k_I = 0.025 \text{ s}^{-1}$, $k_{2,0} = 0.265 \text{ s}^{-1}$, $Ra \sim 21500$; \blacktriangle $g = 4.9 \text{ m s}^{-2}$, $k_I = 0.025 \text{ s}^{-1}$, $k_{2,0} = 0.265 \text{ s}^{-1}$, $Ra \sim 21500$; \blacksquare $g = 30 \text{ m s}^{-2}$, $k_I = 0.025 \text{ s}^{-1}$, $k_{2,0} = 0.265 \text{ s}^{-1}$, $Ra \sim 21500$; \times $g = 9.81 \text{ m s}^{-2}$, $k_I = 0.0125 \text{ s}^{-1}$, $k_{2,0} = 0.265 \text{ s}^{-1}$, $Ra \sim 21500$; \diamond $g = 9.81 \text{ m s}^{-2}$, $k_I = 0.01875 \text{ s}^{-1}$, $k_{2,0} = 0.265 \text{ s}^{-1}$, $Ra \sim 21500$; \square $g = 9.81 \text{ m s}^{-2}$, $k_I = 0.0375 \text{ s}^{-1}$, $k_{2,0} = 0.265 \text{ s}^{-1}$, $Ra \sim 21500$; \triangle $g = 9.81 \text{ m s}^{-2}$, $k_I = 0.025 \text{ s}^{-1}$, $k_{2,0} = 0.132 \text{ s}^{-1}$, $Ra \sim 21500$; \circ $g = 9.81 \text{ m s}^{-2}$, $k_I = 0.025 \text{ s}^{-1}$, $k_{2,0} = 0.265 \text{ s}^{-1}$, $Ra \sim 5000$).

7. Oscillations

The oscillations of a and T in the above systems result from the interaction between chemical kinetics and heat transfer. This truth is not just restricted to Sal’nikov’s reaction (Gray and Scott, 1990), but consideration of Sal’nikov’s system indicates how more complex mechanisms might behave. Previous work in the well-mixed region (e.g. Gray and Scott, 1990) has shown that oscillations in the temperature and the concentration of the intermediate A occur in anti-phase. The observed oscillations are sustained, but in fact are slightly damped (as in Fig. 4(a)), because the precursor, P, is continually consumed during the course of the reaction, so the production of A follows an exponential decay arising from the kinetics of step 1. This oscillatory behaviour is due to the interaction of the highly non-linear thermal feedback, due to the Arrhenius temperature dependence of step 2, the timescales of steps 1 and 2 of reaction (I) and the nature of heat transfer from the reactor. Interestingly, oscillations with T and a in phase can occur; they are discussed elsewhere by Campbell *et al.* (2005b). The entire region of Fig. 3 where oscillations occur has been found by performing very many simulations and is shown approximately in Fig. 10. There are two distinct parts to the oscillatory region. For $Ra < 10^3$, the boundaries between the oscillatory and non-

oscillatory zones are approximately constant, and are very similar to those seen in the purely diffusive case. For $Ra > 10^3$, natural convection dominates over diffusion of heat and mass. Oscillations are observed over a much wider range of parameters when natural convection is important. As Ra increases, the oscillatory region also widens.

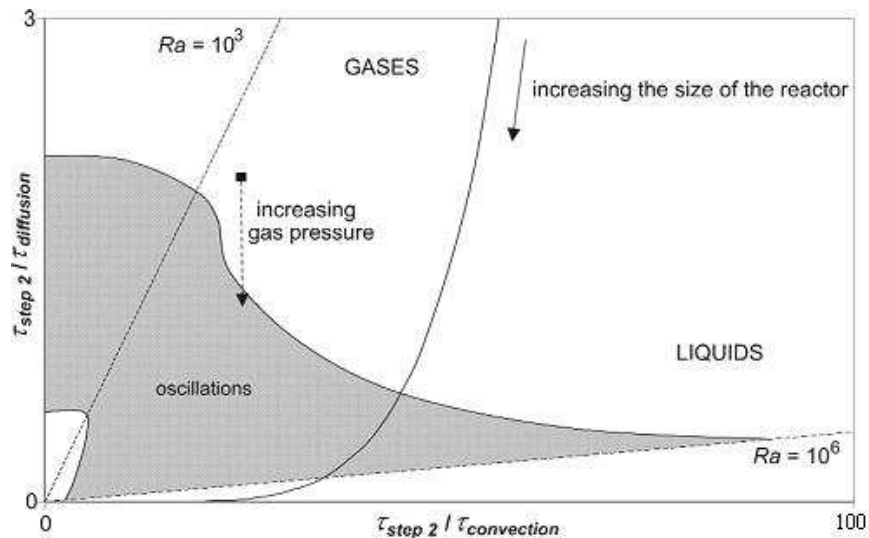


Fig. 10. Regime diagram showing the effect (on the position of the working point in Fig. 3) of increasing the gas pressure, increasing the reactor's size, and the effect of performing the reaction in the liquid-phase. The area in grey denotes approximately where the concentration of the intermediate and the temperature oscillate.

8. The Effect of Varying Parameters

Examination of the form of the scales developed in the previous sections, along with the expression for the Rayleigh number allows us to predict how the system will respond to variations in certain parameters. In particular, it is important to reveal the effects of pressure, the size of the reactor and the phase of the system (*i.e.* gas or liquid) on the intensity of convection in the reactor. Let us first consider the effect of increasing the pressure in a gas-phase reaction. The kinetic theory of gases indicates that ν and κ ; the momentum and thermal diffusivities, are both inversely proportional to pressure. This means that the Rayleigh number is proportional to \mathcal{P}^2 . Thus, increasing the pressure increases the Rayleigh number and therefore the intensity of the convective flow. A system represented by a point on the regime diagram of Fig. 10 actually moves vertically downwards, when the pressure is increased, because the terms in the abscissa are independent of pressure. The system could accordingly move from a situation of negligible convection at low pressure, through one of laminar flow, to eventually turbulent convection, when the pressure is increased.

The effect of increasing the reactor's size is shown by the solid curved line in Fig. 10. (*n.b.* $\tau_{step 2} / \tau_{diffusion} \propto 1/L^2$; $\tau_{step 2} / \tau_{convection} \propto 1/L^{1/3}$). It is clear from this plot that making the reactor smaller significantly reduces the Rayleigh number, thereby making diffusive processes more

significant. Figure 10 shows that when small reactors are considered, even relatively small increases in their size can significantly alter the Rayleigh number, which *ex hypothesi* has an explicit dependence on L^3 . There is also a dependence of ΔT on L via Eq. (9) or (11).

As for the effect of temperature on Ra , for a purely gaseous system in the convective regime, Ra turns out to be inversely proportional to $T_0^{1/3}$, according to the simplest version of the kinetic theory of gases. Otherwise, the main effect of temperature on the location of the working point in Fig. 10 is via the exponential in the Arrhenius function for k_2 . Consequently any increase in temperature reduces $\tau_{step\ 2}$ and so moves the working point towards the origin of Fig. 10, whose abscissa and ordinate are both proportional to $\tau_{step\ 2}$.

The final effect highlighted on Fig. 10 is the effect of moving from a reaction in the gas-phase to one in the liquid-phase. Comparing the relative magnitudes of the terms in the Rayleigh number for typical gases and liquids indicates that Rayleigh numbers will be at least an order of magnitude higher for liquid-phase systems, for similar increases, ΔT , in temperature and identical values of L . Thus comparing Ra for reactions with the same ΔT , g and L in water and air at normal temperature and pressure indicates that Ra with water is some 240 times Ra with air. In fact, ΔT for a reaction in the liquid-phase is likely to be only $\sim 10\%$ larger than for a reaction with the same kinetic parameters (q_2 , k_1 , k_2, \dots) in the gas-phase. The overall result is that gaseous and liquid systems occupy quite different areas of Fig. 10. In a liquid-phase reaction, natural convection is therefore likely to be more vigorous and important than in a gas-phase reaction with similar kinetic parameters. Certainly Fig. 10 indicates that natural convection is likely to be most important (*i.e.* turbulent) in reactors on an industrial scale, because of the dependence on L^3 . Whenever natural convection is stronger, Fig. 10 makes it clear that there is a greater likelihood of oscillations in the reactor. This is because of the quite different portions of the two axes (of Fig. 10) occupied by the region wherein oscillations occur. Thus on the vertical axis, the region for oscillations roughly extends over $0.5 < \tau_{step\ 2} / \tau_{diffusion} < 2$, whereas along the horizontal axis, oscillations occur over approximately $5 < \tau_{step\ 2} / \tau_{convection} < 90$, *i.e.* a change by a factor of 18. No attempt has been made to investigate what happens when $Ra > 10^6$ and turbulence occurs.

9. Conclusions

Scales have been developed for the characteristic concentration of intermediate A, temperature rise and velocity when Sal'nikov's reaction occurs in a closed spherical vessel, both for the case where diffusion is the dominant transport mechanism, and when convection dominates. In both cases the characteristic concentration of the intermediate A was determined purely by the kinetics and the temperature rise was shown to be proportional to the ratio of the characteristic timescales for the dominant transport mechanism and the rate-controlling step of the reaction. It should be noted that this behaviour may differ if the relative magnitudes of the kinetic parameters are significantly altered. Using these scales, along with order of magnitude arguments, predictions have been made as to how the system will respond to changes in parameters, such as gas pressure, the size of reactor and if the reaction is conducted in the liquid-phase. It has been shown that natural convection is favoured by a high pressure in gas-phase reactions, and by a larger reactor. Because liquids have different physical

properties, reactions in the liquid-phase develop more intense convection than gas-phase reactions with similar kinetic parameters. The above analysis reveals when oscillations are possible.

References

- [1] Bardwell, J, Hinshelwood, C.J. (1951) "The cool flame of methyl ethyl ketone." *Proc. Roy. Soc. A.* 205, 375 – 390.
- [2] Campbell, A.N., Cardoso, S.S.S., Hayhurst, A.N. (2005a), "A scaling analysis of Sal'nikov's reaction, $P \rightarrow A \rightarrow B$, in the presence of natural convection and the diffusion of heat and matter." *Proc. Roy. Soc. A.* 461: 1999 – 2020.
- [3] Campbell, A.N., Cardoso, S.S.S., Hayhurst, A.N. (2005b), "The influence of natural convection on the temporal development of the temperature and concentration fields for Sal'nikov's reaction, $P \rightarrow A \rightarrow B$, occurring batchwise in the gas phase in a closed vessel." *Chem. Eng. Sci.*, 60: 5705 – 5717.
- [4] Cardoso, S.S.S., Kan, P.C., Savjani, K.K., Hayhurst, A.N., Griffiths, J.F. (2004a), "The computation of the velocity, concentration and temperature fields during a gas-phase oscillatory reaction in a closed vessel with natural convection." *Combustion and Flame*, 136: 241 – 245.
- [5] Cardoso, S.S.S., Kan, P.C., Savjani, K.K., Hayhurst, A.N., Griffiths, J.F. (2004b), "The effect of natural convection on the gas-phase Sal'nikov reaction in a closed vessel." *Physical Chemistry Chemical Physics*, 6: 1687 – 1696.
- [6] Fairlie, R., Griffiths, J.F. (2001), "A numerical study of spatial structure during oscillatory combustion in closed vessels in microgravity." *Faraday Discussions*, 120: 147 – 164.
- [7] Fairlie, R., Griffiths, J.F. (2002), "Oscillatory combustion in closed vessels under microgravity." *Mathematical and Computer Modelling*, 36: 245 – 257.
- [8] Gray, P., Griffiths, J.F. (1989), "Thermokinetic combustion oscillations as an alternative to thermal explosion." *Combust. Flame*, 78, 87 – 98.
- [9] Gray, P., Scott, S.K. (1990a), "*Chemical Oscillations and Instabilities*," Clarendon Press, Oxford, ch. 4, pp. 83 – 111.
- [10] Gray, P., Scott, S.K. (1990b), "*Chemical Oscillations and Instabilities*," Clarendon Press, Oxford, ch. 10, pp. 264 – 291.
- [11] Griffiths, J.F., Barnard, J.A. (1995) "Flame and combustion," 3rd edn, Blackie, Glasgow, pp. 181 – 205.
- [12] Griffiths, J.F., Kaye, S.R., Scott, S.K. (1988) "Oscillatory combustion in closed vessels: theoretical foundations and their experimental verification." 22nd *Symp. (Int.) on Combustion*, The Combustion Institute, Pittsburgh, p. 1597 – 1607.
- [13] Merzhanov, A.G., Shtessel (1973) "Free convection and thermal explosion in reactive systems," *Astronaut. Acta*, 18, 191 – 199.
- [14] Sal'nikov, I.E. (1949), "Contribution to the theory of the periodic homogeneous chemical reactions." *Zhurnal Fizicheskoi Khimii*, 23: 258 – 272.

- [15] Turner, J.S. (1979), “*Buoyancy Effects in Fluids*,” Cambridge University Press, Cambridge, ch. 7, pp. 207 – 250.
- [16] Tyler, B.J. (1966), “An experimental investigation of conductive and convective heat transfer during exothermic gas-phase reactions,” *Combust. Flame*, 10, 90 – 91.

ACKNOWLEDGEMENTS

The financial support of the Engineering and Physical Sciences Research Council is gratefully acknowledged.

**ՀԱՅԱՍՏԱՆԻ ՀԱՆՐԱՊԵՏՈՒԹՅԱՆ ԳԻՏՈՒԹՅՈՒՆՆԵՐԻ
ԱԶԳԱՅԻՆ ԱԿԱԴԵՄԻԱ
НАЦИОНАЛЬНАЯ АКАДЕМИЯ НАУК РЕСПУБЛИКИ
АРМЕНИЯ**

Հայաստանի քիմիական հանդես **60, №2, 2007** Химический журнал Армении

NOVEL NANOCARBON MATERIALS FOR DIFFERENT APPLICATIONS

Z. MANSUROV

Al- Farabi Kazakh National University, 96A Tole be Str, 050012, Almaty, Kazakhstan

E-mail: Mansurov@kazsu.kz

This paper reviews recent results in the field of novel nanocarbon materials research obtained in the Combustion Problem Institute and their practical applications. They are:

- sorption of gold and ion of heavy metals by carbonized apricot stones;
- mechanochemical encapsulation of quartz particles in metal carbon films;
- novel carbon materials for battery application;
- multifunctional catalysts of oil hydrofining;
- carbon containing refractories;
- fullerenes and nanotubes formation during hydrocarbons combustion

Introduction

Carbon formation and growth during pyrolysis of organic substances on the surface of metal oxides and salts have been attracting the attention of specialists dealing with the study of carbon materials for many years. It is found that the most effective catalyst of carbon formation is Fe, Ni, Co and alloys of these metal particles [1]. As a result of catalytic reaction there are formed carbon sediments on disperse metal particles. These sediments have specific forms and properties which allow considering them as perspective ultradisperse systems. The part of carbon, which forms coke, has extended in fibers tubular morphology during cracking of carbon on metal catalysts and catalyst particle proportional to fiber diameter is discovered in the head of tube.

There are conducted works on obtaining carbonized materials based on local clays and wastes of metal mining industry: chromite and bauxite sludges, agricultural wastes (rice husk, grape and apricot stones) and using them in different applications. Obtained absorption-catalytic systems are applied for purifying metals and radioactive elements, cleaning water from ions of heavy metals and radioactive elements and obtaining improved types of refractory materials, as carriers of catalysts of conversion reactions of hydrocarbons [2-4].

During production of composition systems the special attention is paid to carbon and silica. In this respect mechanochemical treatment is one of the effective methods of creating material of new

quality as a result of profound structural changes including the changes of nanoscale level. Production of powder materials with nanocomposition structure of particles, especially quartz particles, capsulated as a result of mechanochemical treatment into the shell of carbon containing compounds with purposeful structural organization of surface and formation of certain complex of physico-chemical and functional properties of material being synthesized is connected with necessity to determine mechanism of mechanochemical synthesis of surface structures of nanosized scale [5, 6].

Novel carbon materials for lithium batteries.

Electrode materials are of great interest both from viewpoint of progress in the field of lithium-ion accumulators and in connection with developing technological use of carbon nanotubes [7, 8]. From the presented on the market products, lithium-ion batteries are the most perspective. Lithiated carbon (LiC_6) developed by the Japanese investigators is used as an anode material in these devices [9]. Although many types of carbon were studied as materials of anodes for lithium batteries, in practice, natural or synthetical graphite is used, as this material has sufficient capacity of 372 m.A.h/g, good recharging ability and flat profiles of charge. Electrolytes based on propylene carbonate (PC), are attractive because of fine ionic conductivity at the environmental temperature. However, graphite has bad compatibility with electrolytes, based on (PC) due to interlayer incorporation of solvent leading to destroying electrode structure. Search of novel materials with improved characteristics of recycling and good compatibility with solvents of electrolytes is the most perspective. Below there are given experimental data on preparation and characteristics, obtained during electrochemical testing of carbon from apricot stone as an anode for ion batteries.

Anode material was obtained using carbonization of the shell of apricot stones. Samples obtained at 1023 K were used for creating anode after washing them with isopropane and drying at 383 K during 12 hours in vacuum cabinet. Tests of electrochemical half-elements were carried out with using different electrolytes at room temperature.

Figure 1 shows characteristics of recycling for half-elements at various numbers of cycles and with different electrolytes. One can see that carbonized apricot stone has fine stability as an anode in used electrolytes with different salts and solvents at high values of recycling.

a

b

Figure 1 - Cycling performances of cell Li/1 mol LiClO₄ in EC:DEC=1:1/CAS, 1C (a) and of cell Li/1M LiClO₄ in PC/CAS at 1C rate (b)

During the initial cycle, it shows higher initial irreversibility which is related to protective film formation on the electrode surface. However, the system shows high reversibility closer to 100% cycling efficiency during the subsequent cycles which extended up to 200 cycles. In order to investigate the CAS electrode compatibility with the PC electrolyte, the system was tested using 1M solution of LiClO₄ in PC as electrolyte.

Electrochemical tests of the material obtained from carbonized apricot stones as an anode were carried out in cells CR2032 of coin type using method of galvanostatic recycling. It was shown that carbonized apricot stone has fine stability as an anode in used electrolytes with different salts and solvents at high values of recycling.

Multifunctional catalysts of oil hydrofining.

Multifunctional catalysts of hydrofining were developed using modification of aluminium-cobalt-molybdenum catalyst by decationated zeolites [4]. Catalysts were prepared using traditional method of soaking. After formation catalysts were dried at 393-420 K (4 h) and pierced at 823 K for 5 hours. Prepared in this way catalysts were subjected to the process of carbonization in order to obtain active forms of carbon as a carrier. Activation of catalysts was carried out under conditions of reaction using sulphurization of free sulfur, at first at 393-423 K, at hydrogen pressure of 0.7-1.0 MPa for 3 hours, and then sulphurization was carried on at 473 K, at hydrogen pressure of 2.5 MPa for 2.5-3 hours.

Activity of catalysts was tested in laboratory flowing installation in the process of hydrofining of gasoline and diesel fractions of oil at pressure of 2.0 – 4.5 MPa, at temperature of 593 – 673 K and at volume rate of raw materials supply of 1-4 hour⁻¹. To compare catalytical activity characteristics of ΓO – 70 industrial catalyst were determined under similar conditions. Also the degree of hydrodesulphurization was studied on model compounds. Butyl – mercaptan and thiophen diluted in n-decane were used as a model compound. Isomerized activity was tested in cracking reactions of hexane and decane. Developed catalysts showed higher indexes than ΓO-70 industrial catalyst. Degree of hydrodesulphurozation increases from 75.3 to 98.2 %, degree of isomerization increases from 18.3 to 41.7 % with increase in temperature from 593 to 673 K. According to the data of detailed hydrocarbon analysis calculated octane number increased from 70 to 83.5 (table 1).

Table 1 - Activity of carbonized industrial C₆M₀ – catalyst (CC) on characteristics of straight-run gasoline, carbon concentration – 10 %

	Octane number	Boiling temperature	Concentration (mass %)		
			Paraffins	Naphthenes	Sulphur-containing compounds
Initial straight-run gasoline (SRG)	70.8	88.1	21.4	12.9	0.12
SRG after tests on CC	83.5	36.06	12.5	16.0	0.001

Investigation of surface and porosity of catalysts according to the BET method has showed increase in specific surface of catalyst from 80 to 240 m²/g. Catalysts mainly have pores with sizes of less than 50 nm. Electron-microscopic investigation has showed that carbon used catalysts are highly dispersed. Size of the metal particles ranges within 20-40 nm.

Carbonization of vegetable raw materials.

Raw materials based on reprocessing of agricultural products refer to rapidly renewable sources and they are cleaner in ecological respect [10]. During carbonization (pyrolysis in inert medium) of the samples of apricot stones (AS), grape stones (GS) and rice husk main lost of mass occurs in the temperature range of 473-773 K. Nearly 50 % of mass is lost at 773 K for an hour.

Specific surface which reaches to 830 m²/g has been determined using method of thermal desorption of argon. Change of morphology and structure of carbon-containing sorbents depending on temperature, carbonisation time was showed by electron-microscopic method. There is a presence of complex morphological formations (figure 2), having nanoscale structure, and defining, as consequence, a high specific surface of the material.

Distinctive feature of the carbon material obtained by the carbonization of the wheat bran is formation of poorly discernible pounded particles at 723 K on the surface where unique nanotubes with a "bulb" are formed at the basis at 923 K and 1023 K. The processes, occurring in the sample lead to growth inhibition of the "bulbous" nanotubes, and their formation is not observed at the carbonization temperatures 1073 K and above, at all.

Influence of various factors (process temperature, sorption time, nature of activating agent, and pH point) on sorption properties of the synthesized nanocarbon materials for the caesium-137 (¹³⁷Cs), strontium-90 (⁹⁰Sr), lead-210 (²¹⁰Pb) and ions of toxic metals (Sn, Ni, Cd, Cr, Zn, Au) was investigated.

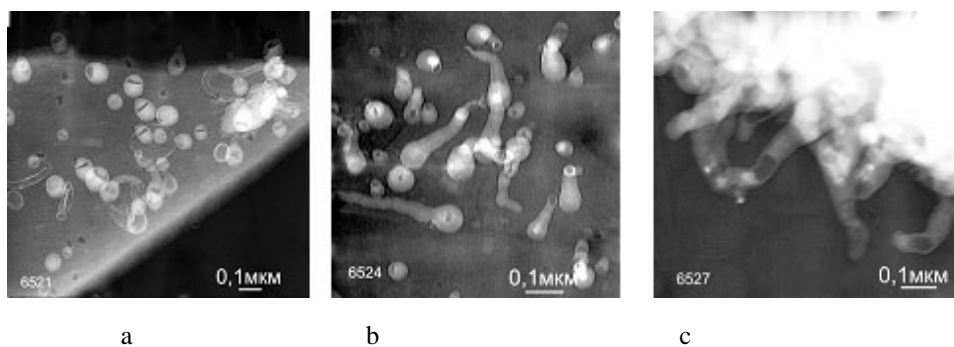


Figure 2 - The electron microscopy images of WB, carbonized at: a) 723 K (nucleuses position); b) 650°C (the beginning of the "bulbous" nanotubes growth on a sample); c) 1023 K (mature nanotubes on the edge of WB sample)

It was noted, that all investigated elements are quantitatively sorbed by activated sorbent for the first 5 minutes and sorption degree doesn't depend on the carbonization temperature under the present experimental conditions.

Table 2 shows dependence of the sorption degree on the pH of solution at the various carbonization temperatures for sorbent, activated by water stream, but, displaying, nevertheless, the general character of dependences for the sorbents, activated by the hydrogen peroxide (H_2O_2) and ammonia (NH_3).

Table 2 - Dependence of the sorption degree of radioactive isotopes on the pH and carbonization temperature of WB, activated by water. Sorption time - 30 min

Ele- ment	PH										Carboni- zation tempera- ture, K
	1.5	3	4	6	7	8	9	10	11	11.5	
	Sorption degree, %										
Sr	37.0	40.1	48.0	56.7	55.2	66.7	69.7	69.4	70.2	70.5	773
Cd	18.8	81.1	83.2	92.6	92.6	98.7	99.5	100.0	99.3	100.0	
Cs	16.1	73.9	73.6	73.6	74.2	74.0	74.2	74.0	74.1	74.0	
Pb	12.8	81.0	93.4	99.3	99.2	100.0	100.0	100.0	100.0	100.0	
Sr	35.8	48.0	51.6	57.5	60.4	59.7	64.9	65.0	65.7	-	873
Cs	17.0	76.5	76.4	75.9	74.8	76.4	76.2	76.5	76.8	-	
Pb	13.1	84.4	90.9	97.7	99.2	100.0	100.0	100.0	100.0	-	
Sr	37.5	44.6	49.0	63.4	61.9	63.4	75.3	76.3	76.6	74.1	973
Cs	19.8	79.0	78.8	79.1	78.4	78.8	79.0	78.5	78.3	78.8	
Pb	22.8	92.0	93.2	98.6	99.0	100.0	100.0	100.0	100.0	100.0	
Sr	36.7	43.0	50.5	64.7	66.4	69.2	72.0	72.0	-	-	1073
Cs	15.0	75.4	78.3	79.4	79.3	80.8	80.0	80.0	-	-	
Pb	12.0	83.0	95.1	98.8	100.0	100.0	100.0	100.0	-	-	

Mechanism of sorption of ions of heavy metals by carbonized sorbents was found by physico-chemical methods of analysis. Carbonized sorbents were found to be effective during absorption of ions of heavy metals and radioactive elements and also gold separation from alkaline solutions.

Fusicoccine extraction on novel carbon-mineral sorbent.

In nanocarbon materials laboratory of Combustion Problem Institute carbon-mineral sorbent (sorbent carbonized from vegetable raw materials –2) based on carbonised raw materials, which contain carbon and silicon oxide and also has nanosized morphology, has been synthesized [11]. This material has specific and unusual properties due to presence of these components. If carbon is hydrophobic material and silicon oxide is hydrophilic one absolutely new combination of hydrophobic-hydrophilic properties emerges. These unusual properties allow offering the given material as a unique nanostructurized sorbent for separating bioorganic compounds.

Sorbent carbonized from vegetable raw materials –2 was synthesized by carbonisation of vegetable raw materials in rotating steel reactor in the temperature range of 573-1073 K for 5-60 min in inert medium. It was found that specific surface of samples increases with increase in temperature reaching maximum at 923 K (920 m²/g) and then decreases.

To separate fusicoccine the technique developed in M.A. Aitkhozhin Institute of Molecular Biology and Biochemistry was used [12]. Taking into account tough climatic conditions of Kazakhstan it was very interesting to study action of biostimulator on stress resistance of the most important grain crops of Kazakhstan. So we studied action of purified fusicoccine on germinating capacity of seeds of wheat of *Nadezhda* sort by adding 2 % of NaCl, that creates condition of strong chloride salinization. Experimental results are presented in table 3. As follows from the table 3, fusicoccine increases germinating capacity of seeds under by 19 % conditions of salinization. Also fusicoccine increases root system of a plant.

Table 3 - Action of fusicoccine on of the seeds of *Nadezhda* sort wheat

Variants	% of germination
2.2% NaCl	67
2. 2% NaCl+MIQ	86

The experiment carried out in the Scientific-industrial center of agriculture and plant growing of the Republic of Kazakhstan in 2004-2005 has showed that application of biostimulator for increasing winter resistance of winter wheat is very promising.

The carried out experiments have showed that application of biostimulator increases mass of 1000 grains by 15 % and productivity by 10%. In the course of further test there were carried out field trials of fusicoccine. The wheat treated by biostimulator was noted to ripen 15 days earlier than the wheat without treating with biostimulator (green sprouts).

One can say with great confidence that application of preparation will allow:

1. accelerating the ripening of wheat, i.e. to start harvesting two weeks earlier;
2. increasing yield in average by 15 %.

Sorption of gold by carbonized apricot stones (CAS) and rice husk (RH).

Carbonization of apricot stones (CAS) and rice husk (RH) was carried out by method [3]. Synthesis of sorbents by carbonization of this agricultural raw materials in the temperature range of 673 – 1073 K in a nitrogen atmosphere for 30 min was investigated. Carbonized sorbents based on apricot stones have a code: CAS-1; CAS-2; CAS-3 and carbonized sorbents based on rice husk have a code: RH-1, RH-2, RH-3. Sorption of gold (III) was studied by electrochemical method on potentiostat P-5848 by the means of recording J-t-curves at constant potential corresponding to extreme current of gold electroreduction (III).

Carbonized sorbents based on vegetative raw material concurrently possess ion-exchanging and reducing properties. Stationary potentials of CAS were measured to reveal their reducing properties. The sorbents of CAS series have relatively low oxidative-reducing potential that in dependence on CAS mark change in range from 0.20 V to 0.25 V.

Measured stationary (real) potential $[AuCl_2]$ muriatic medium is 0.76 V. Difference of potentials between gold-oxidant and sorbent-reducing agent is 0.51-0.56 V. Difference of potentials of 0.24 V is required for practically complete passing of any oxidative - reducing reaction. As follows from these data there is a real opportunity for reducing of gold (III) to metallic state. This opportunity is proved by magnitudes of CAS sorbent potentials after sorption of gold (III) on it.

The results on sorption of gold (III) with RH sorbents in 0.25 N HCl solution using a common method [13]. As it is seen (figure3), RH-1 exhibits the best 100 % sorption capacity with respect to gold (III).

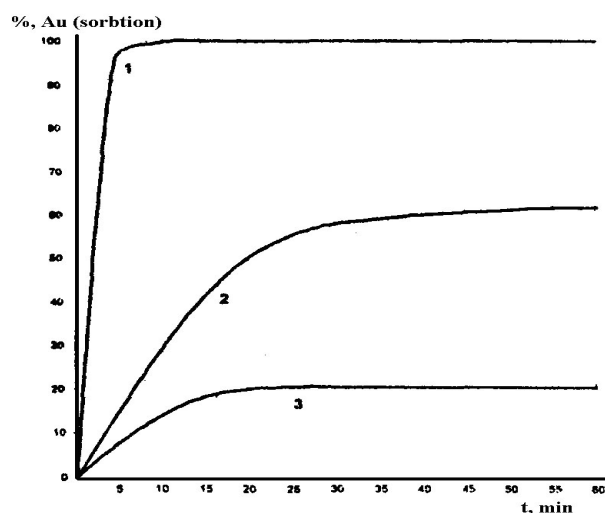


Figure 3 - Kinetic curves of sorption of gold (III) on different sorbents in 0.25 N HCl solution. Mass of the sorbent is 0.2 g, the amount of gold (III) is 0.6 mg, the volume of the solution is 25 ml.

Sorbent: 1 – RH-1; 2 – RH-2; 3 – RH-3

The sorbent RH-2 absorbs about 60 % of gold (III) during 1 hour, and the sorbent RH-3 only absorbs 20 % of gold (III) during the same period of time. In the case of sorbent RH-1, a complete,

practically 100 % sorption is observed within 4 minutes. The shape of the kinetic curves also shows the decrease in the rate of gold (III) sorption as follows: RH-1 > RH-2 > RH-3.

During sorption of gold (III) the grains of RH-1 sorbent are covered by a film of yellow color which is a metallic gold according to electron-microscopic pictures (figure 4, 5).

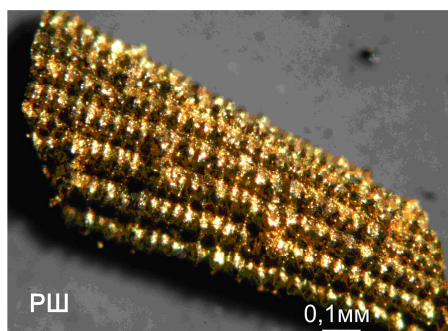


Figure 4 - Microphoto of sorbent
RH-1+Au (III)

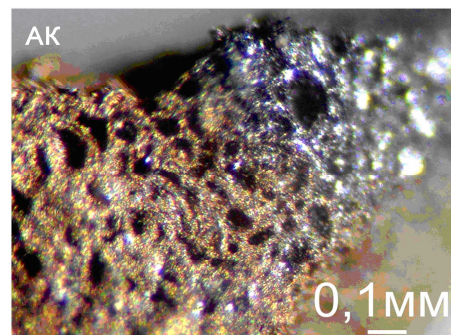


Figure 5 - Microphoto of sorbent
CAS-3+Au (III)

The reducing ability of RH sorbents was verified by the measurements of the values of stationary potentials of these materials, which were carried out with the help of electrode of special construction. This electrode is a fluoroplastic casing with the diameter of 20 mm with a thread at the end face, where platinum electrode with the diameter of 19 mm is fixed. A platinum current collector is brought out from the platinum electrode through the center of the casing. The platinum disk is compressed by a fluoroplastic clutch with a perforated face. When measuring the potential, an ash-free filter is placed on the perforated face, the sorbent that being studied is poured onto the filter. Then the clutch with the sorbent is applied by winding on the fluoroplastic casing, thereby providing an intimate contact of the substance being studied with the platinum electrode. The results of the measurements showed that the sorbents of RH series have a quite low redox potential. The sorbents RH have reducing properties, which are likely to be conditioned by the presence of the carbonized sorbents of reducing carbon groups: aldehyde, ketone, alcohol groups on the surface. Besides, carbon itself may possess reducing properties, the more so, as it is in the form of nanocarbon tubes [13, 14].

The best sorbent is RH-1. The complete (99-100 %) extraction of gold (III) on this sorbent takes place during 3.5–4 min regardless of the initial content of gold (III) in solution. The sorption time of the half of the initial content of gold (III) - $\tau_{1/2}$ is 1.1 min irrespective of its initial concentration, the sorption rate obeys the first order kinetics law (table 4). This order of the reaction is characteristic for the electrochemical process limited by the substance to the surface of the electron donor.

Table 4 - Kinetics of gold (III) sorption on RH-1 sorbent in 0.25 N HCl solution

№	Concentration of Au (III), mg/l	W, mg/c·g (of the sorbent)	$\tau_{1/2}$, min	K_s , s ⁻¹ g ⁻¹
1	5.97	$0.54 \cdot 10^{-2}$	1.18	$7.35 \cdot 10^{-2}$
2	11.95	$1.08 \cdot 10^{-2}$	1.10	$7.15 \cdot 10^{-2}$
3	23.90	$2.26 \cdot 10^{-2}$	1.12	$7.45 \cdot 10^{-2}$

The dynamic sorption capacity of RH-1 sorbent was determined, i.e. the capacity before passing of gold (III) ions through the adsorption column. The passage rate of gold (III) solution with the concentration of 23.9 mg/l was 2.5 ml/min, the amount of the sorbent taken was 0.5 g. The experiments showed that passing of gold (III) ions took place after passing of 220 ml of gold (III) solution that corresponds to the sorption capacity of this sorbent – 10.5 mg of gold / 1 g of sorbent. In the case of sorbents RH-2 and RH-3, when passing the first portion of gold (III) solution of 25 ml, the passing of 60-70% of the initial amount of gold (III) is observed. The sorption capacity of these sorbents is lower by two orders of magnitude than that of the sorbent RH-1 [15-17].

The dynamic sorption capacity of sorbent RH-1 with respect to gold (III) is 10.5 mg/g of the sorbent. The capacity of sorbents RH-2 and RH-3 is by two orders of magnitude lower. The presence of excessive amounts of Ni (II), Co (II), Cd (II), Zn (II), Cu (II), Fe (III), Pt (IV), Hg (II), As (V) does not interfere with the sorption of gold (III). Extraction of metallic gold occurs non-uniformly on a whole surface of CAS particles, and in separate areas where the growth of gold crystals occurs. Hence, the process of metallic gold extraction and sorbent reducing groups oxidation is electrochemical, i.e. there are cathode and anodic areas. Cathode areas are formed in initial moment of sorption where further the reducing of gold (III) occurs.

The increase of gold (III) sorption velocity occurs in presence of copper salt (II) and iron (III) that is connected to catalytic effect of gold (III) reducing. Complete sorption of gold (III) occurs for 5 minutes in the case of presence of copper (II) ions, and in the case of iron (III) - for 1.5 minutes, when in absence of these admixture - for 8 minutes. The dynamic sorption capacity of sorbent RH-1 with respect to gold (III) is 10.5 mg/g of the sorbent. The capacity of sorbents RH-2 and RH-3 is by two orders of magnitude lower.

Mechanochemical encapsulation of quartz particles in metal carbon films.

Mechanochemical synthesis has great advantages compared to other methods in the production of highly disperse nanostructural materials based on silicon containing materials. As it was shown [5, 6], by mechanochemical synthesis it is possible to obtain quartz-based highly disperse materials which exhibit simultaneously magnetic, dielectric and electric properties depending on the regimes of treatment and the conditions of subsequent application.

It is found that there is a certain regularity in the structural transformations taking place on the surface of a quartz particle with the carbon of organic additives during the treatment of the material in a mechanical reactor: from thin dense films with the introduced ultradisperse particles of iron to

porous multiplayer structures with the formations of different configurations grafted to the surface of particles.

Complex investigations of changing structure, state and properties of quartz depending on regimes of mechanochemical treatment without participation and in presence of modifiers have showed that change of the structure of quartz particles in the process of dispersion is of periodical character [5-7] that reflects in the change of their characteristics both macro-, micro- and nanolevels including change of defective structure of their surface layers and size of crystallites (blocks of coherent scattering). It is found that time of the most considerable structural changes is 20 and 45 min under the conditions of the experiments being carried out simultaneously at all considered levels. Result of structural changes during mechanochemical treatment is the change of energy substance state.

It is found that during mechanochemical treatment use of organic additives intensifies effect of modification of quartz particles. It is shown in increasing specific surface, specific volume of pores and decreasing density of powder material, i.e. in significant structural changes of surface layers of quartz particles being dispersed (table 5). Calculation of modification degree of quartz powder has showed that butanol, acrylic acid and polystyrene are effective modifiers providing change of structure of from 30 to 70 % and more of volume. Novel morphological structures are synthesized on the surface of quartz particles, which plays the role of matrix for creating composition powder systems.

Table 5 - Specific surface (S_{sp}), specific volume of pores (V_{sp}), density (ρ) and degree of modification (ζ), of quartz powder

Material	S_{sp} , m ² /g	V_{sp} , cm ³ /g	ρ , g/cm ³		ζ , %
			(ρ_{each})	(ρ_n)	
SiO ₂	5,20	0,11	2,55	2,65	-
SiO ₂ +5% C ₂ H ₅ OH	5,24	0,18	2,03	2,06	17,1
SiO ₂ +5% C ₄ H ₉ OH	6,50	0,32	1,67	1,69	32,4
SiO ₂ +5% C ₂ H ₄ (OH) ₂	10,50	0,24	1,59	1,70	25,8
SiO ₂ +5% C ₃ H ₅ (OH) ₃	15,20	0,29	1,46	1,69	18,5
SiO ₂ + 5% C*	77,60	0,72	0,88	0,91	72,7
SiO ₂ +5% AC**	56,6	0,23	0,82	0,94	74,0
SiO ₂ +5% PS***	41,0	0,30	0,65	0,67	72,5
SiO ₂ + 10% PS	46,7	0,36	0,58	0,62	73,0
SiO ₂ +5% PS+1% NaCl	54,3	0,47	0,73	0,77	74,0
*C – activated coal, **AA – acrylic acid, ***PS – polystyrene					

Electron-microscopic analysis has shown that quartz particles in initial state are dense crystals with clearly shown edges (figure 6a). After mechanochemical treatment particles modified by butanol have nondense, laminated carbon saturated structure of 10-40 nm thickness where are dense ultra-disperse inclusions of iron and its compounds (figure 6b). Modification of quartz particles with both polyatomic and acrylic acid in the process of mechanochemical treatment results in formation of dense sufficiently homogeneous organic film on the surface and presence of highly disperse crystallites in surface polymeric layer. Microdiffraction pattern from surface layer of particles indicates that it belongs to carbonaceous substance with three dimensionally ordered structure. During variation of modification conditions electron diffraction picture show the presence of metal-silicon-carbon compounds or weakly crystallized silicon-carbon substance.

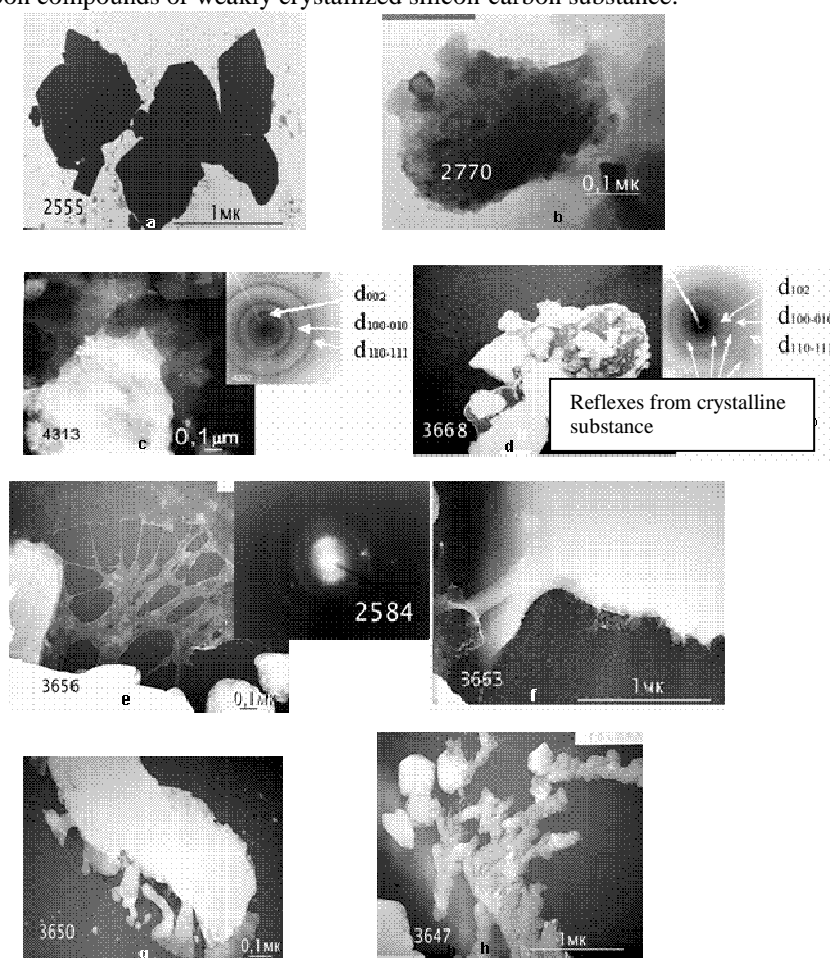


Figure 6 - Electron-microscopic images and electron microdiffraction of quartz particles in initial state (a) and modified in the presence of butanol (b), acrylic acid (c,d) and polystyrene (e-h)

When using polystyrene as a modifier depending on amount of modifier being used (from 3 % to 10 %), time of treatment and also during variation of force conditions of action there are formed structurized or tracery films cross-linked with a particle surface or rolled up in the form of tubes of a different configuration the size of which reaches 50-70 nm (figure 6 f-g). Increase in time of treatment finally leads to coagulation of dispersed particles with modified surface layer and formation of dendrite-like formations (figure 6h). Main element involving in building nanostructurized objects during mechanochemical treatment is carbon. Distinctive feature of carbon nanostructures on quartz surface subjected to mechanochemical treatment in the presence of polystyrene is the presence of texture i.e., favourable orientation of carbonaceous particles inside film formations (figure 6 c, d). Maximal amount of fixed carbon – 2.6 % on the surface of quartz particles was discovered in the samples modified by polystyrene which showed the most diversity of structural forms.

IR-spectra showed decrease in intensity of low frequency both valence and deformation fluctuations and increase in high frequency fluctuations. Dehydration of the surface of particles and shift of all spectra to the region of high frequencies are observed. This data testifies about that during quartz grinding there are accumulation and redistribution of defects. It results in intensifying disordering of lattice, increasing quantity of groups with weak bonds.

After modifying treatment of quartz with organic additives changes of quartz matrix spectrum affects all absorption bands: polystyrene presence results in decrease of intensity and butanol on the contrary to their considerable increase. Transformation of spectrum kind affects only region of frequencies of valence fluctuations ($999-1186\text{ cm}^{-1}$). There is degeneration of bands of 1162 cm^{-1} and 1062 cm^{-1} and shift of middle band to lower frequencies (to 1109 cm^{-1}). Absorption bands of higher than 1400 cm^{-1} which are caused by the presence of carbonate and carboxylic groups of different isotope composition on the surface of Si-O-Si are of special interest.

Directivity of chemical conversion of quartz particle surface during mechanochemical treatment is determined by emerging the whole complex of reaction centers with nonsaturated valency bonds. These are sililene $\equiv\text{Si}^\cdot$, $=\text{Si}^\cdot$, silanone $\equiv\text{SiO}^\cdot$ and peroxide centers $\equiv\text{SiOO}^\cdot$ and also silanol centers $\equiv\text{SiOH}$ and deformed siloxane groups $[\equiv\text{Si-O-Si}\equiv]_{\text{def}}$. Final products of destruction (mechanocracking) of all additives – modifiers being used in the work are radical groups H_3C^\cdot , H_2C^\cdot , $\cdot\text{OH}$ and also H and C during interaction of which with active centers of quartz surface in a complex capsulation with preservation of surface defects of structure is possible.

Change of structure being grinded by quartz particle at all hierarchical levels (from particle volume to distortions within crystal lattice) is determined by the kind and degree of kinetic energy dissipation transferred to the particle at the moment of the shock with a ball and fixed in it in the form of elastic energy of deformed crystal. The structure of the quartz particle surface layer after a mechanochemical treatment may be interpreted as a nanostructural formation containing carbon, silicon, iron and having a complex structure encapsulating a particle. Finally, a composition material is formed consisting of carbon surface layer with introduced inclusions of iron, transition amorphized layer on the basis of silicon and a crystalline quartz base.

Such structural rearrangements of the surface layers of the quartz particles being dispersed result in the change of physical properties of the material. The measurements of specific resistance

of quartz powder after a mechanochemical treatment showed its decrease by more than an order of magnitude. The modified quartz powder after a mechanochemical treatment also exhibits magnetic properties (table 6).

Table 6 - The change of specific resistance and magnetic permeability of quartz powder depending on the time of weathering. Grinding was carried out during 5 minutes

Material	specific resistance, $\rho \times 10^6, \Omega \times m$		magnetic permeability		Both electric and magnetic characteri stics of mechanic
	The time of weathering, $t_{s1}, 24$ hours		the time of weathering, $t_{sb} 24$ hours		
	0	30	0	30	
Ouartz	1.1	6	2.0	2.0	
Ouartz +	6.0	15.0	4.0	3.2	
Ouartz +	2.5	3.5	29.0	27.0	

hemically treated quartz change with time, *i.e.* the material "ages". However, if such "aged" material is placed into an electromagnetic field of definite intensity, its ferromagnetism and conducting characteristics are recovered, it being the result of interaction of a piezoelectric quartz nucleus and a carbon nanostructural film containing ultradisperse inclusions of iron.

Carbon-containing refractory materials.

Carbon-containing refractory materials are obtained using various methods. Incorporation of chromite sludge increases density and mechanical strength in comparison with refractory material "Furnon – XII" insignificantly rising refractory property. Improvement of physico-chemical refractory materials based on clay and carbide of metals is explained by formation of fibrous carbon and carbides of metals [4]. Obtained refractory materials have high sludge resistance, that makes prediction of their use in metallurgical processes of production of precious metals possible.

Composition refractory materials obtained by selfpropagating high temperature synthesis (SHS) have a number of advantages due to their physico-chemical and operational properties as well as power consumption in comparison with conventional composition systems [18,19]. The quality of the material depends on the conditions of synthesis and possibility to control the process and, finally, on its structure and properties. One of the effective methods of influencing SH-synthesis is the use of preliminary mechanochemical activation which changes the chemical activity of reagents, thermodynamics and kinetics of subsequent thermal processes [20]. Treatment of quartz with different organic additives provided modification of the surface of particles. The difference in the morphology of the surface of modified material (quartz) depending on the modifying additives being used was found [5, 6, 21]. In case of using alcohols, in particular butanol, under the conditions of mechanochemical treatment, the surface of particles is carbonized. The degree of carbonization increases with the use of more complex organic compounds. The form and degree of structural organization of carbon containing formations depend on many factors, including the time of the mechanochemical process. Nanosized formations grafted to the surface and containing carbon compounds are formed on the surface of particles (figure 6).

При использовании в качестве модификаторов других соединений, в частности азотсодержащих; ammonia(NH_4OH) and acetamide (CH_3CONH_2) – the structure of modified particles has a number of peculiarities. There are observed filmy, platy, platy-veil and fibrous-veil structures containing nitrogen in modified quartz samples during mechanical treatment with nitrogen-containing compounds (figure 7).

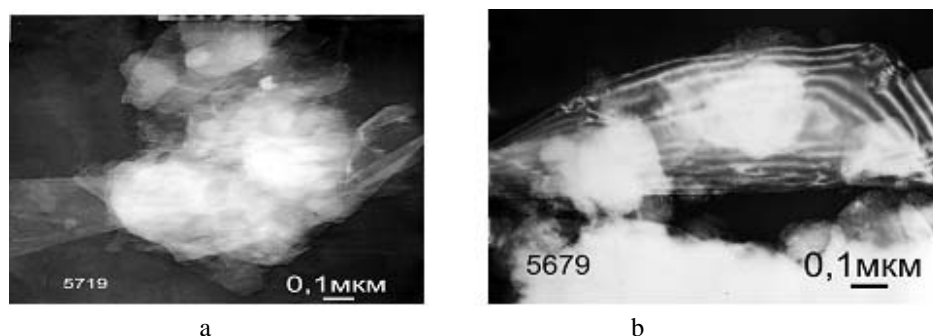


Figure7 - Electron –microscopic pictures of quartz particles after mechanochemical treatment in the presence of 10% CH_3CONH_2 (a) and NH_4OH (b)

The peculiarities of the structure of modified quartz are responsible for specificity of the following processes of interaction of quartz particles with aluminium under the conditions of SH-synthesis. A definite role in these processes is played by carbon which saturates the surface layer in the process of mechanochemical modification. For quartz which was not subjected to mechanochemical treatment, the amount of carbon is 0.08 %. After treatment, the content of carbon in the sample makes up from 1.14 to 2.96 % depending on the modifying additive being introduced. Temperature of combustion of modified quartz with aluminium reaches 2473 K [22]. High combustion temperature form may be accounted for the fact that SiO_2 is reduced not only by aluminium, but also by H, C, CO. These reducing agents are decomposition products of compounds on the surface of quartz particles obtained when treating them with organic additives. It is known that carbide formation reactions give high temperatures in combustion processes. Besides SiC, small amounts of AlC and FeC were registered. The presence of iron compounds in the phase composition of sample being synthesized is due to the uptake of ultradisperse iron particles into the quartz powder from the walls of milling vessels and balls in the process of grinding.

Size variations of synthesized samples on the basis of the system ($\text{SiO}_2 + 37.5\%\text{Al}$) with quartz modified by mechanochemical treatment in the presence of different organic compounds showed that scale factor is an effective way of influencing the course and final results of SHS-process. The diameter of samples varied from 15 to 59 mm, the volume – from 3 to 98 cm^3 . In SHS-systems of samples with activated quartz, the size factor exerts influence not only upon the combustion temperature, but also upon the final result of synthesis, i.e. reaction products. On samples of greater volume there takes place maximum reduction of Si and formation of sialon (it being of two types: $\text{Si}_2\text{Al}_3\text{O}_7\text{N}$ and $\text{Si}_3\text{Al}_3\text{O}_3\text{N}_5$) in synthesis of which nitrogen of air takes part (table 7). The content of

sialon in coarse-grain samples is 18 %. This fact is of great importance, for it indicates the change in combustion kinetics, diffusion rate and the sample structure depending on the volume of the sample. Gaseous phase reactions play a significant role in the formation of phases and structure of such samples. The final results of the peculiarities of combustion of volume samples are the changes in their density and strength. The density values decrease with the time of activation, but the presence of a modified layer on the surface of quartz particles contributes to considerable increase in density (by 20 – 25 %) and strength of the synthesized material (by 50–80 %). Material containing nitrite compounds has also higher indexes of thermal-protective characteristics.

№	τ_{acm} in.	d/ h, mm/mm	SiO ₂ %	Si, %	Al ₂ O ₃ %	3Al ₂ O ₃ 2SiO ₂ %	FeSi ₂ %	SiC %	AlN %	Si ₂ Al ₃ O ₇ N %	XAP** %
O	0	20/20	3.5	21.0	22.0	4.0	1.0	-	-	-	48.5
I	10	20/20	2.2	23.8	27.5	8.6	2.4	-	-	-	35.5
I	20	20/20	5.0	30.0	22.0	17.0	3.5	-	-	-	22.5
I	10	50/50	-	24.6	18.7	10.5	1.9	-	2.1	12.0	30.2
II	10	20/20	3.4	17.6	60.5	-	6.5	-	3.0	-	9.0
II	10	50/50	-	20.0	53.5	1.4	7.0	-	0.5	7.0	10.6
III	10	20/20	7.8	20.5	30.0	5.7	3.2	5.8	5.0	-	22.0
III	20	20/20	3.4	29.0	31.0	3.6	2.0	10	2.0	-	19.0
III	10	50/50	5.7	21.2	38.5	3.0	1.0	5.0	0.3	9.3	16.0
IV	10	20/20	1.6	20.0	50.4	4.5	7.9	6.1	5.0	-	4.5
IV	10	50/50	-	25.0	38.1	-	6.5	5.7	2.0	15.7	7.0
IV	20	50/50	-	30.0	37.0	-	3.0	5.0	-	18.0	7.0

0- (SiO₂+37.5%Al)
 I- [SiO₂]act. +37.5%Al
 II - [SiO₂+37.5%Al]act.

III - [SiO₂+PS*]act. +37.5%Al
 IV -[SiO₂+37.5%Al+PS*]act.
 PS* - polystyrene
 XAP** – X-ray amorphous phase

Fullerenes formation in hydrocarbon flames under electric field.

Influence of the direct electric current of different polarity on flame forms, soot yield, parameters of soot samples microcrystals (L_a , L_c and d_{002}) and soot particles sizes in intensity range from 0.5 to 20 kV at electrode systems «needle-plane» at combustion of benzene-oxygen mixture at the ratio C/O=1.0 with addition of 10 % volume of argon at pressure 40 Torr was investigated [25]. It was found that at positive polarity action of electric field rises to such a degree that at $U > 10$ kV it leads to flame extinction. It is shown that maximum decrease in soot yield is observed at negative polarity. It was found that intensity range of electric field in which soot yield was 10 % more soot yield without applying electric field. It was shown that parameters of soot micro crystals on average remain constant irrespective of intensity and polarity. Fullerenes C_{60} , C_{70} and PAHs were identified in the extracts of soot samples by the method of IR-spectroscopy.

Soot obtained under various conditions was extracted by the method of cold extraction in the medium of benzene (C_6H_6) during 72 hours. For extraction of soot was from soot tank. The extract had sated dark red color. A solution of obtained extract was investigated by using IR-spectrometer. Figure 8 presents spectra of soot extracts that obtained at various type of electric field discharge.

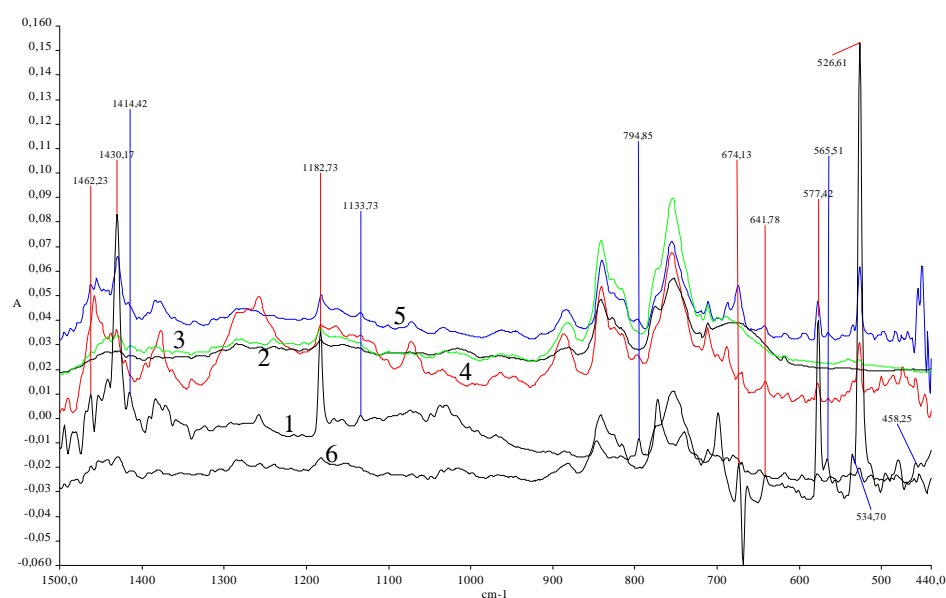


Figure 8 - IR-spectra of dry extracts: 1- standard sample of fullerenes C_{60} and C_{70} ; 2 - dark discharge, $U=0.5$ kV, $I=5 \times 10^{-7}$ A; 3 - glow discharge, $U=10$ kV, $I=2 \times 10^{-3}$ A; 4- glow discharge applied directly on flame front, $U_n=7$ kV, $I=4 \times 10^{-3}$ A; 5- abnormal glow discharge applied directly on flame front, $U_n=7$ kV, $I=7 \times 10^{-3}$ A; 6 - without applying electric field

It is experimentally found that yield of fullerenes significantly starts to grow ($\alpha \geq 13\%$) in the area of the abnormal glow discharge at values of discharge current $I = 7 \times 10^{-3}$ A (figure 8, curve 5), at direct applying electric field on flame front. The analysis of absorption spectrum (figure 8, curve 5) shows, that the lengths of waves corresponding to fullerenes C_{60} (λ - 528, 577, 1183, 1429, nm⁻¹) and C_{70} (λ - 458, 535, 565, 578, 642, 674, 795, 1134, 1414, 1430, 1460, nm⁻¹) are all shown, without exception, except for fullerenes in extract there was a mix of polycyclic aromatic hydrocarbons (PAH). Such connections as pyrene, fluoranthene, coronene, anthracene 1.12- benso[*a*]perylene have been identified.

Identification of fullerenes C_{60} and C_{70} has been conducted by radiographic method during analysis of dry extract thin layer. For this purpose, obtained extract of fullerene containing soot from soot tank, was evaporated on a quartz support and, formed dry residue was investigated by using diffractometer. The analysis of X-patterns of soot samples of dry extracts has shown presence of peaks on reflection angle, peculiar to fullerenes C_{60} and C_{70} . Peaks, according to card file ASTM, correspond to following crystal fullerenes phases: orthorhombic, cubic and hexagonal (C_{70} only hexagonal). Herein, intension ratio is not observed, that is peculiar to amorphous state of fullerene containing dry extract formed as a result of presence in the extract of polycyclic aromatic hydrocarbons.

References

- [1] Buyanova R.A., Chesnokov V.V. Regularities of catalytic formation of carbon filaments in the process of synthesis of novel composite materials. // Chemistry in the interests of stable development. 1995. №3.-p. 177-186.
- [2] Mansurov Z.A. Overcarbonized adsorption-catalytic systems // Eurasian Chemico-Technological Journal. 2000, V. 2, № 1, c. 59-68.
- [3] Mansurova R.M. Physico-chemical basis of synthesis of carbon-containing compositions. Monography, Almaty, XXI century, 2001.
- [4] Mansurov Z.A. Nanocarbon materials. // KazNU Vestnik, chemical series, №2 (30), 2003, p. 29-31.
- [5] Mansurov Z.A., Mofa N.N., Ketegenov T.A., Chervyakova O.V. Carbon containing microcomposition particles with quartz nucleus obtained by mechanochemical synthesis. // Proc. Inter. Symp. "Carbon 2003", Oviedo, Spain. - CD.
- [6] Mansurov Z.A., Mofa N.N., Shabanova T.A. Synthesis of powderlike materials with particles encapsulated in nanostructured carbon containing films. // Proc. Inter. Symp «Carbon 2004», Providence, USA. - CD.
- [7] Mansurov Z.A. Some Applications of Nanocarbon Materials for Novel Devices // R. Gross et al (eds.), Nonoscale-Devices – Fundamentals, 355-368, 2006, Springer, p. 355-368.
- [8] Mansurov Z.A., Kolesnikov B. Ya., Biisenbaev, Kolesnikov A.B., Kurbatov A.P., Mansurova R. M., Zhilybaeva N., Bakenov Zh. Nanocarbon materials for chemical sources of current. // Materials of panel discussion: "Problems of Accumulator Production Development in Kazakhstan" - Almaty, Kazakh University. – 2004., pp. 26-36.

- [9] Ogumi Z., Inaba M. in: B. Scrosati (Eds.), *Advances in Lithium-Ion Batteries*, W.A. van Schalkwijk, Kluwer Academic/Plenum Publishers, New York 2002, pp. 79-101.
- [10] Yemuranov M.M., Bisenbayev M.A., Kabylkakov D., Shilina Yu.A., Zhylybaeva N., Mansurova R.M., Mansurov Z.A. Sorption of Harmful Compounds by Nanostructural Carbon Materials.// *The International Conference on Carbon*, 2006. Aberdeen, Scotland 16-21 July, p.328.
- [11] Gilmanov M.K., Ibragimova S.A., Basyrgaev Zh.M., Sabitov A.N., Musabekov K., Yemuranov M.M., Mansurov Z.A. Hydrophobic chromatography of cytokinin mediator on carbon-silicon sorbent // *Materials of IV International Symposium "Physics and Chemistry" / "Nanoengineering"*, Almaty 2006, p. 26-27.
- [12] Gilmanov M.K. Mechanisms and mediators of signal transduction of cytokinins in plants. // *Kaz GU Vestnik, biological series - Almaty*, №1 (13), 2001, p. 44-48.
- [13] Mansurov Z.A., Zhylybayeva N.K., Ualieva P.S., Mansurova R.M. Preparation and properties of sorbents on the basis of vegetative raw materials. *Chemistry in the interest of stable development*, №10, 2002, pp.339-346.
- [14] Mansurov Z.A., Ryabikin Yu.A., Zhylybayeva N.K., Mansurova R.M. Investigation on the possibility of formation of nanostructures in the process of carbonization of AS by EPR method. *Materials of II Intern.symp. «Physics and chemistry of carbon materials»*, 2002, Almaty, pp.273-275.
- [15] Mansurova R.M., Zhylybayeva N.K., Taipova R.A., Mansurov Z.A. Sorbents on the basis of rice husk. *Vestnik of National engineering academy of RK*, 2004, pp. 97-100.
- [16] Mansurova R.M., Nikolaeva A.F., Zhylybayeva N.K., Bessarabova I.M., Zakharov V.A. New carbon containing sorbents for extraction of gold. *Materials of II Intern.symp. «Combustion and plasmochimistry»*, 2003, Almaty, pp.219-224.
- [17] Mansurov Z.A., Zhylybayeva N.K., Mansurova R.M., Zakharov V.A., Bessarabova I.M., Nikolaeva A.F. Sorption of gold by carbonized sorbents on the basis of vegetative raw material. *An Inter. Conf. on Carbon "Carbon'04"*, Providence, Rhode Island. USA. 2004, A070
- [18] Merzhanov A.G. Selfpropagating high temperature synthesis: twenty years of search and findings / *Preprint*. Chernogolovka. 1989-50p.
- [19] Merzhanov A.G. Processes of combustion and explosion in physical chemistry and technology of inorganic materials // *Successes of chemistry* 72(4) – 2003: P 323-345.
- [20] Heinicke G. *Tribochemistry*. M.: Mir, 1987. 584 p.
- [21] Mofa N.N., Shabanova T.A., Chervyakova O.V., Mansurov Z.A. Electron-microscopic investigations of quartz particles modified by mechanochemical processing // *Eurasian. Chem. Tech Jornal* .2003. 5. P. 201.
- [22] Mofa N.N. The peculiarities of the structure and stages of combustion of systems on the basis of quartz modified by mechanochemical treatment // *Combustion and plasmochimistry*, 2003. V.1. №1. P. 89

- [23] Ilyin A.P., Gromov A.A., Yablunovskij G.V. On the activity of aluminium powders // Physics of combustion and explosion, 2001. V.37. №4. P. 58
- [24] Gromov A.A., Dritz A.A., Vereschagin V.I. Synthesis of aluminium nitride and oxynitride in combustion of powderlike mixtures on the basis of aluminium // Refractories and technical ceramics, 2004. №12. P. 19
- [25] Mansurov Z.A., Prichodko N.G., Mashan T.T., Lesbaev B.T. Study of soot formation at combustion of hydrocarbons at low pressure. Proc. Of the 7th APISCEU, 2004, December 15-17 - Hong-Kong CD, A1-141, p.6.

**ՀԱՅԱՍՏԱՆԻ ՀԱՆՐԱՊԵՏՈՒԹՅԱՆ ԳԻՏՈՒԹՅՈՒՆՆԵՐԻ
ԱԶԳԱՅԻՆ ԱԿԱԴԵՄԻԱ
НАЦИОНАЛЬНАЯ АКАДЕМИЯ НАУК РЕСПУБЛИКИ
АРМЕНИЯ**

Հայաստանի քիմիական հանդես **60, №2, 2007** Химический журнал Армении

**EVOLUTION AND CONJUGATING MODEL OF CARBONIC MATERIAL
THERMOCHEMICAL CONVERSION USING A NONISOTHERMAL KINETIC
APPROACH**

S. I. TSYGANOVA^{a*} and A. D. TSYGANOV^b

^a Institute of Chemistry and Chemical Technology SB RAS, 660036, Krasnoyarsk, Russia

^b Krasnoyarsk State University, 660041, Krasnoyarsk, Russia

Abstract

The evolution of carbonic material thermochemical conversion and the associative conjugating model are presented by the example of pitch carbonization to see the development of the complex system on the whole. Methodological approach is suggested to simplify the kinetics of complicated processes during heating and to calculate apparent activation energies of the product formation processes at various temperatures. The diagnostics of pitch thermochemical conversion is carried out from the point of view of evolutionary conjugated pathway of the complex system development.

1. Introduction

Processes of thermochemical conversion underlie the big-volume raw material processing, resulting with production of coke, oils, electrodes for aluminum or steel industry, carbon fibres, carbon-carbon composites, activated carbons and etc. [1, 2]. At the same time it is one of the basic sources of pollution of the natural environment by toxic carcinogenic substances [3, 4]. Moreover, growing necessity of the carbonic products production leads to exhaustion of natural resources (petroleum, coal, wood and etc.) and abruptly makes worse the ecological balance. So, issue of the day is to bring to light a nature of interaction of the man-caused processes and ecosystem degradation that, in turn, requires grouping of general and specific knowledge as well as a creation of a new methodologies and models for study of the evolution of complex system as a whole. In addition, it can give a chance to establish a connection between structure conversion of living and lifeless carbonic matter.

It is not surprising that there has been continuous research on many aspects of carbonic material thermoconversion such as the dependence of product yields on carbonic material type and reaction conditions, kinetics of processes and etc.. However, the heterogeneous nature of carbonic raw materials and complexity of the carbonization process which includes a multitude of single reactions proceeding

simultaneously have made its very difficult to perform unambiguous experiments to determine the rates and mechanisms in carbonic material conversion [1, 5-9]. The resulting lack of agreement on the rates and mechanisms in carbonic material thermoconversion has hindered the development of predictive methods. Recent years have provided a number of new experimental and theoretical approaches considering the recent progress on kinetics, the formation of volatile products, network models, cross-linking, rank effects, 'two-component' model of coal structure and others [7-11] which, unfortunately, don't give universal simple methodology of thermodynamic consideration of complex carbonic system as evolutionary process in general.

The aim of this paper is to present methodological approach and model considering thermoconversion of carbonic materials as evolutionary process of complex system on the whole by the example of pitch thermochemical conversion.

2. Nonisothermal kinetic approach of thermochemical conversion of carbonic substance

Nonisothermal process at constant heating rates supplies mechanistic and kinetic data on the decomposition of carbonic substances, but a large number of various rates complicates a calculation and analysis of complex process kinetics. To simplify the kinetics of complex processes during heating, to calculate apparent activation energies of the product formation processes and to consider the temperature-time evolution of a system on one scale, there is suggested to use the heating rate of $1^{\circ}\text{C}\cdot\text{min}^{-1}$. The constant heating rate of $1^{\circ}\text{C}\cdot\text{min}^{-1}$ ($dT\cdot dt^{-1}=1$) allows writing the kinetic equation of the process vs time and temperature by one dependence, using simple transformations:

$$V = -dC\cdot dt^{-1} = k\cdot c^n$$

$$dC\cdot dt^{-1} = dC\cdot dt^{-1}\cdot dT\cdot dT^{-1} = dC\cdot dT^{-1}\cdot dT\cdot dt^{-1} = dC\cdot dT^{-1}\cdot\alpha,$$

$$\text{where } \alpha = dT\cdot dt^{-1} = \text{const} = 1$$

By substituting a rate constant from Arrhenius equation, we receive

$$V = -dC\cdot dT^{-1}\cdot\alpha = A\cdot e^{-E/(RT)}\cdot C^n,$$

where n – the order of reaction; A – the pre-exponential factor; E – activation energy; R – universal gas constant; T – temperature; C – concentration of a reagent; t – time.

This equation can be used to calculate the apparent activation energy of product formation process under following assumptions:

- The pre-exponential factor practically doesn't depend on temperature ($A = \text{const}$).
- The first order reaction ($n = 1$). It is quite correct, because the first order reaction is usually considered for description of kinetic of coal, pitch, biomass and other hydrocarbon raw pyrolysis.
- Concentration of reagent is assumed to be a constant ($C=\text{const}$) if the system is in stationary or quasi-stationary state.

Computational exercise of apparent activation energies of gas formation process for carbonization of coal-tar pitch is presented below.

The integral dependences of formation rates of gaseous products (CH_4 , H_2 , C_2H_6 , CO) during carbonization of pitch at heating rate of $1^{\circ}\text{C}\cdot\text{min}^{-1}$ vs temperature were taken from [12] and transformed to the differential dependences which are shown in Figure 1 [13]. On the basis of these data the

apparent activation energies of CH₄, H₂, C₂H₆, CO formation processes are calculated. In Figure 2 lgV - T⁻¹ dependences of CH₄, H₂, C₂H₆ and CO evolution in the temperature interval of 300-800°C are presented. Linear segments are found in two temperature ranges (390-460°C and 580-680°C), for which apparent activation energies of CH₄, H₂, C₂H₆ and CO formation process are calculated and listed in Table.

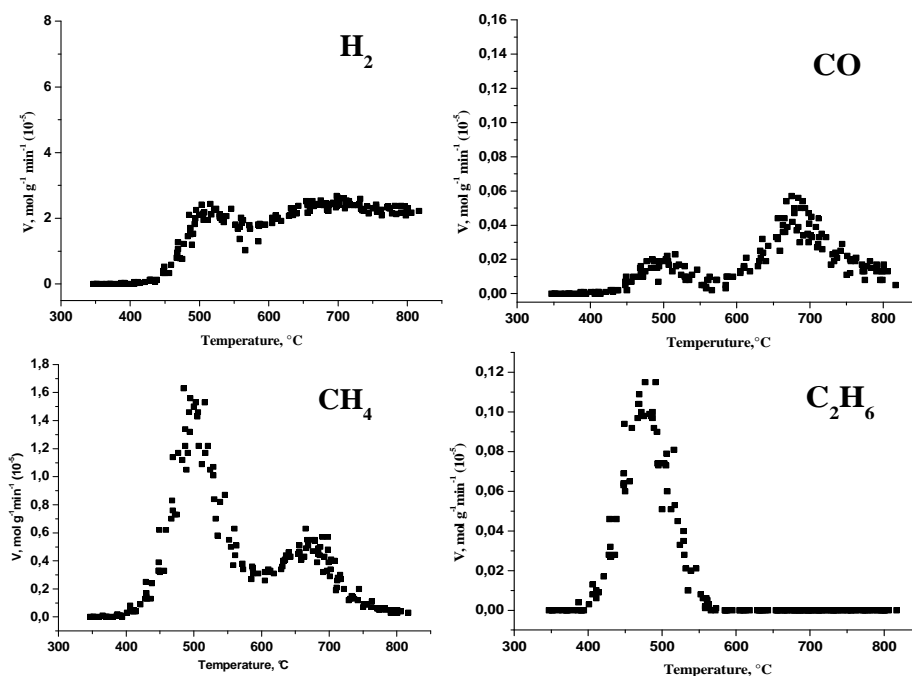


Figure 1. Evolution rates H₂, CH₄, C₂H₆ and CO as a function of temperature for coal tar pitch ($V_{\text{heating}}=1^{\circ}\text{C}\cdot\text{min}^{-1}$).

Table.

Apparent activation energies of gas formation process (kJ·mol⁻¹) during the heating of coal tar pitch.

gas	E ₁	E ₂
H ₂	226±13	30±14
CH ₄	199±10	67±31
C ₂ H ₆	207±20	—
CO	197±27	137±41

E₁ – activation energy determined in the temperature range of 390-460°C

E₂ – activation energy determined in the temperature range of 580-680°C

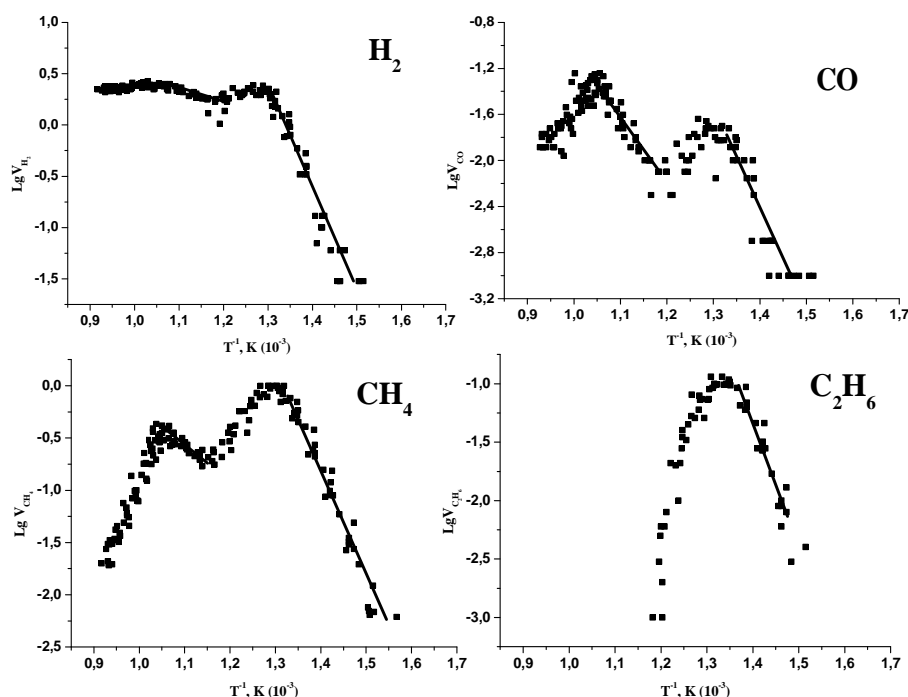


Figure 2. Logarithmic dependence of evolution rates of H_2 , CH_4 , C_2H_6 and CO on reciprocal temperature for coal tar pitch.

Thus, using the only heating rate ($1^\circ\text{C}\cdot\text{min}^{-1}$), the apparent activation energies of product formation process can be calculated in different temperatures (or times) and its changes can be revealed both at the individual stage and at the all system.

3. Principle of carbonic substance evolution modeling and associative conjugating model of pitch thermochemical conversion

It is known that many carbonic materials, including pitch, have paramagnetic properties due to existence of stable radical centers and formation of polyconjugated system during heating [1, 5, 10, 13-15]. So, we can consider the system in stationary or quasi-stationary state during passing of radical processes; it makes the kinetic calculations easier.

We suppose that the principle of energetic conjugation underlies the modeling of complex carbonic system evolution; the term “conjugation” means driving mechanism of physic-chemical conversion caused by availability of high-energy electron-migratory intermediates. It is also suggested the principle of ‘all conjugation’ including conjugation of bonds, reactions, processes, phases and structures in this system.

With regard to the foregoing and also to the data concerning pitch carbonization, we suggest the associative conjugating model of pitch thermoconversion presented in Figure 3 in the form of elementary aryl intermediate – phenyl; here carbon atoms are associatively substituted by specific

products (pitch – mesophase – semicoke – semiconductor – coke – tar) formed at the different stages of pitch conversion.

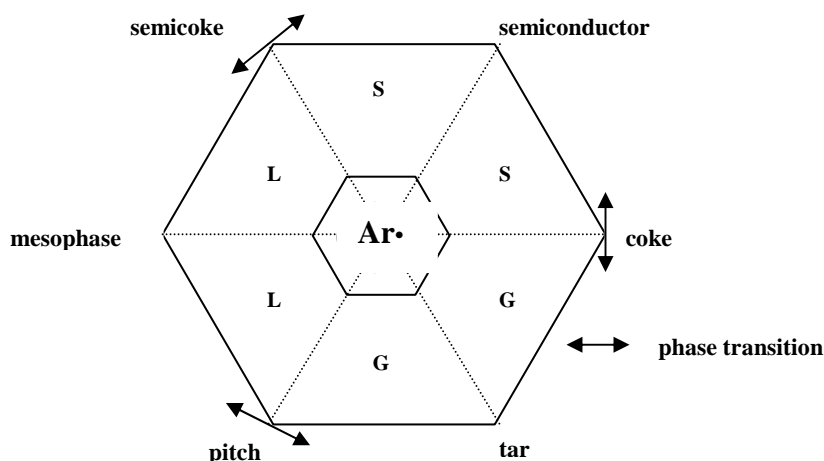


Figure 3. Associative or conjugation model of thermoconversion of pitch (L - liquid phase, S - solid phase, G - gas phase).

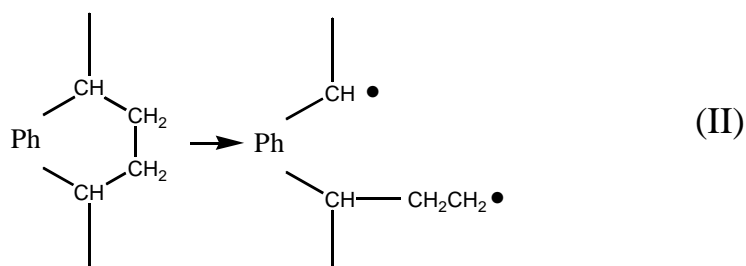
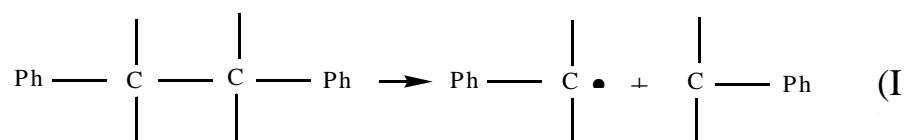
Thermoconversion of pitch is considered as continuous multiplex heterogeneous conjugated process in liquid, solid and gas phases, where initiators of all processes are aromatic π -radicals. Moreover, phase transfers are accompanied by appreciable physico-chemical changes of the system. The description of pitch thermoconversion gives below subject to the conjugating model and the kinetic approach.

4. Diagnostic of pitch thermochemical conversion

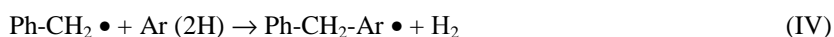
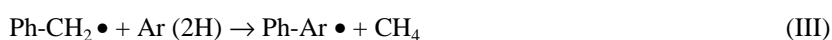
Under heating up to 200-400°C pitch undergoes the liquid-phase process of thermopolymerization that is initiated by the stable radical centers existing in pitch. Propagation of this process leads to accumulation of high-molecular aromatic molecules in pitch and their ordering with formation of anisotropic structure (**mesophase**).

Apparent activation energies of gas formation process (200-230 kJ·mol⁻¹) in low-temperature area (Table) are in close agreement with activation energy of mesophase formation (170-260 kJ·mol⁻¹) [1, 6, 16, 17]. Hence, two-phase states (condensed state - mesophase and gaseous state - gas) in this system are simultaneously formed from the same initial reagents. It characterizes the passing of liquid-phase conjugated processes of polymerization, cracking and polycondensation by the radical mechanism.

The most probable reactions of cracking initiation can be shown in the following way:



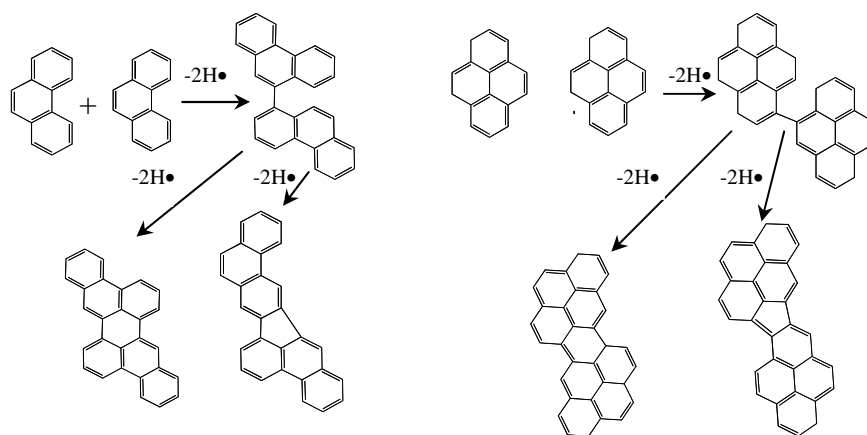
Methylenephenyl (or methilenearyl) radicals (reaction I) interaction with the main components of pitch easily proceeds with formation of high-molecular-weight and gaseous products:



Hydrogen elimination from biradical (reaction II) can leads to diene bond formation and to formation and growth of an aromatic molecule.

Significant thermochemical conversions of pitch and phase change in the system are occurred at heating up to 500°C. Intensive gas evolution (Fig. 1), formation of condensed products, endothermic effects, growth of paramagnetic centers, exchange spin-spin interaction between π -radicals with oriented ordering in short and long ranges are observed for **semicoke** formation (about 500°C) [1, 13, 15]. One can say that conjugated transition of radical processes from liquid-phase to solid-phase medium takes place.

At temperatures above 500°C hydrogen evolution with the constant rate is discovered (Fig. 1), which creates the constant hydrogen pressure in system during further heating due to dehydrocondensation process of aromatic fragments of pitch:



Consequently, reducing medium is produced by system itself at temperatures above 500°C.

The next stage of thermoconversion of pitch (about 600°C) is characterized by appearance of **paramagnetic properties** of the solid product (Fig. 3). Transformation from microdomain structure, where single domains are isolated, to monolithic one takes place; maximization of paramagnetic center concentration is observed [15] and migration of hydrogen becomes a motive force of structure formation to minimize free energy. At this stage, evolution of tar is occurred also [13, 18]. In other words, “defect structures” that are disconnected with basic carbon matrix are accumulated in solid residue and evolved in gas phase. Thus, it is proposed that at this stage, solid-phase conjugated radical processes of microstructural ordering and macrostructural changes start to proceed.

It is our opinion that calculated apparent activation energies of gas formation process in high-temperature area (Table) characterize the pyrolysis and linking processes passing in the condensed phase. One can suppose that low apparent activation energies of the hydrogen formation process in this temperature range are connected with diffusion-controllable process (recombination) – a relay-race migration of hydrogen in condensed phase. Higher values of apparent activation energy of CO formation process than for other gases (Table) can be caused by relay-race effect of long range ordering of oxygen.

At the stage of **coke** formation (about 700°C), as well as **semicoke** formation, the phase transition is observed accompanied by appreciable physical and chemical changes in the system, such as conversion of the carbon residue to single condensed phase, intensive evolution of the gas products, desorption of tar and exothermic effects [13, 18].

According to the presented associative model (Fig. 3), gas-phase processes occur at this stage. Really, at temperatures of 600-1000°C a vapor-phase pyrolysis of aromatic hydrocarbons proceeds forming phenyl(aryl)radicals, which undergo straight nuclear condensation [1]. Therefore, **tar**, including polycyclic aromatic compounds, is subjected to vapor-phase pyrolysis at these temperatures. At the same time, at temperatures above 800°C significant conversion of solid residue doesn't occur - ordering structure of carbon residue is only observed with hydrogen evolution.

Thus, a reducing medium is created in the system that facilitated passing of solid-phase radical processes and it is a “bridge” for realization of process transfer from liquid to solid and then to gas phase. Evolution of this system is an uninterrupted conjugated transfer from processes of synthesis to processes of degradation in each phase. Simultaneously, these processes promote a conjugated transfer of one phase in another as well as conjugated micro-, macrostructure changes.

To return to stating point of our model – **pitch** (Fig. 3) the system must give up the thermal energy to the surrounding environment, approximately such amount that have expended on external influence (heating), except the energy required for proceeding polymerization. Consequently, thermoconversion of pitch as evolution system can pass with insignificant total energy consumption.

Finally, presentation of evolution of this system has shown up elements of self-organization and self-reproduction, which living matter has; so, common features for living and lifeless carbonic matter are found.

5. Conclusion

Nonisothermic process at constant heating rate of $1^{\circ}\text{C}\cdot\text{min}^{-1}$ have been allowed to calculate the apparent activation energies of gas formation process during pitch carbonization. It has been established that the apparent activation energies of gas formation process during of pitch carbonization in low-temperature range are in good agreement with activation energies of mesophase formation.

Suggested associative conjugating model has been well considered the pitch thermochemical conversion as complex system on a whole and revealed a renewal of this system requiring insignificant total energy consumption.

Analysis of experimental and theoretical data concerning thermochemical processes of pitch has been visualized consecutive conjugated transfer from processes of synthesis to processes of degradation in liquid, solid, gas media.

It have been revealed that reducing medium is produced by system itself at temperatures above 500°C which facilitate passing high-temperature processes. We suggest that hydrogen is a “bridge” supporting uninterrupted conjugated transfer from one to other state of system.

References

- [1] Fitzer E., Mueller K., Schaefer W. The chemistry of the pyrolytic conversion of organic compounds to carbon. In: Walker P.L. Jr., editor. Chemistry and physics of carbon, v. 7, New York, 1971.
- [2] Phialkov A.S., Carbon, feedthroughs and composite on basis of theirs, Aspect Press, Moscow, 1997.
- [3] Nordheim E. // Light Metals, 2005, p. 575.
- [4] Eidet T., Guldhav F-Y., Olsvik A., Sorlie M. // Light Metals, 2004, p. 565.
- [5] Das T.K. // Fuel, 2001, v.80, p. 489.
- [6] Yue C., Watkinson A.P. // Fuel, 1998, v.77, p. 695.
- [7] Heek K.H., Hodek W. // Fuel, 1994, v.73, p. 886.
- [8] Solomon P., Hamblen D., Serio M. et al. // Fuel, 1993, v.72, p. 469.
- [9] Solomon P., Fletcher T., Pugmire R. // Fuel, 1993, v.72, p.587.
- [10] Dong G.L., Huttinger K.J. // Carbon, 2002, v.40, p.2515.
- [11] Castets K., Daguerre E., Py X. // Fuel, v.80, p.2075.
- [12] Koptug V.A., Anshits A.G., Savinov V.I. and etc. // Chemistry for sustainable development, v.5, 1997, p.553.
- [13] Tsyganova S.I. Abstract of the thesis “Dynamics and routes of product formation during carbonization of coal tar pitches” of candidate of chem. sci., Krasnoyarsk, ICCT SB RAS, 2002.
- [14] Singer L.S., Lewis I.C., Riffle D.M., Doetschman D.C. // J. Phys. Chem., v.91, 1987, p.2408.
- [15] Shklyev A.A., Miloshenko T.P., Lukovnikov A.Ph. // Chemistry of solid fuel, v.2, 1988, p. 25.
- [16] Marsh H., Martinez-Escandell M., Rodriguez-Reinoso F. // Carbon, v.37, 1999, p.363.
- [17] Rodriguez-Reinoso F., Martinez-Escandell M., Torregrosa P. and etc. // Carbon, 39, 2001, p.61.
- [18] Kurteeva L.I., Tsyganova S.I., Morozov S.V. and etc. // Chemistry for sustainable development, v.4, 2002, p.431.

**ՀԱՅԱՍՏԱՆԻ ՀԱՆՐԱՊԵՏՈՒԹՅԱՆ ԳԻՏՈՒԹՅՈՒՆՆԵՐԻ
ԱԶԳԱՅԻՆ ԱԿԱԴԵՄԻԱ
НАЦИОНАЛЬНАЯ АКАДЕМИЯ НАУК РЕСПУБЛИКИ
АРМЕНИЯ**

Հայաստանի քիմիական հանդես **60, №2, 2007** Химический журнал Армении

**SEMITRANSSPARENT CERAMICS FOR HEAT-INSULATING COVERS
OF THE COMBUSTION CHAMBER**

V.G. MERZLIKIN^a, O.V. SIDOROV^{b*}, V.V. BEZDELKIN^b, M. GUTIERREZ OJEDA^{b}**

^a Moscow Institute of Linguistics, Ecology and the International Attitudes, 119837, Остоженка Moscow, Russia,
merzlikinv@mail.ru

^b Moscow State Technical University "MAMI", Moscow, Russia
^{*}sid_ov@mail.ru

^{**}marcosgutierrez@mail.ru

Theoretical study of the semitransparent heat-insulating coatings used for the combustion chamber (CC) of reciprocating engines is made. These coatings will provide the thermal regime at generation in combustion chamber until 50% radiant component heat flow.

Model of the samples of porous ceramic materials, were offered as heat-insulating coatings. They are based on powders of zirconium, silicon, aluminum oxide which have transparent bands over the range of radiation wavelengths of the inflamed gas mixture in the combustion chamber of high-speed diesel engines. The radiant - conductive theory of subsurface heat of semitransparent coatings combustion chamber walls under the action of intensive radiant and convection heat flow is discussed. Results of simulation have shown that there is a subsurface temperature maximum inside ceramics under intensive visual and short-range infrared radiation. This allows providing an optimum temperature mode in the CC. This will limit the formation of toxic gases and may increase the efficiency of the internal combustion engine.

Introduction

Object of research are heat-insulating covers applied in the combustion chambers of diesel engines. This cover provides regulation of the thermal regime due to selective absorption radiant components of the thermal flow by the gas mixture combustion during the operation of the internal combustion engine. The theory of radiant-conductive subsurface heating of the combustion chamber wall is presented at the influence of intensive radiant component heating. It is the new point of view on radiant heat transfer processes in heat-insulating covers as light-scattering and faintly absorption medium. It has been shown as a functional communication between albedo of the ceramic layer and its scattering and absorption indexes. It has allowed to offer simple optical models for thick ceramics and

directly to calculate the absorbed radiant energy function depending on absorption and scattering indexes. It has been used real thermal physical characteristics of the ceramics on the basis silicon oxide. At the analysis of optical properties, the absorption indexes for porous ceramics are presented by known experimentally measured of monolithic powder. But scattering indexes values of various kinds of a porous ceramics have been considered as modeling.

Analysis of the thermal radiation effects in semitransparent ceramics as heat-insulating or thermal barrier coatings is made.

Ceramic parts and coatings are needed to withstand high temperatures and to reduce an external heat reject in the advanced high-speed diesel engines.

In hot environments, such as in the combustion chambers of these engines, infrared and visible radiation can penetrate into some ceramics and heat them internally.

From numerical simulations follows that the intensive short-wave radiation flux is able to create the subsurface temperature maximum even under small external temperatures including temperatures under zero [3,9]. That is why the temperature in the surface increases its value more slowly than the heated inner layers. It leads to formation of subsurface temperature maximum and may be subsurface fusion and sublimation.

The internal temperatures depend of the radiating effects combined with heat conduction, and of the convection and radiation in the boundary zone of the material.

Since inflamed gas mixture temperatures are high until 1500-2000 K, its radiant emission can be large from them and this radiation can penetrate into semitransparent parts and coatings of CC. This must be included in the heat transfer analysis of the combustion chambers walls.

Transient and steady-state behaviors are both important. During a transient stage, radiant penetration provides more rapid internal heating than conduction alone. The temperature distributions are usually considerably different than for steady-state conditions; this can produce transient thermal stresses.

Therefore in the given research was studied the heating up of the ceramic as a heat-insulating coatings, and have been considered models as thin layers, and real models as thick layers with thickness equals to 1 mm.

Modern analytical and numerical methods allow predicting transient temperatures and heat flows in translucent materials.

A transient processes analysis was done for plane thin and thick layers from:

1) a traditional opaque materials [1, 2]: iron - materials of combustion chamber wall, and its heat-insulating coatings from the industrial ceramic, the sample on the basis of chemically no rectified powder, for example oxide zirconium,

2) an advanced semitransparent and scattering materials [4-6, 8 - 9] from the ceramic sample on the basis of chemically rectified typical powder: ZrO_2 (partial stabilized zircon with yttrium), SiO_2 , Al_2O_3 .

Model description

As have shown researches of last 10-15 years an essential fraction of radiant components up to 50% takes place in chambers of combustion of high-speed diesel engines [1, 2, 10].

It was caused by local combustion of soot particles at temperatures 1500K - 2500K with characteristic wave length of radiation equal to 1-3 μm .

In general, the generation of a short-wave radiation flow q_o can occur in visible and near infra red-ranges of wavelength $\lambda = 0.3\text{-}5 \mu\text{m}$.

Thus, it is necessary to examine radiating heat exchange between the combustion chamber walls and the heat insulating coating.

Then takes place two types of thermal fluxes: radiant and convective (fig.1).

This flux on the wall of the combustion chamber defines superficial and volumetric radiating heating of the insulating heat coverings and walls.

The equations of heat conductivity and radiation were solved in common in one-dimensional approximation [5]. Optical parameters were introduced in two-flux optical model [5, 9]. The profiles of temperature and the temperatures on frontal and back surfaces, and also the maximum temperature sub-surface volume for semitransparent materials (tab. 2) have been calculated.

In known researches [2] of diesel engines for achievement of high efficiency heat insulating coatings are used in the combustion chambers.

With rare exception [4, 7], but materials of these coverings it was not considered as translucent. Besides process plasma deposition for the heat insulating covers leads to essential pollution of a ceramic layer by absorbing particles of metal of electrodes. Therefore considered industrial ceramic heat insulating covers are opaque on the optical properties in a short-wave range.

That is why in experimental development heat insulating coatings absorbed all thermal flux on the surface. It considerably reduced a heat-conducting rejection, the temperature of the internal surface up to 900 K. But there was not raise of efficiency, and it was slightly. At the same time the raise of nitrous oxides was higher. In consequence in 1990 the research and development the combustion chambers of diesel engines has been stopped practically.

In the articles used by authors [4, 9] the mathematical and theoretical models will allow to give the

forecast of development of new types of heat insulating coatings. In these coverings the profile of temperature can be changed due to displacement of the maximum of the temperature in the sub surface-area (fig. 2, tab. 2).

The specified thermal regimen could be reached for porous ceramics while exist scattering with the short-wave radiation. While the part of the radiant component ζ_R is higher, the temperature of the subsurface heating it is also higher (fig. 3). The maximal temperature changes from 830 K to 1300 K in the rise of ζ_R from 21 % up to 50 % with increase in depth of the radiant volumetric heating about 3 mm up to 6 mm.

For thick translucent samples displacement of the temperature profile can reach centimeters. It is determined by a ratio of parameters, these are: absorption and scattering. As have shown technological development [3, 5], as a rule, value of absorption is a constant value conditioned by initial industrial raw material. Therefore only dispersion can be changed due to modeling structural structure of ceramics (the size of the porous), and also the determinate fractional structure of inorganic powders (fig.4). On the graphic clearly that the maximum of temperature changes from 1300 K up to 1800 K with reduction of scattering in 10 times with rise of depth about 5 mm up to 10 mm.

Thus, application of translucent coverings promotes essential reduction of superficial temperature of the heat insulating covers, and also in the boundary zone with the metal wall of the combustion chamber (tab 2, fig 2). The uncovered metal wall with thickness of 1 cm for the period of heating 1 hour changes the correspondent temperatures with about 714 K up to 694 K. Its shelter of opaque ceramics (traditionally used industrial samples) allows keeping the back side of the metal wall at initial reference temperature 500 K for theoretically used thick layer of ceramics. For practical applications with a millimetric layer the gain will be 77 degrees already on the frontal surface of the metal wall.

In case of deposition of the translucent covering (tab. 2, 3-rd line) on the basis of rectified zirconium oxide the superficial and volumetric temperature decreases on 200 degrees. These results correspond to thick heat-shielding coverings which can be used in the space industry.

For creation of real and practical heat insulating coverings we shall consider a layer of 1 mm and a combustion time of its heating in a hot phase of the volume in the combustion chamber in time 1 millisecond [2]. From tab. 2 follows, that application of a translucent covering gives a gain in comparison with opaque up to 10 degrees. These data are agreed with estimations [8] which have been received at creation of heat-shielding coverings for cases of flying object.

At operation of diesel engines it is important to estimate the regimen of temperature of the wall in the combustion chamber at the cyclic heating during hot (1 millisecond) and cold (3 millisecond) phases (figs 6 and 7). The variant for the period of the movement of the piston in the combustion chamber for 4 milliseconds of millimetric thickness without heat rejection has been calculated. Upon termination of one cycle excess of temperature in the surface of an opaque covering in comparison with translucent

will make 8 degrees after a hot phase. The absorbed energy in both cases approximately is identical, since on small thickness processes of heat conductivity are essential. But depth of heating in the scattering material also is more than at opaque coverings (it was obviously observed on big thickness of modeling samples, figs. 2, tab. 2). After the end of a cold phase the difference in temperature makes not less than 2 degrees.

This depth of heating up is a modeling parameter. It depends on the optical parameters determined by the nature of initial substance and its structural composition. Then value of the maximum of temperature and its coordinate can be predicted, and the demanded structure of a covering can be provided corresponding to the technologies of its manufacturing.

Conclusions

Distinctive feature developed of the new translucent heat insulating coverings is their ability to accumulate radiant heat flux from the full thermal flux in the CC. Even with a high part of a radiating flux the temperature on the surface can remain stability due to raise of the penetrating radiation, its subsequent sub-surface absorption and if it is necessary its reject:

1. Out of the external border of the combustion chamber by conductivity.
2. Back to the internal CC volume, in the regime of a cold phase by development of engines with regenerative effect (one among of development directions of Low-Heat- Rejection Diesel Engines).

For first time was possible to estimate a non-stationary temperature profile in a ceramic covers as the semitransparent medium at modeling external conditions of "a hot phase" of high-speed diesel engines at convective -radiant heating.

At use of a semitransparent ceramic layer 1 mm thickness with a absorption indexes in an interval of $1-5 \text{ m}^{-1}$ and a scattering indexes in an interval of $10-100 \text{ m}^{-1}$ subsurface temperature may be exceed the temperature on the surface wall of the combustion chamber 100-400 degrees at the depth up to 1 cm.

Thus, the picked up thermal regimen of the heat insulating coverings will provide necessary temperatures of the internal surface wall and the volume of air fuel mixture and therefore can influence in the rice of the efficiency and in the concentration of formed toxic gases.

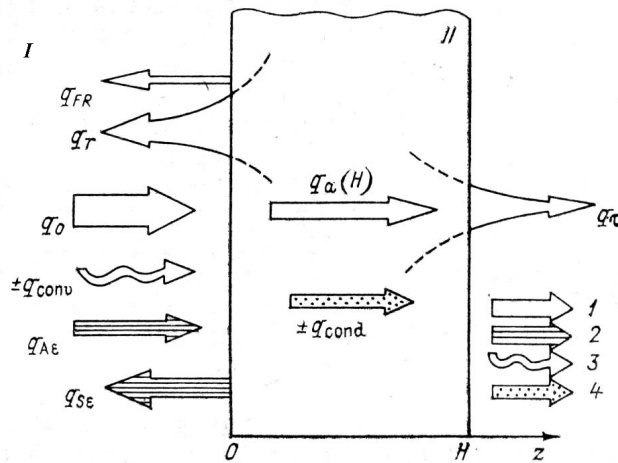


Fig.1. Physical model of the balance of energy in the volume (I) and in the boundary wall (II) of the combustion chamber (CC) in the high speed diesel engines

1. Radiant flux of local volumes of an inflammable gas mixture and its interaction with the thermal insulating coatings of the walls in the combustion chamber:

q_{fr} – the reflected flux from irradiated border (Fresnel),

q_r , q_α , q_τ – the reflected, absorbed and penetrated heat fluxes of short-wave radiation conditioned with the possible dispersion of the heat insulating covers (tab. 1);

2. Radiant long-wave ($\lambda > 5\mu\text{m}$) heat fluxes $q_{A\varepsilon}$, $q_{S\varepsilon}$, where:

$q_{A\varepsilon}$ – heat flux of own radiation of hot gases (air fuel mixture) at temperature $T_A > 800\text{K}$,

$q_{S\varepsilon}$ – heat flux of own radiation of a heated up wall of the combustion chamber;

3. Convective thermal flux q_{conv} , from hot gases with a heat transfer coefficient (B) up to 3000 Bt/m^2 .

4. Conductive thermal flux q_{cond} .

Then the full heat flux will be $q_{in} = q_o + q_{A\varepsilon} + q_{conv}$.

This flux on the wall of the combustion chamber defines superficial and volumetric radiating heating of the insulating heat coverings and walls.

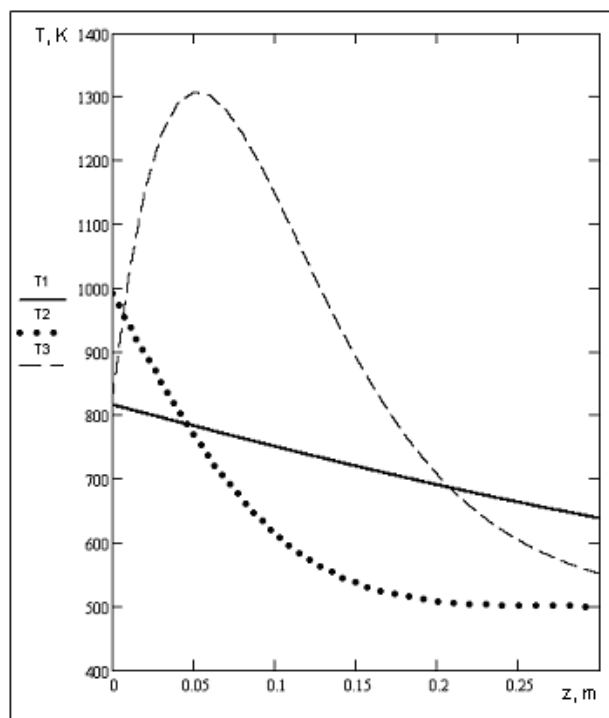


Fig. 2. Distribution of temperature in a flat thick layer of the combustion chamber in the diesel engines at the influence of convective and radiating fluxes $q_{in} = 1,9 \text{ MBT/M}^2$ with a radiant component $\xi_R = 50 \%$. Time of heating 1 hour. (without heat rejection on back border) for the following materials:

- T1 - metal wall (Fe) without covering with boundary factor of reflection Fresnel $R = 0.9$,
- T2 - thick layer of a heat-insulating coating from opaque ceramics with boundary factor of reflection Fresnel $R = 0.4$ (industrial sample on the basis of chemically no rectified powder of stabilized oxide zirconium),
- T3 - a thick layer a thermal barrier coating from translucent ceramics (the model of the sample on the basis of chemically rectify powder stabilized oxide zirconium with a parameter of absorption $\alpha = 1 \text{ m}^{-1}$ and a parameter of scattering $\sigma = 100 \text{ m}^{-1}$ альбедо $A = 87 \%$).

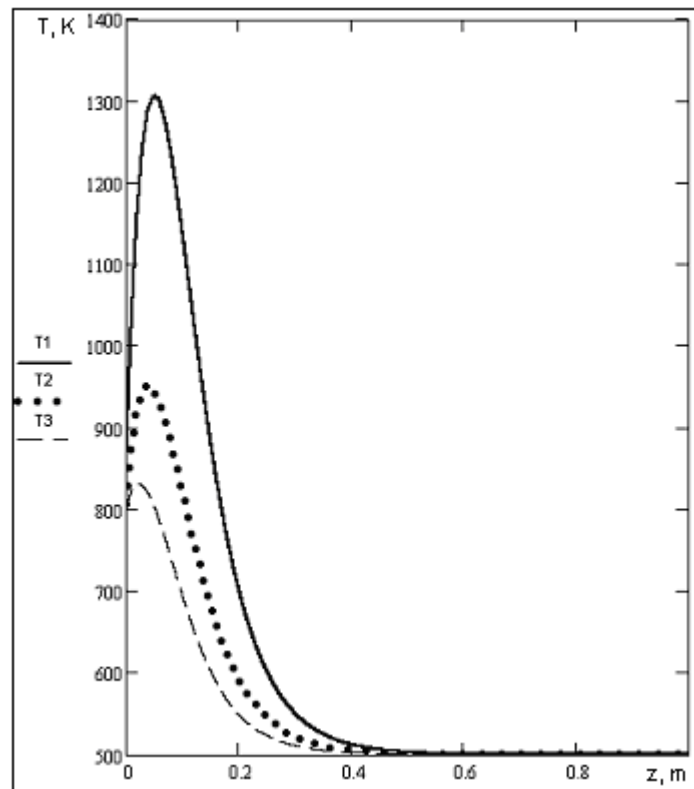


Fig. 3. Distributions of temperature in a flat thick layer of a heat-insulating coating of the combustion chamber in the diesel engine at the influence of a heat flux $q_{in} = 1.9 \text{ MBT/m}^2$ with different radiating components during 1hour heating. (without a heat rejection on back border) for curves:
T1 - $\zeta_R = 50 \%$, T2 - $\zeta_R = 32 \%$, T3 - $\zeta_R = 21 \%$.

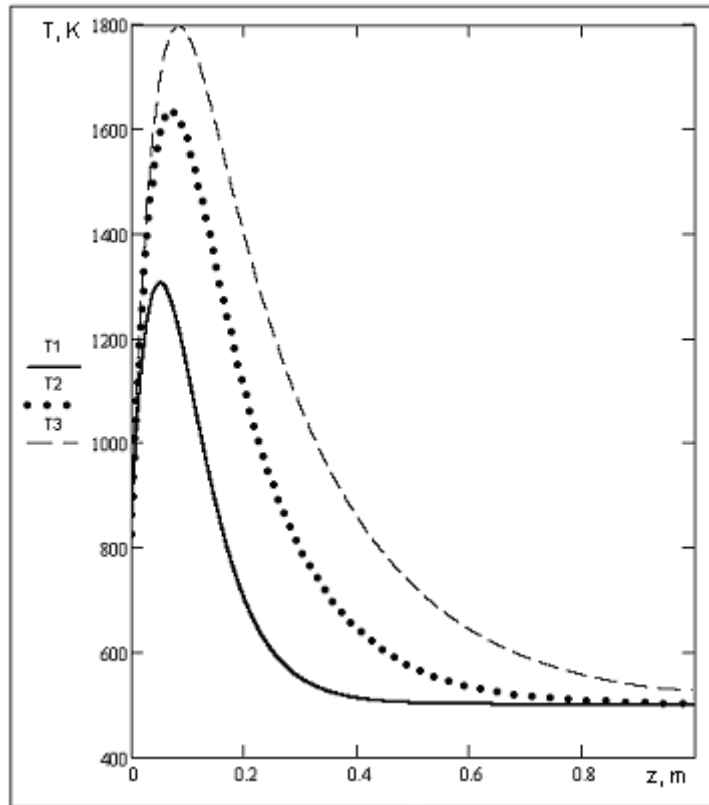


Fig. 4. Distribution of temperature in a flat thick layer of a translucent heat-insulating coating in the walls of the combustion chamber in the high speed diesel engines at influence of a thermal flux $q_{in} = 1,9 \text{ MBT/M}^2$ with a radiating component $\zeta_R = 50 \%$. Time of heating: 1 hour. With a heat rejection on back border $\eta_{out} = 0$ for materials with an identical parameter of absorption $\alpha = 1 \text{ m}^{-1}$ and following values of indexes of scattering and albedo:

- T1 - $\sigma = 100 \text{ m}^{-1}$, $A = 86 \%$,
- T2 - $\sigma = 25 \text{ m}^{-1}$, $A = 75 \%$,
- T3 - $\sigma = 10 \text{ m}^{-1}$, $A = 64 \%$,

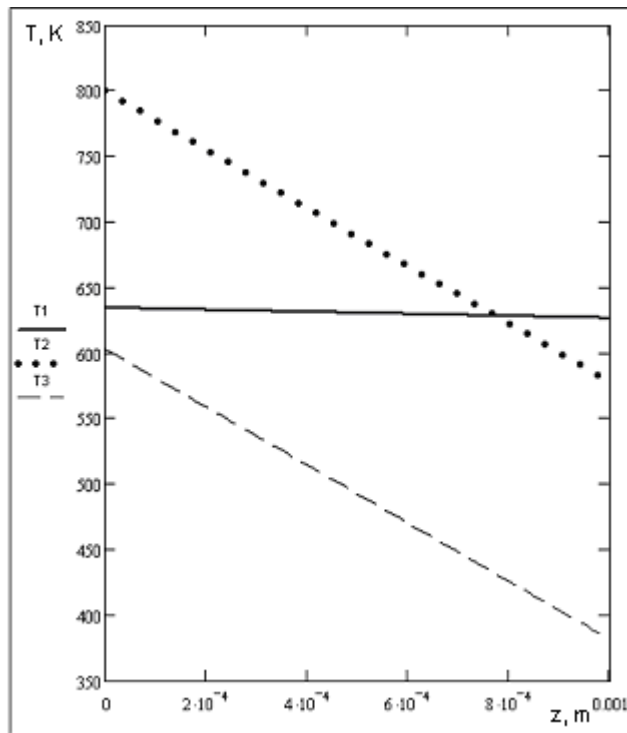


Fig. 5. Distribution of temperature in a flat thin layer (1 mm) in a heat-insulating coating in the combustion chamber walls in the high speed diesel engines at influence of a thermal flux $q_{in} = 1,9 \text{ MBT/M}^2$, $\zeta_R = 50 \%$. Time of heating 1 hour, with a heat rejection on back border $\eta_{out} = 30 \%$ for following materials:

- T1-metal (Fe),
- T2 - opaque ceramics with boundary Fresnel factor of reflection,
- $R = 0.4$ the industrial sample of the heat-insulating coating is on the basis of no chemically rectified powder of stabilized oxide zirconium,
- T3 - translucent ceramic with a parameter of absorption $\alpha = 1 \text{ m}^{-1}$ and a index of scattering $\sigma = 100 \text{ m}^{-1}$, альбе́до 87 % (the model of the sample on the basis of chemically rectified powder stabilized oxide zirconium).

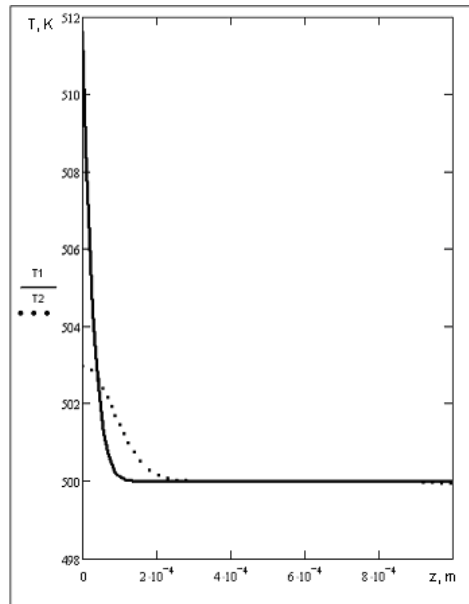


Fig. 6. Distribution of temperature in a flat thin layer 1mm in a heat-insulating coating in the hot (curve T1, time 0.001s with, $q_{in} = 1,9 \text{ MBT/M}^2$, $\xi_R = 50 \%$, $\eta_{out} = 0$) and cold (curve T2, time 0.003s) phases for translucent ceramics on the basis of chemically rectified powder of stabilized oxide zirconium (tab.2).

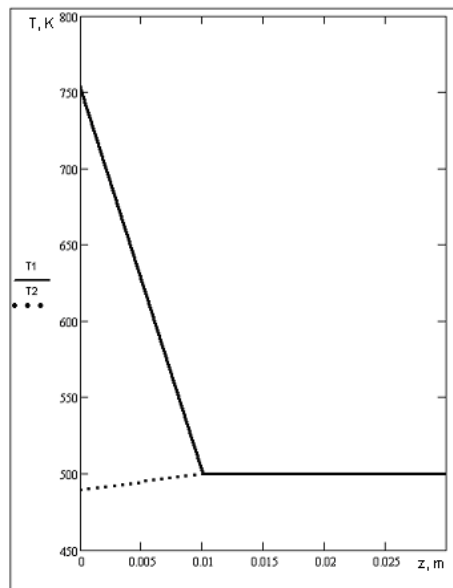


Fig. 7. Distribution of temperature in a flat thick layer in a heat-insulating coating in the walls of the combustion chamber during hot and cold phases (initial data on fig. 6)

Table 1

Thermophysical and optical ** characteristics of the heat insulating coatings of combustion chambers

№	Thermal barrier coating Material	Fresnel Reflectance λ=0.3-6 MKM		Albedo			Emissivity			Density, Kg / m ³	Specific heat capacity, J / Kg K	Thermal conductivity, W / m-K
				Length wave, μm								
				0.3-1.0	1-5	5-10	0.3-1.0	1-5.0	10			
1	Opaque material Iron.	40-90%		0	0	0.6-0.8	0.6-0.1	0.6-0.1		7870	440	76.2
2	Opaque heat insulating coating (the industrial sample on the basis of chemically no clean powder of stabilized oxide zirconium).	10-40%		0	0	0.8-0.9	0.9-0.6	>0.9	0.9	6030	450	2.7
3	Semitransparent heat insulating coating from translucent ceramics (the model of the sample on the basis of chemically clean powder).	*ZrO ₂	0.1	0.8	0.8-0.9	0.8-0.9	0.2	0.1	0.8	6030	450	2.7
		SiO ₂	0.04-0.08	0.9-0.99	0.1	0.2	0.1	0.93	0.88	2200	700	1.4-2
		Al ₂ O ₃	0.1	0.9-0.96	0.7-0.8	0.8-0.9	0.1	0.3-0.2	0.2-0.1	3984	755	33

- *As PSZ (partial stabilized zircon with yttrium)
- ** Novitski L. A. Optical properties of materials in low temperatures. Mashinostroyeniye. 1980. Pag. 243.

Table 2.

Calculated temperatures (T, K) of combustion chamber walls of the high-speed diesel engines

with

various heat-insulating coatings (HIC), $q_0 = 1.9 \text{ MBT} / \text{M}^2$, $\zeta_R = 50 \%$, $T_A = 800\text{K}$, $T_o = 500\text{K}$.

Materials of the wall		Internal surface CC	$T_{\max} / z, (\text{M})$	External surface HIC	External surface CC wall $/z, (\text{M})$
Metallics walls without heat –insulating coating.	Thin layer with out heat reject $t = 1 \text{ h}$	714	714	-	694/ 0.01
	Thick layer with out heat reject $t = 1 \text{ h}$	991	991 / 0	500	<500
Opaque heat-insulating coatings from the industrial ceramic sample (Item 2, tabl. 1)	*Thin layer 1 mm, $t = 1 \text{ h}$	800	800 / 0	577	<577
	*Thin layer 1 mm, $t = 0.001 \text{ s}$	519	519 / 0	580	<500
	Thick layer with out heat reject $t = 1 \text{ час}$	819	1307 / 0.05	500.	500
Semitransparent heat insulating coating from translucent porous ceramics (the model of the sample on the basis of chemically clean powder of stabilized oxide zirconium), semitransparent near and in the visual ranges of the waves lengths.	*Thin layer 1 mm, $t = 1 \text{ h}$	602	602 / 0	381	<500
	*Thin layer 1 mm, $t = 0.001 \text{ s}$	511	511 / 0	492	<500
	Thick layer with out heat reject $t = 1 \text{ час}$	819	1307 / 0.05	500.	500

* Heat rejection in the external surface $\eta_{out} - 30 \%$ from the full thermal flux in the combustion chamber.

References

- [1] Amann C. A. Perspectives and problems of the diesel engines with low heat loose. Actual Mashinostroyenye. Seria A. 1989, No. 5.
- [2] Kavtaradze R. Z. Local heat transfer in the piston engines. Bauman MGTU. 2001.
- [3] Krass M. S., Merzlikin V. G. Radiant thermophysics of snow and ice. Hydrometeoizdat. Leningrad 1990.
- [4] Merzlikin V. G. Semitransparent ceramics as heat insulating coating in the combustion chambers. Material MNTK, Pag. 2 «Piston and turbine engines», Moscow. MGTU “MAMI”- 2005. – Chap.2. Pag. 43-46.
- [5] Merzlikin V. G., Cutugin V. G., Shabligin M. V. Fibrous and porosity light-scattering materials. Chemical Fibre –2002.- No.2. Pag.50-54.
- [6] Merzlikin V. G., Tovstonog V.A. Thermal coating of elements and or units of the diesel engine in the combustion chamber. Patent No.2240430. Russia, 2004.
- [7] Novitski L. A. Optical properties of materials in low temperatures. Mashinostroyenye. 1980. Pag. 243.
- [8] Siegel, R. Internal Radiation Effects in Zirconia’s Thermal Barrier Coatings, AIAA J. Thermophysics Heat Trans., vol. 10, No. 4, 1996. Pag. 707-709.
- [9] Tovctonog V. A. Thermophysics of scattering materials: Problems and solutions. Vestnik MGTU. Mashinoestroyenye, 2000. No. 3. Pag. 67-85.
- [10] Tovctonog V. A Chirin K. V., Merzlikin V. G. Experimental stand for the model of combined heat flux. Vestnik Baumana Mashinostroyenye 2006. Pag. 62- 66.

STEADY CONDITIONS OF AUTOCATALYTIC NONISOTHERMAL REACTIONS IN
CSTR

B. L. KORSOUNSKII ^{a,b,*}, N. G. SAMOILENKO ^b, A. O. ILCHENKO ^c

^aN. Semenov Institute of Chemical Physics, Russian Academy of Sciences

^bInstitute of Problems of Chemical Physics, Russian Academy of Sciences

^cMoscow Engineering Physical Institute, Russia

*119991 Moscow, Kosygin Street, 4. N. Semenov Institute of Chemical Physics, Russia kors@polymer.chph.ras.ru

Abstract. The simulation CSTR has been carried out, in which the exothermal autocatalytic reaction proceeds. As distinct from a simple first order kinetics, in case of autocatalytic process in dimensionless coordinates “conversion – temperature” a rather diverse picture of possible types of thermal isoclinic line, including isola, is observed. It is established, that on the unstable branch of an isoclinic line only one steady state can exist. The analysis of oscillatory modes has shown that at change of governing parameter γ depending on other parameters, both smooth and rigid decay of limit cycle is possible. The adiabatic CSTR is steady always, and oscillatory modes in it are impossible.

The exothermal reactions in CSTR (continuously stirred tank reactor) are a significant object of macrokinetics [1]. In this field the bridge is thrown over the theory of thermal ignition and kinetics of chemical reactions in open systems.

For the first time, CSTR in which exothermal reaction proceeds has been analyzed by Zeldovich [2, 3]. In his papers, as well as in number subsequent publications, the simplest kinetic law, i.e. the first order reaction, was considered. It was found, that, depending on the values of parameters, the considered system can have one or three steady states.

Further development of the considered area has been realized in work of Salnikov and Volter [4]. These authors have confirmed the existence of one or three steady states in an exothermal first order reaction in CSTR and, besides, have considered a problem of stability of steady states.

Vaganov, Samoilenko and Abramov [5] have analyzed the stability of steady states. They have determined also the main types of phase portraits. It was shown that even in such simple process as first order reaction an extremely diverse picture arises: there are possible at least 35 different phase portraits.

Already in the first Zeldovich's works the fundamental analogy between exothermal processes in CSTR and phenomena of ignition and combustion was observed. Later Abramov and Merzhanov have analyzed in detail the conditions of thermal ignition in reactors of a similar kind [6].

In overwhelming number of the works dealing with exothermal reactions in CSTR, the simplest kinetic law, i.e. first order equation was used. At the same time a non-solved problem remains: how will be the behavior of such reactors in case of more complex kinetic law. Here we consider autocatalytic reactions. Note, that the conditions of thermal ignition in CSTR for a case of autocatalytic reactions have been reviewed earlier [7].

Further we follow the methodologies used in cited above papers (see, for example, [5]).

Let's accept following designations: α (cal/cm²·s·deg) – heat-transfer coefficient; S (cm²) – surface area of reactor; V (cm³) – volume of reaction mixture in reactor; T (K) – temperature of reaction system in reactor; T_0 (K) – ambient temperature; T_{input} (K) – temperature of reaction mixture entered into reactor; T_{initial} (K) – initial temperature in reactor; Q (cal/cm³) – heat effect of reaction; ρ (g/cm³) – density of reaction system (on input and output supposed identical); c_p (cal/g·deg) – thermal capacity of reaction system (supposed a constant); q (cm³/s) – volume rate of a mixture flow at input and at output; η – conversion (dimensionless); η_0 – conversion in reaction system on input into reactor; t (s) – time; E (kcal/mol) – activation energy; k_0 (s⁻¹) – preexponential factor.

The system behavior in reactor, in which autocatalytic reaction proceeds, is described by the following equations:

$$c_p \rho (dT/dt) = k_0 Q \exp(-E/RT) (1 - \eta) (\eta_0 + \eta) - \alpha (S/V) (T - T_0) - c_p \rho (q/V) (T - T_{\text{input}}) \quad (1)$$

$$d\eta/dt = k_0 \exp(-E/RT) (1 - \eta) (\eta_0 + \eta) - (q/V) \eta \quad (2)$$

The equation (1) is an equation of heat balance. Its left-hand part is the rate of heat accumulation in a reaction system, first member of the right-hand part is the rate of heat accumulation due to exothermal autocatalytic reaction, second member is the rate of heat loss through reactor walls into environment, and third member is the rate of heat consumption for heating of an influent. The equation (2) is an equation of chemical kinetics. Its left-hand part represents the rate of change of reactant concentration in the reactor, first member of the right-hand part is the rate of concentration change as a result of a chemical reaction, and second member is a rate of reactant concentration change in the reactor due to output of a flow from reactor.

Initial conditions: $t = 0$, $\eta = \eta_{\text{input}}$, $T = T_{\text{initial}}$.

Let's introduce some new designations. Let $T^* = (\alpha S T_0 + c_p \rho q T_{\text{input}}) / (\alpha S + c_p \rho q)$. The value T^* has the sense of scale temperature, as at $q = 0$ we have $T^* = T_0$, and at $q \rightarrow \infty$ we have $T^* = T_{\text{input}}$. Let's accept the following notation for two last members in an equation (1): $(\alpha S/V) + c_p \rho q/V = (\alpha S/V)^*$.

Then after simple transformations the equation (1) will take the form:

$c_p \rho (dT/dt) = k_0 Q \exp(-E/RT) \cdot (1 - \eta) (\eta_0 + \eta) - (\alpha S/V)^* (T - T^*)$, that is formally equivalent to Semenov equation for thermal explosion [8].

Let's proceed now to dimensionless variables. Let $\tau = t k_0 \exp(-E/RT^*)$, $\theta = E(T - T^*)/RT^{*2}$, $\gamma = (RT^*/E)(p c_p T^*/Q)$, $\beta = RT^*/E$, $Da = (V/q) k_0 \exp(-E/RT^*)$, $Se = (E/RT^{*2}) [QV/(p c_p q + \alpha S)] k_0 \exp(-E/RT^*)$. Here τ is dimensionless time, θ is dimensionless temperature. Da is Damköhler parameter,

describing a dimensionless mean time of the presence of a matter in reactor, Se is dimensionless parameter being analogue of Semenov parameter in theory of thermal explosion.

With introduced notations, the equations (1) and (2) can be written to a dimensionless kind:

$$\chi d\theta/d\tau = (1 - \eta)(\eta_0 + \eta)\exp[\theta/(1+\beta\theta)] - \theta/Se \equiv F(\eta, \theta) \quad (3)$$

$$d\eta/d\tau = (1 - \eta)(\eta_0 + \eta)\exp[\theta/(1+\beta\theta)] - \eta/Da \equiv G(\eta, \theta) \quad (4)$$

Initial conditions: $\tau = 0$, $\eta = \eta_{\text{input}}$, $\theta = E(T_{\text{initial}} - T^*)/RT^2$.

Steady states of the system under consideration can be obtained by equating derivatives in the above-stated equations to zero. In outcome we have:

$$(1 - \eta)(\eta_0 + \eta)\exp(\theta/(1+\beta\theta)) - \theta/Se = 0 \quad (5)$$

$$(1 - \eta)(\eta_0 + \eta)\exp(\theta/(1+\beta\theta)) - \eta/Da = 0 \quad (6)$$

Term by term subtraction of (5) from (6) results in:

$$\theta = \frac{Se}{Da} \eta \quad (7)$$

In the system of three equations (5) – (7) only two are linearly independent, and we can use any pair of these equations.

As the equations (5) and (6) correspond to constant (zero) values of derivatives, graphically they are described by the respective isoclinic lines. The kind of these isoclinic lines in co-ordinates $\eta - \theta$ depends on parameters of the process, first of all, on the Se value. The isoclinic line depicted by the equation (5) corresponds to a steady state on temperature. Hereinafter we shall call it as thermal isoclinic line.

To obtain a full picture of the types of thermal isoclinic line, we shall address to the equation (5). It is quadratic equation relative to η . Its solution is:

$$\eta_{1,2} = \frac{1 - \eta_0}{2} \pm \sqrt{\frac{(1 + \eta_0)^2}{4} - \frac{\theta}{Se} e^{-\frac{\theta}{1+\beta\theta}}} \quad (8)$$

Let's introduce following notations:

$$f(\theta) = \theta e^{-\frac{\theta}{1+\beta\theta}}$$

$$g(\eta) = Se \frac{(1 + \eta_0)^2}{4}$$

It is evident that the sign of the subduplicate in (8) (and, therefore, the number of solutions of this equation) depends on the ratio between $f(\theta)$ and $g(\eta)$. It is suitable to observe the indicated ratio graphically showing the functions $f(\theta)$ and $g(\eta)$ with θ as abscissa. Then $f(\theta)$ will be described by curve 1 on Fig. 1 and $g(\eta)$, as it does not depend from θ , will be represented by horizontal lines 2 – 6. On Fig. 1 such relations for the case $\beta = 0.2$ are shown, and the values $g(\eta)$ for horizontal lines (bottom-up) are equal accordingly 0.3; 0.35; 0.4; 0.48 and 0.5.

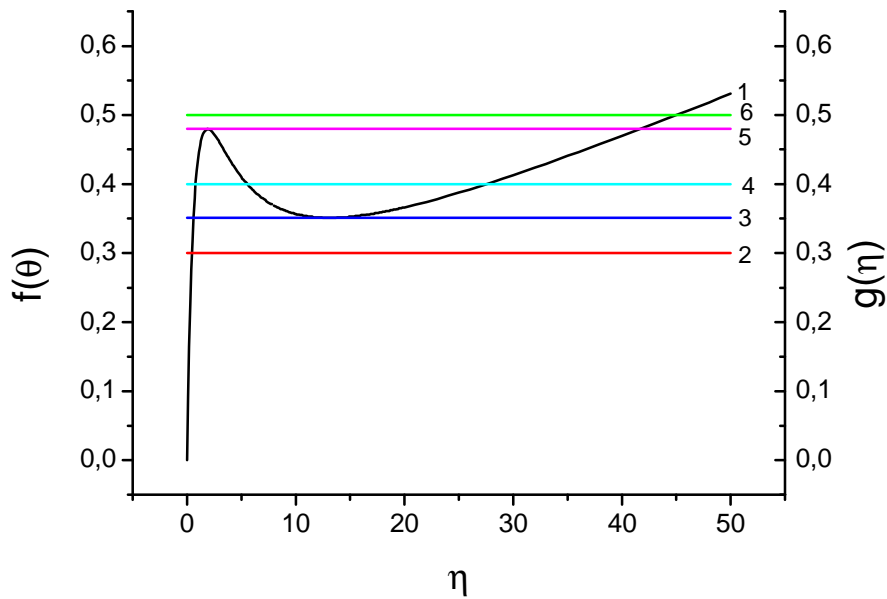


Figure 1. Functions $f(\theta)$ (1) and $g(\theta)$ (2 – 6) at $\eta_0 = 0.01$, $\beta = 0.2$. For 2 – 6 Se values are equal 1.176; 1.377; 1.568; 1.880 and 1.961 consequently.

We see, that, depending on the ratio between $f(\theta)$ and $g(\eta)$, five different situations are possible (for horizontal lines bottom-up): one interception with the left-hand branch, one interception and one contact, three interceptions, one contact and one interception with a right-hand branch, one interception with a right-hand branch.

Let's look now, as these different situations will be exhibited on a phase plane in co-ordinates $\eta - \theta$. For this purpose, supposing $\eta_0 = 0.01$, we select values Se so that the function $g(\eta)$ being equal to mentioned above values 0.3, 0.35, 0.4, 0.48 and 0.5. The corresponding Se values are equal 1.176; 1.377; 1.568; 1.880 and 1.961 respectively.

For the solution of this problem we shall use the equation (5).

The case $Se = 1.176$. The thermal isoclinic line for this case is shown on Fig. 2. It represents a curve with maximum.

The case $Se = 1.377$. The thermal isoclinic line is shown on Fig. 3. It represents a curve and a point arranged from above.

The case $Se = 1.568$. The thermal isoclinic line presented on Fig. 4 consists of two parts, lower branch and isolated upper branch, which is isola. Between them a “forbidden region” exists. This region covers the temperature range, which is inaccessible in steady conditions at selected values of parameters irrespective of the initial conditions. Such nature of isoclinic line has merely kinetic nature and is a consequence of non-linear kinetics. “Forbidden region” exists because we decided a quadratic equation (5), not having the solutions at negative value of the subduplicate in (8). Nothing similar is observed in simple first order kinetics [5].

The case $Se = 1.88$. The thermal isoclinic line is shown on Fig. 5. Here there is a coalescence of the lower branch of isoclinic line with isola. The coalescence occurs, when the contact of a curve 1 and straight line 5 in Fig. 1 takes place. For this case we have [7]:

$$Se = \frac{4\theta_s}{(1+\eta_0)^2} \cdot e^{-\frac{\theta_s}{1+\beta\theta_s}}, \text{ where } \theta_s = \frac{1-2\beta+\sqrt{1-4\beta}}{2\beta^2}$$

The case $Se = 1.961$. The thermal isoclinic line is shown on Fig. 6.

The reviewed examples cover all diversity of kinds of a thermal isoclinic line, which can arise in the studied autocatalytic reaction. The Figs. 2 – 6 demonstrate, as the evolution of isoclinic line proceeds at Se value increasing. At small Se values the isoclinic line represents a curve with a maximum (Fig. 2). At subsequent Se value increasing some value is reached, when isola arises (Fig. 3). It exists in some range of Se values (Fig. 4), and then disappears at some Se values, joining with the lower branch of isoclinic line (Fig. 5). In the course of further increasing Se values, the branches of isoclinic line diverge to the right and to the left, and isoclinic line takes the form shown on Fig. 6. It is interesting to note, that the right-hand branch of isoclinic line presented on Fig. 6 rather resembles an isoclinic line for the case of a simple first order reaction [5]. In other words, the transition from a simple kinetics to an autocatalytic reaction as though “adds” the left-hand branch of isoclinic line on Fig. 6. As a whole it is possible to draw a conclusion that the transition from a simple kinetics to complex one (on an example of autocatalysis) results in a large diversification of kinds of thermal isoclinic line.

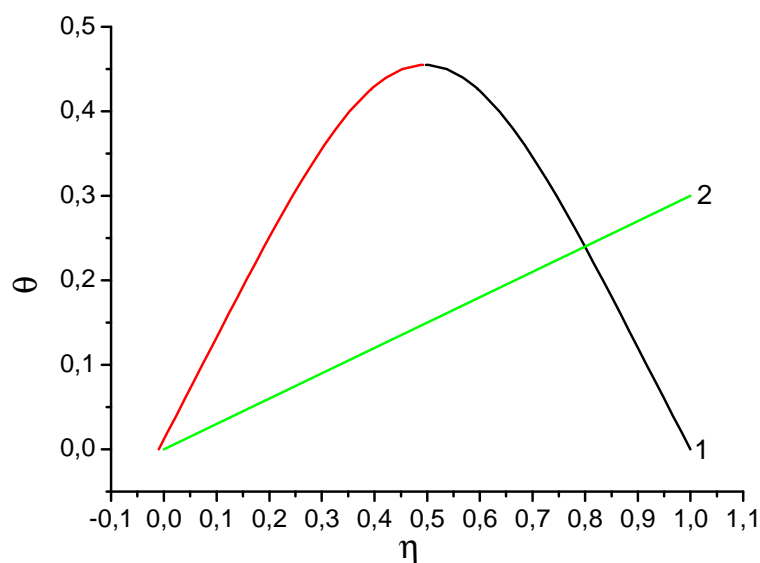


Figure 2. Dependences (7) and (8) at $\eta_0 = 0.01$, $\beta = 0.2$, $Se = 1.176$.

The steady states of investigated system can be found by solution of a system of equations (5) and (7). The thermal isoclinic lines corresponding to equation (5) are shown in Fig. 2 - 6, and equation (7) is presented with straight lines coming from the point of origin. As an example such straight lines are

shown on Fig. 2 and 6. Comparing the indicated straight lines with thermal isoclinic lines on Fig. 2 - 6, it is easy to see that the considered system can have either one, or three steady states.

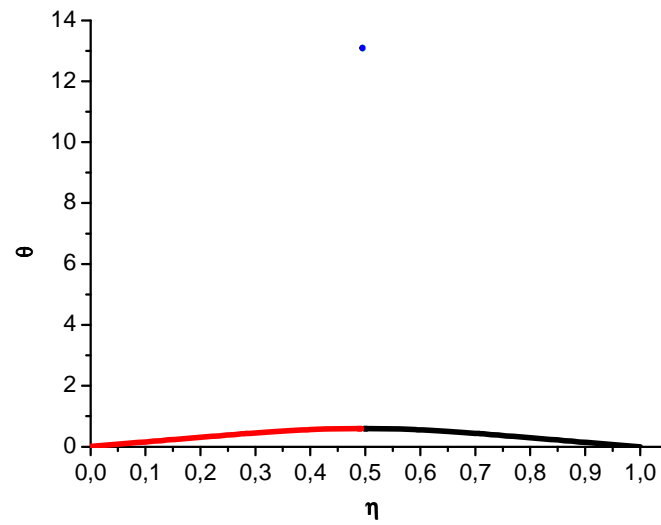


Figure 3. Dependences (7) and (8) at $\eta_0 = 0.01$, $\beta = 0.2$, $Se = 1.377$.

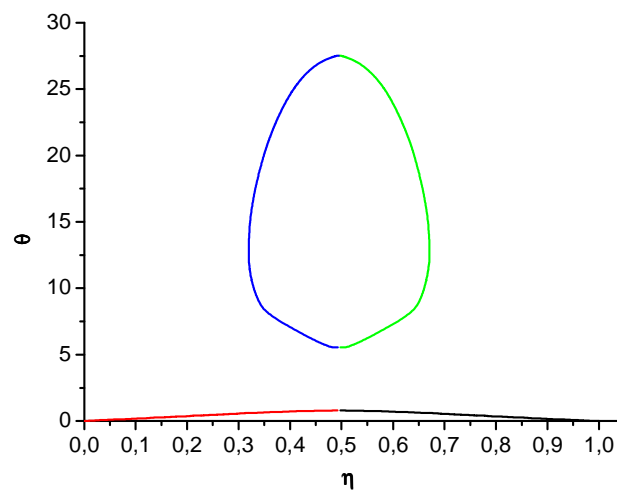


Figure 4. Dependences (7) and (8) at $\eta_0 = 0.01$, $\beta = 0.2$, $Se = 1.568$.

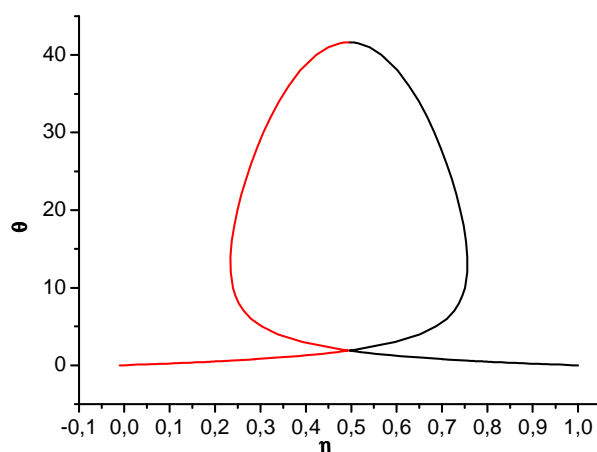


Figure 5. Dependences (7) and (8) at $\eta_0 = 0.01$, $\beta = 0.2$, $Se = 1.880$.

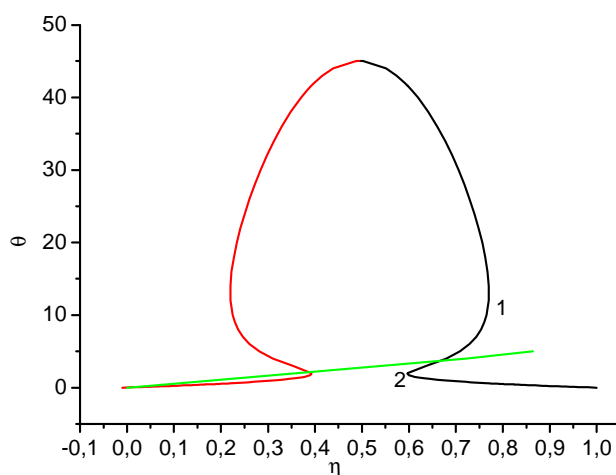


Figure 6. Dependences (7) and (8) at $\eta_0 = 0.01$, $\beta = 0.2$, $Se = 1.961$.

The main problem in research of processes proceeding in open systems is the problem of stability of steady states. The approaches to the stability analysis of dynamic systems are well-known [1, 9]. In frame of these approaches, it is possible to determine the types of stability of steady states at different values of parameters. On Fig. 7, on the basis of the analysis of equations (5) and (7) in co-ordinates $Se - Da$, the areas of existence of one (top of a figure) and three (bottom) steady states are divided. On Fig. 8 the result of analysis resulting in determination of the type of steady state stability is shown. As it was just marked, the bottom of a figure corresponds to the area of three steady states; the stability region only of one of them (high temperature) is here presented. The similar analysis has shown, that the low temperature steady state is stable (stability of the “stable node” type), and the steady state corresponding to medium temperatures, is absolutely unstable (instability such as “saddle”).

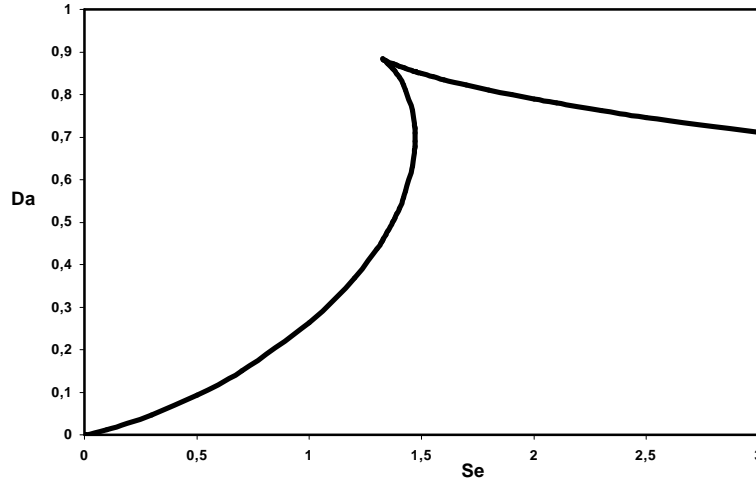


Figure 7. The regions of steady state stability at $\beta = 0.02$, $\gamma = 0.02$, $\eta_0 = 0.01$.

At the research of stability of steady states, one of main problems is that of the mechanism of stability change. From equations (3) and (5) it follows, that parameter γ does not influence on the position of steady state. On the other hand, it affects on the type of its stability undoubtedly. Let's consider a part of right-hand branch of a thermal isoclinic line of Fig. 6 between points 1 and 2. These points correspond to extremes on the dependence of η on θ for a right-hand branch. The given part is selected because at very small value of γ (a limit at $\gamma \rightarrow 0$), i.e. at very large heat effects of reaction, a limit cycle takes place, i.e. the system is in unstable oscillatory state (for reaction of first order this problem is reviewed in [5]). Therefore hereinafter we shall call the branch between points 1 and 2 as unstable branch.

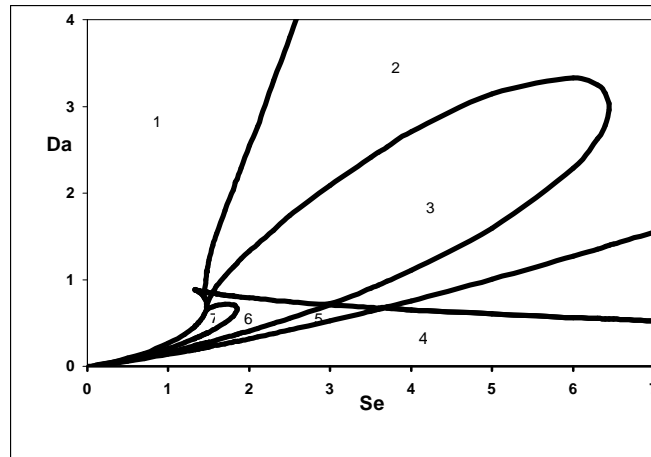


Figure 8. The regions of steady state stability at $\beta = 0.02$, $\gamma = 0.02$, $\eta_0 = 0.01$.

1 – stable node, 2 – stable focus, 3 – unstable focus, 4 – stable node, 5 – stable focus, 6 – unstable focus, 7 – unstable node.

On Fig. 6 straight line coming from point of origin, intercepts a thermal isoclinic line in three points, i.e. for a system three steady states are possible. At that two interceptions take place on the left-hand branch and only one – on right hand one. There is a problem: whether always it so? Whether there is a situation, when all three interceptions take place on right-hand branch? Let's show, that it is impossible.

In point of intersections of thermal isoclinic line with straight line coming from point of origin, the equations (7) and (8) are simultaneously valid. As we are interested with the right-hand branch of thermal isoclinic line only, we shall take from the equation (8) only a solution signed plus. Placing (7) into (8) and having entered notation $\sigma = Se/Da$, after simple transformations we receive

$$e^{\frac{\sigma\eta}{1+\beta\sigma\eta}} = \frac{Da}{\eta}(\eta + \eta_0)(1 - \eta) \quad (9)$$

The right member of this equation as function of η is described by monotonically decreasing curve without inflection points. The left-hand part of equation at positive values of parameters is also described by monotonically decreasing curve without inflection points. Therefore, for these curves three and more interception is impossible. Two interceptions are also impossible, because in this case reactor would have an even number of steady states that is invalid. This implies that at positive values of parameters the equation (9) can have not more than one solution, quod erat demonstrandum. Thus, at the given values of parameters on unstable branch of thermal isoclinic line the only unstable steady state and the only oscillatory regime are possible.

We already noted that at very small values of γ a limit cycle takes place. If γ is increased, the limit cycle step-by-step changes, and at some value $\gamma = \gamma_0$ it depletes. The value of γ_0 can be found from the relationship [5] $\partial F/\partial \theta + \gamma_0 \partial G/\partial \eta = 0$.

Two mechanisms of limit cycle decay, smooth and rigid, are possible [10]. In the first case increasing the value of γ is accompanied by monotonic decreasing the oscillation amplitude. Finally, at $\gamma = \gamma_0$ the amplitude becomes equal to zero, i.e. the oscillations cease and limit cycle contracts into the point. In the second case at $\gamma = \gamma_0$ steady state becomes stable, generating an unstable limit cycle. At further growth of γ this cycle joins with a stable limit cycle, forming semi-stable limit cycle, which then depletes.

It is possible to judge on character of stability variation by value of the third focal factor [9, 10]. If it is negative, there is a smooth decay of limit cycle, and if it is positive, rigid decay takes place.

We calculated the third focal factor using a methodology described in [11] (we don't show the expression for the third focal factor in view of its inconvenience). The results presented in Fig. 9 show that both types of stability change are possible. At smaller values of θ the mechanism of smooth decay of a limit cycle will be realized, and at the larger values of θ rigid decay takes place. Note, that the kind of dependence presented in Fig. 9, in many respects is determined by β value. Therefore at other β the character of this dependence can be different.

In conclusion it is useful to consider a special case of adiabatic reactor, when the heat loss from reactor is absent. In this case $\tau = 0$, and using given above expressions for Se , Da and γ in dimensional quantities, we obtain

$$Da/Se = \gamma(10)$$

Subtracting term by term (3) and (4), we shall receive

$$\gamma \frac{d\theta}{d\tau} = \frac{d\eta}{d\tau} + \frac{\eta}{Da} - \frac{\theta}{Se}$$

or in other kind

$$\frac{d(\gamma\theta - \eta)}{d\tau} = -\frac{1}{Da}(\gamma\theta - \eta)$$

Integration to an arbitrary constant gives

$$\gamma\theta - \eta = e^{-\frac{\tau}{Da}}$$

This means that at tendency of τ to infinity the following relation takes place:

$$\theta \rightarrow \frac{1}{\gamma}\eta$$

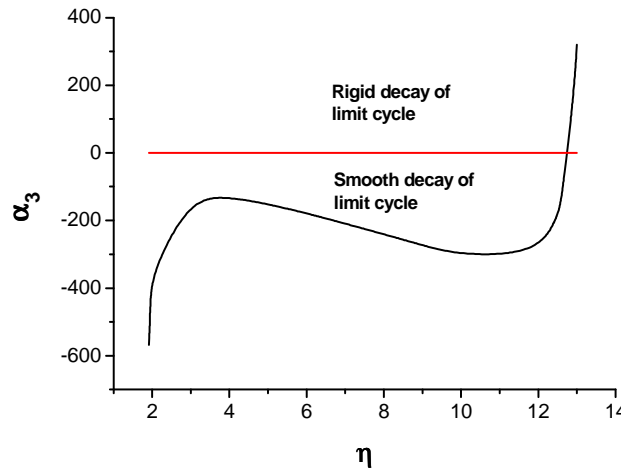


Figure 9. Dependence of third focal factor from θ at $\eta_0 = 0.01$, $\beta = 0.2$, $Se = 2$.

Thus, the phase trajectory approaches at a straight line depicted by equation (7), not intercepting it (we remind, that the case is considered, when the equation (10) is fulfilled). It is evident, that at such behavior of phase trajectory the oscillation regime is impossible, and, therefore, adiabatic reactor is always steady. Let's remark, that this conclusion is obtained without use of a kind of the reaction kinetic law, so that it is correct for any process following to mass action law. It, in turn, means that origin of instability in CSTR is largely connected with the process of a heat loss.

The work was carried out under financial support of the Russian Foundation of Basic Researches, grant № 06-03-32053.

References

- [1] Frank-Kamenetskii D. A. Diffusion and heat transfer in chemical kinetics. Moscow, Nauka, 1987. 492 p. (in Russian).
- [2] Zeldovich Ya. B. To the theory of thermal intensity. Accomplishment of exothermal reaction in stream. I. // Zhurnal tekhnicheskoi fiziki, 1941, vol. 11, N 6, p. 493 – 500 (in Russian).
- [3] Zeldovich Ya. B., Zysin Yu. A. To the theory of thermal intensity. Accomplishment of exothermal reaction in stream. II. Taking into account of heat release during reaction. // Zhurnal tekhnicheskoi fiziki, 1941, vol. 11, N 6, p. 501 – 508 (in Russian).
- [4] Salnikov I. E., Volter B. V. Investigation of the modes of a flow chemical reactor under accomplishment of exothermal unimolecular reaction. // Doklady Akademii nauk SSSR, 1963, vol. 152, № 1, p. 171 – 174 (in Russian).
- [5] Vaganov D. A., Samoilenko N. G., Abramov V. G. Periodic regimes of continuous stirred tank reactors. // Chem. Eng. Sci., 1978, vol. 33, N 8, p. 1133 – 1140.
- [6] Abramov V. G., Merzhanov A. G. Thermal explosion in homogeneous flow reactors. // Fizika goreniya i vzryva, 1968, vol. 4, № 4, p. 548 – 556 (in Russian).
- [7] Abramov V. G., Samoilenko N. G., Solomonov V. B. Critical condition of thermal explosion of autocatalytic reaction in continuous stirred tank reactors. // Doklady Akademii nauk SSSR, 1977, vol. 237, № 3, p. 623 – 626.
- [8] Semenov N. N. Some problems of chemical kinetics and reactivity. Moscow: Izdatelstvo Akademii nauk SSSR, 1958. 686 p. (in Russian).
- [9] Andronov A. A., Vitt A. A., Khaikin C. E. The theory of oscillations. Moscow: Nauka, 1981. 568 p. (in Russian).
- [10] Bautin N. N. The behavior of dynamic systems near the boundaries of stability region. Leningrad: Gosudarstvennoye izdatelstvo tekhniko-teoreticheskoi literatury, 1949. 164 p.
- [11] Zhabotinsky A. M. Concentrational self-oscillations. Moscow: Nauka, 1974. 179 p. (in Russian).

**ՀԱՅԱՍՏԱՆԻ ՀԱՆՐԱՊԵՏՈՒԹՅԱՆ ԳԻՏՈՒԹՅՈՒՆՆԵՐԻ
ԱԶԳԱՅԻՆ ԱԿԱԴԵՄԻԱ
НАЦИОНАЛЬНАЯ АКАДЕМИЯ НАУК РЕСПУБЛИКИ
АРМЕНИЯ**

Հայաստանի քիմիական հանդես **60, №2, 2007** Химический журнал Армении

**SYNTHESIS AND INVESTIGATION OF YFeTiO₅ - YFeSnO₅ MULTICOMPONENT
SYSTEM**

R. H. GRIGORYAN

Institute of structural macrokinetics and problems of Materials Science

E-mail: rud@ism.ac.ru

It was firstly investigated YFeTiO₅ - YFeSnO₅ multi component system by x -rays methods.

Samples of YFeTi_{1-x}Sn_xO₅ ($0 \leq x \leq 1,0$, $\Delta x = 0,1$) were synthesized from oxides of appropriate metals in hydrogen - oxygen flames low temperature plasma [1] and classical ceramic technology. All synthesized samples were roasted at $T = 1170\text{K}$ during four hours. The X-ray diffractions of samples with equal composition synthesized by different ways are identical. Comparison powder diffractograms of samples have shown structural uniformity of system YFeTiO₅ - YFeSnO₅, representing continuous number of firm solutions with which reach on all concentration intervals. The formed firm solutions crystallize in rhombic system of pseudo-brookite structure. The parameters of an elementary cell are determined. The results were provided in table 1.

Table 1. The parameters of an elementary cells of YFeTi _{1-x} Sn _x O ₅ hard solutions					
Compound	a, Å	b, Å	c, Å	d, g/sm ³	
	± 0,005			x-ray	Picn..
YFeTiO ₅	10,746	9,922	3,849	4,412	4,35
YFeTi _{0,9} Sn _{0,1} O ₅	10,746	9,922	3,852	4,454	4,41
YFeTi _{0,9} Sn _{0,1} O ₅	10,746	9,922	3,852	4,454	4,41
YFeTi _{0,7} Sn _{0,3} O ₅	10,744	9,923	3,858	4,660	4,58
YFeTi _{0,6} Sn _{0,4} O ₅	10,744	9,923	3,863	4,771	4,72
YFeTi _{0,5} Sn _{0,5} O ₅	10,743	9,923	3,865	4,905	4,87
YFeTi _{0,4} Sn _{0,6} O ₅	10,744	9,923	3,866	5,004	4,91
YFeTi _{0,3} Sn _{0,7} O ₅	10,743	9,923	3,868	5,113	5,02
YFeTi _{0,2} Sn _{0,8} O ₅	10,742	9,924	3,871	5,189	5,13
YFeTi _{0,1} Sn _{0,9} O ₅	10,742	9,925	3,874	5,333	5,30
YFeSnO ₅	10,742	9,925	3,878	5,516	5,42

The replacement of titanium atoms on atoms of tin in connection YFeTiO_5 does not result in essential changes of a crystal lattice. The parameters of an elementary cell vary insignificantly and are in rectilinear dependence on structure. Density of samples most considerably vary, which meanings too have rectilinear dependence on composition (figure 1). Some increase of the sizes of an elementary cell at transition from YFeTiO_5 up to YFeSnO_5 , is conditioned different ionic radius tin and titanium (effective ionic radius of Sn^{4+} is 0,690 Å and effective ionic radius of Ti^{4+} is 0,605 Å [2]).

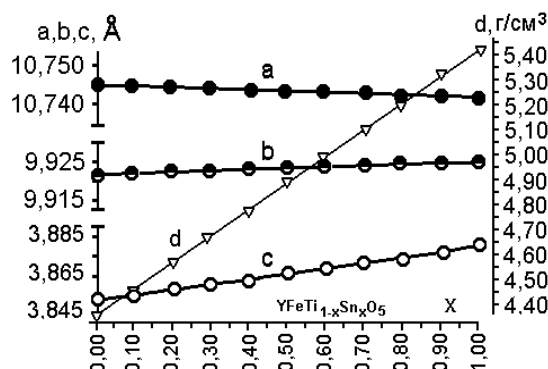


Figure 1. The dependency of parameters of elementary cells and density of hard solutions $\text{YFeTi}_{1-x}\text{Sn}_x\text{O}_5$ from tin contents.

The received results give the basis to assume similar cation distribution in firm solutions of structures YFeTiO_5 - YFeSnO_5 with those in pseudo-brookite (Fe_2TiO_5) structure [3]. The atoms of tin, replacing atoms titanium in octahedral interstice, occupy the same positions. Hence, in the formed firm solutions of structures YFeTiO_5 - YFeSnO_5 atoms titanium and tin have identical octahedral coordination, while atoms yttrium, as well as the not replaced atoms of iron have characteristic for pseudo-brookite "unusual coordination" [3], which can be considered or as deformed octahedron, or as deformed tetrahedron.

Table 2. The conductivity (σ), dielectric permeability (ϵ) and widths of the forbidden zone (E) of hard solutions $\text{YFeTi}_{1-x}\text{Sn}_x\text{O}_5$

	$\sigma, \text{OM}^{-1} \cdot \text{cm}^{-1}$	ϵ	ΔE	P	α
YFeTiO_5	$3,969 \cdot 10^{-8}$	26	0,875	55,177	2,188
$\text{YFeTi}_{0,9}\text{Sn}_{0,1}\text{O}_5$	$3,963 \cdot 10^{-8}$	27	0,885	58,614	2,325
$\text{YFeTi}_{0,8}\text{Sn}_{0,2}\text{O}_5$	$3,062 \cdot 10^{-8}$	27	0,892	60,001	2,380
$\text{YFeTi}_{0,7}\text{Sn}_{0,3}\text{O}_5$	$2,100 \cdot 10^{-8}$	29	0,915	58,559	2,322
$\text{YFeTi}_{0,6}\text{Sn}_{0,4}\text{O}_5$	$1,503 \cdot 10^{-8}$	30	0,940	58,465	2,319
$\text{YFeTi}_{0,5}\text{Sn}_{0,5}\text{O}_5$	$7,261 \cdot 10^{-9}$	31	0,975	58,091	2,304
$\text{YFeTi}_{0,4}\text{Sn}_{0,6}\text{O}_5$	$3,622 \cdot 10^{-9}$	32	0,985	58,251	2,310
$\text{YFeTi}_{0,3}\text{Sn}_{0,7}\text{O}_5$	$1,791 \cdot 10^{-9}$	33	1,005	58,169	2,307
$\text{YFeTi}_{0,2}\text{Sn}_{0,8}\text{O}_5$	$9,204 \cdot 10^{-9}$	35	1,040	58,448	2,318
$\text{YFeTi}_{0,1}\text{Sn}_{0,9}\text{O}_5$	$4,887 \cdot 10^{-10}$	35	1,045	58,093	3,304
YFeSnO_5	$2,23 \cdot 10^{-10}$	35	1,074	57,215	2,269

The research of physical properties of the synthesized firm solutions (table 2.) shows, that all of them are dielectric, with semi-conductor character electro conductivity replacement of atoms титана by atoms tin results to natural (practically rectilinear) change of these parameters. The complete replacement $Ti \rightarrow Sn$ results in decrease specific electro conductivity of samples up to two orders, as result of increase of energy of activation (width of the forbidden zone).

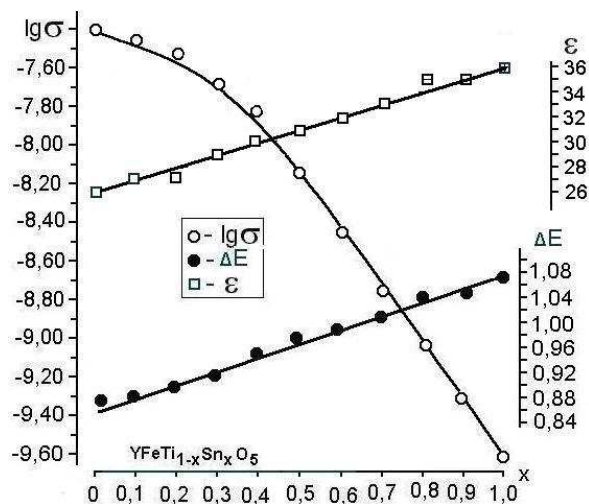


Figure 2. Dependency of conductivity (σ), dielectric permeability (ϵ and widths of the forbidden zone (E) of hard solutions $YFeTi_{1-x}Sn_xO_5$ from tin contents.

The dependence of the logarithm specific electro conductivity from structure rejects from straightforwardness a little. The replacement up to 40 % titanium results less than three-multiple reduction specific electro conductivity (from $3,969 \cdot 10^{-8}$ up to $1,503 \cdot 10^{-8} \text{ om}^{-1} \cdot \text{cm}^{-1}$). The further introduction of tin results in its faster decrease. In this area of concentration the diagram the dependence of the logarithm specific electro conductivity from structure has rectilinear character (figure 2).

References

- [1] Grigoryan R.A., Grigoryan L.A., Babayan G.G. Synthesis of $ZnFe_2O_4 - Zn_2ZrO_4$ Solid Solutions. Inorganic Materials, 2001, V. 37, No. 3, pp. 298 -301
- [2] Shanon R.D. Revised Effective Ionic Radii and Systematic Studies of Interatomic Distances in Halides and Chalcogenides. Acta Crystallogr, 1976, V. A32, P. 751 - 767.
- [3] Уэллс А. Структурная неорганическая химия. перевод с англ. под ред. М.А. Порай-Кошиц. М.: Мир, 1987, Т.2, С.324.

**ՀԱՅԱՍՏԱՆԻ ՀԱՆՐԱՊԵՏՈՒԹՅԱՆ ԳԻՏՈՒԹՅՈՒՆՆԵՐԻ
ԱԶԳԱՅԻՆ ԱԿԱԴԵՄԻԱ
НАЦИОНАЛЬНАЯ АКАДЕМИЯ НАУК РЕСПУБЛИКИ
АРМЕНИЯ**

Հայաստանի քիմիական հանդես **60, №2, 2007** Химический журнал Армении

**THE SYNTHESSES AND INVESTIGATION OF THE SYSTEM
CaTiSiO₅ - CaSnSiO₅**

R. A. GRIGORYAN^{a*}, L. A. GRIGORYAN^b

^a Institute of Structural Macro kinetics and Materials Science RAS

^b Institute of Problem of Chemical Physics RAS

*rud@ism.ac.ru

It was installed that at ≥ 700 °C the system CaTiSiO₅ - CaSnSiO₅ is single-phase [1]. In the persisting message are brought results x-rays, UR studies of the multi-components system CaTiSiO₅ - CaSnSiO₅ at 1173 K and electro physical characteristics of formed hard solutions. Samples of CaTi_{1-x}Sn_xSiO₅ ($0 \leq x \leq 1,0$; $\Delta x = 0,05$) were synthesized from oxides of appropriate metals in hydrogen - oxygen flames low temperature plasma [2] and classical ceramic technology.

The X-ray data identification, which was realized with use parameters, provided in work [3], shows, the CaTiSiO₅ ($x = 0$) crystallizes in monoclinic structure. The Ca²⁺ Ions are located inwardly polyhedral emptiness formed by seven oxygen atoms, formed by oxygen atoms of the octahedral TiO₆ and tetrahedral SiO₄.

In structure of titanite crystallize as well as formed hard solutions composition CaTi_{1-x}Sn_xSiO₅. Partial or full change Ti⁴⁺ ion by Sn⁴⁺ ion in titanite lattice at the temperature 1173K does not bring phase conversions. Entering Sn⁴⁺ ions occupy the inwardly octahedral emptiness of oxygen packing, ear earlier occupied Ti⁴⁺ ions. The parameters of an elementary cell are determined. The results were provided in table 1.

Table 1. The parameters of an elementary cells of
CaTi_{1-x}Sn_xSiO₅ hard solutions

Состав	a	b	c	$\beta, ^\circ$
CaTiSiO ₅	7,061±0,004	8,710±0,005	6,568±0,005	113,86 ± 0,04
CaTi _{0,9} Sn _{0,1} SiO ₅	7,06± 0,01	8,72± 0,01	6,57± 0,01	113,84± 0,05
CaTi _{0,8} Sn _{0,2} SiO ₅	7,06± 0,01	8,74± 0,01	6,57± 0,01	113,83± 0,05
CaTi _{0,7} Sn _{0,3} SiO ₅	7,06±0,01	8,76± 0,01	6,57± 0,01	113,83± 0,05
CaTi _{0,6} Sn _{0,4} SiO ₅	7,07± 0,01	8,78± 0,01	6,57± 0,01	113,72± 0,05
CaTi _{0,5} Sn _{0,5} SiO ₅	7,07± 0,01	8,80± 0,01	6,57± 0,01	113,82± 0,05
CaTi _{0,4} Sn _{0,6} SiO ₅	7,07± 0,01	8,82±0,01	6,57± 0,01	113,82± 0,05
CaTi _{0,3} Sn _{0,7} SiO ₅	7,07±0,01	8,84±0,01	6,57± 0,01	113,80± 0,05
CaTi _{0,2} Sn _{0,8} SiO ₅	7,08± 0,01	8,85± 0,01	6,58± 0,01	113,78± 0,05
CaTi _{0,1} Sn _{0,9} SiO ₅	7,08±0,01	8,86± 0,01	6,58± 0,01	113,78± 0,05
CaSnSiO ₅	7,08 ± 0,01	8,88 ± 0,01	6,58 ± 0,01	113, 77± 0,05

Herewith exists the linear growing a parameter elementary cell, given big, than beside changed titanium ion, radius tin ion. The parameters of an elementary cell vary insignificantly and are in rectilinear dependence on structure (figure 1).

Using offered author [4, 5] acceptance to got by us parameter brings about conclusion that in synthesized us sample possible to expect that as a result silicon - a deficit in tetrahedral position are found ~ 4 % atoms of titanium. However result of the chemical analysis synthesized us sample [SAO - (28,8 0,3)%, TiO_2 - (40,2 0,3)%, SiO_2 - (30,6 0,4)%, $[\text{SAO}] : [\text{TiO}_2] : [\text{SiO}_2] = (0,977 \pm 0,007) : (1,000 \pm 0,004) : (0,985 \pm 0,004)$] point to not more than 1,5% silicon deficit.

There are bands of the absorption IR spectrum all synthesized composition with maximum at frequency $465 - 470 \text{ cm}^{-1}$ and $495 - 500 \text{ cm}^{-1}$, referred fluctuations of SiO_4 tetrahedron. The maximum in the field of $555 - 565 \text{ cm}^{-1}$ were referred to oscillatory absorption of SnO_6 and TiO_6 octahedrons. On measure of the increase the contents tin on UR spectrum appears clearly denominated maximum under 565 cm^{-1} , referred oscillatory absorption SnO_6 octahedron, which already under $x = 0,4$ masks weakly denominated maximum (565 cm^{-1}), belong to TiO_6 octahedron. they was determined factors of the refraction hard solutions

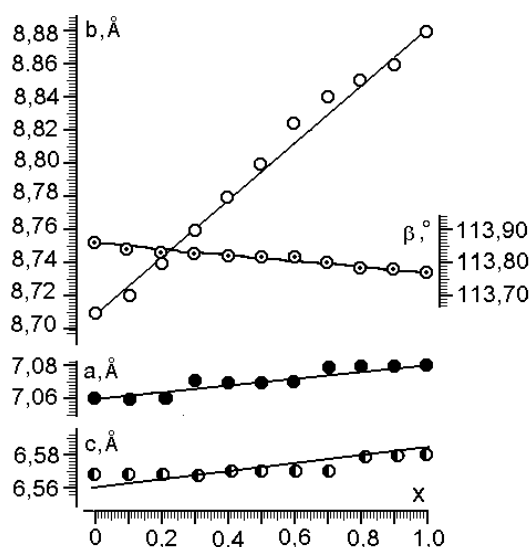


Figure 1. The dependency of parameters of elementary cells of $\text{CaTi}_{1-x}\text{Sn}_x\text{SiO}_5$ hard solutions

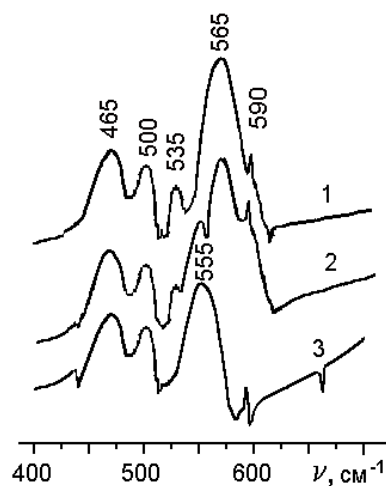


Figure 2. Infra-red spectra of (1) CaSnSiO_5 , (2) $\text{CaTi}_{0.7}\text{Sn}_{0.3}\text{SiO}_5$ and (3) CaTiSiO_5

Parameters of refractions of the hard solutions were installed. The results were provided in table

2.

Table 2. Parameters of refractions of the $\text{CaTi}_{1-x}\text{Sn}_x\text{SiO}_5$ hard solutions

Состав	n_g	n_p
CaTiSiO_5	$\sim 1,876$	
$\text{CaTi}_{0.8}\text{Sn}_{0.2}\text{SiO}_5$	1,862	$\sim 2,37$
$\text{CaTi}_{0.6}\text{Sn}_{0.4}\text{SiO}_5$	1,855	$\sim 2,37$
$\text{CaTi}_{0.4}\text{Sn}_{0.6}\text{SiO}_5$	1,862	$\sim 2,37$
$\text{CaTi}_{0.2}\text{Sn}_{0.8}\text{SiO}_5$	$\leq 1,890$	1,869
CaSnSiO_5	2,08	$\leq 2,68$

Table 2. Specific electro-conductivity (σ), dielectric permeability (ϵ), width of the forbidden zone (energy of activation ΔE), molar polarization (P) and molecular polarizability (α) of hard solutions $\text{CaTi}_{1-x}\text{Sn}_x\text{SiO}_5$

	$\sigma (\text{om}^{-1} \cdot \text{cm}^{-1})$	ϵ	$\Delta E (\text{ev})$	P	$\alpha \cdot 10^{23}$
CaTiSiO_5	$3,802 \cdot 10^{-12}$	39	0,973	51,62	2,0472
$\text{CaTi}_{0.9}\text{Sn}_{0.1}\text{SiO}_5$	$2,884 \cdot 10^{-12}$	43	0,970	52,09	2,0659
$\text{CaTi}_{0.8}\text{Sn}_{0.2}\text{SiO}_5$	$2,239 \cdot 10^{-12}$	43	0,983	52,27	2,073
$\text{CaTi}_{0.7}\text{Sn}_{0.3}\text{SiO}_5$	$1,905 \cdot 10^{-12}$	48	1,005	52,65	2,088
$\text{CaTi}_{0.6}\text{Sn}_{0.4}\text{SiO}_5$	$1,489 \cdot 10^{-12}$	53	1,028	53,30	2,114
$\text{CaTi}_{0.5}\text{Sn}_{0.5}\text{SiO}_5$	$1,318 \cdot 10^{-12}$	56	1,055	53,53	2,123
$\text{CaTi}_{0.4}\text{Sn}_{0.6}\text{SiO}_5$	$1,000 \cdot 10^{-12}$	62	1,073	54,00	2,142
$\text{CaTi}_{0.3}\text{Sn}_{0.7}\text{SiO}_5$	$7,244 \cdot 10^{-13}$	65	1,097	54,19	2,149
$\text{CaTi}_{0.2}\text{Sn}_{0.8}\text{SiO}_5$	$4,721 \cdot 10^{-13}$	70	1,118	54,30	2,154
$\text{CaTi}_{0.1}\text{Sn}_{0.9}\text{SiO}_5$	$2,884 \cdot 10^{-13}$	75	1,144	54,63	2,1667
CaSnSiO_5	$2,366 \cdot 10^{-13}$	79	1,165	54,91	2,178

All of synthesized solid solutions are dielectrics with semiconductor nature of conduction. Change ion Ti^{4+} on Sn^{4+} brings the small reduction the specific conductivity.

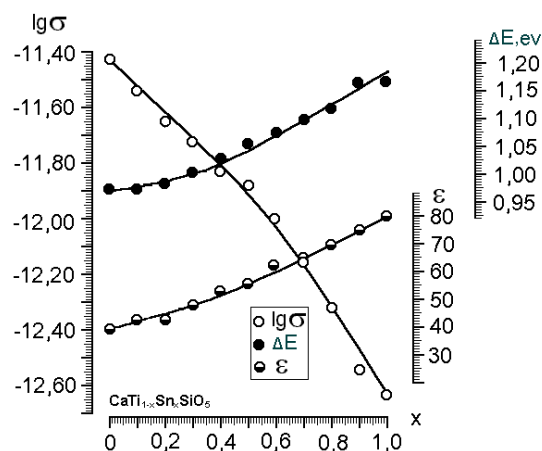


Figure 2. The specific conductivity, width of the forbidden zone (energy of activation) and dielectric permeability of the $\text{CaTi}_{1-x}\text{Sn}_x\text{SiO}_5$ hard solutions.

Under full change ion Ti^{4+} on ions Sn^{4+} conduction sample decreases on one order. Herewith exists small increase the width of the forbidden zone, dielectrical permeability and molecular polarization.

References

- [1] Takenouchi S., Hydrothermal Synthesis and Consideration of Genesis of Malayaite. Mineral. Deposita, 1971, V. 6, P.335 – 347
- [2] Grigoryan R.A., Grigoryan L.A., Babayan G.G. Synthesis of $\text{ZnFe}_2\text{O}_4 - \text{Zn}_2\text{ZrO}_4$ Solid Solutions. Inorganic Materials, 2001 V. 37, No. 3, p. 298.
- [3] Speer J.A., Gibbs G.V. The crystal structure of synthetic titanite, CaTiOSiO_4 , and the domain texture of natural titanite. Am. Mineral., 1976, V. 61, P. 238 - 247.
- [4] Hollanbaugh C.L., Rosenberg P.E. Substitution of Ti for Si in Titanite and New End-member Cell Dimension for Titanit. Am. Mineralogist, 1983, V. 68, № 1-2, P. 177 – 180.
- [5] Buison G. J. Etude Par rayon's X at Neutrons de la Isomorphe ATiTO_5 . Phys. Chem. Solids, 1970, V. 3, № 5, P. 1171 –1183.

**ՀԱՅԱՍՏԱՆԻ ՀԱՆՐԱՊԵՏՈՒԹՅԱՆ ԳԻՏՈՒԹՅՈՒՆՆԵՐԻ
ԱԶԳԱՅԻՆ ԱԿԱԴԵՄԻԱ
НАЦИОНАЛЬНАЯ АКАДЕМИЯ НАУК РЕСПУБЛИКИ
АРМЕНИЯ**

Հայաստանի քիմիական հանդես **60, №2, 2007** Химический журнал Армении

THE FOREST FIRES

A. M. GRISHIN

Tomsk State University
36, Lenin Street, 634050, Tomsk, Russia,
Phone (83822)529669, Fax (83822) 529895, e-mail: fire@mail.tsu.ru

The main founders of the theory of inflammation and combustion in Russia are considered to be academician N.N. Semenov, academician Ya. B. Zeldovich, professor O.M. Todes, the corresponding member of the Academy of Science of the USSR D.A. Franc-Kamenetsky. Further this theory was developed by a group of the specialists under leadership of academician Russian Academy of Sciences A.G. Merzhanov. Elaborate experimental investigations were carried out. Solid-phase mathematical model was developed. A number of one-dimensional and two-dimensional problems of the theory of inflammation and combustion of the solid rocket fuels was solved. Method of numerical solution of the critical conditions of ignition and boundary conditions of combustion spread was also developed and the methods of a numerical determination of the critical conditions of combustion and the limiting conditions of the combustion spread were also developed. Self-spreading high temperature synthesis has been opened [1 – 7].

In Tomsk State University since 1976 experimental and theoretical investigations of the forest fire initiation and spread have been carried out using the methods developed in the theory of combustion by academician A.G. Merzhanov with his co-workers. Semi-natural experiments of investigating the forest fires were carried out. General physical and mathematical model of the forest fires was developed. New methods of a numerical solution of the problems of the forest fire theory were developed.

Unlike Merzhanov's models mentioned above the forest was considered to be a multiphase blown through reactive medium.

As a result of physical experiments, analytical and numerical investigations a new determinate-probability model of the forest fire initiation was developed and boundary conditions of their spread were found out. On this basis new methods and facilities for localizing and suppressing forest fires were proposed.

The science of forest fires - forest pyrology has had a descriptive nature, and up to 1981 it has been founded on particular semiempiric models [8–10], within the limits of which it was impossible to predict limiting conditions for forest fire spread and their ecological impacts.

Based on the results of investigations carried out in the Tomsk State University, for twenty last years principal concepts of the mathematical theory of forest fires are formulated [11–14], general physical and mathematical models of forest fires are discussed [11–15], the structure of the fire front and limiting conditions for its spread are considered, methods of the direct and inverse problem are enumerated [16–19].

In conclusion, perspectives of a general mathematical model usage for solving problems of aerospace monitoring and prediction of ecological impacts of forest fires are discussed.

Key words: mathematical and physical model of forest fires, forest fuel, multiphase reactive medium, normal speed of spread, of pyrolysis of organic mass, mathematical and physical modeling.

Short review. Substantial review of papers published before 1989 on mathematical simulating problem of Forest Fires Spreading is presented in [20]. As an analysis shows, all the forest fire mathematical models can be divided into *four* groups:

1. Models for Prediction of forest fire propagation rate;
2. Models for prediction of forest fire contours;
3. Models for prediction of characteristics of flow, heat and mass transport in Fire's front and it's zone;
4. General mathematical models, in the frames of which there can be predicted all the characteristics (speed of spreading, forest fire's contours, temperature's field, species concentrations and speeds) in forest fire front and the zone [12–15].

Of the most interest there are two scientific investigations. They were not considered in [20] since they were completed only in 1997. In [21] are used in multi-phase reacting media together with a method of particles in pockets, which was developed by his scientific supervisor prof. F. Harlow. In this work physical and mathematical model of turbulent flows in forest fires is presented. On the basis of this model two-dimensional tasks of fuel bed forest fires were solved and there were obtained the fields of velocities, temperatures and species concentrations in vertical spatial cut x, z and known effect of acceleration of forest fire's propagation on the slope was numerically corroborated.

To main defects one can classify:

1. the lack of accurate physical model of forest fire as a set of reason-consequences connections, influencing wildfire behavior;
2. neglecting of the fact that physical and chemical processes in forest fire zone are finite;
3. a lot of various empirical constant temperatures of evaporation, ignition, oxidation of carbon, burning of hydrocarbons. Indeed they are not constant, but functions of time and coordinates;
4. neglecting of effect of air-elasticity of forest vegetation.

In [22] they use multi-phase reacting media theory and well known SIMPLE algorithm for numerical solving of convective transport equations of Patankar–Spalding. With use of mentioned above methods in [22] also a problem on propagation of wildfire in fuel bed, located on inclined plane, was resolved numerically.

As a defect of the model we may consider an assumption about spherical shape of forest vegetation elements, short number of species in gas phase, lack of substantial model of turbulence and neglecting of effect of air-elasticity of forest vegetation.

Below the most principle experimental and theoretical results are discussed, which were obtained when working for general mathematical models of the first [11, 12] and of the second generations [13–

15].

Besides, in the paper a determinate-probability model of predicting the forest fire danger is given [23].

Principal concepts of the mathematical theory of forest fires. Forest fires spread as a result of burning forest fuels. Forest fuels (FF) are called hydrocarbon fuels to which belong thin twigs, needles or leaves in the tree crowns and leaves fallen on the ground, as well as the ground cover (grass, bushes, moss, lichen), marshy plants, peat.

Burning forest fuels result in the formation of final combustion products - ash and undercombustion - combination of not burnt forest fuels of black and greyish-brown colours and which are enriched (processed) with carbon. A convection column - jet (flow) heated products of complete and non-complete FF burning (particles of black and ash in the form of smoke) arises over the forest fire spot. The greater the amount of heat released during burning, the higher is a convection column, since the main moving force of combustion products - buoyance force.

Forest fire is a phenomenon of uncontrolled multistage combustion in the open space on the forest covered area within which interrelated processes of convection and radiation energy transfer, heating, drying and pyrolysis of forest fuels take place, and burning of gaseous FF pyrolysis products burning down of condensed FF pyrolysis products occurs.

Forest fires are subdivided into surface, top crown, underground (fires in peat layers) and mass forest fires. During surface forest fires, fallen FF (fallen twigs, needles and needles), ground cover (grass, moss, lichen) and bushes burned.

During mass crown fires, FF mentioned above and FF in the forest cover which is the totality of tree crowns, burn simultaneously (see Fig. 1).



Fig. 1. Photograph of general crown fire front spreading through a forest strip of young pines. Width of strip — 3 m; length — 10 m; height of pine stand — 3.5 m; ground cover — layer of *Cladonia* lichen 0.1 m thick [12–14]

During crown fires, only FF in the forest cover burn.

Underground forest fires are the ones in peat layers when a spot of burning occurs in the peat bed layer.

Except the types of forest fires which are initiated by point sources of ignition (lighting camp fire not extinguished, cigarette-butt, etc.), on the underlying surface in exceptional cases (air nuclear explosion, “collision” catastrophe, etc.) as a result of a powerful radiation source in the atmosphere, FF ignition occurs on huge thousands of ha).

At any instant, on the territory covered with forest one may separate quite a large controlled volume of medium - a fire zone within which parameters of the medium state as a result of physico-chemical transformations, caused by forest fires, differ from undisturbed values defined by weather conditions and vegetation type figures 1a,b give a diagram of forest fire.

The greatest change of the medium state parameters takes place in a particular forest fire zone called a fire front which spreads at a speed on the area covered with forest. A forest fire front visually is observed in the form of a radiant (shining) forest fire spot zone.

The surface 1 (Fig. 2a,b) separating the front from non-burnt FF is called an external edge of forest fire front. Its projection into the underlying surface is called a forest fire contour. A fire contour length increases with the time increase for usual forest fires. When mass forest fires occur, a powerful convection column arises, and a strong “peculiar” (“own”) wind directed to the fire spot centre which prevents from flaming up a fire spot, and therefore the mass forest fire contour doesn’t almost change with the time increase. The external edge which spreads in the wind direction is called a leading edge, and opposite the wind - a trailing edge of the forest fire front.

The diagram of forest fire zone (see Figures 2 a, b) shows Γ - boundary of the forest fire zone, 1- forest fire contour (Fig. 2a) and forest fire front edge (Fig. 2b), 2 - inner edge of the fire front (Fig. 2 b) and projection of its edge onto the horizontal underlying surface (Fig. 2a); horizontal arrows (Fig. 2b) an undisturbed wind velocity for different heights, and vertical velocities w of blowing of gas and dispersion combustible products of burning from the fire front into the atmospheric ground layer.

Spreading speed of the forest fire is directed normal to the forest fire contour, therefore it is called a normal speed of spread and is defined according to the formula:

$$\omega_n = \lim_{\Delta t \rightarrow 0} \frac{\Delta n}{\Delta t} \quad (1)$$

where Δn is the distance between the two points of counter at moments t and $t+\Delta t$ calculated normal to the forest fire contour at the moment t .

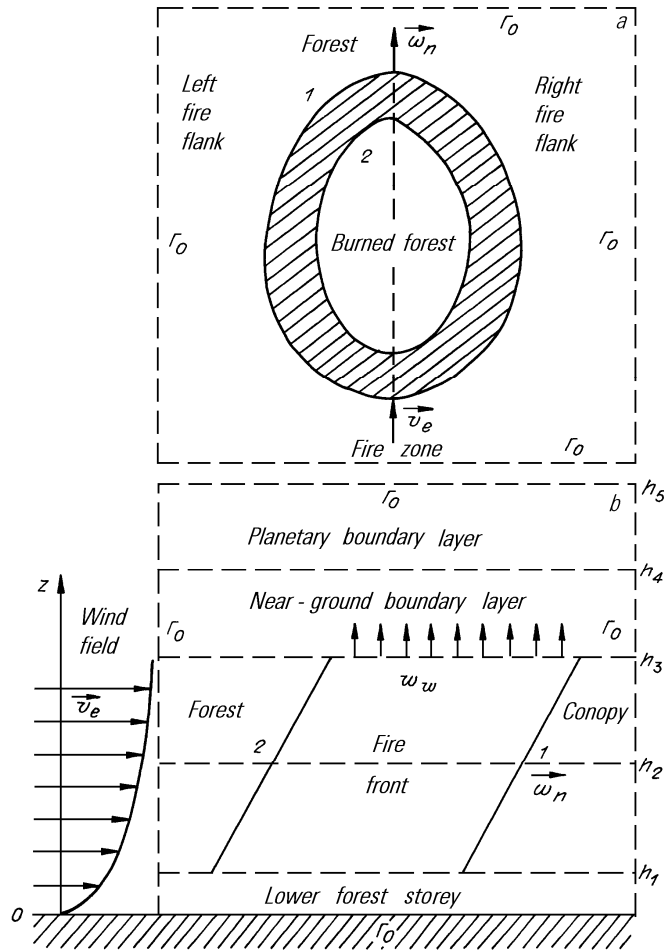


Fig. 2 a,b. The diagrams of forest fire zone (top view 1a) and view in the vertical plane. The darkest colour shows a fire front

Surface 2 (see Fig. 2a,b) separating the front fire from burnt FF is called internal edge of the forest fire. It may move both in the wind direction and opposite the wind. In the latter case it spreads at a lower speed than the leading external edge which spreads in the wind direction. As a result the front width for various fires may change depending on the time, wind velocity and FF capacity which differs not greatly from undisturbed values.

The boundary of forest fire zone is called the surface Γ -on which state parameters do not differ almost from state parameters of undisturbed medium (temperature, wind velocity, component concentration).

Principal sections of the mathematical theory of forest fires. The basis for creating a mathematical theory of forest fires were basic half-scale experimental data which enabled to create a

general physical model of forest fire totality of casual-consequential relation, which corresponds to this phenomenon. These data are given below.

1. The structure of surface and crown forest fire fronts has an intricate nature, and includes zones of warm-up, drying and pyrolysis of forest fuels, as well as zones of diffusion burning of gaseous pyrolysis products and burning down condensed pyrolysis products and burning down condensed pyrolysis products [11–13], (see Fig. 3).

2. Temperature profiles of gaseous and condensed phases in the crown forest fire front have a kind of Gauss curve, and the temperature of condensed phase is lower than that of gaseous phase, maximum difference being 200–300 K [12, 13].

3. The crown forest fire arises as a result of tree crown ignition from the surface forest fire torch. Relatively steady spread of crown forest fire on tree crowns is observed if the wind velocity in the forest cover exceeds 2.5 m/s [12, 13].

4. The gas flow in the forest fire front and convection column over a fire spot is turbulent, which results in fluctuations of temperature and gas phase characteristics [12], (see Fig. 3). The temperature in a convection column drops quickly with the height increase [11, 12].

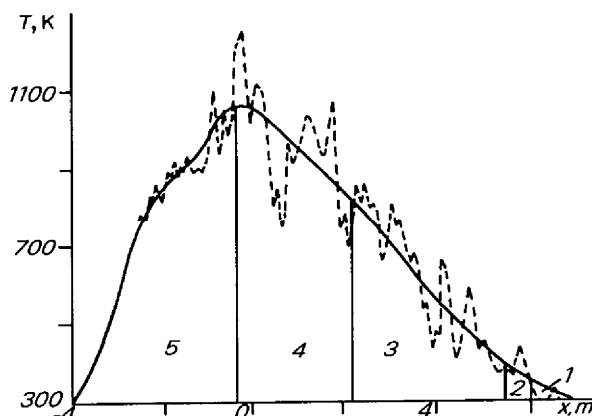


Fig. 3. Profiles of average (solid curve) and real temperature (dash curve) in the crown forest fire in young pine growth and fire front structure. Numbers mean the following: 1- the zone of warm-up; 2 - the zone of drying FF; 3 - the zone of FF pyrolysis; 4, 5 - the zones of burning gaseous pyrolysis products and burning down condensed pyrolysis products

Besides, many laboratory experiments of registering FF mass decrease as a result of drying and pyrolysis, which enabled to determine thermokinetic constants of these processes [11, 12].

On the basis of generalizing experimental and theoretical data in the work [11], physical (see Fig. 4) and mathematical models of the first generation forest fires were offered within which the forest was modelled with the porous-dispersion medium, and its skeleton was considered to be a non-deformed solid body.

As a significant constituent part of the forest fire theory is a physical model of the phenomenon. A set of reason-resulting connections obtained on the basis of both experimental data and laws of nature explaining investigated phenomenon is called physical model (fig 4)

The main components of the theory is the mathematical model - totality (set) of mathematical equations, limiting and initial conditions which in brief coded mathematical symbols on the numerical level reflect main casual-consequential relations of principal physico-chemical phenomena which arise at forest fire spreading.

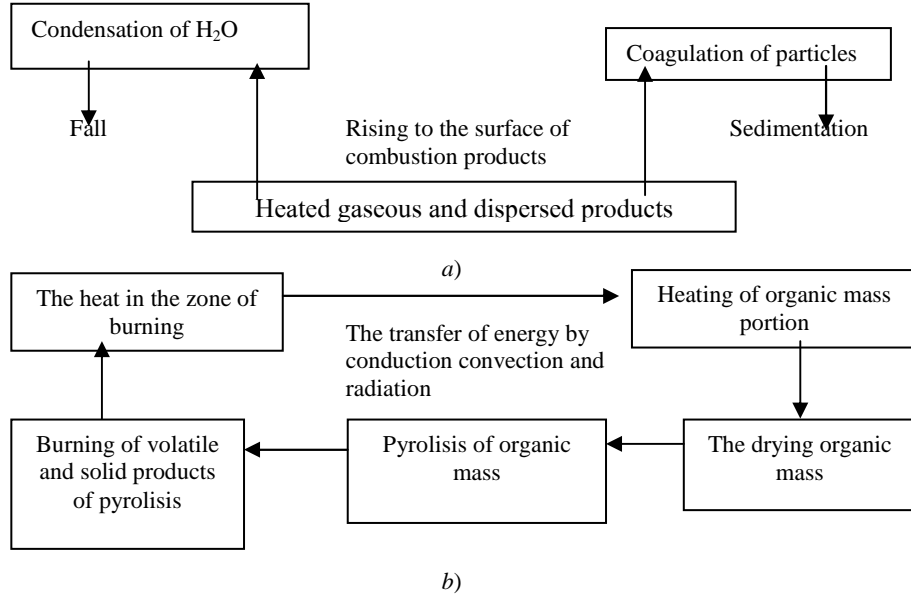


Fig. 4. Scheme of physicochemical processes at forest front (a) and in near-ground atmospheric layer (b)

General models of forest fires of the first and the second generation are described in detail in books [11] and [14]. Time and spatial coordinates of the point inside a fire area are taken as known values in the model, while temperature, gas dispersed and condensed phases, pressure, a velocity of a flow of a gas dispersed phase, a density of the flow of gas dispersed phase, concentration of the components in a gas dispersed medium C_α and volume fractions of phases φ_i are taken as values sought (required).

The basic system of equations. The last (refined) version of the general mathematical model of the forest fires was published in [15] and is presented below

$$\frac{\partial \rho}{\partial t} + \frac{\partial \rho v_j}{\partial x_j} = Q, \quad j = 1, 2, 3, \quad \varphi = \sum_{i=5}^8 \varphi_i; \quad (2)$$

$$\rho \frac{dv_i}{dt} = -\varphi \frac{\partial p}{\partial x_i} + \rho F_i + \frac{\partial \tau_{ij}}{\partial x_j} - Q v_i - \rho C_d s \left(v_i |\vec{v}| + \frac{1}{2} \sum_{i=1}^3 (\overline{v'_i - v'_{is}})^2 \cos \alpha_i + \right.$$

$$+ \sum_{j=1}^3 \overline{(v'_i - v'_{is})(v'_j - v'_{js}) \cos \alpha_j} \Bigg) \vec{F} = \vec{g} + (\vec{\Omega} \times \vec{r}) \times \vec{\Omega} + 2\vec{v} \times \vec{\Omega}, \quad (3)$$

$$i, j = 1, 2, 3;$$

$$\begin{aligned} \frac{dT}{dt} \sum_{i=5}^8 \rho_i \varphi_i C_{pi} &= \sum_{i=5}^8 \varphi_i \frac{dp}{dt} + \rho F_j v_j + \frac{\partial}{\partial x_j} \left(\lambda_{\vartheta TMj} \frac{\partial T}{\partial x_j} \right) + \frac{\partial T}{\partial x_j} \left(\rho \sum_{\alpha=1}^N D_{\vartheta TM\alpha} C_{p\alpha} \frac{\partial c_\alpha}{\partial x_j} \right) - \\ &-(\kappa + \kappa^{(s)})[cU_R - B(T)] + \alpha_V (T_s - T) + c_{ps} (T_s - T)(1 - \alpha_c) R_{1s} + \\ &+ c_{p7} (T_s - T) R_{2s} + q_{3s} R_3^{(s)} + q_{52} R_{52} + q_{53} R_{53} + q_{54} R_{54} + \\ &+ q_{2s} (R_{8-}^{(s)} - R_{8+}^{(s)}); \end{aligned} \quad (4)$$

$$\rho \frac{d_\alpha c_\alpha}{dt} = R_\alpha + \frac{\partial}{\partial x_j} \left(\rho D_{\vartheta \Phi \alpha} \frac{\partial c_\alpha}{\partial x_j} \right) - c_\alpha Q, \quad \alpha = 1, 2, \dots, N; \quad (5)$$

$$\begin{aligned} \sum_{i=1}^4 \rho_i \varphi_i c_{pi} \frac{\partial T_s}{\partial t} &= \frac{\partial}{\partial x_j} \left(\lambda_{sj} \frac{\partial T_s}{\partial x_j} \right) - \kappa_s [cU_R - B(T_s)] + \\ &+ q_{1s} R_{1s} - q_{2s} R_{2s} + q_{3s} R_{3s} + \alpha_V (T - T_s); \end{aligned} \quad (6)$$

$$\rho_1 \frac{\partial \varphi_1}{\partial t} = -R_{1s}, \quad \rho_2 \frac{\partial \varphi_2}{\partial t} = -R_{2s}; \quad (7)$$

$$\rho_3 \frac{\partial \varphi_3}{\partial t} = \alpha_C R_{1s} - \frac{M_C}{M_1} R_{3s} - \alpha_4 R_{3s} - R_6^{(s)}, \quad \rho_4 \frac{\partial \varphi_4}{\partial t} = \alpha_4 R_{3s} - R_7^{(s)}; \quad (8)$$

$$\sum_{\alpha=1}^8 c_\alpha = 1, \sum_{i=1}^8 \varphi_i = 1, P = \rho_r RT \sum_{\alpha=1}^{N_r} \frac{c_{\alpha r}}{M_\alpha}, N_r = N - 3; \quad (9)$$

$$Q = (1 - \alpha_c) R_{1s} + R_{2s} + \frac{M_C}{M_1} R_3 + R_6^{(s)} + R_7^{(s)} + R_8^{(s)}; \quad (10)$$

$$\tau_{ij} = \tau_{ij}^{(1)} + \tau_{ij}^{(2)}, \tau_{ij} = \mu \left(\frac{\partial v_i}{\partial x_j} + \frac{\partial v_j}{\partial x_i} \right), i = 1, 2, 3, j = 1, 2, 3. \quad (11)$$

Here t is the time; r is the radius vector of any point; x_j are the Cartesian coordinates; α , $\alpha^{(s)}$ and α_s are the integral coefficients of absorption for the gas, dispersed particles, and condensed phase, respectively; B is the Planck function; U_R is the integral-radiation or density; c_{pi} , c_{p7} , and c_{ps} are the specific heats of individual phases, water vapor, and gaseous pyrolysis products at constant pressure; v_j and $|\vec{V}|$ are the components and magnitude of the average velocity of the gas and the dispersed particles; v' and V'_s are the pulsation components of the flow velocity and of the bending oscillations of the FF components; ρ_i is the true density of the i -th phase; $R_{8-}^{(s)}$ and $R_{8+}^{(s)}$ are the mass rates of water-vapor condensation and free-water evaporation in the gas-dispersed phase; Q_{1s} , Q_{2s} , and Q_s are the heats of pyrolysis, evaporation of bound water, and combustion of coke breeze; Q_2 is the heat of evaporation (condensation) of free water; p is the gas pressure; $\tau_{ij}^{(1)}$ and $\tau_{ij}^{(2)}$ are the laminar and turbulent components of the tangential-stress tensor; C_α is the mass concentration of the α -component in the gas dispersed medium; N is the number of components in the gas-dispersed medium; R_α is the mass rate of formation of the α -component in the gas-dispersed medium due to pyrolysis of FF, evaporation of water, and heterogeneous and homogeneous chemical reactions; $R_6^{(s)}$, $R_7^{(s)}$ and $R_8^{(s)}$ are the mass rates of formation of smoke particles, black-carbon particles, and water droplets; $\rho = \rho_5 \phi_5 + \rho_6 \phi_6 + \rho_7 \phi_7 + \rho_8 \phi_8$ is the density of the gas-dispersed mixture; D_α and D_T are the coefficients of molecular and turbulent diffusion; λ and λ_T are the coefficients of molecular and turbulent heat conduction of the gas phase; μ and μ_T are the coefficients of molecular and turbulent viscosities, $D_{N-2,ef}$, $D_{N-1,ef}$ and $D_{N,ef}$ effective coefficients of diffusion of smoke particles, where $N - 2$ corresponds to carbon black particles, $N - 1$ to ash particles, and N to water droplets; $D_{\alpha ef} = D_\alpha + D_T$ is the effective diffusion coefficient of the α -component; a_v is the coefficient of internal heat exchange; R_{is} are the mass rates of formation (diminution) of the condensed-phase; T and T_s are the temperatures the gas and condensed phases; λ_s is the heat conductivity of the porous condensed phase; \vec{q}_R , \vec{q}_{Rs} are the density vectors of the thermal radiation flux in the gas-dispersed phase and porous medium; \vec{q}_R and \vec{q}_{Rs} are the components of the vectors \vec{q}_R and \vec{q}_{Rs} ; $\cos \alpha_i = v_i / v$ are the direction cosines of the average-velocity vector of the gas-dispersed phase; Q_k are the heats of chemical reactions ($k = 1, 2$, and 3 , where 1 corresponds to pyrolysis, 2 to the

mass rate of evaporation of bound water, and 3 to the heterogeneous-combustion velocity of coke breeze); α_c is the coking values of the FF; R is the molar gas constant; M_C and M_1 are the atomic and molecular masses of carbon and oxygen; M_a is the molecular mass of the α -component of the gas phase; g is the acceleration of gravity; $\vec{\Omega}$ is the angular velocity of rotation of the Earth; $\lambda_{ef} = \lambda + \lambda_T$ and $\mu_{ef} = \mu + \mu_T$ are the effective thermal conductivity and viscosity: of gas; C_d is the vegetation resistance coefficient; $\alpha_v = s\alpha_s$ is the coefficient of the volume heat exchange between a FF component and the medium, s is the specific surface area of the FF in a given forest, stratum; a is the heat-exchange coefficient; F_j are the components of the vector \vec{F} and the subscript s corresponds to the reactions involving condensed material and superscript s corresponds to the dispersed-phase characteristics.

In Eq. (5), the total derivative for the gas-phase components at $\alpha = 1, 2, \dots, N-3$ has the form

$$\frac{d_\alpha}{dt} = \frac{\partial}{\partial t} + v_1 \frac{\partial}{\partial x_1} + v_2 \frac{\partial}{\partial x_2} + v_3 \frac{\partial}{\partial x_3}$$

and for the dispersed-phase components ($\alpha = N-2, N-1$, and $= N$) it has the form

$$\frac{d_\alpha}{dt} = \frac{\partial}{\partial t} + v_1 \frac{\partial}{\partial x_1} + v_2 \frac{\partial}{\partial x_2} + (v_3 - v_{3\alpha}^{(s)}) \frac{\partial}{\partial x_3}$$

Here $v_{3\alpha} = 18g\mu / \rho_\alpha^{(s)} d_\alpha^2$ is the Stokes velocity of sedimentation of dispersed particles; μ is the molecular dynamic viscosity of the gas phase; g is the free-fall acceleration; and $\rho_\alpha^{(s)}$ and d_α^2 are the density and diameter of dispersed particles.

Thus, in accordance with [14], the medium is considered to be two-velocity. This allows to take into account the sedimentation of particles due to gravity.

Equation (2) is the law of conservation of mass for the gas-dispersed phase. Equations (3) express the laws of conservation of momentum for the gas-dispersed phase in terms of components along the Cartesian axes. The latter equations contain terms that are due to the force interaction between the gas-dispersed flow and the skeleton of the porous-dispersed medium. Equation (4) represents the law of conservation of energy in the gas-dispersed flow with allowance for the energy transfer due to both convection and radiation and also with allowance for the release and absorption of thermal energy due to various physical and chemical processes. Equation (5) is the law of conservation of mass for individual components in the gas-dispersed flow with allowance for convection and diffusion processes and also physicochemical transformations. Equation (6) is the law of conservation of energy in the condensed phase. Equation (7) describes the kinetics of pyrolysis and drying of the FF. Equations (8) describe the balance of mass for coke breeze (an intermediate condensed product of FF pyrolysis) and

ash (the final condensed product of combustion).

The first and second relations in (9) are an algebraic integral of the basic system of equations, while the third is the equation of state for the gas phase.

Relation (10) defines the rate of generation of the gas and dispersed phases by evaporation and chemical reactions.

Relations (11) specify the tangential components of the stress tensor in terms of derivatives of the velocity components of the averaged flow.

The turbulence models. Different types of flows are observed in the vicinity of different forest fires. In particular, if FF burn near the underlying surface, that is, the ground cover burns (forest surface fire), then the flow is of a transient (mixed) type. Attachment conditions hold immediately on the underlying surface (at $z = 0$), and the flow is laminar within the FF layer, while laminar-to-turbulent flow transition occurs above the FF layer. A developed turbulent flow is realized in the convection column above the forest-fire site.

Equations (2)–(10) are the Navier-Stokes equations for a multiphase reactive medium, averaged after Reynolds. We assume here that the characteristic time of turbulent pulsations $t' \ll t_*$, where t_* is the characteristic time of process, (duration of the forest fire). When the flow velocities are small, $\mu \gg \mu_t$, $\lambda \gg \lambda_t$, $D_\alpha \gg D_{\alpha_t}$, and Eqs. (2)–(10) become Navier-Stokes equations for a multicomponent reacting medium. When the flow velocities (or Reynolds numbers) are large, the flow is turbulent. In this case, $\mu_t \gg \mu$, $\lambda_t \gg \lambda$, $D_{\alpha_t} \gg D_\alpha$, and Eqs. (1)–(10) become Reynolds equations for a multicomponent reacting medium. Similar equations have been obtained previously for chemically reacting multicomponent gas flows [12–14].

Unlike in [12–14], in deriving Eqs. (2)–(11), we assumed that the averaging procedure influenced neither the form of the equation of state of a multicomponent gas nor the expression for the chemical-reaction rates. Sometimes, instead of the Reynolds method, initial equations are averaged by the, Favre procedure [12–14], in which the averaged velocity components are determined by the formula:

$$\tilde{v}_i(x_i) = \overline{\rho v_i(x_i)} / \bar{\rho}(x_i) \quad i = 1, 2, 3 \quad (12)$$

Here the tilde indicates averaging with respect to mass, the bar refers to averaging with respect to time, and ρ and v_i are the instantaneous values of the density and velocity components. We refer to [15–17] for the expressions relating quantities averaged by the Reynolds and Favre methods.

Using the Favre transformation, it is easy to obtain a system of equations which is essentially equivalent to system (2)–(11) but is written for mass-average flow parameters (velocity, temperature, etc.) except for pressure. A disadvantage of the Favre averaging procedure is that those terms in the Navier-Stokes equation that characterize molecular transfer, including the stress-tensor components τ_{ij} , take a more complex form. Moreover, to determine experimentally the thermodynamic parameters averaged by the Favre method, one needs to know the instantaneous density p and its average value.

This is not required for experimental determination of the quantities averaged by the Reynolds method. For this reason, we used the latter method in deriving Eqs. (2)–(11)

In [12–14] for unidirectional turbulent flows in near-ground atmospheric layers, the van Driest formulas were used

$$v_T = (0.4z)^2 \left[1 - \exp\left(-\frac{x}{A}\right) \right]^2 \left| \frac{\partial u}{\partial z} \right|, \quad A = 26v \left(\frac{\tau_w}{\rho} \right)^{-\frac{1}{2}}, \quad (13)$$

$$v_T = 0.0168 \gamma_1 \left| \int_0^{\delta} (u_e - u) dz \right|, \quad \gamma_1 = \left[1 + 5.5 \left(\frac{z}{\delta} \right)^6 \right]^{-1}. \quad (14)$$

Here τ_w is the friction stress at $z = 0$; $v = \mu/\rho$, $v_T = \mu_T/\rho$ are the laminar and turbulent kinematic viscosities; $u = V_1$ is the x component of velocity (the direction of the x axis coincides with the wind velocity); δ is the thickness of the boundary layer.

Formula (13) was used to calculate flow characteristics in the interior of the boundary layer and formula (14) was used for the exterior. In accordance with [14–17], the effective kinematic viscosity was determined by the formula

$$V_{ef} = V + V_T. \quad (15)$$

As calculations have shown [12–14], formulas (13)–(14) enable one to find the velocity and temperature fields ahead of the forest-fire front for unidirectional flow.

In calculation of developed turbulent flows, components of both the tangential–stress tensor and the components q_{ir} of the density vectors of thermal turbulent flow and also the densities of the diffusion flow for the α -component $q_{i\alpha}$ are determined from the formulas [12–14]

$$\tau_{ij} = -\rho \overline{v'_i v'_j} = \mu_T \left[\left(\frac{\partial v_i}{\partial x_j} + \frac{\partial v_j}{\partial x_i} \right) - \delta_{ij} \operatorname{div} \vec{v} \right] - \frac{2}{3} \rho K \delta_{ij}, \quad i, j = 1, 2, 3, \quad (16)$$

$$q_{iT} = -\rho c_p \overline{v'_i T'} = \Gamma_T \frac{\partial T}{\partial x_i}, \quad \Gamma_T = \frac{\mu_T c_p}{Pr_T}, \quad Pr_T = \frac{\mu_T c_p}{\rho \lambda_T}, \quad i = 1, 2, 3, \quad (17)$$

$$q_{i\alpha} = -\rho \overline{v'_i c'_\alpha} = \Gamma_\alpha \frac{\partial c_\alpha}{\partial x_i}, \quad \Gamma_\alpha = \frac{\mu_T}{Sc_{T\alpha}}, \quad Sc_{T\alpha} = \frac{\mu_T c_p}{\rho \lambda_T} \quad i = 1, 2, 3, \quad (18)$$

$$\mu_T = l^2 \left\{ \kappa_d^2 \left[\left(\frac{\partial u}{\partial y} + \frac{\partial v}{\partial x} \right)^2 + \left(\frac{\partial w}{\partial x} + \frac{\partial u}{\partial z} \right)^2 + \left(\frac{\partial w}{\partial y} + \frac{\partial v}{\partial z} \right)^2 \right] + 2 \left[\left(\frac{\partial u}{\partial x} \right)^2 + \left(\frac{\partial v}{\partial y} \right)^2 + \left(\frac{\partial w}{\partial z} \right)^2 \right]^{1/2} + \kappa_b^2 \left| \frac{g}{\theta} \frac{\partial \theta}{\partial z} \right|^{1/2} \right\}, \quad (19)$$

$$\sqrt{K} = \frac{\mu_T}{\rho c'_\mu}, \quad l = \frac{0.4 z}{1 + 2.5 z \sqrt{c_d} S / h}, \quad l = 0.4 z. \quad (20)$$

Here $x = x_1$, $y = x_2$, $z = x_3$ and $z=x_3$ are the Cartesian coordinates; h is the thickness of vegetation; l is the characteristic length (that is, the displacement, which was calculated from the second formula in (19) for the vegetation layer and from the third formula outside the vegetation layer; c'_μ is the constant introduced by Rodi [12–14]; K is kinetic energy of turbulence; Pr_τ is the Prandtl number for turbulent flows; $Sc_{\alpha\tau} = \nu_\tau / D_{\tau\alpha}$ is the Schmidt number for turbulent flows; λ_τ , and $D_{\tau\alpha}$ are the turbulent thermal conductivity and diffusivity; $\kappa_d = 0.2$, $\kappa_b = 0.2$ for $\partial\theta / \partial z < 0$ or $\partial\theta / \partial z > 0$, respectively; $\theta = T_{oe} (1000 / P_e)^{\gamma-1/\gamma}$ is the potential temperature; T_{oe} undisturbed temperature at $z = 0$; P_e is the pressure of the undisturbed medium; $\gamma = c_p / c_v$, is the ratio of specific heats of air outside the forest-fire zone; and the rest of the notation was given above.

To estimate the error due to the assumption of equilibrium between dissipation and generation of the kinetic energy of turbulence, the temperature and flow-velocity field for an axisymmetric surface fire were obtained in [20] by using the full ($K - \epsilon$) model of turbulence. The same model is used in [21].

In [12–15], turbulence models for a pure gas were used, although the near-ground atmospheric layer contains smoke and black-carbon particles. Little is known about the influence of condensed particles suspended in and gas flow on turbulence characteristics. The influence of a heavy admixture in the form of equal-sized spherical particles on the turbulent structure of a jet has been studied theoretically [22]. The turbulent transfer and sedimentation of aerosols on the tube walls have been studied both experimentally and theoretically [23]. As was shown in these works, if the volume and mass fractions of particles are small ($\sim 10^{-4}$), their influence on the turbulence is negligible. This condition holds in forest fires. It seems promising to use the methods for solving inverse problems of the mechanics of reacting media [24] to determine the turbulent heat conductivity and diffusivity.

Radiation model for forest fires. Within the framework of the first-generation model, the assumption of a "gray" medium was introduced [11]. This assumption does not hold in real situation, since in the near-infrared range (740–1200 nm) the FF components (green leaves and coniferous needles) reflect a considerably greater portion of radiation than in the visible range. Therefore, it is expedient to use the group diffusion model for energy transfer by radiation. Equations for the energy transfer by radiation with allowance for the spectral properties of the FF and dispersed-phase particles have the form [14, 15]

$$\text{div} \vec{q}_{Rn\Sigma} + \kappa_{n\Sigma} c_n U_{Rn} = Q_{Rn}, \quad n = 1, 2, \dots, \mu; \quad (21)$$

$$\vec{q}_{Rn\Sigma} = \frac{1}{3} \int_{v_n}^{v_{n+1}} \frac{c_v \text{grad} U_v}{k_{v\Sigma}} dv, \quad k_{n\Sigma} c_n U_{Rn} = \int_{v_n}^{v_{n+1}} k_v c_v U_{Rv} dv, \quad (22)$$

$$Q_{Rn} = \int_{v_n}^{v_{n+1}} Q_{Rv} dv, \quad Q_{Rv} = 4\pi [(\kappa_v + \kappa_v^{(s)}) B_v(T) + \kappa_{vs} B_v(T_s)], \quad (23)$$

where $\vec{q}_{Rn\Sigma}$ is the group approximation of the total spectral radiation flux in multiphase porous dispersed medium; U_{Rv} is the radiation density in the multiphase medium; c_v and c_n are the spectral velocity of light and its group approximation; $\kappa_{n\Sigma}$ is the group approximation for the total absorption coefficient of medium; $k_{v\Sigma}$ is spectral coefficient of radiation attenuation; B_v is the spectral Planck function for radiation equilibrium; κ_v , $\kappa_v^{(s)}$, $\kappa_{n\Sigma}$ are the spectral absorption coefficients for the gas, dispersed particles, and condensed phase. respectively; v is the radiation frequency; and μ is the total number of wavelength groups.

On closing the main system of equations. It should be noted that upon deriving the main system of equations it was assumed that the particles of air, soot, smoke and little drops of water occurring above the fire area in the atmosphere, have the same speed. This allowed to use the so-called one pressure model to determine velocity fields, that considerably simplified the main system of equations. At the same time it makes necessary to obtain additional equations for determining $\Phi_5, \Phi_6, \Phi_7, \Phi_8$, since in the main system of equations only four equations (7), (8) are given to determine volume shares $\Phi_1, \Phi_2, \Phi_3, \Phi_4$.

It is apparent, that to determine $\Phi_5, \Phi_6, \Phi_7, \Phi_8$ it is necessary to write down additional relationships. Let mass concentrations C_α ($\alpha = 1, 2, 3, 4, 5, 6, 7, 8, 9, 10$) for oxygen, carbon monoxide, hydrogen, carbene dioxide, nitrogen, water vapour, soot, particles of smoke and drops of water are known. Then, using determinations of these values

$$c_\alpha = \rho_\alpha / \rho, \quad \alpha = 1, 2 \text{ K } 10, \quad \rho = \sum_{\alpha=5}^8 \rho_\alpha \Phi_\alpha, \quad (24)$$

$$\rho_r = \rho \sum_{\alpha=1}^7 c_{\alpha}, \rho_r = \frac{P}{RT \sum_{\alpha=1}^7 \frac{c_{\alpha}}{M_{\alpha}}} \quad (25)$$

and a relationship (9) of the main system of equations it is possible to obtain additional equations to determine $\Phi_5, \Phi_6, \Phi_7, \Phi_8$.

Actually, determining ρ_r from the last equations seven first relationships (24) by a from 1 to 7, we have

$$\rho_6^{(c)} \Phi_6 = c_8 \rho. \quad (26)$$

By definition of the partial densities of the particles of soot, smoke and drops of water we have the equations

$$\rho_7^{(s)} \Phi_7 = c_9 \rho, \quad (27)$$

$$\rho_8^{(w)} \Phi_8 = c_{10} \rho. \quad (28)$$

Here $\rho_6^{(c)}, \rho_7^{(s)}, \rho_8^{(w)}$ – actual densities of the particles of soot, smoke and drops of water.

It should be noted, that mass velocities of initiation (disappearance) of soot R_8, R_9 – for particles of smoke and R_{10} – for drops of water should coincide with expressions $R_6^{(s)}, R_7^{(s)}$ and $R_8^{(s)}$. Otherwise a total balance of mass in a unit of the medium volume in the fire area will be disturbed, that is intolerable. In other words, after summarizing left and right parts of the equation (5) over all N a result of summarizing should be zero both in the right and in the left parts.

Thus, if c_{α} are known, then to determine $\Phi_5, \Phi_6, \Phi_7, \Phi_8$ we have equations (25)–(28).

The boundary and initial conditions. To solve the problem of initiation and spread of forest fires, it is necessary to have not only equations but also boundary and initial conditions. In the general three-dimensional case, the fire zone is a parallelepiped. Let the faces Γ_1 and Γ_2 of the parallelepiped be perpendicular to the x axis which is directed along the wind velocity of wind, the lower face Γ_0 and the upper face Γ_3 be perpendicular to the z axis which is directed upward, and the side faces Γ_4 and

Γ_5 be perpendicular to the y axis. The origin of the x, y, z system is located at the point of the temperature maximum of the initial tire site. In this case, the state parameters of the medium at the boundaries $\Gamma_1, \Gamma_3, \Gamma_4$, and Γ_5 coincide with the undisturbed values:

$$\vec{v}|_{\Gamma_i} = \vec{v}_e, T|_{\Gamma_i} = T_e, T_s|_{\Gamma_i} = T_{se}; \quad (29)$$

$$C_\alpha|_{\Gamma_i} = C_{\alpha e}, \varphi_i|_{\Gamma_i} = \varphi_{ie}, i = 1, 3, 4, 5, \quad (30)$$

where the subscript e corresponds to the undisturbed parameters of the medium. The so-called mild boundary conditions must be used at the boundary Γ_2 :

$$\left. \frac{\partial T_s}{\partial x} \right|_{\Gamma_2} = \left. \frac{\partial T}{\partial x} \right|_{\Gamma_2} = 0, \left. \frac{\partial c_\alpha}{\partial x} \right|_{\Gamma_2} = 0, \left. \frac{\partial \vec{v}}{\partial x} \right|_{\Gamma_2} = 0. \quad (31)$$

On the underlying surface, the boundary condition has the form

$$\left. \frac{\partial T}{\partial z} \right|_{\Gamma_0} = 0, \left. \frac{\partial T_s}{\partial z} \right|_{\Gamma_0} = 0, \left. \frac{\partial c_\alpha}{\partial z} \right|_{\Gamma_0} = 0, v_1|_{\Gamma_0} = 0, \rho v_3|_{\Gamma_0} = f_0. \quad (32)$$

where $z = x_3$, $v_1 = v_x, v_2 = v_y, v_3 = v_z$, and f_0 is the mass velocity of combustion of the ground cover. For the spectral radiation density, the following boundary conditions are used:

$$q_{R \nu n_i}|_{\Gamma_i} = -\frac{c U_\nu}{2}|_{\Gamma_i}, \quad i=1,3,4,5. \quad (33)$$

$$q_{R \nu n_i}|_{\Gamma_0} = \begin{cases} \epsilon_\nu B_\nu(T_{\Gamma_H}), & M \in G_\Gamma \\ \epsilon_\nu B_\nu(T_e), & M \notin G_\Gamma \end{cases}$$

Here M is any point in the fire zone; G_Γ is the region of space corresponding to the combustion

site; \mathcal{E}_v is the spectral coefficient of radiation; and the subscript Y refers to the parameters of the medium at the fire 'site.' The first relation in (26) is the condition of the medium's transparency, and the second characterizes the radiation of the surface fire site.

If the forest fire propagates from a fire site of finite size, the initial conditions have the form

$$T_s = T|_{t=0} = \begin{cases} T_{\Gamma H} & \text{при } M \in G_\Gamma, \\ T_e & \text{при } M \notin G_\Gamma; \end{cases} \quad c_\alpha|_{t=0} = \begin{cases} c_{\alpha \Gamma H} & \text{при } M \in G_\Gamma, \\ c_{\alpha e} & \text{при } M \notin G_\Gamma; \end{cases} \quad (34)$$

$$\Phi_i|_{t=0} = \begin{cases} \Phi_{i \Gamma H} & \text{при } M \in G_\Gamma, \\ \Phi_{ie} & \text{при } M \notin G_\Gamma; \end{cases} \quad \vec{v}|_{t=0} = \begin{cases} \vec{v}_{\Gamma H} & \text{при } M \in G_\Gamma, \\ \vec{v}_{\Gamma e} & \text{при } M \notin G_\Gamma. \end{cases} \quad (35)$$

In as much as boundary conditions must reflect the geometrical and physicochemical features of problems of the theory of forest fires, they are specified for each problem separately. Forest, as a rule, is a multistratum system. Hence, it is reasonable to use conjugate boundary conditions [14, 15] at the boundaries of individual strata, which are discontinuities in the structure of forest phytocenoses:

$$(\rho w)|_{z=h+0} = (\rho w)|_{z=h-0} + \left(\sum_{i=1}^5 s_i^{-1} R_{is} \right)|_{z=h}; \quad (36)$$

$$\left(\mu_{\varphi} \frac{\partial u}{\partial z} \right) \Big|_{z=h+0} = \left(\mu_{\varphi} \frac{\partial u}{\partial z} \right) \Big|_{z=h-0}; \quad (37)$$

$$\left(\mu_{\varphi} \frac{\partial v}{\partial z} \right) \Big|_{z=h+0} = \left(\mu_{\varphi} \frac{\partial v}{\partial z} \right) \Big|_{z=h-0}; \quad (38)$$

$$\left(\mu_{\varphi} \frac{\partial w}{\partial z} \right) \Big|_{z=h+0} = \left(\mu_{\varphi} \frac{\partial w}{\partial z} \right) \Big|_{z=h-0}; \quad (39)$$

$$\left(\lambda_{\varphi} \frac{\partial T}{\partial z} + q_{RZ}^{(s)} \right) \Big|_{z=h+0} = \left(\lambda_{\varphi} \frac{\partial T}{\partial z} \right) \Big|_{z=h-0}, \quad q_{RZ}^{(s)} = \varphi q_{RZ\Sigma}; \quad (40)$$

$$\left(\rho D_{\varphi TM} \frac{\partial c_\alpha}{\partial z} \right) \Big|_{z=h+0} + R_{\alpha w} = \left(\rho D_{\alpha \varphi TM} \frac{\partial c_\alpha}{\partial z} \right) \Big|_{z=h-0},$$

$$R_{\alpha w} = \sum_{i=1}^3 s_i^{-1} R_{is} c_{i\alpha s} \Big|_{z=h}; \quad (41)$$

$$\begin{aligned} \lambda_s \frac{\partial T_s}{\partial z} \Big|_{z=h+0} + q_{Rsz} \Big|_{z=h+0} + \sum_{i=1}^3 q_i s_i^{-1} R_{is} = \\ = \lambda_s \frac{\partial T_s}{\partial z} \Big|_{z=h-0} + q_{Rsz} \Big|_{z=h-0}; \end{aligned} \quad (42)$$

$$q_{RZS} = (1 - \Phi) q_{RZ\Sigma}, q_{Rz} \Big|_{z=h+0} = q_{Rz} \Big|_{z=h-0}. \quad (43)$$

$$T \Big|_{z=h+0} = T \Big|_{z=h-0}, c_\alpha \Big|_{z=h+0} = c_\alpha \Big|_{z=h-0}, U_R \Big|_{z=h+0} = U_R \Big|_{z=h-0}, \quad (44)$$

$$u \Big|_{z=h+0} = u \Big|_{z=h-0}, v \Big|_{z=h+0} = v \Big|_{z=h-0}, w \Big|_{z=h+0} = w \Big|_{z=h-0}. \quad (45)$$

Here h is the elevation of the structural discontinuity; u , v , and w are the velocity components; $q_{RZ\Sigma}$ is the z -component of the total density of the thermal radiation flux; $\mu_{\alpha\phi}$, $\lambda_{\alpha\phi}$, $D_{\alpha\phi}$ are effective values of the dynamic viscosity, thermal conductivity, and diffusivity of the gas-dispersed phase; $q_{RZ}^{(s)}$ and q_{RZS} are the vector z -components of the total density of thermal radiation flux in the gas-dispersed and condensed phases; $c_{i\alpha s} = v'_{i\alpha} M_\alpha / v_{is} M_{is}$ are the emission coefficients for the α -component in the i -th reaction; v_{is} and $v'_{i\alpha}$ are the stoichiometric coefficients of the starting condensed material and gas-dispersed α -component in the i th reaction; and M_{is} and M_α are the molecular masses of the starting condensed material and the gas-dispersed α -component.

Boundary conditions (36)–(45) relate the state parameters to the magnitude of fluxes on both sides of the structural discontinuity. Therefore, these conditions can be called conjugate boundary conditions. They generalize the well-known boundary conditions of the fourth kind which were introduced by academician A.V. Lykov for the solution of conjugate problems of heat transfer theory for homogeneous inert media.

Using the conjugate conditions and some additional considerations, one can obtain various boundary conditions. For instance, assuming that the temperature of the ground cover in a surface fire does not depend on z and the spectral absorption coefficient as for forest fuel is known, we obtain

$$(c/3\alpha) \frac{\partial U_{Rv}}{\partial z} \Big|_{z=h_0+0} = \frac{1}{\sqrt{3}} (4\sigma T^4 f - c U_{Rv}) \Big|_{z=h_0-0}, \quad (46)$$

where $f = 1 - \exp(-\alpha_{sv} h_0 \sqrt{3})$, α_v , α_{sv} are the spectral attenuation coefficients for the medium above,

the surface fire site and in the ground cover, respectively; h_0 is the ground-cover height; and z is the vertical coordinate measured from the upper boundary of the ground cover.

An advantage of the obtained condition over conditions (33) is that it does not contain the constant $\varepsilon_{v,}$, which has to be determined empirically.

The Database of the General mathematical fire model and methods of numerical simulation of the problems. The basic system of equations (2)-(11) and the boundary initial conditions contain thermophysical coefficients, rates of drying, pyrolysis, and combustion, and a number of empirical constants. Together, they constitute the database of the general mathematical model. The components of the database were determined from the data available in the literature, on the one hand, and from experimental data by solution of inverse problems of the mechanics of reacting media, on the other hand [16]. All components of the database must be consistent with one another. This was achieved by varying the components within their accuracy range and choosing them in such a way as to achieve the best correlation between the corresponding experimental and theoretical data. It is important that solutions of direct and inverse problems of the mathematical theory of forest fires be determined with a controllable accuracy. This is a complicated mathematical problem, inasmuch as the basic system of equations (2)-(11) is nonlinear. In [11-16], problems of the mathematical theory of forest fires were solved by the iterative-interpolation method developed at the Tomsk State University [17] and by special methods of numerical simulation [18] which are based on the Patankar-Spaulding method [18].

Object and the main problems of the forest fire theory. The main object of the forest fire theory is prediction of limiting conditions of forest fire's beginning and spread and also their ecological results.

All the problems of the forest fire theory are divided into direct and inverse ones. A direct problem is formulated in this way: given - a controlled volume of the medium (sphere of specifying solution of the main set of equations), external forces, chemical reaction rate, thermal-physical coefficients and transfer constants, as well as fields of sought-for functions (velocity, pressure, phase temperature, density, component concentration of gas-dispersed phase, volumetric fractions of phases) and their values at the boundaries of the controlled volume (limiting values). Required: field of functions in the controlled volume which is called a forest fire zone at any instant. In other words, a direct problem enables to predict main characteristics of forest fires (contour, fields of sought-for values in the fire area, spreading speed and others); if initial data are given. According to the nature of dependence of sought-for functions on space variables, direct problems are classified into one-, two-, three-dimensional. Due to great computational difficulties, only a few one-, two- metric problems of the forest fire theory published mainly in monographs [11-15] have been solved.

An inverse problem cannot be formulated in the only way, since its setting up and solution depend essentially on a type and precision (accuracy) of experimental data used for its decision. Probably, when solving inverse problems one should account for not only experimental data but the totality of casual-sequential relations (a physical model of phenomenon) and a general mathematical model of forest fires, which reflect in a strict numerical form laws of mass conservation, conservation of momentum and energy. According to Adamar, inverse problems are incorrect problems of mathematical physics, and to solve them one should apply either a trial-and-error method (solution-

fitting) which is mainly reduced to multiple solution of a related direct problem, or the method of regularization of academician A.I. Tikhonov [16].

The most important inverse problem of the forest fire theory is detection of forest fires and identification of a fire type discovered by using airborne sensing devices aboard aircraft and satellites. These devices record the density of radiant heat flux q_λ in different spectral bands, and first of all in the infrared one. Therefore the principal problem of airspace monitoring of forest fires is formulated in the following way:

given: value q_λ in the function of time and coordinates at the upper boundary of the forest fire;
required: to detect a forest fire, its type and ecological impacts.

Some of the results of mathematical and physical modelling. 1. A large forest fire is a fundamentally unsteady and three-dimensional aerothermochemical process in which the Coriolis force plays a significant part [11].

2. Comprehensive physical modeling of forest fires is impossible without complete agreement between full-scale model fire characteristics and [11].

3. Types of forest fires can be identified by means of important similarity criteria such as the Strouhal, Froude, Coriolis, and Reynolds numbers and also values of the dimensionless injection and dimensionless temperature at the fire front [11-14].

The results of the numerical simulation of plane two-dimensional problems of the aerodynamics of forest fires lead to the conclusion that the interaction of wind with the combustion products injected from the I fire front results in two limiting flow types: a unidirectional flow (a jet-like boundary layer) and a convection column (a tilted jet of hot gas-dispersed combustion products). In the latter case, a large toroidal vortex forms I ahead of the forest-fire front. As a result, the flow velocity has different directions near the underlying surface and in the near-ground atmospheric layer, the wind velocity increasing near the fire front in the near-ground atmospheric layer [11-14] (see Fig. 5).

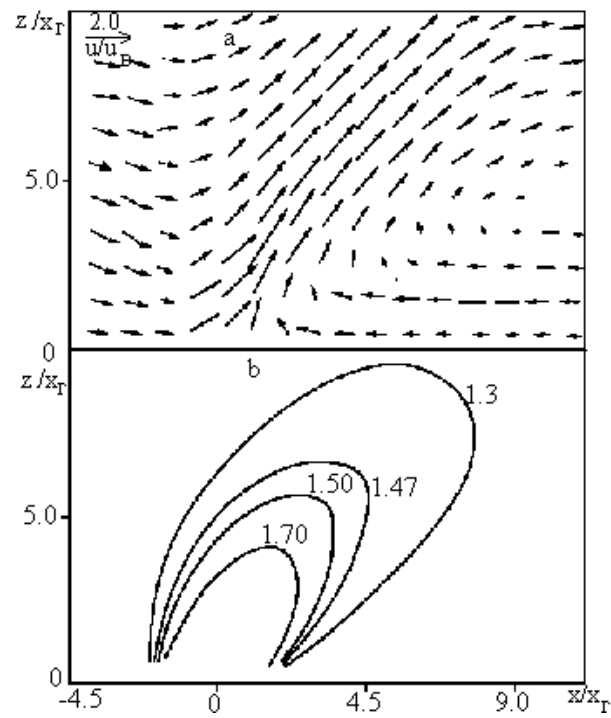


Fig. 5. Velocity field (a) and isotherms (b) above a plane forest fire front for an inclined convective column [12–15]. U_b -speed of wind at the height of 10 m and far from forest fire front

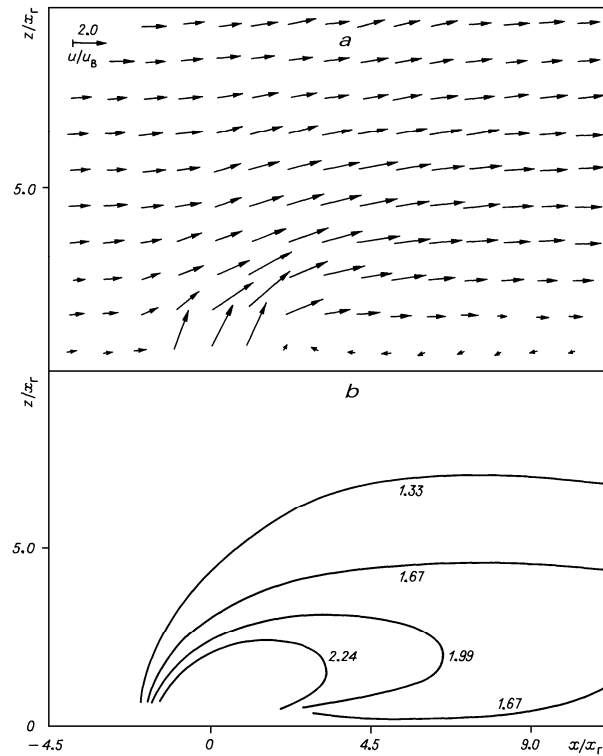


Fig.6. Velocity field (a) and isotherms (b) above a plane forest fire front for a jet boundary layer ("plumage" type flow) [12–15]. U_b -speed of wind at height of 10 m and far from forest fire front

5. The calculations show that ahead of the fire front the friction stress drops abruptly and the sign of the thermal flux changes. This indicates that, when the wind velocity is considerable, the unidirectional flow and heat transfer in the near-ground atmospheric layer in the vicinity of the fire front have the characteristics of a heat screen. In this case, the free convection of hot combustion products affects only slightly the magnitude of convective heat flux ahead of the fire front [11-14] (see Fig.6,7).

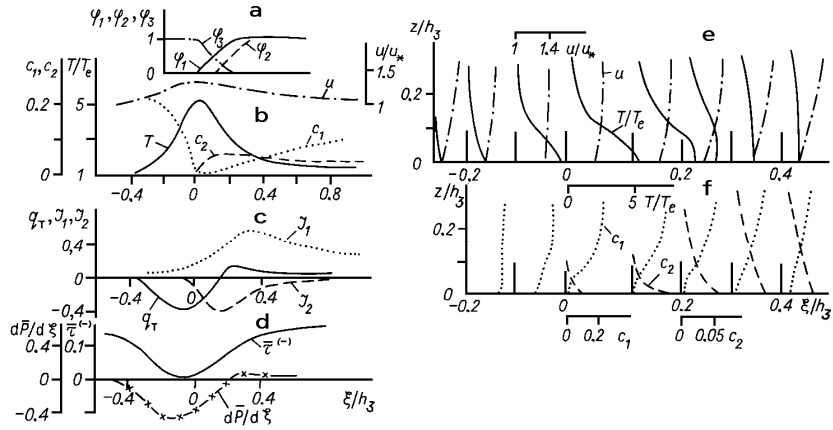


Fig 7. Profiles of state variables at the front of a top fire, and in the near-ground layer of atmosphere above it [12–15]: T is temperature, C_1 and C_2 are concentrations O_2 and CO . q_r , I_1, I_2 are -densities of turbulent of flow heat and diffusional flows of oxidizing agent and gas product of pyrolysis; $\bar{\tau}$, $\frac{d\bar{p}}{d\xi}$ are dimensionless turbulent shear stress and gradient of pressure, ξ is a horizontal coordinate h_3 is height of the forest.

6. The propagation of burning particles ahead of the fire front was studied. The particles' flight range increases with an increase in wind velocity, angle of departure, and particle temperature, and it decreases as the particle size and density increase [12–15].

7 The numerical simulation of the problem of aerodynamics of an axisymmetric forest fire shows that a large toroidal vortex forms in the vicinity of the fire. The vortex ensures heat and mass exchange between the combustion zone and the surrounding medium. To describe steady turbulent flows, one can use the equilibrium ($K - \epsilon$)-model of turbulence or the modified Prandtl model. For unsteady flows, use of a simplified model leads to significant errors in determining the temperature and velocity fields [12–15].

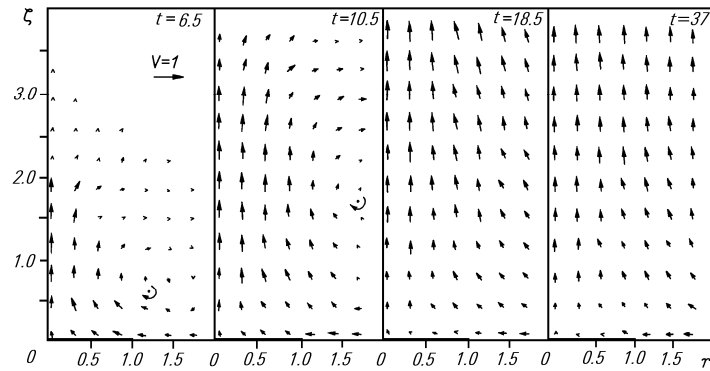


Fig.8. Vector velocity fields at various moment of time above a round (planform) forest fire source. The thick line on the abscissa indicates the size of the source

8. It is shown within the framework of the theory of thermics that the path of the center of mass of the thermic originating during a forest fire is significantly influenced by the Coriolis force [11–15].

9. A consistent mathematical model of crown forest fires is proposed that, within the framework of the laws of conservation of mass, momentum, and energy, takes into account accurately the heat and mass exchange between the near-ground atmospheric layer and the canopy during forest fires. The numerical simulation of the problem of origin and spread of a crown fire yielded a front structure identical to that obtained in experiments. Furthermore, it was established that combustion at the fire front is of a diffusion character, i.e., the combustion is limited by the indraft of oxidizer and gaseous combustible products of pyrolysis into the combustion zone. Most of the energy in this zone is released in combustion of the gaseous pyrolysis products [12-15].

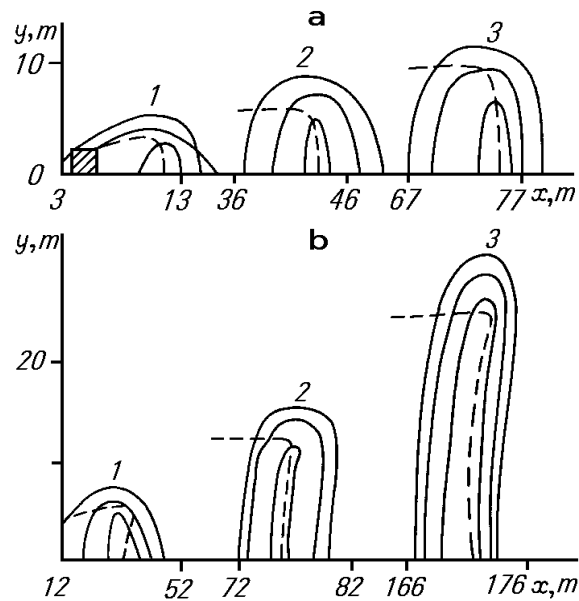


Fig.9. Isotherms at the crown forest fire front: a — $u_{\infty} = 2$ m/s; $W = 0.6$ (1 — $t = 7$ s, $\omega_x = 1.3$ m/s,

$\omega_y = 0.7 \text{ m/s}$; 2, 3 — $t = 30$ and 50 , respectively, $\omega_x = 1.5 \text{ m/s}$, $\omega_y = 0.1 \text{ m/s}$; b — $u_\infty = 5 \text{ m/s}$, $W = 0.4$ (1 — $t = 8 \text{ s}$, $\omega_x = 3.6 \text{ m/s}$, $\omega_y = 0.5 \text{ m/s}$; 2 — 20 s , 3.6 m/s , 0.5 m/s ; 3 — 50 s , 3.5 m/s , 0.5 m/s) Here ω_x and ω_y are projections of the normal speed of spread to X-axis and Y -axis [12–15]

10. Stability of the contour of a forest fire with allowance for the complex structure of the fire front was studied theoretically (by the method of small perturbations) and numerically. The forest-fire contour is absolutely unstable against small perturbations. For large forest fires, in which the linear dimensions of the fire site exceed a certain value, the contour loses its initial shape and becomes concave-convex. This result agrees well with forest-fire observations [12–15] (See Fig.9).

11. It was established numerically and by the method of small disturbances that the limiting conditions of spread of forest fires depend on the store of FF and its moisture content, wind velocity, and rate of heat and mass exchange [12–15] (See Fig.1).

12. The mathematical and physical modeling of the heat- and mass-transfer processes in forest phytocenoses during a forest fire shows that, in top crown fires that propagate in drafty forest phytocenoses, most of the energy from the fire front is transferred to the phytocenoses mainly by forced convection (by wind), where as the energy transfer by radiation plays the key role in surface fires and large-scale crown fires [12-15].

13. Simplifying assumptions made it possible to obtain approximate analytical formulas for the propagation velocity of forest surface and crown fires, density of the total thermal flux, and width of the forest-fire front. The formulas agree well with the results of numerical simulations of [12-14].

14. It is established numerically and analytically that forest-fire screen are more effective from the viewpoint of fire suppression than forest firebreaks [12, 14].

15. The mathematical modeling of transition of surface fire into crown fire shows that-for the pine forest this phenomenon occurs when the lower boundary of crowns is $h_l - h_o \approx 0.7 \text{ m}$ above the ground cover, provided that the specific thermal impulse to the canopy is more than 2600 kJ/m^2 This agrees with the experimental data of []. The radiation coefficient is a function of time and depends parametrically on the pyrogenous properties of the surface fire and forest phytocenoses. Canopy ignition is of a gas-phase character, and neglect of the two-temperature character of the medium in the canopy leads to a 40-50% decrease in the critical height of the forest canopy [15].

It was found theoretically [12–15] and experimentally [11, 12, 14] that blast waves are amplified in the interaction with the pyrolysis zone at the forest-fire front. This effect can be explained by explosion of a mixture of air and gaseous pyrolysis products. It opens up 25 new possibilities for forest-fire fighting.

The Problem of the Forest Fire Initiation. In the book [23] a critical analysis of existing methods of predicting the forest fire danger is given. It is stated that the forest fire initiation has a probability character and depends not only on the level of the anthropogenic load, the wind velocity, moisture content of the forest fuels and reactive capability of these materials. According to [23] there exist stationary and dynamic models of the forest fire danger. In the framework of the first ones a prediction for the whole forest fire season is given. In the framework of the second one the prediction is given for every day of the current season. A diagram of the forest fire initiation is presented in fig.10.

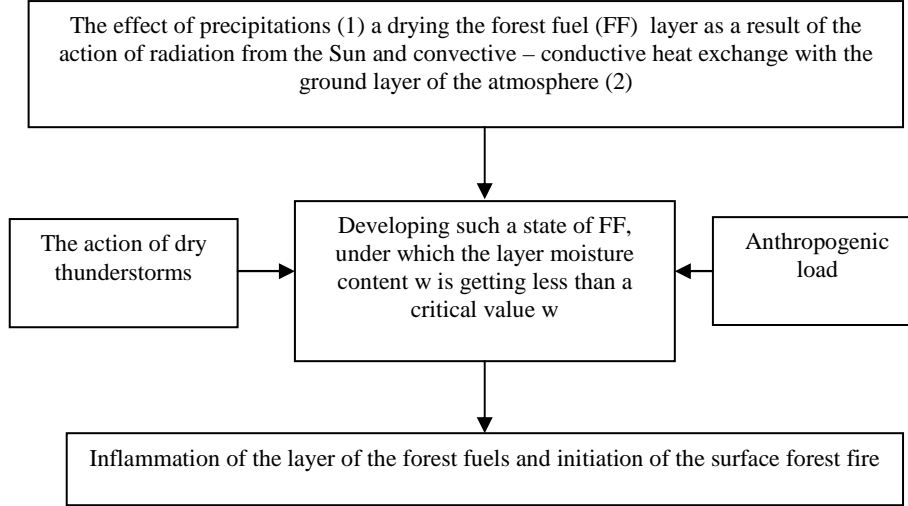


Fig. 10. Physical model of the forest fire danger

Using the theory of probabilities and physical considerations we get the following formula (a dynamic model) for estimating the probability of the forest fire initiation [23]:

$$P_j = \sum_{i=1}^N \left[P_{ij}(A) P_{ij}(III/A) + P_{ij}(M) P_{ij}(III/M) \right] P_{ij}(C), F = \sum_{i=1}^N F_i,$$

$$P_{ij}(C) = \begin{cases} 0 \\ \frac{F_i}{F} \exp \left[-(\Delta \bar{\varphi}_{ij})^2 \right] \end{cases} \quad \Delta \varphi_{ij} = \frac{\varphi_{2ij} - \varphi_{2ij}^*}{\varphi_{2ij}^*}. \quad (47)$$

Here P_j is a probability of the forest fire initiation on the controlled forest territory; F is the area of the forest territory of a particular forestry, area or region; F_i is the area of the forest territory covered with the forest of the i -th type (coniferous or deciduous species and etc); N is a total number of the forest types on the area F ; A_i is the weight multiplier characterizing the part of the forest fires

caused by anthropogenic load; $P_{ij}(A)$ is the probability of anthropogenic load sufficient for ignition of the FF; $P_{ij}(ZP/A)$ is the probability of the fire initiation caused by anthropogenic load on the area F_i ; $B(M)$ is the weight multiplier characterizing the part of the forest fires caused by thunderstorms; $P_{ij}(M)$ is the probability of initiating dry thunderstorm on the area F_i for them are given in [24];

$P_{ij}(ZP/A)$ is the probability of the forest fire initiation caused by thunderstorm under the condition, that dry thunderstorms can take place on the area F_i [24]; index j corresponds to the day of the fire danger season; $P_{ij}(C)$ is the probability of the fact, that at 3 p.m. of the local time moisture content of the FF layer will be less than critical one (the probability of the fire initiation according to meteorological conditions), φ_{2ij} and φ_{2ij}^5 are the current and critical meaning of the moisture content for the forest fuel for the ji -th time interval of the fire danger season on the i -th area of the territory covered with the forest.

Formula (47) has a probability character, that allows to use it for refining currently existing probability criterion of the atomic, enterprise safety, in the framework of which an action of the forest fires on these dangerous enterprises is not taken into account.

References

- [1] Merzhanov A.G. On quasistationary theory of z thermal explosion. Proceedings of the Academy of Sciences of the e USSR. Volume 140, N 3. 1961.
- [2] Merzhanov A.G., Abramov V.G., Yantkovskaya V.T. On the conditions of transfer from self-inflammation to ignition. Proceedings of the Academy of Sciences of the USSR. Volume 141, N 1. 1963.
- [3] Merzhanov A.G., Barzikin V.V., Gantkovskaya V.T. The problem on the source thermal explosion. Proceedings of the Academy of Sciences of the USSR, Volume 148, N 2, 1963.
- [4] Merzhanov A.G., Filonenko A.K. On the thermal self-inflammation of homogeneous gaseous mixture in the Academy of Sciences of the USSR, Volume 152, N 1. 1965.
- [5] Merzhanov A.G., Highkin B.I., Shkadinsky K.G. The Formation of a Stationary Flame Spread Caused by a gas Ignition by Heated Surface. Applied Mechanics and Technical Physics. N 5. 1969.
- [6] Merzhanov A.G., Borovinskaya I.P. Self-Spreading High Temperature Synthesis of Refractory Non-Organic Compounds. Proceedings of the Academy of Sciences of the USSR. Volume 204. 1972. N 3, p.366.
- [7] Merzhanov A.G., Nonisothermal Methods in Chemical kinetics. Physics of Combustion and Explosion. Volume 9. N 1. 1973.
- [8] Dorrer G.A. 1979, Mathematical models of forest fire dynamics. M.: Lesnaya promishlennost, 160 pages.

- [9] Konev E.V. 1977, Physical foundations of burning of Novosibirsk Vegetation materials: Nauka, 239 pages.
- [10] Valendik E.N., Matveev N.Ya., Safronov M.A. 1979 Large-scale fires., M.: Nauka, 196 p.
- [11] Grishin A.M., 1981. Mathematical modelling of forest fires. Tomsk: Publishing House of the Tomsk State University, 277 p.
- [12] Grishin A.M., 1992. Mathematical modelling of forest fires and new methods of fighting them. Novosibirsk: Nauka, 407 p.
- [13] Grishin A.M. A general model of forest fires and its application. // *Fiz. Goreniya Vzryva* *, 1996, v. 32, No. 5, p. 35-54.
- [14] Grishin A.M. 1997 Mathematical modelling of forest fires and new methods of fighting them (Translated by Marek Czuma, Chikina and L. Smokotina; Edited by Frank Albini) , Tomsk: Publishing House of the Tomsk State University, 390 p.
- [15] Grishin A.M. General Mathematical Models of the Forest and Peat Fires and Their Application // *Successes of Mechanics*. Volume 1. N 4. 2002. p.p. 41 – 89.
- [16] Tikhonov A.N., Arsenin V.Ya., 1986. Methods of solving non-correct problems. M.: Nauka, 287 p.
- [17] Grishin A.M., Ephimov K.N., Subbotin A.N., Yakimov A.S. 2004. Iteration-interpolation method and its application. Tomsk: Publishing House of the Tomsk State University, 319 p.
- [18] Patankar S.V. Numerical methods of solving problems of heat exchange and liquid dynamics. M.: Energoatomizdat, 1984, 152 p.
- [19] Grishin A.M., Zinchenko V.I., Kuzin A.Ya. и др. 2006. Solution of some non-correct inverse problems of mechanics of reactive. Tomsk: Publishing House of the Tomsk State University, 418 p.
- [20] Weber R.O. 1990 Modelling fire spread through fuel beds // *Prog. Everg. Combust. Sci*, vol. 17, p.65-82.
- [21] Linn R.R. A Transport Model for Prediction of Wild fire Behavior Los Alamos National laboratory, USA, 1995, 195 p.
- [22] Porterie B., Morvan D., Larini M., Lorand J.C. Wild fire Propagation. A two-dimensional Multiphase Approach // *Physica gorenia e vzryva Russia*, 1998, № 2. P. 261–278.
- [23] Grishin A.M. Modelling and Prediction of the Catastrophies. Tomsk, Publishing House of the Tomsk State University, 2003. P.523.
- [24] Grishin A.M. Forest Fire Physics. Tomsk, Publishing House of the Tomsk State University, 1999. P.P. 207.

* From the day of foundation in 1985 the “Physics of burning and explosion” magazin has been published in USA in English by Publishing House “Plenum Publishing Corporation” under the title “Combustion Explosion and Shock Waver”.

**ՀԱՅԱՍՏԱՆԻ ՀԱՆՐԱՊԵՏՈՒԹՅԱՆ ԳԻՏՈՒԹՅՈՒՆՆԵՐԻ
ԱԶԳԱՅԻՆ ԱԿԱԴԵՄԻԱ
НАЦИОНАЛЬНАЯ АКАДЕМИЯ НАУК РЕСПУБЛИКИ
АРМЕНИЯ**

Հայաստանի քիմիական հանդես **60, №2, 2007** Химический журнал Армении

**ON THE MECHANISM ACTIVATION OF HYDROGEN AND HYDROCARBONS ON
THE CARBIDES AND HYDRADES OBTAINED
BY NON-ISOTHERMAL CONDITIONS**

P. S. GUKASYAN

Institute of Chemical Physical of NAS of Armenia, Yerevan
P. Sevak str. 5/2, Yerevan, RA.

Activation of $ZrNiH_3$ hydride and TiC_x carbides obtained by Self-propagating-High Temperature Synthesis (SHS) method, as well as of natural clinoptilolite was investigated by hydrogen and hydrocarbon in non-isotherm conditions. Positive influence of small quantities of oxygen was observed on activation process. It has been shown that after preliminary activation of carbides and the zeolite surface modified by Cr_2O_3 can be used as substrate in CO hydration process carried out by spillover method in soft conditions. The modified zeolite or activated carbide combined with hydrogen activator, in our case $ZrNiH_3$ hydride, can be efficiently used for rendering harmless the CO toxic gas ejecting into atmosphere, particularly turning it into useful hydrocarbons. The mechanism of hydride and carbide activation, and CO hydration by Spillover method had been discussed.

Introduction

Hazardous carbon monoxide resulting from chemical processes is ejected into environment. The abolition and utilization of even small quantities of this gas is a serious ecological problem. CO is usually oxidized and utilized due to expensive catalytic systems based on noble metals – Pt, Pd, etc. Highly oxidative substances, such as H_2O_2 , are also used for CO oxidation. Along with these the development of new methods and approaches is actual, which could be more efficient for the utilization of this compound. Especially actual are those that are based on the use of less expensive catalysts and are able to carry on the utilization process at less temperatures. It is of great importance for the utilization of this gas to have it converted into valuable compounds – into hydrocarbon and other organic compounds. From this viewpoint the hydration of CO by hydrogen spillover method could be of interest [1,2], which is the main objective of present investigation. By this method, activated hydrogen is formed on solid material surface, which, with surface spillover is taken to corresponding adsorbent and is used as a reaction component. In this case it is necessary to have efficient of CO adsorbents. According to literature data Cr_2O_3 has a quality of this kind. It is precipitated on Armenian natural zeolite, which has a big surface, and the modified zeolite is used as heterogeneous catalyst for $CO + H_2$ reaction. $TiC_{0.6}$ activated carbide was used as an inert carrier in some experiments.

Experimental

Investigations have been carried out in a reactor of special construction, made for that very purpose, the scheme of which is shown in Fig 1.

The hydrogen participating in hydration is activated in I reaction zone, then it is transferred to II reaction zone, via surface, where it reacts with CO adsorbed on carrier substrate. This is a unique means of bifunctional catalysis, the advantage of which over other catalytic methods is that in this case only one of reagents, the relatively pure one, contacts with catalyst, the other reagents (in our case CO) and the products formed by them do not contact with hydrogen activator, which excludes the toxication of the latter in reactional environment.

As we have already mentioned, the obtaining of active hydrogen should be carried out in the first stage of the process. As hydrogen activator, in our case, ZrNiH_3 hydride obtained by method of self-propagating high temperature synthesis (SHS) at Institute of Chemical Physics NAS Armenia, was used [3].

Results and Discussion

Activation of hydride

The construction of reactor allows obtaining active hydrogen from hydride without pausing the process – in dynamic conditions. Here is how it is realized: a glass-net, on which 1cm thick hydride layer was put, was installed in horizontal section in a 2 cm perimeter Pyrex tube put vertically. The tube-reactor containing hydride was installed in electric stove.

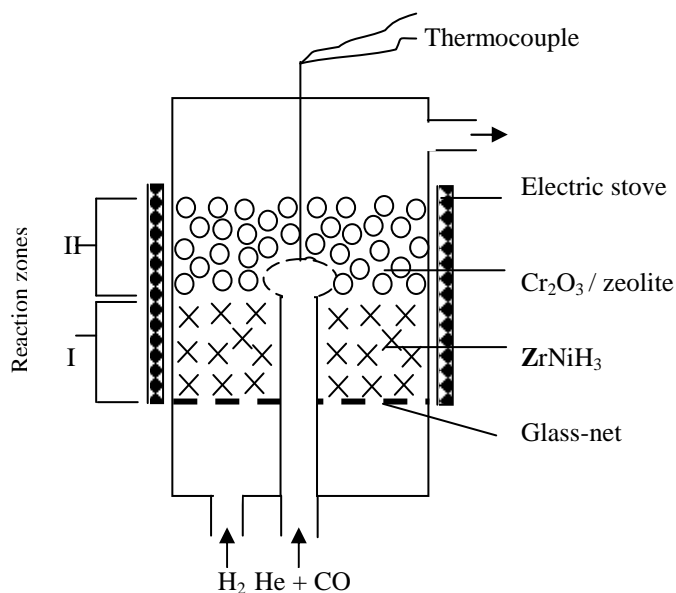


Fig.1. Reactor scheme.

A hydrogen flow of atmospheric pressure was released in $\sim 12 \text{ cm}^3 \text{ min}^{-1}$ constant speed through hydride layer and the stove temperature was slowly risen ($\sim 10 \text{ degrees.min}^{-1}$). Up to 300°C no hydrogen flow change has been encountered. At temperatures higher than that H_2 flow rate self-increase was observed.

If the hydride temperature is kept constant in those conditions, than in ~20 minutes the flow increases, reaches the highest value and again decreases – reaching the previous value. After that no more changes are being encountered. Such hydrogen flow rate change occurs in case of every temperature increase. Increasing and decreasing the hydride temperature many times, it, the hydride, is not only brought to active state, but its activation threshold temperature decrease is observed.

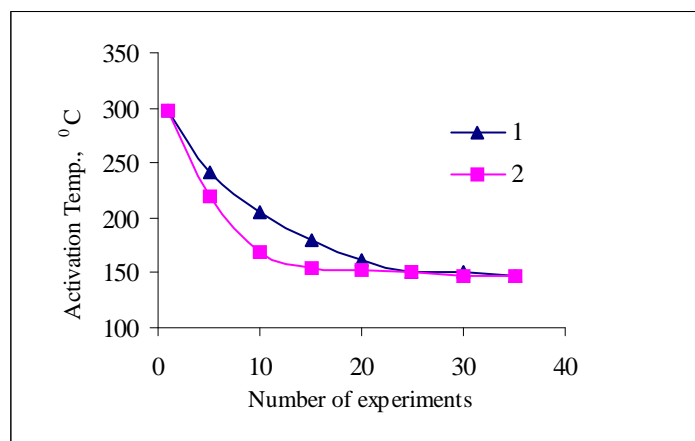
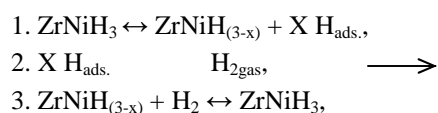


Fig. 2. *ZrNiH₃ activation threshold temperature dependence from the number of activating experiments: 1 – by pure hydrogen; 2 – 1% oxygen is added to hydrogen.*

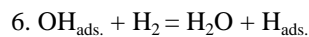
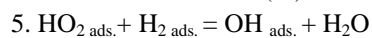
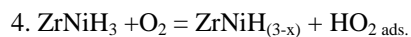
In our experiments we have succeeded in decreasing it from 300 °C up to 150 °C (see Fig. 2, Curve 1). Hydride properties, activated in that way, are maintained for a long time. This way of hydrogen activation provides a process with stable regime, therefore - reproducible results. Obtained experimental data can be explained in the following way: the activated hydride is in direct and reverse heterogeneous-homogeneous reactions with molecular hydrogen. The balance established among hydrogen amounts having been separated from the hydride and those again joining it are carried out by means of the following reactions:



where X is the hydrogen amount having been separated from one mol of hydride.

Considering the fact, that the presence of the smallest amount of molecular oxygen very often results in heterogeneous catalyst surface state variation, than it was of interest to find out such influence of oxygen on hydride activation process. Experiments showed that if we add only 1% O₂ to hydrogen flow, the activation threshold temperature is established in fewer cases of experiments (see Fig.2, Curve 2). Most probably in the presence of oxygen the decrease in number of activation threshold experiments is conditioned by hydrogen oxidation reactions taking place on the surface. Perhaps in this

case such reactions result in the increase of the number of active centers present on the surface. That process can be presented as follows:



According to reactions mentioned above, in the presence of oxygen, besides H atoms, OH and HO₂ radicals are also formed on the surface, which provide more efficient course of oxygen activation, than is in case of only molecular hydrogen (see Fig.2).

Hydride Surface Microstructure

Considering the fact, that during heterogeneous catalytic processes surface state as well as surface layer morphological changes take place, ZrNiH₃ initial and activated states surfaces' microstructures have been thoroughly studied (see Fig.3).

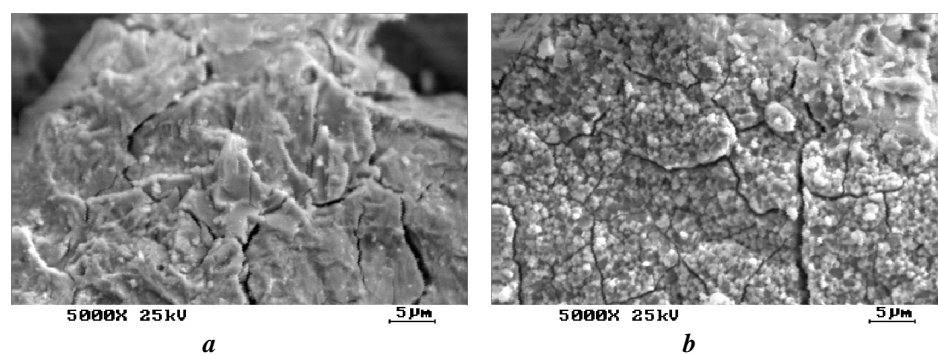


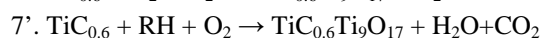
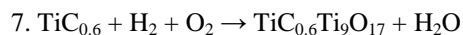
Fig. 3. Not activated (a) and activated (b) ZrNiH₃ hydride surface microstructure.

Investigations have been realized by “BS-300” electronic microscope connected to the computer Pentium III. Fig. 3a and Fig. 3b comparison shows, that in activated state the surface becomes rough, acquires fine porous structure, and covers with fine grind particle formations. Data evaluations presented in figures show, that diameter of particles reaches 3-5 μm. Investigations have shown that microstructures of samples surfaces activated by pure hydrogen and those by hydrogen-oxygen mixture are the same. These morphological changes of the surface result in surface area increase, which, in its turn, results in reaction rate increase, and is observed in experiment.

Activation of carbide

The TiC, TiC_{0.8} and TiC_{0.6} carbides obtained by the method SHS [4]. Activation this carbides by hydrogen and hydrocarbon with presence of small quantities of oxygen was also implemented by hydride activation method. It has been shown, that TiC_{0.6} carbide is most effectively subjected to activation. X-ray phase analysis of the latter has shown, that activated sample contains not only TiC_{0.6}, but Ti₉O₁₇ phases as well [5].

The summary activation mechanism of $\text{TiC}_{0.6}$ carbide by hydrogen and hydrocarbon may be expressed by reaction



Activation and modification of clinoptilolite

In the second stage of the process CO hydration by means of active hydrogen is realized on carrier-substrate. As carrier-substrate, in our case, the RA Novemberyan region clinoptilolite zeolite modified by Cr_2O_3 oxide, was used. The choice of clinoptilolite is conditioned by the fact, that with its natural supplies, its purity and qualitative properties, it has productive importance.

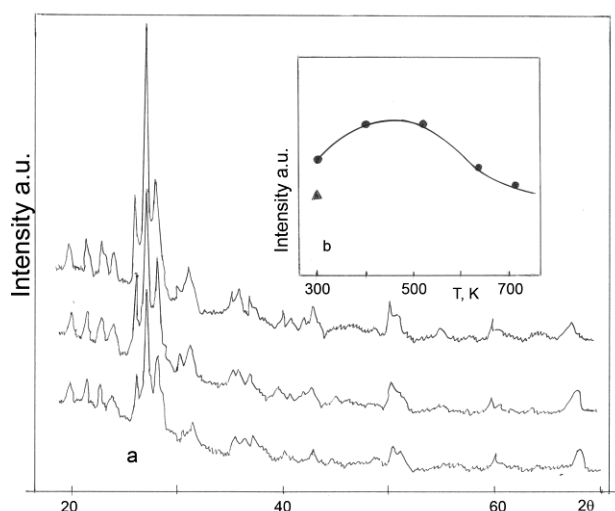


Fig.4. a) XRD spectra of the clinoptilolite activated at different conditions 1-300K, $P=760$ Torr; 2-300K, $P=10^{-2}$ Torr. b) ▲- $P=760$ Torr and; ●- $P=10^{-2}$ at different temperatures.

After preliminary cleaning the natural zeolite was ground and fractionated. A 0.02-0.03 cm fraction was used, which, according to literature data [1], is considered optimal for such cases. The X-ray phase analysis has shown, that the raw zeolite used by us contains quite a big amount of water. That is why it was subjected to thermal treatment under $\sim 10^{-2}$ Torr pressure. X-ray phase analysis was carried out by means of Dron-2D diffractometer. Experiments have shown, that depending on treatment conditions, the intensity of the main components' crystalline states existing in the content of zeolite, passes through maximum (see Fig.4).

As we see the crystalline state's quantity of SiO_2 in the range of 250-300 °C is the biggest. Surface microstructure investigation [6,7] has also been carried out in this range, which shows, that the surface acquires fine porous structure ($\sim 1-2 \mu\text{m}$). The clinoptilolite having been subjected to such treatment was used as a carrier-substrate, on which the Cr_2O_3 was precipitated. The choice of the latter is conditioned by the fact, that compared to CO it has high adsorption properties, which has significant importance in heterogeneous hydration processes of carbon monoxide. Control experiments have been

carried out for being convinced of it. For that purpose, “Ch. c” marked Cr_2O_3 was ground by vibration mill for 4 hours, particles having $\sim 1 \mu\text{m}$ size, were obtained. Then the clinoptilolite surface was covered by suspension of that powder. After drying the zeolite, a thin layer of oxide was left on its surface.

Zeolite particles, having been subjected to such treatment, by a 1cm layer were put on the hydride present in the reactor. The hydrogen being filtered through activated hydride provides stable yield of H atoms. The latter get transferred to zeolite surface by means of the spillover, where they react with CO given by a separate tube.

Carbon Monoxide Hydration

Experiments were realized as follows: the molecular hydrogen with the rate of $12\text{cm}^3\text{min}^{-1}$, has been given through the lower part of reactor (Fig.1), and CO mixed with He in 5:1 ratio, with the rate of $2\text{cm}^3\text{min}^{-1}$ has been given to clinoptilolite modified by Cr_2O_3 , 0.3 cm above hydride layer. Hydration is observed starting from 180°C . Temperature increase results in hydration process rate increase.

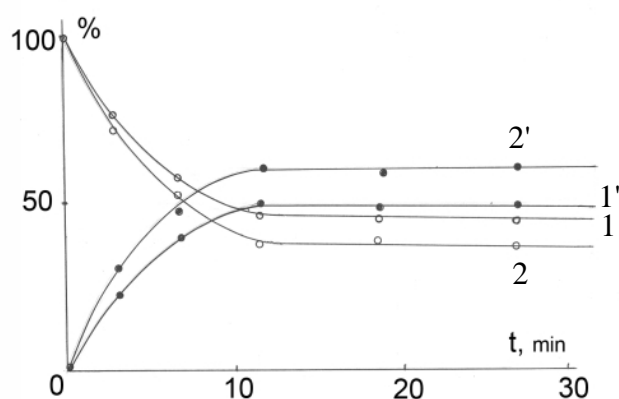
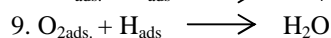
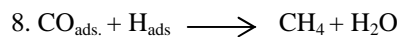


Fig. 5. CO hydration kinetics by spillover method: 1 – CO waste, 2 – methane accumulation 1, 2 – The inert carrier is activated and modified clinoptilolite. 1', 2' – The inert carrier is $\text{TiC}_{0.6}$.

Fig. 5 shows the waste of CO and accumulation of methane for two conditions. The results of CO hydration experiments at 230°C . In these conditions about 60% of CO turns to methane. In the case when the carrier substance is the activated $\text{TiC}_{0.6}$ the CO waste enhanced 62%. The main products of the reaction are CH_4 and H_2O . High hydrocarbons appear in tiny amounts.

Oxygen additions have interesting effect on hydration process. If oxygen, to extent of CO quantities, together with H_2 is given to I zone (Fig.1), than it does not have essential effect on hydration process. But if O_2 is given to II zone together with He + CO mixture, on zeolite surface modified by Cr_2O_3 (Fig.1), than CO hydration decrease is observed. This is a result of the fact, that active hydrogens, which get transferred from I zone to II zone, react also with O_2 , which results in the decrease of their

concentration and therefore in the decrease of CO conversion rate. It can be presented by competing reactions 7 and 8.



It is natural, that in case of O_2 absence the rate of reaction 8 will increase. Therefore, in hydration process CO should be in advance cleaned from oxygen. By special experiments it has been shown, that by using not activated hydride and not modified clinoptilolite, no CO hydration is observed in conditions mentioned above.

К МЕХАНИЗМУ АКТИВАЦИИ ВОДОРОДА И УГЛЕВОДОРОДА НА ГИДРИДАХ И КАРБИДАХ, ПОЛУЧЕННЫХ В НЕИЗОТЕРМИЧЕСКИХ УСЛОВИЯХ

П. С. ГУКАСЯН

Изучен процесс активации гидрида ZrNiH_3 , карбидов TiC_x водородом и углеводородом, а также клиноптилолита в неизотермических условиях. Наблюдалось промотирующее действие следов кислорода на процесс активации. ZrNiH_3 и TiC_x синтезированы методом высокотемпературного самораспространяющегося синтеза. Показано, что активированный гидрид или карбид, комбинированный с модифицированным клиноптилолитом, можно успешно использовать для гидрирования CO в мягких условиях. Рассмотрен механизм активации гидрида и карбида водородом и углеводородом, а также гидрирование CO методом спилловера водорода.

ՈՉ ԻԶՈԹԵՐՄ ՊԱՅՄԱՆՆԵՐՈՒՄ ՍՏԱՑՎԱԾ ՀԻԴՐԻԴԻ ԵՎ ԿԱՐԲԻԴՆԵՐԻ ՎՐԱ ՋՐԱԾՆԻ ԵՎ ԱԾԽԱԶՐԱԾԻՆՆԵՐԻ ԱԿՏԻՎԱՑՄԱՆ ՄԵԽԱՆԻԶՄԻ ՄԱՍԻՆ

Պ. Ս. ՂԱԻԿԱՍՅԱՆ

Հետազոտվել է բարձրջերմաստիճանային ինքնատարածման սինտեզի (ԲԻՍ) մեթոդով ստացված ZrNiH_3 հիդրիդի և TiC_x կարբիդների, ինչպես նաև բնական կլինոպտիլոլիտի ջրածնով և ածխաջրածնով ակտիվացումը ոչ իզոթերմ պայմաններում: Նկատվել է թթվածնի հետքերի դրական ազդեցությունը ակտիվացման գործընթացի վրա: Ցույց է տրվել որ ակտիվացումից հետո հիդրիդը և կարբիդները զուգակցելով ակտիվացված և մոդիֆիկացված ցեոլիթի հետ, էֆեկտիվ կերպով իրականացնում են CO-ի հիդրում մեղմ պայմաններում: Քննարկվել է հիդրիդի և կարբիդի վրա ջրածնի ակտիվացման և CO-ի հիդրման ժամանակ ածխաջրածնի առաջացման մեխանիզմը:

References

- [1] Poladyan E.A., Gukasyan P.S., Nalbandyan A.B.// DAN USSR, 1984, v.274, №6, p.1417.
- [2] Gukasyan P.S., Mantashyan A.A.// Chem.J.Arm., 1996, v.49, №4, p.81.
- [3] Akopyan A.G., Dolukhanyan S.K., Merzhanov A.G.// Problems of Technological Burning, Chernogolovka, 1981, v.2, p.35.
- [4] Kharatyan S.L., Sardaryan Yu.S., Sarkisyan A.A., Merzhanov A.G.// J Chem. Phys, 1984, v.3, №11, p.1604.
- [5] Hovannesian Ts. K., Gukasyan P.S., Nalbandyan A.B.// Arm. Chim. J., 1988, v.41, №1-2, p.50.
- [6] Gukasyan P.S., Grigoryan G.L.// Investigation of clinoptilolite's surface modified by Cr_2O_3 used in CO hydration process by means of electronic microscope; The 11th Conferece of AEMS, Yerevan, November 20-21, 2003, p.58.
- [7] Gukasyan P.S., Grigoryan G.L.// Information Technologies and Management, 2006, №1, p.130.

**ՀԱՅԱՍՏԱՆԻ ՀԱՆՐԱՊԵՏՈՒԹՅԱՆ ԳԻՏՈՒԹՅՈՒՆՆԵՐԻ
ԱԶԳԱՅԻՆ ԱԿԱԴԵՄԻԱ
НАЦИОНАЛЬНАЯ АКАДЕМИЯ НАУК РЕСПУБЛИКИ
АРМЕНИЯ**

Հայաստանի քիմիական հանդես **60, №2, 2007** Химический журнал Армении

УДК 536.46:546.28:546.621

**ЗАКОНОМЕРНОСТИ ГОРЕНИЯ СИСТЕМЫ $\text{SiO}_2\text{-Al-N}_2$ И СВ СИНТЕЗ
МОНОСИАЛОНА И КОМПОЗИТОВ НА ОСНОВЕ НИТРИДА КРЕМНИЯ**

Л. С. АБОВЯН и С. Л. ХАРАТЯН

Институт химической физики им. А.Б. Налбандяна
НАН Республики Армения, Ереван
Ереванский государственный университет

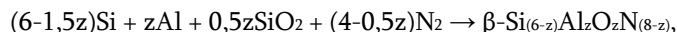
Исследована возможность СВ синтеза композита $\text{Si}_3\text{N}_4/\text{Al}_2\text{O}_3$ и однофазного сиалона (моносиалона) при относительно низких давлениях азота (0,1-6,0 МПа) с использованием диоксида кремния (кварцевого песка) в качестве кремниевого сырья. Выявлены основные факторы, влияющие на закономерности горения системы $\text{SiO}_2\text{-Al-N}_2$, полноту азотирования кремния, а также микроструктуру и состав конечных продуктов. Показано, что азотирование смесей $\text{SiO}_2\text{-Al}$ и $\text{SiO}_2\text{-Al-Si}_3\text{N}_4(\text{Al}_2\text{O}_3)$ в режиме горения всегда сопровождается образованием сиалонов (SiAlON). При этом в зависимости от количества и природы разбавителя (Si_3N_4 , Al_2O_3) получаются композиты $\text{Si}_3\text{N}_4\text{-Al}_2\text{O}_3\text{-SiAlON}$ с различным содержанием компонентов и свободного кремния. Состав и микроструктуру композитов можно контролировать изменением соотношения составляющих в исходной смеси и давления газовой среды. Установлено, что при горении смесей $\text{SiO}_2\text{-Al-Si}_3\text{N}_4$ при низких давлениях азота можно синтезировать моносиалон $\text{Si}_3\text{Al}_3\text{O}_3\text{N}_5$ и композит $\text{Si}_3\text{N}_4/\text{Si}_3\text{Al}_3\text{O}_3\text{N}_5$ с различным содержанием нитрида кремния.

Рис. 8, библи. ссылок 8.

Горение системы $\text{SiO}_2\text{-Al-N}_2$ представляет интерес с целью одностадийного синтеза нитридной керамики и моносиалона или композита на его основе. В этой системе процесс горения сопровождается различными химическими и физическими превращениями и в зависимости от условий процесса возможно образование однофазных или многофазных продуктов. Предполагается также, что при обеспечении необходимых условий горения системы $\text{SiO}_2\text{-Al-N}_2$ можно синтезировать однофазный сиалон и композит на основе нитрида кремния.

Как показано в работах [1-4], азотирование кремния и/или его соединений при высоких давлениях азота (30-200 МПа) обеспечивает не только получение тугоплавких соединений и практически беспористых материалов с высоким содержанием азота и контролируемой микроструктурой, но и изделий из нитрида кремния и композитов на его основе. При высоких давлениях получены также однофазные сиалоны и композиты на их основе.

Образование сиалоновой керамики (сиалон и композиты на его основе: SiAlON-SiC, SiAlON-BN, SiAlON-SiC-BN, SiAlON-TiN) в режиме CBC при высоких давлениях азота (150 МПа) обычно представляется в виде реакции:



где коэффициент z меняется в пределах 1-5.

Для оптимизации условий синтеза в состав исходных компонентов вводятся разбавители ($\beta\text{-Si}_{(6-z)}\text{Al}_z\text{O}_z\text{N}_{(8-z)}$, SiC, TiB₂ и др.) и регуляторы спекания – нитрид бора или элементарный бор, обеспечивающие образование нитрида бора в процессе горения [1-4].

Керамические материалы на основе нитрида кремния (например, Si₃N₄-Y₂O₃, Si₃N₄-MgO, Si₃N₄-BN, Si₃N₄-Al₂O₃, Si₃N₄-B₄C) обычно изготавливаются по технологии горячего прессования или спекания смесей, включающих отдельно синтезированные компоненты. Использование различных наполнителей спекания (Al₂O₃, Y₂O₃, MgO) обеспечивает более высокие характеристики керамических материалов при изготовлении режущих инструментов или их работы в агрессивных химических средах в составе конструкционных материалов. Керамические материалы на основе сиалона, в том числе двухфазные композиты, аналогично нитридной керамике, применяются также в составе инструментальной и конструкционной керамики [1-4]. Ряд сиалонов ($\beta\text{-Si}_4\text{Al}_2\text{O}_2\text{N}_6$, $\beta\text{-Si}_2\text{Al}_4\text{O}_4\text{N}_4$ и $\beta\text{-Si}_3\text{Al}_3\text{O}_3\text{N}_5$) получают из пирофилита (Al₂O₃·4SiO₂·H₂O) и каолина (Al₂O₃·2SiO₂·2H₂O) с использованием метода карботермического восстановления и азотирования [5].

В работах [6-8] нами исследованы закономерности горения модельной системы 3SiO₂-4Al-3C с целью выяснения возможности использования кварцевого песка в качестве кремниевого сырья для одностадийного синтеза композита SiC/Al₂O₃ и определения оптимальных условий проведения процесса.

Цель настоящей работы: а) исследование закономерностей горения системы 3SiO₂-nAl-N₂ при низких давлениях азота с использованием кварцевого песка в качестве сырья кремния вместо полупроводникового кремния или его смеси с диоксидом кремния, применяемых в исследованиях [1-4]; б) изучение возможности получения композита Si₃N₄/Al₂O₃, а также однофазного сиалона и его композитов в режиме горения азотированием смесей 3SiO₂-nAl при наличии разбавителей (оксид алюминия или нитрид кремния); в) определение оптимальных условий синтеза композитов на основе нитрида кремния и моносиалона нужного состава.

Экспериментальные результаты и их обсуждение

Методика эксперимента. Эксперименты проводились в бомбе постоянного давления в среде газообразного азота. Для приготовления исходных смесей использовались: измельченный кварцевый песок, поликристаллический кремний Кр-1 и CBC-нитрид кремния, порошкообразный алюминий марки АСД-4, оксид алюминия марки “ч.д.а.” с размером частиц менее 50 мкм. Из исходных смесей изготавливались цилиндрические образцы диаметром 30 мм и высотой 35-55 мм (свободная засыпка в стакане из

металлической сетки) и сжигались в атмосфере азота путем инициирования волны горения с помощью нагретой электрическим током вольфрамовой спирали (с верхнего торца образца). Относительная плотность (Δ) образцов составляла 0,4-0,5, а давление азота менялось в интервале от 0,1 до 6,0 МПа. Для измерения температуры (T_r) и скорости (U_r) горения использовались вольфрам-рениевые термопары диаметром 0,2 мм. Управление экспериментом и запись сигналов термопар осуществлялись с помощью подключенного к установке персонального компьютера.

Сгоревшие образцы подвергались рентгенофазовому (на дифрактометре “ДРОН-3,0”) и химическому (определялось содержание азота и свободного кремния) анализам. Микроструктуры изломов образцов изучались с помощью растрового электронного микроскопа “BS-300”.

Закономерности горения системы $3SiO_2-nAl-N_2$. При горении смесей $3SiO_2-nAl$ при низких давлениях азота процесс азотирования осуществляется в режиме фильтрационного горения аналогично случаю горения пористых металлических и неметаллических образцов. При этом существенное влияние на закономерности горения и на конечный состав продуктов оказывают состав исходной смеси, давление азота, плотность и диаметр образцов, наличие разбавителей в исходной смеси и т.д.

В рамках проведенных экспериментов изучались закономерности горения системы $3SiO_2-nAl-N_2$ (где $n=2-6$) в зависимости от следующих параметров: состава исходной шихты, давления газа, количества алюминия, разбавителя и поликристаллического кремния в исходной смеси.

Для нахождения оптимальных режимов реализации процесса проводился предварительный термодинамический анализ исследуемых систем. Возможность осуществления реакции SiO_2-Al-N_2 в режиме горения для стехиометрической и нестехиометрических смесей при наличии и отсутствии разбавителей исследовалась по программе “THERMO”, разработанной в ИСМАН РФ. Были рассчитаны равновесный состав продуктов сгорания и адиабатическая температура горения ($T_{ад}$).

Согласно термодинамическим расчетам, в системе $3SiO_2-4Al-2N_2$ при наличии необходимого количества (или избытка) газообразного азота и отсутствии разбавителя образуются многофазные продукты: Si_3N_4 (тв.), Al_2O_3 (тв., ж.), AlN (тв.), Si (ж.), SiO (г.). Изменение давления газовой среды начиная с 4,5 МПа не оказывает существенного влияния на содержание жидкого кремния в конечном продукте. Уменьшение количества или полное исчезновение Si (ж.) в продуктах сгорания наблюдается лишь при разбавлении исходной смеси оксидом алюминия или нитридом кремния.

Экспериментальные исследования горения системы $3SiO_2-4Al-N_2$ при различных давлениях азота показали, что в результате азотирования, вместо ожидаемых тройных композитов $Si_3N_4-Al_2O_3-AlN$ с разным содержанием свободного кремния, получаются многофазные продукты с различным содержанием компонентов: Si , $Si_3Al_3O_3N_5$, $Si_3Al_6O_{12}N_2$, $\alpha-Al_2O_3$, следы $\beta-Si_3N_4$ (подтверждено химическим и рентгенофазовым анализами). При этом увеличение давления азота приводит к росту U_r и незначительному уменьшению T_r , а также к повышению количества свободного кремния ($m_{Si(своб.)}$) и уменьшению содержания

связанного азота (m_N) в продуктах сгорания (рис.1). Анализ термограмм горения при различных давлениях азота приводит к выводу, что указанное явление (резкое уменьшение m_N) может быть обусловлено значительным увеличением скорости роста температуры по мере повышения давления, приводящего к быстрому закупориванию пор в образце в результате плавления реагентов. Последнее, в свою очередь, приводит к фильтрационным затруднениям поступления газообразного реагента в зону реакции и уменьшению длительности зоны догорания в волне горения, что в конечном итоге снижает степень азотирования реагентов.

Результаты, представленные на рис.2, получены при фильтрационном горении смесей $3SiO_2-nAl$ в среде азота ($P_{N_2}=5,0$ МПа) при варьировании количества алюминия ($n(Al)$) в исходной смеси. Из рисунка видно, что с ростом величины параметра n температура и скорость горения системы $3SiO_2-nAl-N_2$ увеличиваются. При этом, как и в предыдущем случае (рис.1), развиваемая в волне горения температура превышает значение температур плавления алюминия, кремния и SiO_2 , что может вызывать фильтрационные затруднения для подвода азота в реакционную зону. К тому же, снижению степени азотирования кремния и увеличению его содержания в свободном виде в конечных продуктах способствует частичная диссоциация образовавшегося Si_3N_4 , усиливающаяся с повышением содержания алюминия в исходной смеси.

По данным рентгенофазового и химического анализов, в исследованном интервале изменения $n(Al)$ получаются многофазные продукты с различным содержанием азота (от 7 до 10%, с минимальным значением m_N при $n=5$) и свободного кремния (от 1 до 10%, с максимальным значением $m_{Si(free)}$ при $n=4$). В зависимости от значения параметра n продукты горения имеют следующий фазовый состав:

- SiO_2 , $Si_3Al_6O_{12}N_2$, $Si_3Al_3O_3N_5$ (при недостатке восстановителя: $n=2$),
- Si , $Si_3Al_6O_{12}N_2$, $Si_3Al_3O_3N_5$, $\alpha-Al_2O_3$ (при стехиометрии: $n=4$),
- Si , $Si_3Al_3O_3N_5$, $\gamma-Al_2O_3$, $\epsilon-Al_2O_3$ (при избытке восстановителя: $n=6$).

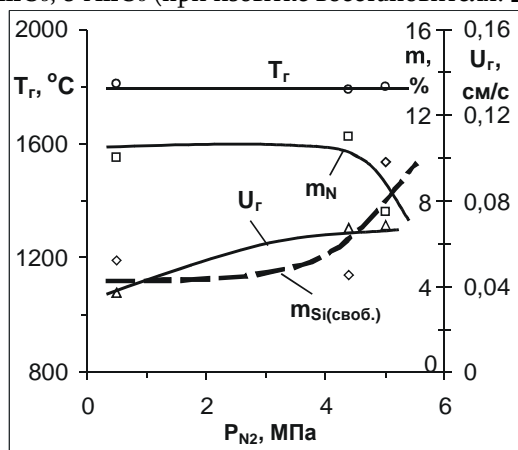


Рис. 1. Зависимости температуры (T_r) и скорости (U_r) горения, содержания азота (m_N) и свободного кремния ($m_{Si(своб.)}$) в конечном продукте от давления азота для смеси $3SiO_2+4Al$.

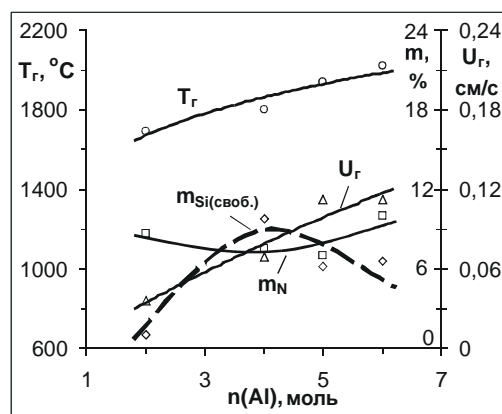
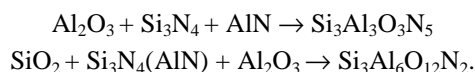


Рис. 2. Зависимости температуры (T_g) и скорости (U_g) горения, содержания азота (m_N) и свободного кремния ($m_{Si(своб.)}$) в конечном продукте от количества алюминия в исходной смеси $3SiO_2+nAl$ при ее горении в азоте ($P_{N_2}=5,0$ МПа).

В процессе горения, кроме восстановления SiO_2 , азотирования алюминия и восстановленного кремния, возможно также образование оксинитридов, в том числе и сиалонов, по следующим реакциям:



С целью улучшения условий азотирования кремния и подавления диссоциации Si_3N_4 , а также уменьшения числа образующихся фаз в конечном продукте был применен способ разбавления исходной шихты конечными продуктами. В качестве разбавителей при горении системы **3SiO₂-nAl-N₂** использовались оксид алюминия или нитрид кремния. Такой подход, на наш взгляд, может привести к получению моносиалонов и композитов Al_2O_3/Si_3N_4 , $Al_2O_3/Si_3Al_3O_3N_5$ или $Si_3N_4/Si_3Al_3O_3N_5$.

Согласно результатам проведенных исследований, введение различных разбавителей в исходную шихту при горении системы **3SiO₂-4Al-N₂** приводит к снижению T_g и U_g , $m_{Si(своб.)}$ и повышению m_N в конечном продукте (рис. 4). При этом, однако, продукты остаются многофазными. Так, при разбавлении исходной шихты оксидом алюминия конечный продукт имеет следующий фазовый состав: $Si_3Al_3O_3N_5$, $\alpha-Al_2O_3$, $Si_3Al_6O_{12}N_2$ и следы $\beta-Si_3N_4$, а при использовании нитрида кремния в качестве разбавителя получается многофазный продукт, содержащий $\beta-Si_3N_4$, $Si_3Al_3O_3N_5$, $Si_3Al_6O_{12}N_2$.

Электронно-микроскопические исследования продуктов сгорания свидетельствуют (рис.3, а-е), что микроstructures конечных продуктов во многом определяются составом исходной смеси. Наблюдается существенное различие в микроstructures при отсутствии (рис.3, а-в) и наличии (рис.3, г-е) разбавителей в исходной смеси.

Исходя из полученных результатов были проведены дальнейшие исследования по горению системы **3SiO₂-nAl-N₂** для оптимизации исходной смеси по следующим параметрам: а) количество алюминия $n(Al)$ при одинаковом количестве разбавителя Al_2O_3 в исходной смеси; б) количество разбавителя $k(Si_3N_4)$ и в) количество поликристаллического кремния

$f(\text{Si})$ при одном и том же содержании алюминия. Необходимость проведения подобных исследований частично обусловлена использованием в качестве восстановителя металла (Al), способного взаимодействовать с азотом в процессе горения. В конечном итоге все эти исследования были направлены на: а) увеличение степени азотирования кремния или алюминия и уменьшению содержания свободного кремния в конечном продукте; б) исключение возможности образования сложного оксинитрида $\text{Si}_3\text{Al}_6\text{O}_{12}\text{N}_2$, а также простых оксинитридов в конечных продуктах; в) обеспечение синтеза моносилалона $\text{Si}_3\text{Al}_3\text{O}_3\text{N}_5$ и композиций на основе Si_3N_4 или $(\text{Si}_3\text{Al}_3\text{O}_3\text{N}_5)$; г) выяснение возможности образования моносилалона (например, $\text{Si}_4\text{Al}_2\text{O}_2\text{N}_6$), отличающегося по составу от $\text{Si}_3\text{Al}_3\text{O}_3\text{N}_5$.

Влияние содержания алюминия в исходной смеси на закономерности горения и фазообразования изучалось на системе $3\text{SiO}_2\text{-nAl-1,5Al}_2\text{O}_3\text{-N}_2$. Влияние же количества нитрида кремния и поликристаллического кремния на параметры горения и состав продуктов исследовалось на системах $3\text{SiO}_2\text{-6Al-kSi}_3\text{N}_4\text{-N}_2$ и $\text{SiO}_2\text{-6Al-fSi-(3-f/3)Si}_3\text{N}_4\text{-N}_2$. Результаты этих исследований представлены на рис.4-6.

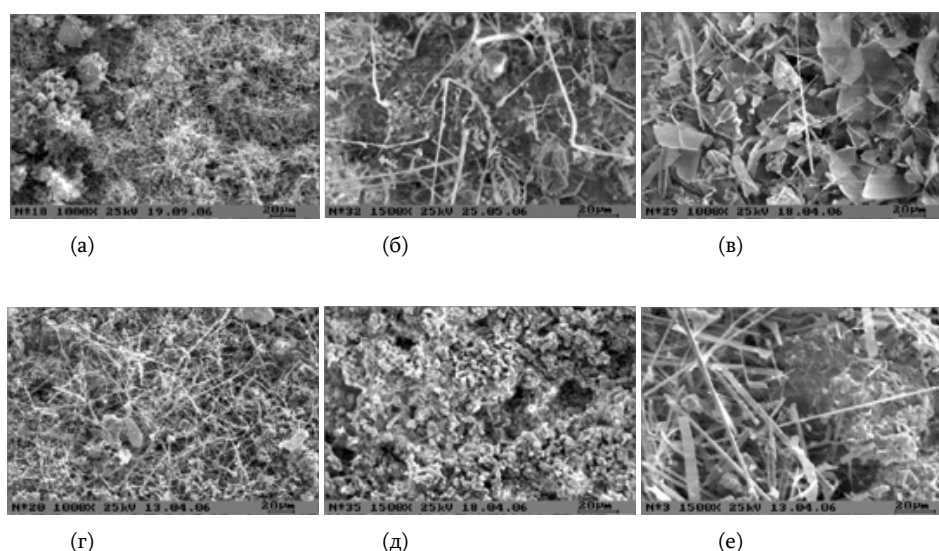


Рис. 3. Микроструктуры конечных продуктов, полученных при горении смесей: $\text{SiO}_2\text{-nAl}$ (а, б, в), $\text{SiO}_2\text{+6Al+kSi}_3\text{N}_4$ (г, д) и $\text{SiO}_2\text{+6Al+1,5Al}_2\text{O}_3$ (е) при различных значениях n, k : (а) - $n=2$; (б) - $n=4$; (в) - $n=6$; (г) - $n=6, k=1$; (д) - $n=6, k=2$.

Анализ влияния количества алюминия в исходной смеси на закономерности горения смеси $3\text{SiO}_2\text{+nAl+1,5Al}_2\text{O}_3$ свидетельствует о том, что T_f и U_f увеличиваются с ростом параметра n . При этом наблюдается также увеличение $m_{\text{Si(соеб.)}}$ и m_N в продуктах сгорания (рис.4).

Следует отметить, что применение Al_2O_3 в качестве разбавителя также не способствует образованию двухфазных продуктов: композитов $\text{Al}_2\text{O}_3/\text{Si}_3\text{N}_4$ или $\text{Al}_2\text{O}_3/\text{Si}_3\text{Al}_3\text{O}_3\text{N}_5$. При этом, как и в отсутствие разбавителя, также формируются многофазные продукты. В частности, только при $n=6$ наблюдалось формирование простого оксинитрида алюминия ($\text{Al}_3\text{O}_3\text{N}$), а при

$n=4$ в продуктах не обнаруживался свободный кремний. Возможность образования Al_3O_3N в режиме горения при азотировании алюминия в присутствии разбавителя Al_2O_3 была подтверждена нами также результатами контрольных экспериментов: при горении смеси $2Al+1,5Al_2O_3$ в среде азота получен двухфазный продукт, содержащий Al_3O_3N и AlN .

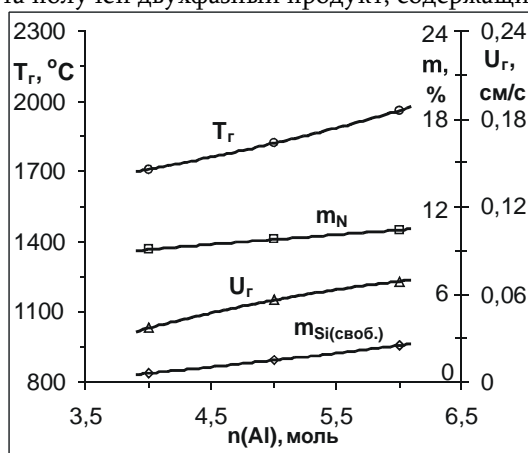


Рис. 4. Зависимости температуры (T_g) и скорости (U_g) горения, содержания азота (m_N) и свободного кремния ($m_{Si(своб.)}$) в конечном продукте от количества алюминия при горении смеси $3SiO_2+nAl+1,5Al_2O_3$ ($P_{N_2}=5,0$ МПа).

Разбавлением исходной смеси нитридом кремния (горение системы **$3SiO_2-6Al-kSi_3N_4-N_2$**), с одной стороны, улучшаются условия азотирования кремния, а с другой, обеспечиваются необходимые условия для получения моносиалона или композита на его основе. В результате получены однофазный ($Si_3Al_3O_3N_5$) или двухфазный ($Si_3N_4/Si_3Al_3O_3N_5$) продукты, с содержанием нитрида кремния в последнем от 10 до 33%. При этом также установлено, что увеличение параметра k приводит к уменьшению T_g и U_g , снижению содержания свободного кремния и повышению количества азота в конечном продукте (рис.5).

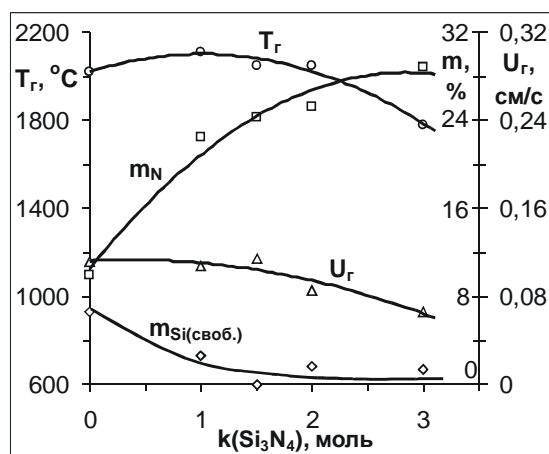


Рис. 5. Зависимости температуры (T_g) и скорости (U_g) горения, содержания азота (m_N) и свободного кремния ($m_{\text{Si(своб.)}}$) в конечном продукте от количества нитрида кремния при горении смеси $3\text{SiO}_2+6\text{Al}+k\text{Si}_3\text{N}_4$ в азоте ($P_{\text{N}_2}=5,0$ МПа).

Следует также отметить, что, аналогично случаю применения Al_2O_3 в качестве разбавителя при горении системы $3\text{SiO}_2-n\text{Al}-\text{N}_2$, не приведшего к образованию двухфазного продукта (композиов $\text{Al}_2\text{O}_3/\text{Si}_3\text{N}_4$, $\text{Si}_3\text{N}_4/\text{Si}_3\text{Al}_3\text{O}_3\text{N}_5$, $\text{Al}_2\text{O}_3/\text{Si}_3\text{Al}_3\text{O}_3\text{N}_5$), горение смеси $3\text{SiO}_2+6\text{Al}+3\text{Si}_3\text{N}_4$ также не приводит к образованию моносиалона $\text{Si}_4\text{Al}_2\text{O}_2\text{N}_6$, хотя состав смеси соответствует получению данного сиалона.

Вышеуказанный сиалон не образуется также в результате горения системы $3\text{SiO}_2-6\text{Al}-3\text{Si}_3\text{N}_4-\text{N}_2$, в которой часть нитрида кремния заменяется поликристаллическим кремнием. Изучение влияния количества поликристаллического кремния $f(\text{Si})$ в исходной смеси на закономерности горения и состав конечных продуктов для системы $3\text{SiO}_2-6\text{Al}-f\text{Si}-(3-f/3)\text{Si}_3\text{N}_4-\text{N}_2$ свидетельствует о том, что при различных значениях параметра f получаются многофазные продукты – в исследованных условиях образование однофазного продукта $\text{Si}_4\text{Al}_2\text{O}_2\text{N}_6$ не имеет места. В зависимости от величины f наблюдается образование трехфазного или четырехфазного конечных продуктов: $\beta\text{-Si}_3\text{N}_4$, $\text{Si}_3\text{Al}_3\text{O}_3\text{N}_5$ и следы SiO_2 (при $f=0$); $\text{Si}_3\text{Al}_3\text{O}_3\text{N}_5$, $\beta\text{-Si}_3\text{N}_4$, $\text{Si}_{4,69}\text{Al}_{1,3}\text{O}_{1,3}\text{N}_{6,69}$ (при $f=2,25$); $\text{Si}_3\text{Al}_3\text{O}_3\text{N}_5$, $\text{Si}, \beta\text{-Si}_3\text{N}_4$ (при $f=4,5$); $\text{Si}_3\text{Al}_3\text{O}_3\text{N}_5$, $\text{Si}, \beta\text{-Si}_3\text{N}_4$ и $\text{Si}_{4,69}\text{Al}_{1,3}\text{O}_{1,3}\text{N}_{6,69}$ (при $f=6$). Из проведенных опытов следует (рис.6), что с ростом f параметры T_g и U_g проявляют тенденцию к насыщению, а также имеет место увеличение количества свободного кремния и уменьшение содержания азота в конечном продукте.

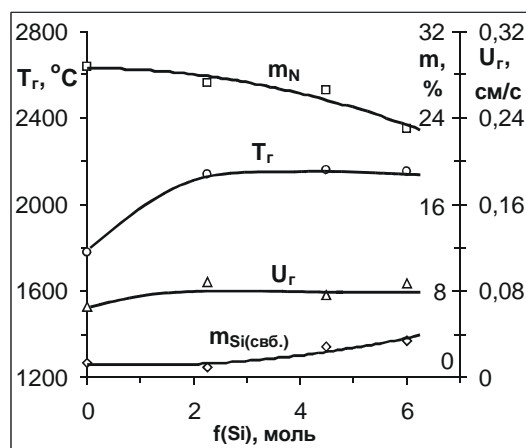


Рис.6. Зависимости температуры (T_r) и скорости (U_r) горения, содержания азота (m_N) и свободного кремния ($m_{Si(своб.)}$) в конечном продукте от количества кремния при горении смеси $3SiO_2+6Al+fSi+(3-f/3)Si_3N_4$ в азоте ($P_{N_2}=5,0$ МПа).

Таким образом, при сопоставлении полученных результатов для различных систем, можно констатировать, что только при горении системы **$3SiO_2-6Al-kSi_3N_4-N_2$** при относительно низких давлениях газа можно осуществить СВ синтез моносиалона $Si_3Al_3O_3N_5$ и его композита $Si_3N_4/Si_3Al_3O_3N_5$ с различным содержанием нитрида кремния. В остальных случаях получаются многофазные продукты. На рис.7 приведены рентгенограммы однофазного продукта – моносиалона $Si_3Al_3O_3N_5$ (а) и двухфазного продукта – композита $Si_3N_4/Si_3Al_3O_3N_5$ (б), полученных при горении смеси **$3SiO_2+6Al$** в среде азота в присутствии разбавителя Si_3N_4 . Здесь же для сравнения приведена рентгенограмма многофазного продукта Si , $Si_3Al_3O_3N_5$, $\gamma-Al_2O_3$, $\epsilon-Al_2O_3$ (в), полученного в отсутствие разбавителя.

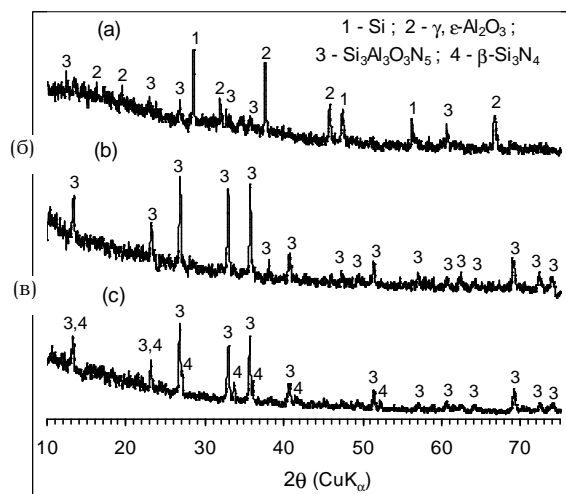


Рис.7. Рентгенограммы конечных продуктов, полученные при горении смесей $3\text{SiO}_2+6\text{Al}$ (а), $3\text{SiO}_2+6\text{Al}+\text{Si}_3\text{N}_4$ (б) и $3\text{SiO}_2+6\text{Al}+2\text{Si}_3\text{N}_4$ (в) в среде азота ($P_{\text{N}_2}=5,0 \text{ МПа}$).

В системах $3\text{SiO}_2\text{-nAl-N}_2$, $3\text{SiO}_2\text{-nAl-1,5Al}_2\text{O}_3\text{-N}_2$, $3\text{SiO}_2\text{-6Al-kSi}_3\text{N}_4\text{-N}_2$ и $3\text{SiO}_2\text{-6Al-fSi-(3-f/3)Si}_3\text{N}_4\text{-N}_2$ варьирование параметров n , k и f существенно влияет не только на параметры горения, химический и фазовый составы, но и на формирование микроструктур конечных продуктов. Микроструктуры конечных продуктов, полученных при горении смесей с различным содержанием поликристаллического кремния в исходной смеси, приведены на рис.8. Из сравнения с данными, представленными на рис.3, следует, что существенное различие в микроструктурах наблюдается как при отсутствии (рис.3, а-в) и наличии разбавителя (рис.3, г-е), так и при использовании поликристаллического кремния (рис.8, а-в). Эти микроструктуры определяются также значениями параметров n , k и f . При этом в конечных продуктах зарегистрировано формирование нитевидных кристаллов и зернистой структуры, соотношение которых зависит от условий проведения процесса. В определенных условиях, например, при горении смесей $3\text{SiO}_2\text{-6Al-kSi}_3\text{N}_4$ (при $k=2$) и $3\text{SiO}_2+6\text{Al+fSi+(3-f/3)Si}_3\text{N}_4$ (при $f=2,25$), формируется только зернистая структура (рис.3, д и рис.8, а), что также может представлять определенный интерес с точки зрения получения материалов с регулируемой микроструктурой.

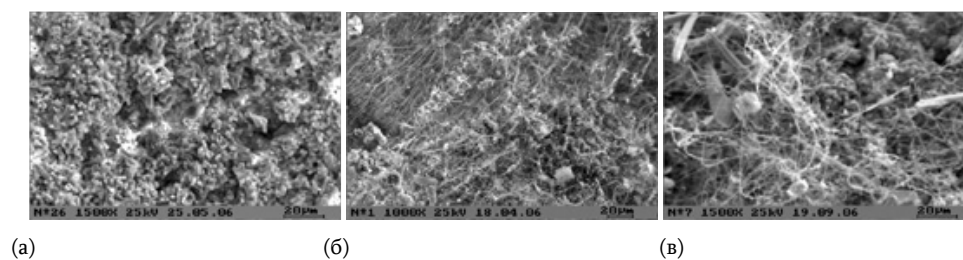


Рис. 8. Микроструктуры конечных продуктов, полученных при горении смеси $3\text{SiO}_2+6\text{Al+fSi+(3-f/3)Si}_3\text{N}_4$ при различных значениях f : (а) - $n=6$, $f=2,25$; (б) - $n=6$, $f=4,5$; (в) - $n=6$, $f=6$.

Выводы

1. Выявлены основные факторы, влияющие на закономерности горения системы $\text{SiO}_2\text{-Al-N}_2$, полноту азотирования кремния, а также микроструктуру и состав конечных продуктов. Показано, что азотирование смесей $\text{SiO}_2\text{-Al}$ и синтез композита $\text{Si}_3\text{N}_4/\text{Al}_2\text{O}_3$ сопровождаются образованием сиалонов и его композитов с различным содержанием компонентов и свободного кремния.
2. Установлено, что состав и микроструктуру конечных продуктов можно контролировать изменением соотношения составляющих в исходной смеси и давления газовой среды. Конечные продукты получают в виде нитевидных кристаллов или зерен, соотношение которых меняется в зависимости от условий проведения процесса.
3. Показано, что при горении смесей $\text{SiO}_2\text{-Al-Si}_3\text{N}_4$ при низких давлениях азота можно синтезировать однофазный сиалон $\text{Si}_3\text{Al}_3\text{O}_3\text{N}_5$ и композиты $\text{Si}_3\text{N}_4/\text{Si}_3\text{Al}_3\text{O}_3\text{N}_5$ с различным содержанием нитрида кремния.

$\text{SiO}_2\text{-Al-N}_2$ ՀԱՄԱԿԱՐԳԻ ԱՅՐՄԱՆ ՕՐԻՆԱԶՄՓՈԻԹՅՈՒՆՆԵՐՆ ԵՎ ՄԻԼԻՑԻՈՒՄԻ ՆԻՏՐԻԴԻ ՀԻՄԱՆ ՎՐԱ ԿՈՄՊՈԶԻՏՆԵՐԻ ՈՒ ՄՈՆՈՍԻԱԼՈՒԻ ՄԻՆԹԵԶԸ

Լ. Ս. ԱՐՈՎՅԱՆ և Ս.Լ. ԽԱՌԱՅՅԱՆ

Ուսումնասիրվել է միաֆազ սիալոնի (մոնոսիալոնի) և $\text{Si}_3\text{N}_4/\text{Al}_2\text{O}_3$ կոմպոզիտի ԲԻ սինթեզի հնարավորությունը ազոտի համեմատաբար ցածր ճնշումների (0,1-6,0 ՄՊա) դեպքում, որպես սիլիցիումի հումք օգտագործելով կվարցային ավազը: Բացահայտվել են $\text{SiO}_2\text{-Al-N}_2$ համակարգի այրման օրինաչափությունների, սիլիցիումի ազոտացման աստիճանի, ինչպես նաև վերջանյութերի բաղադրության ու միկրոկառուցվածքի վրա ազդող հիմնական գործոնները: Ցույց է տրվել, որ $\text{SiO}_2\text{-Al}$ և $\text{SiO}_2\text{-Al-Si}_3\text{N}_4(\text{Al}_2\text{O}_3)$ խառնուրդների ազոտացումն այրման ռեժիմում միշտ ուղեկցվում է սիալոնների (SiAlON) առաջացումով: Ընդ որում, կախված նոսրացուցիչի քանակից և բնույթից (Si_3N_4 , Al_2O_3) ստացվում են բաղադրիչների ու ազատ սիլիցիումի տարբեր պարունակությամբ $\text{Si}_3\text{N}_4\text{-Al}_2\text{O}_3\text{-SiAlON}$ կոմպոզիտներ: Կոմպոզիտների բաղադրությունն ու միկրոկառուցվածքը կարելի է կարգավորել ելային խառնուրդում բաղադրիչների հարաբերակցության և միջավայրի ճնշման փոփոխությամբ: Ցույց է տրվել, որ $\text{SiO}_2\text{-Al-Si}_3\text{N}_4$ խառնուրդների այրումը ազոտի ցածր ճնշումների տակ իրականացնելիս կարելի է սինթեզել $\text{Si}_3\text{Al}_3\text{O}_3\text{N}_5$ մոնոսիալոն և տարբեր քանակությամբ սիլիցիումի նիտրիդ պարունակող $\text{Si}_3\text{N}_4/\text{Si}_3\text{Al}_3\text{O}_3\text{N}_5$ կոմպոզիտներ:

COMBUSTION LAWS IN THE $\text{SiO}_2\text{-Al-N}_2$ SYSTEM AND SYNTHESIS OF MONOSIALON AND SILICON NITRIDE-BASED COMPOSITES

L. S. ABOVYAN and S. L. KHARATYAN

The possibility on SH synthesis of $\text{Si}_3\text{N}_4/\text{Al}_2\text{O}_3$ composite and single-phase sialon (monosialon) at relatively low nitrogen pressures (0.1-6.0 MPa) has been studied using silicon dioxide (silica sand) as a silicon precursor. The main factors influencing on the combustion laws of the $\text{SiO}_2\text{-Al-N}_2$ system, completeness of silicon nitriding, as well as on the microstructure and composition of end-products were revealed. It was shown that nitriding the $\text{SiO}_2\text{-Al}$ and $\text{SiO}_2\text{-Al-Si}_3\text{N}_4(\text{Al}_2\text{O}_3)$ mixtures under the combustion mode was always accompanied by formation of sialons (SiAlON). Depending on amount and the type of the diluent $\text{Si}_3\text{N}_4\text{-Al}_2\text{O}_3\text{-SiAlON}$ composites with various contents of components and free silicon were obtained. The composition and microstructure of composites may be controlled by changing the ratio of components in the initial charge and the pressure of gas atmosphere. It was established that at low nitrogen pressures combustion of $\text{SiO}_2\text{-Al-Si}_3\text{N}_4$ mixtures may result in $\text{Si}_3\text{Al}_3\text{O}_3\text{N}_5$ monosialon and $\text{Si}_3\text{N}_4/\text{Si}_3\text{Al}_3\text{O}_3\text{N}_5$ composite with different contents of silicon nitride.

ЛИТЕРАТУРА

- [1] Боровинская И.П. Самораспространяющийся высокотемпературный синтез: Теория и практика / под ред. А.Е. Сычева. Черноголовка, Территория, 2001, с.237.
- [2] Смирнов К.Л., Боровинская И.П. // Известия ВУЗов, сер. «Цветная металлургия», 2002, № 4, с.56.
- [3] Borovinskaya I.P., Smirnov K.L. // Refractory Technical Ceramics, 1999, №3, p.15.
- [4] Smirnov K.L., Borovinskaya I.P. // Key Engineering Materials, 2002, v. 217, p.159.
- [5] Krestan J., Sajgalik P. and Panek Z. // Journal of the European Ceramic Society, 2004, v. 24, iss. 5, p.791.
- [6] Nersisyan H.H., Abovyan L.S., Kharatyan S.L. // International Journal of Self-Propagating High-Temperature Synthesis, 1999, v. 8, №2, p.153.
- [7] Абовян Л.С., Нерсисян Г.А., Харатян С.Л. // Физика горения и взрыва, 2000, т. 36, №2, с.51.
- [8] Abovyan L.S., Nersisyan H.H., Kharatyan S.L., Saiu R., Orru R., Cao G., Zedda D. // Ceramics International, 2001, v. 27, №2, p.163.

**ВЗАИМОДЕЙСТВИЕ Sc, Gd, Nd И Pr С ВОДОРОДОМ
В РЕЖИМЕ ГОРЕНИЯ И В ПУЧКЕ УСКОРЕННЫХ ЭЛЕКТРОНОВ**

А. Г. АЛЕКСАНЯН, С. К. ДОЛУХАНИЯН И А. Г. АКОПЯН

Институт химической физики им. А.Б. Налбандяна
НАН Республики Армения, Ереван

В работе представлены результаты исследований радиационно-термических процессов, протекающих в системах Me-H₂ (Me – Sc, Gd, Pr и Nd) под пучком ускоренных электронов и в процессе самораспространяющегося высокотемпературного синтеза.

Показано, что при облучении образцов пучком электронов в присутствии водорода инициируется экзотермическая реакция Me+H₂, приводящая к синтезу гидридов. Предварительно облученные в вакууме образцы металлов способны начать взаимодействие с водородом при относительно низких температурах (60°C и ниже) с образованием гидрида. Показано, что в режиме горения можно получать ди- и тригидриды металлов третьей группы.

Рис. 2, табл. 7, библиографических ссылок 8.

Способность РЗМ металлов связывать значительные количества водорода, сравнительно большие сечения захвата тепловых нейтронов (табл.1) [1] и относительно высокие температуры разложения гидридов делают их привлекательными материалами как для защиты от тепловых нейтронов, так и в качестве материалов для регулирования ядерных процессов в реакторах. Редкоземельные металлы и их соединения представляют интерес также как материалы для современных электронных и оптических устройств, батарей, катализаторы, абразивы и пр. В связи с этим поиск лучших методов синтеза гидридов РЗМ является актуальным.

Для решения этих проблем были изучены возможности образования гидридов методом самораспространяющегося высокотемпературного синтеза (СВС) [2,3] и под воздействием ускоренных электронов [4] в системах Sc и РЗМ (Gd, Nd, Pr) – H₂.

Сечения захвата тепловых нейтронов для РЗМ

Элемент	σ , барн	Элемент	σ , барн
La	8.9	Gd	46000
Ce	0.70	Tb	44
Pr	11.2	Dy	1100
Nd	46	Ho	64
Pm	60	Er	166
Sm	5500	Tm	36
Eu	4600	Lu	108

Металлы третьей группы и лантаноиды образуют гидриды состава от MeH_2 до MeH_3 . Исключение составляют скандий и европий, которые гидрируются до состава MeH_2 . Кристаллическая структура этих металлов, как правило (в большинстве случаев, кроме самария), гексагональная (ГПУ), а у гидридов – гранецентрированная кубическая (ГЦК, со структурой типа флюорита). Для легких РЗМ (La, Ce, Pr, Nd) при переходе от дигидридов MeH_2 к тригидридам MeH_{3-x} наблюдается постепенное заполнение октаэдрических пустот решетки флюорита атомами водорода. Это сопровождается сжатием решетки гидрида – уменьшается параметр ГЦК решетки. В порошковой металлургии традиционным методом получения гидридов Sc и РЗ металлов является синтез в вакуумной установке типа установки Сиверса [1,6]. Заранее очищенный металл помещают в реактор и дегазируют в вакууме 10^{-5} мм рт.ст. при 800°C в течение нескольких часов. В систему впускают водород до давления 1 атм и выдерживают металл 5-8 ч до полного поглощения, о чем судят по изменению давления в системе. Этим достаточно длительным методом получают дигидриды РЗМ, а для получения тригидридов требуются более жесткие условия: так, для получения тригидрида гадолиния нужны длительные выдержки до 40 ч.

В последние десятилетия в материаловедении признан и успешно развивается процесс самораспространяющегося высокотемпературного синтеза, который основан на проведении экзотермической реакции между химическими реагентами в режиме горения. В случае, когда один из реагентов газ (азот, водород), взаимодействие в зоне химической реакции происходит путем фильтрации активного газа из внешней среды. При этом после локального инициирования процесса формируется тепловая волна, которая самопроизвольно распространяется по исходному веществу, приводя к получению ценных конденсированных продуктов реакции.

Представляет интерес также инициированное воздействием ускоренных электронов поглощение водорода металлами и сплавами [4,5]. При воздействии на твердые тела ионизирующего облучения, в том числе и пучка ускоренных электронов, часто наблюдается нарушение их структуры и образование дефектов. Вследствие накопления радиационных дефектов возможно изменение межплоскостных расстояний в кристаллической решетке, появление дефектов упаковки (выражающееся в изменении чередования плотности упаковки

атомных слоев кристаллической решетки и возможного отступления от того порядка, который свойственен ГПУ и ГЦК структурам). Возникающие радиационные дефекты оказывают значительное влияние на физико-химические свойства исходного материала, в частности на их диффузионные свойства, реакционную способность и т.д. При изучении воздействия пучка ускоренных электронов на процессы $\text{Me}+\text{H}_2$ было установлено два режима поглощения водорода металлами и сплавами четвертой и пятой групп – радиационно-термический синтез (РТС) и «холодный синтез» (ХС) [4].

Экспериментальная часть

Техника эксперимента. Исследования по синтезу гидридов в режиме горения проводились по известной методике СВС [2] в бомбе постоянного давления. В процессе работы применяли газообразный водород электролизной чистоты при давлениях 1-60 *атм*. Температуры и скорости процесса измерялись вольфрам-рениевой термопарой.

Исследования радиационно-термических процессов проводились на линейном ускорителе электронов «ЛУЭ-5» Ереванского физического института с энергией пучка 4 *МэВ* при силе тока до 150 *А* в специальной камере, обеспечивающей электронно-лучевую обработку материалов в вакууме и в водороде при 1-2 *атм*. Облучение образцов проводилось в интервале мощностей дозы 0,025-1,3 *Мрад/с*. Измерение температур протекающих процессов при облучении образцов осуществлялось платина-платинородиевой термопарой.

В экспериментах использовались скандий Sc-2, гадолиний ГДМ-1 (99, 90%), празеодим ПрМ-1 (99,3%) и неодим НМ-1 (99,91%). Металлическая стружка, полученная механическим измельчением кускового металла (0,3-0,5 *мм*), прессовалась в цилиндрические образцы диаметром 20 и высотой 5 *мм* с относительной плотностью 0,3-0,4. После облучения гидрированные образцы празеодима и неодима транспортировались в специальных пластиковых контейнерах во избежание длительного контакта с внешней средой. В случае скандия и гадолиния такой необходимости не было, поскольку их гидриды устойчивы.

Аттестация полученных материалов проводилась методами химического анализа на содержание водорода пиролизом, рентгенофазового анализа («ДРОН-0,5») и дифференциально-термического анализа («Q-1500»).

СВС процессы в системах $\text{Me}^{\text{III}}-\text{H}_2$. При исследовании процессов горения скандия и РЗ металлов в водороде было установлено, что температуры СВС процесса гидрирования лантаноидов по сравнению с температурами горения металлов IV группы несколько выше. Дисперсность, плотность и геометрия образцов, как и в случае металлов IV и V групп, не оказывали существенного влияния на температуры и скорости СВС. Скорости и температуры горения ряда металлов, измеренные при давлении водорода 3 *атм*, приведены в табл. 2.

Таблица 2

Характеристика процессов СВС в системах РЗМ–H₂

Металл	Скорость горения, см/с	Температура горения, °C	T _{пл} металла, °C
Pr	8,31	1265	935
Nd	8,25	1240	1024
Sm	10,27	1250	1072
Dy	9,69	1340	1407
Ho	6,25	1460	1461
Gd	12,4	1315	1312
Sc	8,7	1500	1541

Как видно из приведенных данных, температуры горения легких лантаноидов (празеодима и неодима) выше температур плавления соответствующих металлов, однако это не является препятствием при внедрении атомов водорода в кристаллическую решетку металла. В процессе образования и формирования конечных продуктов образцы не деформируются, хотя на изломе образцов некоторых гидридов РЗМ имеются расплавленные участки. Исходные образцы имели серебристый блеск металла, после гидрирования продукты получались с характерными для каждого гидрида оттенками (темно-синим, темно-фиолетовым и др).

В отличие от металлов IV группы, при горении РЗМ изменение давления сильно влияет на химический и фазовый составы гидридов (табл. 3). Конечными продуктами СВС-гидрирования празеодима и неодима при давлениях водорода <3 атм являются дигидриды, при давлениях 5 атм и выше формируются тригидридные фазы Pr и Nd с неполной стехиометрией (H/Me = 2,20-2,98). У гадолиния фаза дигидрида гадолиния с ГЦК структурой формируется при давлениях водорода до 10 атм. Дальнейшее увеличение давления приводит к появлению наряду с кубической фазой дигидрида тригидридной фазы гадолиния с гексагональной плотной упаковкой (ГПУ), а при 60 атм водорода в результате горения формируется однофазный GdH_{2,88} с ГПУ структурой.

Таблица 3

Характеристики синтезированных СВС-гидридов

Металл	P_{H_2} , атм	Сод. H_2 в продукте, масс. %	Кристалл. решетка	Параметр решетки, Å	Формула гидрида
Sc	10	4,25	ГЦК	$a = 4,7828$	$ScH_{2,0}$
Pr	3	1,41	ГЦК	$a = 5,512$	$PrH_{2,0}$
	60	2,08	ГЦК	$a = 5,491$	$PrH_{2,8}$
Nd	3	1,43	ГЦК	$a = 5,459$	$NdH_{2,1}$
	60	1,78	ГЦК	$a = 5,446$	$NdH_{2,6}$
Gd	5	1,26	ГЦК	$a = 5,513$	$GdH_{2,0}$
	60	1,79	ГПУ	$a = 3,373$; $c = 6,710$	$GdH_{2,8}$

Радиационно-термический синтез гидридов металлов III группы. РТС в системе Sc–H₂. В ходе экспериментов было показано, что РТС в системе Sc–H₂ реализуется при высоких мощностях дозы 1-1,5 Мрад/с. Аналогично металлам четвертой группы [4] здесь после нагрева скандия под пучком ускоренных электронов происходит тепловой взрыв. Температуру начала взаимодействия водорода с образцом четко не удалось зафиксировать, однако наблюдается резкий скачок температуры до 1010-1130°C. В результате РТС содержание водорода в продукте достигло 3,3-3,4 масс.%. Надо отметить, что исходный скандий содержал до 15% окисной фазы Sc₂O₃. По данным рентгенофазового анализа, получен дигидрид скандия с ГЦК кристаллической решеткой. К сожалению, окисная фаза Sc₂O₃ в процессе РТС осталась неизменной (табл. 4).

Таблица 4

Радиационно-термический синтез в системе Sc–H₂

Мощность дозы, Мрад/с	Доза, Мрад	T _{нагр.} , °C	T _{реакции} , °C	Сод. H_2 в продукте, масс. %	Фазовый состав
0,2-0,5	200	190-385	–	0,57-0,86	Sc + Sc ₂ O ₃ .
1,0-1,5	100	300-560	900-1140	3,0-3,40	ScH _x + Sc ₂ O ₃ (~15%)

РТС гидридов РЗМ. Эксперименты по радиационно-термическому синтезу в системах РЗМ–H₂ проводились в диапазоне мощностей доз 0,3-1,0 Мрад/с при давлении водорода 1 атм. При воздействии более слабых пучков электронов реакция гидрирования не наблюдалась. Начальные температуры радиационного разогрева в водороде достигают 200-300°C, а температуры реакции взаимодействия РЗМ с водородом под пучком ускоренных электронов – одни из самых высоких среди исследованных систем Me–H₂ – 800-1000°C (рис. 1).

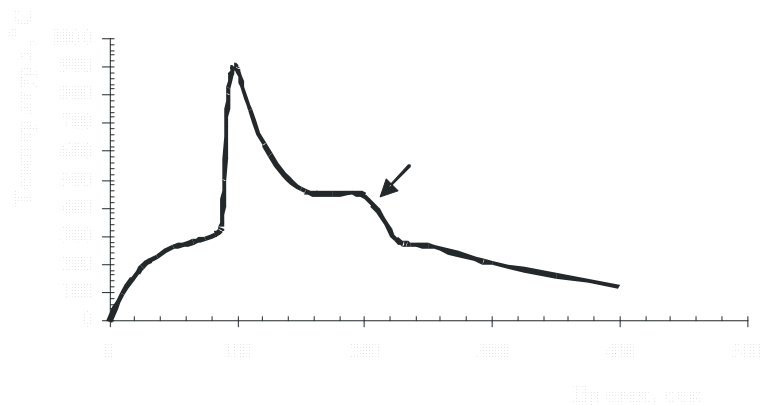


Рис. 1. Радиационно-термические процессы в системе неодим–водород при облучении электронным пучком с мощностью дозы 0,5 *Мрад/с* (стрелкой обозначен момент выключения пучка).

Рентгенофазовый и химический анализы продуктов радиационного воздействия на неодим и празеодим показали, что в результате РТС при 1 *атм* водорода формируются сразу тригидридные фазы MeH_{3-x} , чего не было при получении этих гидридов методом СВС. Здесь, вероятно, играет роль радиационный фактор генерации активных центров (табл. 5).

«Холодный синтез» гидридов РЗМ. В ранних работах при исследованиях радиационно-термических процессов в системах $\text{Me}^{\text{IV}}\text{-H}_2$, Me-C(N)-H_2 , $\text{Me-Me}^{\text{I}}\text{-H}_2$ и др. обнаружено новое явление – пост-радиационное взаимодействие металлов и некоторых нестехиометрических соединений с водородом или так называемый «холодный синтез» [4]. Сущность его состоит в том, что после предварительного облучения металлов в вакууме после выключения пучка электронов и понижения температуры образцов до 25-60°C в реакционную зону (камеру) подается водород, и через несколько секунд термопара регистрирует резкий скачок температуры, что свидетельствует о протекании экзотермической реакции данного металлического образца с водородом (рис. 2).

Таблица 5

РТС в системах РЗМ - H₂

Система	Мощность дозы, Мрад/с	Доза, Мрад	T _{нач.} , °C	T _{макс.} , °C	Конц-ия водорода в продукте, масс. %	H/Me
Pr + H ₂	0,3	55	220	890	1,68	2,41
	0,4	76	220	925	1,70	2,50
	0,5	94	278	900	1,79	2,57
Nd + H ₂	0,3	100	300	800	1,75	2,58
	0,5	100	305	935	1,76	2,60
	0,7	100	305	860	1,84	2,71
Gd + H ₂	0,4	60	305	925	1,14	1,82
	0,6	45	305	960	0,97	1,55
	1,0	110	305	1005	1,09	1,74

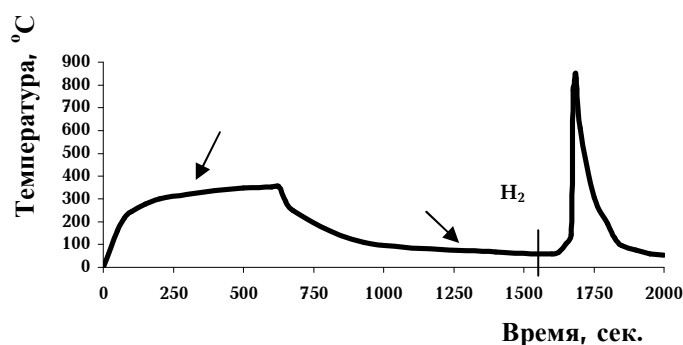


Рис. 2. «Холодный синтез» в системе празеодим–водород (мощность дозы 0,2 Мрад/с). (стрелками обозначены моменты выключения пучка и подачи водорода в камеру).

Рентгенофазовый и химический анализы полученных продуктов взаимодействия показали, что в результате этой реакции образуются гидриды. Надо отметить, что у каждого металла есть свои условия протекания пострадиационного взаимодействия с водородом и образования гидрида в режиме «холодного синтеза». Оптимальные условия, при которых реализуется этот процесс, для образцов РЗМ приведены в табл. 6.

Гидрирование образцов РЗМ в режиме "холодного синтеза"

Система	Мощность дозы, <i>Мрад/с</i>	Доза, <i>Мрад</i>	Предварительный радиацион. разогрев, °C	Темп-ра подачи водорода, °C	T_{xc} , °C	Конц-ия водорода в продукте, масс. %	H/Me
Pr + H ₂	0.025	100	140	30	Нет реакции		
	0.05	100	240	30	610	1,56	2,31
	0.05	100	295	60	650	1,71	2,52
	0,1	100	355	60	680	1,60	2,35
	0,2	100	365	60	840	1,72	2,54
	0,3	100	585	60	825	1,63	2,40
	0,3	100	555	30	715	1,63	2,40
	0,3*	100	420	30	725	1,65	2,42
	0,5	100	600	60	Нет реакции		
	0,7	100	955	60	Нет реакции		
Nd + H ₂	0,05	50	185	60	Нет реакции		
	0,1	52	330	60	775	1.85	2,66
	0,1	60	460	60	850	1.70	2,50
	0,2	120	425	60	790	1,73	2,50
	0,3	120	560	60	855	1,68	2,41
	0,4	60	610	60	Нет реакции		
	0,5	88	600	60	Нет реакции		
Cd + H ₂	0,1				Нет реакции		
	0,2	100	420	60	755	1,28	2,07
	0,4			60	Нет реакции		

* – подача водорода произведена спустя 45 мин.

Отметим, что при облучении более мощными пучками электронов возникшие в металле дефекты исчезают (отжиг дефектов), а при слабых мощностях доз в процессе охлаждения они исчезают в результате рекомбинации [7, 8].

Интересно отметить, что в результате взаимодействия образцов празеодима и неодима с водородом при давлении газа 1 атм в режиме «холодного синтеза» формируются тригидридные фазы, т. е. взаимодействие празеодима и неодима с водородом под воздействием радиации всегда приводит к образованию гидридов с соотношением H/Me(2).

У образцов гадолиния при облучении той же дозой 0,2 *Мрад/с* в водороде реакция радиационно-термического синтеза не наблюдается. Однако при предварительном облучении металла в вакууме даже при низких мощностях доз (0,2 *Мрад/с*) в образце создаются достаточно высокие концентрации радиационных дефектов и происходит накопление избыточной энергии. После выключения пучка электронов за время остывания до 60-30 °C в образце сохраняется значительное превышение концентрации радиационных

дефектов, образующихся в результате воздействия пучка электронов над равновесным уровнем. Таким образом, при радиационно-термических условиях синтеза происходит снятие диффузионных сопротивлений, и синтез гидридов переходных и РЗ металлов протекает в режиме ускоренной диффузии, что при облучении связано с избыточной концентрацией радиационных точечных и протяженных дефектов и с избытком накопленной энергии в образцах. Этим определяется повышенная активность некоторых металлов и обуславливается их взаимодействие с водородом при необычно низких температурах, а также тот факт, что при давлении водорода уже 1 атм в результате взаимодействия водорода и металла сразу образуются высшие гидриды почти стехиометрического состава, чего не было в условиях СВС.

Холодный синтез в системе Sc – H₂ не удалось реализовать ни при каких условиях в диапазоне мощностей дозы 0,2-0,5 Мрад/с с общей дозой облучения до 200 Мрад.

Ниже приводятся характеристики синтезированных гидридов РЗМ и гидроксида скандия (табл. 7).

Таблица 7

Характеристики синтезированных гидридов

Металл	Метод синтеза	H/Me	Кристал. решетка	Параметры, Е
Pr	СВС	2,00	ГЦК	5,512
	СВС *	2,80	ГЦК	5,468
	РТС	2,33 - 2,56	ГЦК	5,467-5,479
	ХС	2,57-2,72	ГЦК	5,440-5,482
Nd	СВС	2,1	ГЦК	5,459
	СВС *	2,26	ГЦК	5,439
	РТС	2,52-2,70	ГЦК	5,402-5,443
	ХС	2,40-2,60	ГЦК	5,417-5,449
Gd	СВС	1,82-2,0	ГЦК	5,266 – 5,274
	СВС *	2,88	ГПУ	a=3,373; c=6,71
	РТС	1,82	ГЦК	5,274
	ХС	2,07	ГЦК	5,270
Sc	СВС	2,0	ГЦК	4,7828
	РТС	2,0	ГЦК	4,772

* – при высоких давлениях водорода

Сравнение ДТА для гидридов, полученных разными методами (РТС, СВС, ХС), показывает что характер их разложения не зависит от метода получения этих гидридов.

Работа выполнена при финансовой поддержке Международного научно-технического центра (МНТЦ- Грант А-192).

**Sc, Gd, Nd եւ Pr-ի Փոխազդեցութեան Զրաժարման Հետ Ազդեցող Ռեժիմներում
Արագացված Էլեկտրոնային Փաշերի
Ազդեցութեան ՏԱԿ**

Ա. Գ. ԱԼԵՔՍԱՆՅԱՆ, Ս. Կ. ԴՈԼՈՒԽԱՆՅԱՆ և Հ. Գ. ՀԱԿՈԲՅԱՆ

Ներկայացվող աշխատանքում բերված են այրման պրոցեսների՝ բարձրջերմաստիճանային ինքնատարավող սինթեզի (ԲԻՍ) և արագացված էլեկտրոնների փնջի ազդեցության տակ ընթացող ռադիացիոն-թերմիկ պրոցեսների ուսումնասիրությունների արդյունքները Me^{III} - ջրածին ($\text{Me} - \text{Sc, Gd, Pr}$ և Nd) համակարգերում:

Ուսումնասիրվել են ԲԻՍ և ռադիացիոն-թերմիկ եղանակներով հիդրիդների ձևավորման գլխավոր օրինաչափությունները: Ցույց է տրված, որ հազվագյուտ հողային մետաղների այրումը (ԲԻՍ) ջրածնում ընթանում է առավելապես բարձր ջերմաստիճաններում և վերջնային հիդրիդների ձևավորման վրա ազդում է ջրածնի ճնշումը: Այրման ռեժիմում սինթեզվել են Sc -ի երկհիդրիդ, և վերևում նշված հազվագյուտ հողային մետաղների երկհիդրիդներ և եռհիդրիդներ ($H/\text{Me} = 2,20-2,98$):

Ռադիացիոն-թերմիկ սինթեզը ուսումնասիրելիս օգտագործվել է “LAE-5” գծային էլեկտրոնային արագացուցիչ՝ 4 MeV արագացված, ֆոկուսացված էլեկտրոնների փունջ: Ստացված են ռադիացիոն-թերմիկ պրոցեսների գլխավոր օրինաչափությունները: Ցույց է տրված, որ հազվագյուտ հողային մետաղների ճառագայթումը ջրածնի միջավայրում բերում է նրանց հիդրիդների սինթեզին: Հաստատված է, որ ճառագայթման դոզայի աճը բերում է նմուշի ջերմաստիճանի աճին մինչև 200-300°C, որին անմիջապես հետևում է ջերմաստիճանի թռիչքաձև աճ: Փաստորեն տեղի է ունենում $\text{Me} + \text{H}_2$ ռեակցիան ջերմային պայթման ռեժիմում: Ցույց է տրված նաև, որ վակուումի մեջ հազվագյուտ հողային մետաղների ճառագայթման դոզայի ցածր հզորության դեպքում նախնական ճառագայթումից հետո նմուշներում առաջանում են մեծ թվով ռադիացիոն դեֆեկտներ, ինչի հետևանքով նմուշում կուտակվում է ավելցուկային էներգիա: Էլեկտրոնային փնջի անջատումից և նմուշի սառեցումից հետո մինչև 60°C (և ավելի ցածր) կետային դեֆեկտների կոնցենտրացիան մնում է համեմատաբար անփոփոխ մակարդակի հետ զգալիորեն ավել: Սրանով է պայմանավորված նմուշի բարձր ակտիվությունը և ցածր ջերմաստիճաններում՝ 25-60°C ռեակտոր ներարկվող ջրածնի հետ փոխազդեցության հանգամանքները (սառը սինթեզ): Սառը սինթեզը բերում է $\text{NdH}_{2.26-2.80}$, $\text{PrH}_{2.43-2.73}$, and $\text{GdH}_{2.07}$ բաղադրությամբ հիդրիդների ձևավորմանը:

**THE INTERACTION OF Sc, Gd, Nd, AND Pr WITH HYDROGEN IN THE MODE OF
COMBUSTION AND IN THE ACCELERATED ELECTRONS BEAM**

A. G. ALEKSANYAN, S. K. DOLUKHANYAN and H. G. HAKOBYAN

In the present work, the results of investigation of combustion (SHS) and thermal-radiation processes (TRS) in the systems Me^{III} -hydrogen (Me: Sc, Gd, Pr and Nd) under action of accelerated electrons' beam (AEB) are demonstrated. The main regularities of hydrides creation in SHS and TRS modes are studied. We have shown that SHS of REMs proceeds at rather high temperature, and the hydrogen pressure also influences the formation of final hydride. In the combustion regime, hydride

and dihydride of Sc and dihydrides and three-hydrides of above mentioned REMs are synthesized ($H/Me = 2.20 - 2.98$).

The high-current 4 MeV LAE-5 with a focused accelerated electron beam has been used in investigation of TRS. The main peculiarities of the thermal-radiation processes have been obtained. It was shown, that at irradiation of the metals in hydrogen environ, the thermal-radiation synthesis of their hydrides took place. It was established, that at the increasing of irradiation dose, the temperature of sample increases up to 200-300°C, after which, sharp temperature jump was observed. Actually, the reaction $Me+H_2$ proceeds in a thermal explosion regime. It was shown also that after preliminary irradiation of REMs in vacuum even at low dose rate (0.2 Mrad/sec), the radiation defects of high concentration were created, and the energy excess is accumulated in the sample. After switching off the electron beam, and cooling down to 60°C (and lower), the point defects concentration in the significant excess relative to the equilibrium level remained in the sample. Those determine the high activity of sample, and condition its interaction with supplied to the reactor hydrogen at as low temperature as 25-60°C (Cold Synthesis, CS). CS results in the formation of hydrides of compositions: $NdH_{2.26-2.80}$, $PrH_{2.43-2.73}$, and $GdH_{2.07}$.

ЛИТЕРАТУРА

- [1] Гидриды металлов / под ред. В. Мюллера, Д. Блекледжа, Дж. Либовица. Пер. с англ., М., Атомиздат, 1973, с. 432.
- [2] Мержанов А.Г., Боровинская И.П.// ДАН СССР, 1972, т. 204, №2, с. 366.
- [3] Dolukhanyan] S.K.// J. Alloys Comp., 1997, v. 253-254, p. 10.
- [4] Dolukhanyan S.K, Shekhtman V.Sh., Aghajanyan N.N., Abrahamyan K.A., Harutyunyan Kh.S., Aleksanyan A.G., Hakobyan H.G., Ter-Galstyan O.P. // J. Alloys Comp., 2002, 330-332, p. 551.
- [5] Адигамов Б.Я., Лунин В.В., Мирошниченко И.И., Пантелеев Д.М., Садовническая М.В., Соловецкий Ю.И., Талецкий Ю.В. // Журнал физической химии, 1989, № 11. с. 3119.
- [6] Антонова М.М., Морозова Р.А. Препаративная химия гидридов. Справочник. Киев, Наукова Думка, 1976, с. 99.
- [7] Пикаев А.К. Современная радиационная химия. Твердые тела и полимеры. Прикладные аспекты. М., Наука, 1987, с.448.
- [8] Своллоу А. Радиационная химия. Пер.с англ., (Англия, 1973), М., Атомиздат, 1976, 280 с.

ВЗАИМОДЕЙСТВИЕ В ТРОЙНОЙ СИСТЕМЕ
 $\text{Rb}_3\text{ErF}_6\text{-Rb}_3\text{PrF}_6\text{-Rb}_3\text{YF}_6$

Р. Х. АДАМЯН, М. Г. АРУТЮНЯН, Г. Г. БАБАЯН и С. К. ГРИГОРЯН

Ереванский государственный университет

Методами термографического, рентгенографического, кристаллооптического анализов и определением удельной электропроводности исследованы бинарные системы $\text{Rb}_3\text{ErF}_6\text{-Rb}_3\text{PrF}_6$, $\text{Rb}_3\text{ErF}_6\text{-Rb}_3\text{YF}_6$ и тройная система $\text{Rb}_3\text{ErF}_6\text{-Rb}_3\text{PrF}_6\text{-Rb}_3\text{YF}_6$ с построением диаграммы плавкости. Показано, что в бинарных системах образуется непрерывный ряд твердых растворов I типа по классификации Розебома, а в тройной системе – непрерывный ряд твердых растворов как в жидком, так и в твердом состоянии.

Рис. 5, библи. ссылок 6.

Неорганические фториды, особенно фториды редкоземельных элементов, находят широкое применение во многих областях современной техники, таких, как микроэлектроника, лазерная техника, полупроводниковые и люминофорные материалы и т.д.

Дальнейший прогресс в использовании фторидных материалов зависит от выявления закономерностей взаимодействия между различными классами неорганических фторидов. Исследования взаимодействия между фторидами $\text{Me}'\text{Me}'''\text{F}_6$ (Me' – щелочной металл, Me''' – элементы III группы), проведенные методами физико-химического анализа, выявили образование ряда сложных соединений постоянного и переменного составов [1-2]. Однако в литературе мало сведений о системах, в состав которых входят комплексные фторэрибаты, фтор-празеодиматы и фториттраты редких щелочных металлов. Благодаря особенностям строения щелочных катионов их комплексные соединения обладают большой склонностью к образованию новых фаз переменного состава, обладающих физико-химическими свойствами, представляющими практический интерес. В связи с изложенным исследование химического взаимодействия между этими соединениями может привести к обнаружению новых фаз и дать сведения об их свойствах.

Основной целью данной работы является систематическое исследование химического взаимодействия в двойных системах $\text{Rb}_3\text{ErF}_6\text{-Rb}_3\text{PrF}_6$, $\text{Rb}_3\text{ErF}_6\text{-Rb}_3\text{YF}_6$ и тройной системе $\text{Rb}_3\text{ErF}_6\text{-Rb}_3\text{PrF}_6\text{-Rb}_3\text{YF}_6$ с графическим построением их диаграмм плавкости, а также

выявление общих закономерностей образования твердых фаз в исследуемых системах и выяснение возможностей их практического применения.

Экспериментальная часть

Для построения диаграммы плавкости тройной системы $\text{Rb}_3\text{ErF}_6\text{-Rb}_3\text{PrF}_6\text{-Rb}_3\text{YF}_6$ первоначально были исследованы бинарные системы $\text{Rb}_3\text{ErF}_6\text{-Rb}_3\text{PrF}_6$ и $\text{Rb}_3\text{ErF}_6\text{-Rb}_3\text{YF}_6$, составляющие стороны треугольника $\text{Rb}_3\text{ErF}_6\text{-Rb}_3\text{P}_2\text{F}_6\text{-Rb}_3\text{YF}_6$, а данные о системе $\text{Rb}_3\text{PrF}_6\text{-Rb}_3\text{YF}_6$ были взяты из литературы [3]. Последовательному изучению подвергались тройные сплавы, которые были взяты на разрезах, исходящих из угла Rb_3ErF_6 , с постоянными массовыми отношениями гексафторэрибата к гексафториттрату, равными 9:1, 7:3, 1:1, 3:7 и 1:9. Синтез исходных компонентов осуществлялся сплавлением простых фторидов марки “х.ч.” в платиновых тиглях при температурах, на 20-30°C превышающих температуры плавления синтезированного соединения [4-5]. Индивидуальность синтезированных соединений была доказана методами физико-химического анализа.

Учитывая тот факт, что исходные компоненты окисляются, все исследования проводились в инертной среде с подачей фторирующего агента.

На основании согласующихся между собой данных химического, термографического, рентгенофазового, кристаллооптического анализов и измерением удельной электропроводимости были построены диаграммы плавкости бинарных систем $\text{Rb}_3\text{ErF}_6\text{-Rb}_3\text{PrF}_6$, $\text{Rb}_3\text{ErF}_6\text{-Rb}_3\text{YF}_6$ и тройной системы $\text{Rb}_3\text{ErF}_6\text{-Rb}_3\text{PrF}_6\text{-Rb}_3\text{YF}_6$.

По термограммам были определены температуры фазовых превращений в системах $\text{Rb}_3\text{ErF}_6\text{-Rb}_3\text{PrF}_6$ и $\text{Rb}_3\text{ErF}_6\text{-Rb}_3\text{YF}_6$. Для подтверждения данных термического анализа были проведены рентгенофазовые и кристаллооптические исследования некоторых твердых фаз. Для этой цели образцы были приготовлены методом твердофазного синтеза. Хорошо растертые в агатовой ступке образцы, находящиеся в боксе, высыпались в платиновые тигли и выдерживались в сосудах из оптического кварца при 650°C в вакууме 10^{-3} мм рт.ст. в течение 10-15 ч, затем закачивались в четыреххлористом углероде. На основании этих анализов были построены диаграммы плавкости бинарных систем $\text{Rb}_3\text{ErF}_6\text{-Rb}_3\text{PrF}_6$ (рис. 1) и $\text{Rb}_3\text{ErF}_6\text{-Rb}_3\text{YF}_6$ (рис. 2) [6].

Данные ликвидуса были подтверждены измерением электропроводности расплавов.

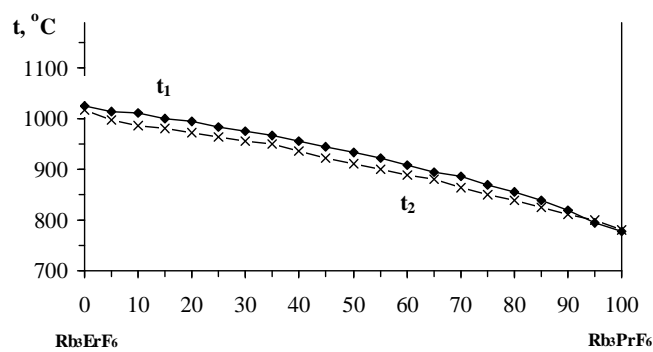


Рис. 1. Диаграмма плавкости бинарной системы Rb_3ErF_6 - Rb_3PrF_6

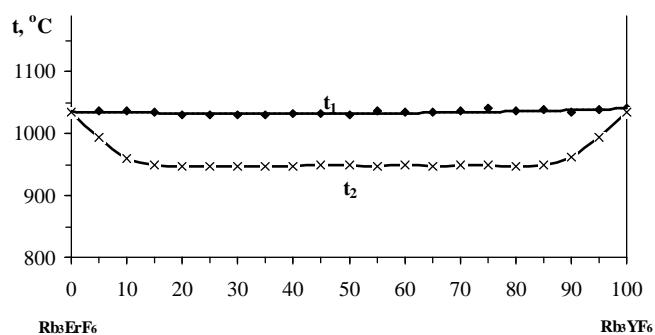


Рис. 2. Диаграмма плавкости бинарной системы Rb_3ErF_6 - Rb_3YF_6

В вышеуказанных бинарных системах образуется непрерывный ряд твердых растворов I типа по классификации Розебома. Образование непрерывного ряда твердых растворов подтверждается плавным изменением показателей преломления образцов (рис. 3 и 4).

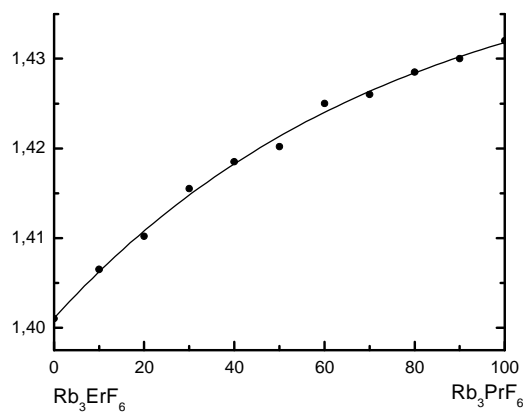


Рис. 3. Изменение показателей преломления в системе Rb_3ErF_6 - Rb_3PrF_6

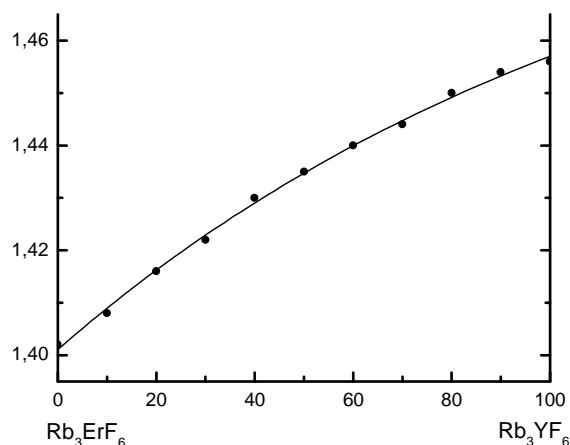


Рис. 4 Изменение показателей преломления в системе Rb_3ErF_6 - Rb_3YF_6

Изоструктурность исходных компонентов (все они кристаллизуются в кубической сингонии с параметрами $a=9,4\text{Å}$ для Rb_3ErF_6 , $a=9,401\text{Å}$ для Rb_3PrF_6 и $a=9,3\text{Å}$ для Rb_3YF_6) также подтверждает образование твердых растворов. Образовавшиеся твердые растворы кристаллизуются в кубической сингонии, причем параметры их элементарных ячеек закономерно возрастают с увеличением концентрации празеодиматов и эрбиатов рубидия.

Исходя из литературных данных и на основании результатов, полученных при изучении двух указанных выше двойных систем и пяти политермических разрезов, построена диаграмма плавкости трехкомпонентной системы, состоящей из гексафторэрбиата рубидия, гексафторпразеодимата рубидия, гексафториттрата рубидия (рис. 5), представленной неограниченной взаимной растворимостью исходных компонентов как в жидком, так и в твердом состоянии.

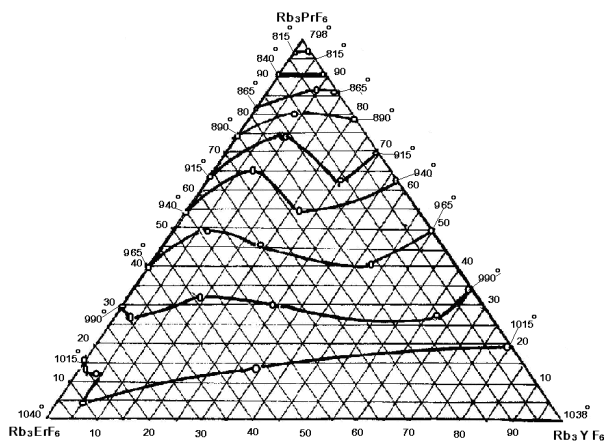


Рис. 5. Диаграмма плавкости тройной системы Rb_3ErF_6 - Rb_3PrF_6 - Rb_3YF_6

**ՓՈԽԱԶՂԵՑՈՒԹՅՈՒՆԸ $\text{Rb}_3\text{ErF}_6\text{-Rb}_3\text{PrF}_6\text{-Rb}_3\text{YF}_6$
ԵՌԿՈՄՊՈՆԵՆՏ ՀԱՄԱԿԱՐԳՈՒՄ**

Ռ. Խ. ԱԴԱՄՅԱՆ, Մ. Գ. ՀԱՐՈՒԹՅՈՒՆՅԱՆ, Հ. Գ. ԲԱԲԱՅԱՆ և Ս. Կ. ԳՐԻԳՈՐՅԱՆ

Թերմոգրաֆիկ, ռենտգենոգրաֆիկ, բյուրեղաօպտիկ անալիզների եղանակներով և տեսակարար էլեկտրահաղորդականության որոշման միջոցով ուսումնասիրվել են $\text{Rb}_3\text{ErF}_6\text{-Rb}_3\text{PrF}_6$, $\text{Rb}_3\text{ErF}_6\text{-Rb}_3\text{YF}_6$ բինար և $\text{Rb}_3\text{ErF}_6\text{-Rb}_3\text{PrF}_6\text{-Rb}_3\text{YF}_6$ եռկոմպոնենտ համակարգերը: Հալույթային դիագրամի կառուցմամբ ցույց է տրվել, որ բինար համակարգերում առաջանում է Ռոզեբոմի դասակարգմամբ I տիպի պինդ լուծույթների անընդհատ շարք, իսկ եռկոմպոնենտ համակարգում՝ պինդ լուծույթների անընդհատ շարք՝ ինչպես հեղուկ, այնպես էլ պինդ վիճակում:

THE INTERACTION IN THE $\text{Rb}_3\text{ErF}_6\text{-Rb}_3\text{PrF}_6\text{-Rb}_3\text{YF}_6$ TERNARY SYSTEM

R. Kh. ADAMYAN, M. G. HAROUTYUNYAN, H. G. BABAYAN and S. K. GRIGORYAN

Fluorides of rare-earth elements and their binary salts with fluorides of alkaline and alkaline-earth metals serve as matrix for high-effective antistokes luminophors. In this connection studying the interaction in the $\text{Rb}_3\text{ErF}_6\text{-Rb}_3\text{PrF}_6\text{-Rb}_3\text{YF}_6$ system and graphical construction of fusibility diagrams, as well as revealing general laws on solid phase formation in this system are of significant practical and theoretical interest.

Interaction in the ternary $\text{Rb}_3\text{ErF}_6\text{-Rb}_3\text{PrF}_6\text{-Rb}_3\text{YF}_6$ system has been studied by thermogravimetric, XRD, crystallooptics analysis and by measuring specific electroconductivity of melts. Binary $\text{Rb}_3\text{ErF}_6\text{-Rb}_3\text{YF}_6$, $\text{Rb}_3\text{ErF}_6\text{-Rb}_3\text{PrF}_6$ systems have been studied for designing the fusibility diagram of $\text{Rb}_3\text{ErF}_6\text{-Rb}_3\text{PrF}_6\text{-Rb}_3\text{YF}_6$ ternary system (data of $\text{Rb}_3\text{YF}_6\text{-Rb}_3\text{YF}_6$ has been taken in literature).

Ternary alloys which have been taken on cuts starting from a corner Rb_3ErF_6 with constant mass relation (9:1; 7:3; 1:1; 3:7 and 1:9) of rubidium hexafluorine proseodimate to rubidium hexafluorine yttriumate were subjected to consecutive research.

Above-mentioned investigation methods showed that in binary $\text{Rb}_3\text{ErF}_6\text{-Rb}_3\text{YF}_6$ systems and $\text{Rb}_3\text{ErF}_6\text{-Rb}_3\text{PrF}_6$ continuous row of solid solutions (by Rosebome classification) are formed.

In the $\text{Rb}_3\text{YF}_6\text{-Rb}_3\text{PrF}_6$ system solid solutions are formed with rupture of homogeneity in the range 12-25 mol% of Rb_3YF_6 .

Resulting from the data obtained the fusibility diagram of the ternary $\text{Rb}_3\text{ErF}_6\text{-Rb}_3\text{PrF}_6\text{-Rb}_3\text{YF}_6$ system has been constructed which was presented by unlimited mutual solubility of initial components both liquid and solid states.

ЛИТЕРАТУРА

- [1] Всесоюзный симпозиум по химии неорганических фторидов. Днепропетровск, 27-30 июня 1978. Тезисы докладов АН СССР и др. М., Наука, 1978, 312 с.
- [2] Коршунов Б.Г., Сафонов В.В., Дробот Д.В. Фазовые равновесия в галогенидных системах, М., Металлургия, 1979, 182 с.
- [3] Арутюнян Р.В., Тер-Аракелян К.А., Бабаян Г.Г. // Уч. записки ЕГУ, 1978, №1, с.46.
- [4] Adamyan R.Kh., Grigoryan S.K., Babayan G.G., Nersisyan S.A. // Chemical Environ. Res., 2001, v.10, p.263.
- [5] Adamyan R.Kh., Grigoryan S.K., Nersisyan S.A., Babayan G.G. // Chemical Environ. Res., 2004, v. 13, p.173.
- [6] Адамян Р.Х. // Информационные технологии и управление, 2001, №1, с.62.

ПРАВИЛА ДЛЯ АВТОРОВ

1. "Химический журнал Армении" публикует на русском, армянском и английском языках оригинальные статьи, письма в редакцию, а также обзорные статьи по специальному заказу редакции. В журнале публикуются статьи, посвященные вопросам общей, физической, неорганической, органической, аналитической химии, химии элементоорганических, высокомолекулярных, природных, биологически активных соединений, а также химической технологии.

2. Объем оригинальной статьи, как правило, не должен превышать 10-12 страниц, обзорной – 25 страниц машинописного текста.

3. Письма в редакцию должны содержать существенно новые результаты, требующие закрепление приоритета. Объем не должен превышать 2-х страниц.

Необоснованное разделение материала по одному вопросу на несколько статей не рекомендуется. Редакция сохраняет за собой право принимать решение о сокращении и объединении материалов.

4. Текст статьи должен быть напечатан через 2 интервала, заголовки не подчеркиваются. Формулы и буквенные обозначения следует четко вписывать черными чернилами.

5. Авторы должны снабжать статьи индексом Универсальной десятичной классификации (УДК).

6. В статьях должно быть принято в основном следующее расположение материала:

а) Заглавие статьи, инициалы и фамилии авторов, полное название учреждения и города.

б) Краткое резюме (500-600 знаков), содержащее изложение основных результатов исследования. Использование сокращений и условных обозначений в резюме недопустимо. К статьям, написанным на русском языке, дополнительно следует представить резюме на армянском и английском языках. Английское резюме рекомендуется представить объемом в одну полную страницу в тщательно отредактированном виде. К статьям, написанным на английском языке, следует представить резюме на русском и армянском языках.

в) Вводная часть, содержащая краткое критическое рассмотрение ранее опубликованных работ в данной области и цель работы.

г) После вводной части следуют разделы: 1) "Методика эксперимента"; 2) "Результаты экспериментов"; 3) "Обсуждение результатов"; 4) "Выводы" (при необходимости). По усмотрению авторов разделы 2 и 3 можно объединить в раздел "Результаты и их обсуждение". Соблюдение данной структуры статьи преследует цель четко выделить в разделе "Методика эксперимента" методы и технику эксперимента, использованные реагенты и аппаратуру, условия проведения эксперимента (состав реагирующей системы, давление, концентрация, диапазон температур и т.п.). В разделе "Результаты эксперимента" приводятся основные экспериментальные данные, включая таблицы, графики. Обсуждение

результатов содержит интерпретации экспериментальных зависимостей и фактов, выявление новых характеристик и закономерностей на их основе, а также обобщение и выводы.

д) В конце статьи приводится список цитированной литературы.

Примерные образцы библиографических описаний

Книги, монографии

[1] Ингольд К., Робертс Б. Реакции свободнорадикального замещения. М., Мир, 1974, с.255.

Статьи из журналов

[1] Григорян Г.О., Мурадян А.Б., Григорян К.Г., Григорян О.В. //Хим. ж. Армении, 1996, т.49, №1, с.35.

Авторские свидетельства и патенты

[1] Лукьянова Р.С., Панасевич-Коляда В.И., А.с. 371220 (1972) //Б.И. 1973, 111.

[2] Пат. 2309747 (1973). ФРГ//С.А. 1973, vol.79, 126622.

Авторефераты диссертаций

[1] Кулешов В.Г. Автореф. дисс. "....." канд. хим. наук. М., МГУ, 1979.

7. Все вновь полученные соединения должны быть названы. Для названий следует пользоваться номенклатурой, рекомендованной ИЮПАК (см. Номенклатурные правила ИЮПАК по химии. М., 1979).

8. Для краткости и наглядности соединения рекомендуется нумеровать, используя римские цифры; при многократном упоминании соединений дается ссылка на их номер. Для распространенных реагентов, растворителей допускается использование буквенных сокращений (напр., ТГФ, ДМСО и т.п.). В остальных случаях сокращения не допускаются.

9. Рисунки выполняются на белой бумаге форматом А4 или А5 четко, черными чернилами или тушью и прилагаются к статье. Размер рисунка не должен превышать 150-200 мм. Кривые на рисунках нумеруются арабскими цифрами, расшифрованными в подписях к рисункам, которые сдаются на отдельных листах бумаги. В тексте статьи указывается место рисунка. На обороте рисунков карандашом указываются фамилии авторов, название статьи, номер рисунка. Не допускается дублирование материала в таблицах, на рисунках и в тексте.

10. Размерность единиц дается в соответствии с Международной системой единиц СИ.

11. Рукопись представляется в трех экземплярах, подписанных всеми авторами. Следует также приложить текст статьи, набранный на дискете в программе Microsoft Word.

12. В случае возвращения статьи автору для доработки первоначальный текст обязательно возвращается в Редакцию вместе с исправленным текстом.

При задержке статьи автором более чем на 1 месяц без уважительных причин первоначальная дата поступления не сохраняется.

13. В авторской корректуре допускаются лишь исправления ошибок, допущенных при наборе.

14. Рукопись статьи представляется в редакцию с приложением обычной документации (направление, акт экспертизы), точного адреса и телефона автора, с которым следует вести переписку.

15. Сокращения названий журналов проводить в соответствии с принятыми в "Реферативном журнале".

CONTENTS

<i>Jones J.C.</i> Reflections on combustion principles as they relate to a miscellany of practical fuels	174
<i>Sandri Tussiwand G., Maggi F., Bandera A., De Luca L.T.</i> Intrinsic structural-ballistic interactions in composite energetic materials. Part I – Experiments.	186
<i>Sandri Tussiwand G., Maggi F., Bandera A., De Luca L.T.</i> Intrinsic structural-ballistic interactions in composite energetic materials. Part I – Modeling	201
<i>Campbell A.N., Cardoso S.S.S., Hayhurst A.N.</i> A scaling and numerical analysis of the effects of natural convection when Sal'nikov's reaction: $P \rightarrow A \rightarrow B$ occurs, together with diffusion and heat transfer in a spherical batch reactor	216
<i>Mansurov Z.</i> Novel nanocarbon materials for different applications.....	235
<i>Tsyganova S.I., Tsyganov A.D.</i> Evolution and conjugating model of carbonic material thermochemical conversion using a nonisothermal kinetic approach	254
<i>Merzlikin V.G., Sidorov O.V., Bezdelkin V.V., Gutierrez Ojeda M.</i> Semitransparent ceramics for heat-insulating covers of the combustion chamber	262
<i>Korsounskii B.L., Samoilenko N.G., Ilchenko A.O.</i> Steady conditions of autocatalytic nonisothermal reactions in CSTR.....	276
<i>Grigoryan R.H.</i> Synthesis and investigation of $YFeTiO_5$ - $YFeSnO_5$ multicomponent system.....	287
<i>Grigoryan R.A., Grigoryan L.A.</i> The syntheses and investigation of the system $CaTiSiO_5$ - $CaSnSiO_5$	290
<i>Grishin A.M.</i> The forest fires	294
<i>Gukasyan P.S.</i> On the mechanism activation of hydrogen and hydrocarbons on the carbides and hydrides obtained by non-isothermal conditions	322
<i>Abovyan L.S., Kharatyan S.L.</i> Combustion laws in the SiO_2 -Al- N_2 system and synthesis of monosialon and silicon nitride-based composites.....	330
<i>Aleksanyan A.G., Dolukhanyan S.K., Hakobyan H.G.</i> The interaction of Sc, Gd, Nd and Pr with hydrogen in the mode of combustion and in the accelerated electrons beam.....	342
<i>Adamyany R.Kh., Haroutyunyan M.G., Babayan H.G., Grigoryan S.K.</i> The interaction in the Rb_3ErF_6 - Rb_3PrF_6 - Rb_3YF_6 ternary system.....	353
Rules for Authors	358